Sunpreet Singh
Chander Prakash
Seeram Ramakrishna
Grzegorz Krolczyk   *Editors*

Advances in Materials Processing

Select Proceedings of ICFMMP 2019

Springer

Lecture Notes in Mechanical Engineering

Lecture Notes in Mechanical Engineering (LNME) publishes the latest developments in Mechanical Engineering - quickly, informally and with high quality. Original research reported in proceedings and post-proceedings represents the core of LNME. Volumes published in LNME embrace all aspects, subfields and new challenges of mechanical engineering. Topics in the series include:

- Engineering Design
- Machinery and Machine Elements
- Mechanical Structures and Stress Analysis
- Automotive Engineering
- Engine Technology
- Aerospace Technology and Astronautics
- Nanotechnology and Microengineering
- Control, Robotics, Mechatronics
- MEMS
- Theoretical and Applied Mechanics
- Dynamical Systems, Control
- Fluid Mechanics
- Engineering Thermodynamics, Heat and Mass Transfer
- Manufacturing
- Precision Engineering, Instrumentation, Measurement
- Materials Engineering
- Tribology and Surface Technology

To submit a proposal or request further information, please contact the Springer Editor of your location:

China: Dr. Mengchu Huang at mengchu.huang@springer.com
India: Priya Vyas at priya.vyas@springer.com
Rest of Asia, Australia, New Zealand: Swati Meherishi at swati.meherishi@springer.com
All other countries: Dr. Leontina Di Cecco at Leontina.dicecco@springer.com

To submit a proposal for a monograph, please check our Springer Tracts in Mechanical Engineering at http://www.springer.com/series/11693 or contact Leontina.dicecco@springer.com

Indexed by SCOPUS. The books of the series are submitted for indexing to Web of Science.

More information about this series at http://www.springer.com/series/11236

Sunpreet Singh · Chander Prakash ·
Seeram Ramakrishna · Grzegorz Krolczyk
Editors

Advances in Materials Processing

Select Proceedings of ICFMMP 2019

Springer

Editors
Sunpreet Singh
Centre for Nanofibers and Nanotechnology
National University of Singapore
Singapore, Singapore

Seeram Ramakrishna
Centre for Nanofibers and Nanotechnology
National University of Singapore
Singapore, Singapore

Chander Prakash
School of Mechanical Engineering
Lovely Professional University
Phagwara, India

Grzegorz Krolczyk
Mechanical Engineering
Opole University of Technology
Opole, Poland

Contents

About the Editors

Dr. Sunpreet Singh is researcher in NUS Nanoscience & Nanotechnology Initiative (NUSNNI). He has received Ph.D in Mechanical Engineering from Guru Nanak Dev Engineering College, Ludhiana, India. His area of research is additive manufacturing and application of 3D printing for development of new biomaterials for clinical applications. He has contributed extensively in additive manufacturing literature with publications appearing in Journal of Manufacturing Processes, Composite Part: B, Rapid Prototyping Journal, Journal of Mechanical Science and Technology, Measurement, International Journal of Advance Manufacturing Technology, and Journal of Cleaner Production. He has authored 10 book chapters and monographs. He is working in joint collaboration with Prof. Seeram Ramakrishna, NUS Nanoscience & Nanotechnology Initiative and Prof. Rupinder Singh, manufacturing research lab, GNDEC, Ludhiana. He is also editor of 3 books- "Current Trends in Bio-manufacturing", "3D Printing in Biomedical Engineering", and "Biomaterials in Orthopaedics and Bone Regeneration - Design and Synthesis". He is also guest editor of 3 journals- special issue of "Functional Materials and Advanced Manufacturing", Facta Universitatis, series: Mechanical Engineering (Scopus Indexed), Materials Science Forum (Scopus Indexed), and special issue on "Metrology in Materials and Advanced Manufacturing", Measurement and Control (SCI indexed).

Dr. Chander Prakash is Associate Professor in the School of Mechanical Engineering, Lovely Professional University, Jalandhar, India. He has received Ph.D in mechanical engineering from Panjab University, Chandigarh, India. His areas of research are biomaterials, rapid prototyping & 3-D printing, advanced manufacturing, modeling, simulation, and optimization. He has more than 11 years of teaching experience and 6 years of research experience. He has contributed extensively to the world in the titanium and magnesium based implant literature with publications appearing in Surface and Coating Technology, Materials and Manufacturing Processes, Journal of Materials Engineering and Performance,

Journal of Mechanical Science and Technology, Nanoscience and Nanotechnology Letters, Proceedings of the Institution of Mechanical Engineers, Part B: Journal of Engineering Manufacture. He has authored 60 research papers and 10 book chapters. He is also editor of 3 books: "Current Trends in Bio-manufacturing"; "3D Printing in Biomedical Engineering"; and "Biomaterials in Orthopaedics and Bone Regeneration - Design and Synthesis". He is also guest editor of 3 journals: special issue of "Functional Materials and Advanced Manufacturing", Facta Universitatis, Series: Mechanical Engineering (Scopus Indexed), Materials Science Forum (Scopus Indexed), and special issue on "Metrology in Materials and Advanced Manufacturing", Measurement and Control (SCI indexed).

Prof. Seeram Ramakrishna is Co-Director, NUS Nanoscience & Nanotechnology Initiative (NUSNNI). He has received Ph.D form University of Cambridge. He is a global leader in electrospinning and nanostructured materials. Since 2001, Seeram's team has contributed significantly to the scientific knowledge in basic research, advances in the process and the applications of Nanofibers. His research resulted in $\sim$ 1,000 peer reviewed articles with $\sim$ 70,000 citations and $\sim$ 120 H-index. He has authored 5 books and $\sim$ 25 book chapters. He has been recognized as a Highly Cited Researcher in Materials Science (www.highlycited.com) for the past four years. Thomson Reuters listed him among the Most Influential Scientific Minds in the World. He has served as NUS vice-president (research strategy), dean of Faculty of Engineering, founding director of NUSNNI, and Bioengineering, founding chair of Global Engineering Deans Council, vice-president of International Federation of Engineering Education Societies, board member of Asia Society for Innovation & Policy. EC/FP7 report lists him among the top four researchers of Singapore. He is recognized as world's number one in nanofiber technologies. He also generated intellectual property in the form of 20 patents, and licensed technologies to industry and start-ups. He mentors Singapore based start-ups namely-Biomers International, Insight Bio Ventures, ceEntek, Hyperion Core and Everest Capital. Moreover he works with companies such as HP, Schlumberger, BASF, Interplex, GE, Mann Hummel, Kaneka, Mitsubishi, Toray, Unitex, GSK, AMT, etc. for value capture in Singapore.

Prof. Grzegorz Krolczyk is Professor in the Opole University of Technology. He is an originator and a Project Manager of OUTech's new Surface Integrity Laboratory. In his career he has held positions such as: head of unit design and technology, product engineer, production manager, product development engineer and production director. He is the co-author and project leader of a project Innovative, energy-efficient diaphragm flow device of a new generation. He is connected with the mechanical industry, where he managed teams from a few to over a hundred people. His industrial engineering experience was gained while working in a European holding company involved in machining of construction materials and plastic injection, where he was responsible for contacts with

companies on technical issues such as quotation and implementation of new products. In professional career he was responsible from the implementation to production of products such as peristaltic pumps, ecological sprayers to spray organic pesticides and many pressure equipment operating e.g. in chemical plants. As a production manager, he was responsible from implementation to production and launching the assembly line for innovative sprayer ultra-low volume spraying system. He is author and co-author of over 80 scientific publications and nearly 20 studies and implementation of industry. The main directions of scientific activity are surface metrology, optimization of geometrical and physical parameters of surface integrity, optimization of production and cutting tool wear analysis in dry machining process of difficult-to-cut materials. He is also editor of various journals and books.

Experimental Investigations on FSW of AA6082-T6 Aluminum Alloy

Tipu, Ramesh Kumar Garg, and Amit Goyal

1 Introduction

Aluminum alloys are getting increased in demand for the manufacturing sector to reduce the weight of the manufactured goods without compromising the strength. Nowadays, these alloys are applied as an alternative to ferrous metals in many applications due to high strength, low density, and good machinability [1]. Aluminum alloys having magnesium and silicon as major alloying element belongs to 6xxx series aluminum alloys and is known to be potential materials for numerous industrial applications [2]. The joining of these alloys has never been easier using conventional welding techniques due to the involvement of several unavoidable drawbacks such as oxidation, loss of alloying elements, porosity, cracks, etc., and continuous research is carried out by researchers and technologists in this field to develop better welding technique for joining these materials [3].

Friction stir welding (FSW) is rising as a new joining practice and having enough competence to weld the materials having a low melting point, especially aluminum alloys. This technique is proving itself a better alternative because of its attractive environmental, metallurgical, mechanical benefits over fusion welding methods [4]. The tensile strength of welded specimens produced by FSW is reported up to 30% greater than that of fusion welding joints [5]. In FSW, a revolving tool is enforced to penetrate the work piece until the probe is fully plunged into the material and the shoulder touches the top facade of the specimens. The heat generated as a result of friction between the workpiece and tool shoulder gets utilized to soften the metal. The rotating probe stirs the softened material and initiates its flow. The axial load applied by the tool shoulder presses the material and a simultaneous extrusion and forging

Tipu · R. K. Garg (✉)
Deenbandhu Chhotu Ram University of Science & Technology, Murthal, Haryana 1310027, India
e-mail: romeshkgarg@gmail.com

A. Goyal
SRM Institute of Science and Technology, Delhi NCR Campus, Modinagar, UP 201204, India

action comes into picture which results in the formation of solid bands between the workpieces [6]. The weld quality of joints produced using FSW is significantly affected by input parameters like welding speed, number of passes, delay/dwell time, tool tilt angle, pin profile, tool material, rotational speed, etc. [7, 8]. FSW of 6xxx series aluminum alloys is the area of great interest for researchers as increasing demand for these alloys added challenges to improve the welding techniques. The quality of joints fabricated from any of the welding methods is the most desirable aspect to avoid any hazardous incidents. Many of the undesired incidents happened in past decades just because of the failure of the weld joints of the structures. Quality can be measured in terms of various performance characteristics of the welding joints like ultimate tensile strength, yield strength, microhardness, microstructure, fatigue strength, corrosion rate, bending strength, etc.

AA6082 alloy belongs to 6xxx series of wrought aluminum alloy series and is commonly used in aerospace, automotive, and recreation industries. Cabibbo et al. compared the conventional pin and pinless FSW with a new approach, namely DS-FSW for joining 6082 aluminum alloy sheets. Nanoindentation characterization and microstructural investigation were carried out to explore the process [9]. Silva et al. studied the impact of FSW parameters on the weld quality of 3 mm-thick AA6082-T6 joints [10]. Three different configurations of joints, viz. butt, lap, and T were fabricated in the study and the input parameters were optimized using Taguchi's technique. Liu et al. carried out a comparative analysis of 1.5 mm-thick AA 6082 joints fabricated by two different welding techniques, namely FSW and laser beam welding [11]. Aval explored the influence of the pin geometry on weld characteristics of FSWed AA 6082 aluminum alloy butt joints [12].

The thorough study of the literature revealed that most of the research work in the area of FSW of AA6082 is limited to studying the effect of a range of input parameters. But the influence of "number of passes" and "rotational speed" simultaneously has not been studied yet. The present investigation is an endeavor to explore the impact of "number of passes" and "rotational speed", on the quality of AA6082-T6 aluminum alloy joints produced using FSW. The study involves the investigation of the macro-structural and mechanical behavior of the welded joints.

2   Materials and Method

In the current work, a 6-mm-thick rolled sheet of the 6082-T6 alloy is used as the base material. A cutting press is used to sever the sheet into 150 mm × 75 mm sized workpieces. The workpiece edges were prepared to ensure the appropriate butt configuration of two pieces to be held together for welding. The chemical composition and mechanical properties of AA6082-T6 alloy are presented in Tables 1 and 2, respectively.

As suggested by the literature, H13 steel is used as a tool material. The geometry of the welding tool was kept constant for all the experiments carried out in the present investigation. Due to more suitability and influential appliance, the square

Table 1 Chemical Composition of the base material

Element	Cr	Cu	Si	Fe	Mg	Mn	Ti	Zn	Al
Weight (%)	0.06	0.04	0.89	0.23	0.78	0.52	0.02	0.05	Balance

Table 2 Mechanical
properties of the base material

Property	Value
Density	2700 kg/m^3
Hardness	121 HV
Yield strength	212 MPa
Young's modulus	70 GPa
Percentage elongation	14%
Ultimate tensile strength	251 MPa
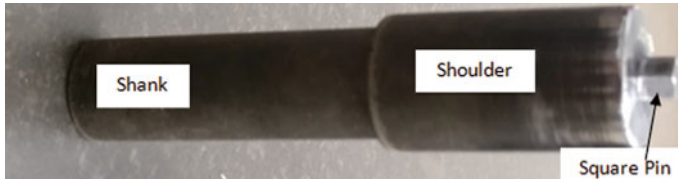
Fig. 1 Tool used for FSW

Table 3 FSW tool
parameters

Parameter	Value
Shank diameter	16 mm
Shoulder diameter	20 mm
Shoulder length	40 mm
Pin diameter	6 mm
Pin profile	Square
Pin length	5.75 mm

pin profiled tool, as presented in Fig. 1, was utilized for welding in the current investigation. Table 3 presents the tool parameters.

The workpieces were positioned using a special fixture during the welding process. The welding was done on a vertical milling machine having an auto-feeding facility, as shown in Fig. 2.

The "number of passes" and "rotational speed" was varied during the experimentation to investigate their effect on the weld characteristics. Table 4 presents the combination of these parameters used for the fabrication of the joints. The FSW parameters other than these two were kept constant as 0.1 mm plunge depth, 63 mm/min welding speed, and 10 s delay/dwell time and 2° tilt angle. Figure 3 shows all the 12 joints fabricated with different combinations of input parameters.

The welded specimens were examined visually to find any welding defects like surface cracks, pinholes, weld line, offsetting, etc. The macro-structural inspection of the weldments was carried out to observe any visible flash and quality of the welded surface.

The specimens for tensile testing were sliced out of the joints in a direction normal to the welding direction as per the ASTM-E8 M04 standard. Two specimens were
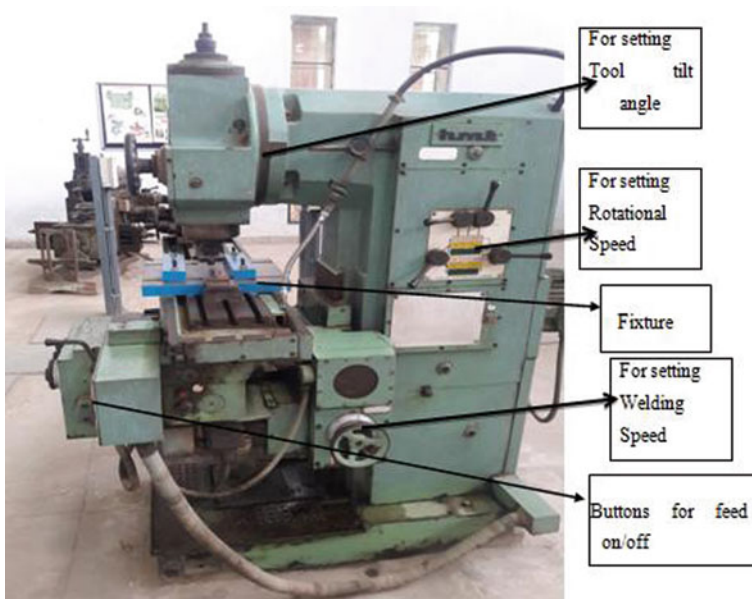
Fig. 2 FSW setup

Table 4 Combination of input parameters for experimentation

Experiment no.	Rotational speed (RPM)	No. of passes
1	700	1
2	700	2
3	700	3
4	900	1
5	900	2
6	900	3
7	1120	1
8	1120	2
9	1120	3
10	1400	1
11	1400	2
12	1400	3

taken from each joint to minimize the experimental error. A hydraulically assisted UTM (Aimil limited, 1000 KN capacity) was utilized to perform tensile tests of the so produced samples and ultimate tensile strength (UTS), percentage elongation (EL), and yield strength were recorded. Figure 4 presents the prepared tensile test specimens.

Fig. 3 FSWed joints of AA6082-T6 aluminum alloy

Fig. 4 Tensile test specimens

The samples for the microhardness test were sliced perpendicular to the direction of welding. A diamond indenter was enforced with 500 g load for 10 s to mark the indent on the specimens in Vicker's Microhardness tester (loading capacity 10–1000 g, make: Rockwell Testing Aids). A metallurgical optical microscope was used for microstructural investigations of the fabricated joints. The polishing of the

samples was done using different grit sizes emery sheets, i.e., C400, C100, C1200, C2000, and C2500. The final polishing of the samples was done using velvet cloth and alumina powder of very fine mesh of 1–3 μm followed by polishing using a diamond paste of very fine mesh. The polished samples were etched for 20 s using modified Keller's reagent for grain boundary delineation.

3 Results and Discussion

The current investigation focuses on the impact of rotational speed and the number of passes on FSWed joints of 6-mm-thick AA6082-T6 alloy. The selection of tool rotational speed in FSW is critical, as these are responsible for heating, softening, and stirring the material. The improper selection of FSW parameters leads to the formation of defects, which consequently affects the weld quality. The improper selection of FSW parameters leads to the formation of defects, which consequently affects the weld quality. The occurrence of defects notably reduces the percentage elongation and strength of the joints. The macro-structural view showing the weld nugget zone and defects in the welded specimens is presented in Fig. 5. The top surface of all samples appears to be smooth except specimens S9 and S12, which were having flashes and a rough top surface. These flashes are created due to the flow of softening material outside the nugget region during the FSW process. The weld nugget of the specimens S1, S3, S11, and S12 were observed to have tunnel defects. Specimen S1 and S3 were fabricated at very low rotational speed, i.e., 700 rpm and the heat generated may be insufficient during the process at a low rotational speed. The low heat input leads to improper fusion of material resulting in tunnel defects. An appropriate combination of "tool rotational speeds" and "number of passes" provides a suitable amount of heat generated and proper environment for adequate material flow during stirring, resulting in defect-free welds.
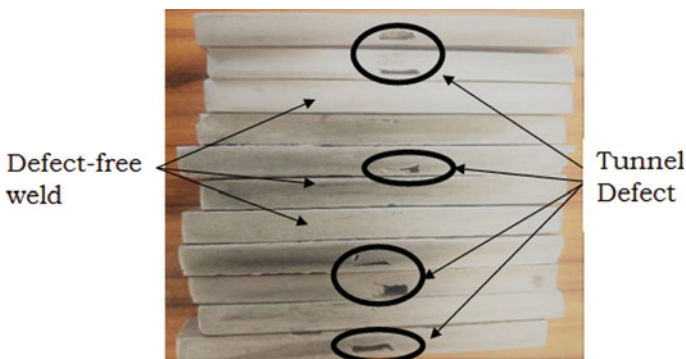
Fig. 5 Macrostructure of the joints

The quality characteristics of the fabricated joints were studied in terms of mechanical properties like tensile strength, microhardness, and microstructure of the weld nugget zone. Table 5 presents the outcome of the mechanical testing of the specimens.

Figure 6 presents the variation in UTS of the joints with rotational speed and the number of passes during the welding. The UTS of all the joints were observed to be lower than that of the parent metal, i.e., 251 MPa. The UTS was observed to be lower for single-pass welded joints irrespective of the rotational speeds. For all three passes, i.e., (1, 2, and 3), the UTS was lowest at 700 rpm. The UTS increases with augmented in rotational speed up to 900 rpm and then a sudden decrease in UTS was observed and this trend was common for all three numbers of passes. This pattern may be described by the refinement of grain size with the augment in the rotational speed up to 900 rpm and then coarsening of grains at very high rotational speeds due to turbulence in the flow of the softening material. The joints fabricated with two

Table 5 Results of mechanical testing of the joints

Experiment no.	UTS (MPa)	YS (MPa)	EL (%)	Microhardness NZ (HV)	Microhardness TMAZ (HV)
1	165.7	129.4	12	75.5	76.2
2	172.5	158.4	4.5	75.0	77.1
3	169.7	146.8	5.5	67.7	66.8
4	175.5	147.1	6.0	68.6	78.8
5	193.9	170.9	4.5	78.4	83.5
6	203.5	174.2	15	86.4	86.3
7	197.7	168.2	6.0	79.6	81.8
8	196.6	166.8	13	72.7	81.1
9	171.1	161.1	2.5	71.8	72.1
10	184.3	163.2	7.0	77.7	76.9
11	184.3	157.3	7.0	70.2	70.1
12	180.3	151.6	8.0	69.3	66.6

Fig. 6 Effect of FSW parameters on UTS
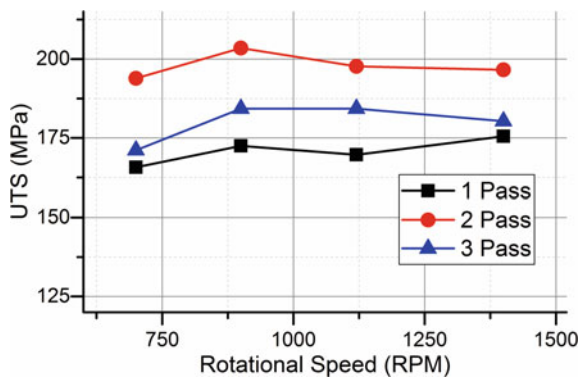
numbers of passes exhibit the highest UTS among their counterparts irrespective of the rotational speed. The joint fabricated at 900 rpm with two numbers of welding passes showed maximum joint strength among all the 12 joints.

The variation of YS of the joints fabricated with different combinations of FSW input parameters is shown in Fig. 7.

The joints made by three pass welding show better YS as compared to the counterparts for all values of rotational speed. The joints fabricated with three numbers of welding passes exhibits better YS than that of fabricated with a single welding pass. The joints produced at 900 rpm rotational speed showed the highest strength among their counterparts for all three numbers of passes. The overall highest UTS were observed for the joint fabricated at 900 rpm rotational speed with two welding passes.

Figure 8 shows the % EL of the joints fabricated with different combinations of FSW input parameters. The joints made by two numbers of welding passes showed better % EL as compared to the counterparts for all values of rotational speed except at 700 rpm, where joint fabricated with single-pass welding showed better % EL. For single-pass welded joints, the highest % EL was observed at 700 rpm, which falls as the rotational speed increases up to 900 rpm and then it increases with further

Fig. 7 Effect of FSW parameters on YS
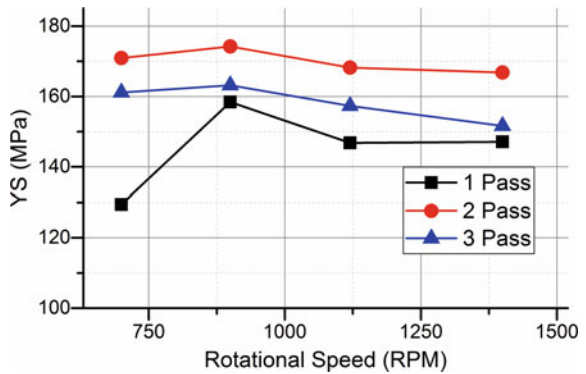
Fig. 8 Effect of FSW parameters on % EL
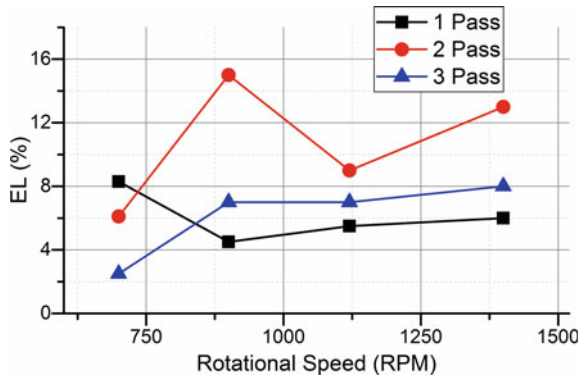
increase in rotational speed. The joint fabricated with two numbers of welding passes showed a different trend of % EL variation, where the least % EL was observed at 700 rpm. The % EL rises with the augment in rotational speed up to 900 rpm and then a sudden fall in % EL was observed at 1120 rpm rotational speed. A continuous increase in % EL was observed as the rotational speed increases from 700 rpm to 1400 rpm, for the joints fabricated with three numbers of welding passes.

Figure 9 presents the microhardness of the weld nugget zone (NZ) of the joints produced by different combinations of input parameters. It can be observed from the figure that weld nugget hardness increases with an increase in tool rotational speed up to 900 rpm and then starts decreasing with further increase in rotational speed and this trend was common for all the joints fabricated with a different number of welding passes. At 700 rpm, the joint fabricated with single-pass welding exhibit higher nugget microhardness than that of fabricated with three numbers of welding passes. But at all other rotational speeds, i.e., 900–1400 rpm, the joints fabricated with three welding passes showed better weld nugget hardness than single-pass welded joints. The highest weld nugget hardness was observed for the joint fabricated at 900 rpm rotational speed with two number of welding passes.

The variation in the microhardness of thermomechanically affected zone (TMAZ) of the joints produced by different combinations of input parameters is shown in Fig. 10.

It can be clearly seen from the figure that TMAZ hardness of the joints fabricated with two numbers of welding passes is higher than their counterparts for all corresponding values of tool rotational speeds. For the joints fabricated with two numbers of welding passes, the TMAZ microhardness increases with an increase in tool rotational speed up to 900 rpm and then starts decreasing with further increase in rotational speed. At 700 and 1400 rpm, the joint fabricated with single-pass welding exhibit higher TMAZ microhardness than that of fabricated with three numbers of welding passes. But at all other rotational speeds, i.e., 900 and 1120 rpm, the joints fabricated with three welding passes showed better TMAZ microhardness than single-pass welded joints. The highest TMAZ microhardness was observed for the joint fabricated at 900 rpm rotational speed with two numbers of welding passes. The input parameters control the heat input and material flow during the FSW process

Fig. 9 Effect of FSW parameters on NZ microhardness
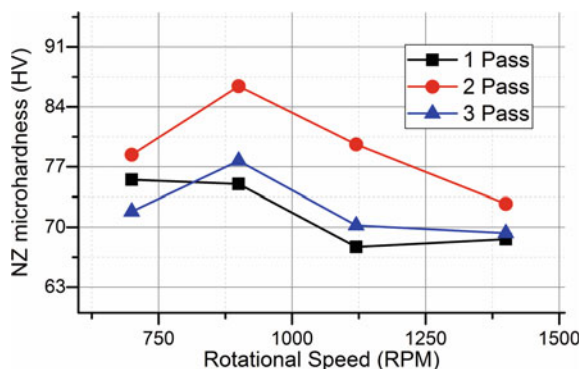
Fig. 10 Effect of FSW parameters on TMAZ microhardness
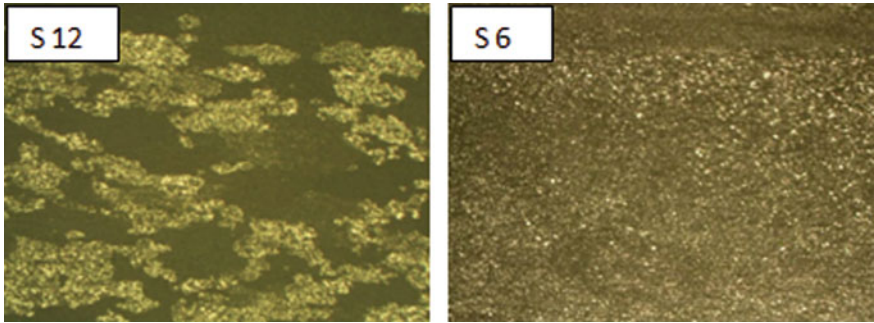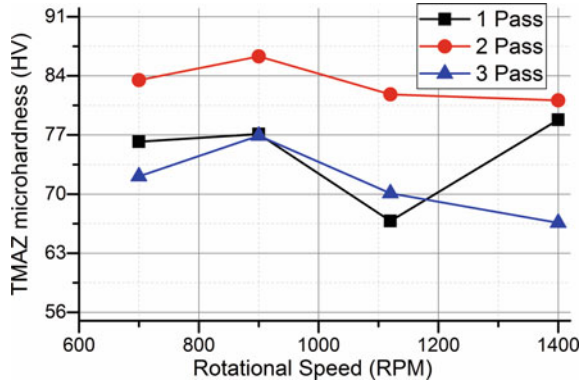
Fig. 11 Microstructure of the weld nugget zone of the joints

which consequently controls the quality of the fabricated weld joint. The dynamic recrystallization of the softening material governs the grain refinement in the weld nugget area, which in turn controls the weld quality. At lower rotational speed, the insufficient amount of heat input causes the defects in the weld bead which ultimately results in deterioration of the weld properties.

Figure 11 shows the grain distribution of samples S6 and S12. The average grain size in the nugget zone of sample S6 (900 rpm, 2 pass) was finer than that of sample S12 (1400 rpm, 3 pass). The fine grains lead to an increase the strength properties of the joint.

4 Conclusion

The present investigation focused on the impact of tool rotational speed and the number of passes during FSW of AA6082-T6 aluminum alloy. The comparative analysis was carried out to study the weld quality in terms of mechanical and microstructural

properties. It was concluded that FSW can be successfully applied to join 6-mm-thick AA6082-T6 aluminum alloy plates in a butt configuration. Low rotational speed leads to produce defected welds as the heat generated is insufficient for appropriate softening and flowing to the material. Tunnel defects were seen in the specimens joined with very high as well as very low rotational speeds. It was revealed that 900 rpm rotational speed with two numbers of passes produces a better quality joint.

References

1. Goyal, A., Garg, R.K.: Establishing mathematical relationships to study tensile behavior of Friction stir welded AA5086-H32 aluminium alloy joints. Silicon **11**(1), 51–65 (2019)
2. El-Danaf, E.A., El-Rayes, M.M.: Microstructure and mechanical properties of friction stir welded 6082 AA in as welded and post weld heat treated conditions. Mater. Des. **46**, 561–572 (2013)
3. Goyal, A., Garg, R.K.: Effect of tool rotational and transverse speed on mechanical properties of friction stir welded AA5086-H32 aluminium alloy. Int. J. Microstruct. Mater. Prop. **12**(1–2), 79–93 (2017)
4. Singh, K., Singh, G., Singh, H.: Review on friction stir welding of magnesium alloys. J. Magnes. Alloys **6**(4), 399–416 (2018)
5. Jamalian, H.M., Farahani, M., Givi, M.B., Vafaei, M.A.: Study on the effects of friction stir welding process parameters on the microstructure and mechanical properties of 5086-H34 aluminum welded joints. Int. J. Adv. Manuf. Technol. **83**(1–4), 611–621 (2016)
6. Goyal, A., Garg, R.K.: Selection of FSW tool parameters for joining Al-Mg4. 2 alloy: an experimental approach. Metallogr. Microstruct. Anal. **7**(5), 524–532 (2018)
7. Ilangovan, M., Boopathy, S.R., Balasubramanian, V.: Effect of tool pin profile on microstructure and tensile properties of friction stir welded dissimilar AA 6061–AA 5086 aluminium alloy joints. Def. Technol. **11**(2), 174–184 (2015)
8. Krasnowski, K., Hamilton, C., Dymek, S.: Influence of the tool shape and weld configuration on microstructure and mechanical properties of the Al 6082 alloy FSW joints. Arch. Civil Mech. Eng. **15**(1), 133–141 (2015)
9. Cabibbo, M., Forcellese, A., El Mehtedi, M., Simoncini, M.: Double side friction stir welding of AA6082 sheets: microstructure and nanoindentation characterization. Mater. Sci. Eng. A **590**, 209–217 (2014)
10. Silva, A.C., Braga, D.F., de Figueiredo, M.A.V., Moreira, P.M.G.P.: Ultimate tensile strength optimization of different FSW aluminium alloy joints. Int. J. Adv. Manuf. Technol. **79**(5–8), 805–814 (2015)
11. Liu, J., Wang, L.L., Lee, J., Chen, R., El-Fakir, O., Chen, L., Dean, T.A.: Size-dependent mechanical properties in AA6082 tailor welded specimens. J. Mater. Process. Technol. **224**, 169–180 (2015)
12. Aval, H.J.: Influences of pin profile on the mechanical and microstructural behaviors in dissimilar friction stir welded AA6082–AA7075 butt joint. Mater. Des. **67**, 413–421 (2015)

Plasma Spray Deposition of HA–TiO$_2$ Composite Coating on Ti–6Al–4V Alloy for Orthopedic Applications

Harjit Singh, Prashant Kulbushan Rana, Jasvinder Singh, Sunpreet Singh, Chander Prakash, and Grzegorz Królczyk

1 Introduction

Titanium and its alloys have been used in medical implants for replacement or repair of organs of the human body in the past few decades, as one of the most common metal biomaterials [1]. Among all the titanium alloys mainly the alpha-beta alloys were widely used in orthopedics and dental applications. This was mainly due to their identical characteristics to human bones such as good fatigue strength, excellent biocompatibility, corrosion resistance, and low specific mass [2]. Although Ti alloys were highly reactive metals which form an oxide (TiO$_2$) layer on the surface, which is extremely stable and it is preventing the material from corrosion [3]. This layer protects Ti alloys against pitting corrosion, intergranular corrosion, and crevice corrosion, causing Ti alloys to be extremely biocompatible and biomimetic [4]. But, it was observed that with the passage of time, the TiO$_2$ oxide layer was degraded and unable to prevent the materials from corrosion in the host body [5]. So, the researchers were actively engaged in developing a suitable coating and their technique to improve the stability of implants in the human body [6]. In recent studies, the development/deposition of a composite on the surface of Ti-based implants to improve the mechanical, wear, corrosion, and bioactivity were found the best solution [7].

The human body, with temperature 37 °C, has an acidic oxygenated saline solution of 7.4 pH, which was a highly corrosive environment and Ti–6Al–4V starts to corrode in this environment [8]. To overcome this problem, materials' surface needs to be modified by deposition of the biocompatible layer on the surface of the material that will standby for longer life span in the human body [9]. The coating or surface

H. Singh · P. K. Rana · J. Singh · S. Singh · C. Prakash (✉)
School of Mechanical Engineering, Lovely Professional University, Phagwara, Jalandhar, India
e-mail: achander.mechengg@gmail.com

G. Królczyk
Opole University of Technology, 76 Proszkowska Street, 45-758 Opole, Poland

modification has been done by various types of deposition processes such as sol-gel [10], biomimetic [11], electrolytic [12], sputtering ion coating [13], physical vapor deposition [14], plasma thermal spray [15], etc. Among them plasma spray deposition process was found potential because their coating characteristics like coating thickness, roughness, chemical composition, and surface porosities can be easily controlled. Moreover, the deposited surface has excellent fatigue, wear, and corrosion resistance [16].

A number of coating materials were deposited by plasma spray deposition for improving the chemical, mechanical, and biological properties of Ti–6Al–4V substrate, which was used as composite coatings. Titania (TiO_2), Alumina (Al_2O_3), and Zirconia (ZrO_2) were used as a composite coating with hydroxyapatite (HA–$Ca_{10}(PO_4)_6OH_2$) in various ratio to boost the mechanical and biological properties of HA coating [17]. But, HA was the bioactive ceramic material which is suitable for surface coating. HA was the main inorganic component of bone. However, it was brittle and has poor mechanical properties [18]. To avoid this, Titania (TiO_2) was preferred as a composite coat with HA due to its corrosion resistance, biological properties, and capability of enhancing the cell growth [19]. The coating layer protects against the release of a metallic ion from the substrate. So, coating particle size has a significant effect on the properties of the coating in the substrate [20]. Properties get improved by decreasing the size of the particles. Recent, advancements in nanotechnology have led to the development of nanocomposite coating [12]. In order to avoid the above-said drawback, owing to its corrosion resistance and biological properties, Titania (TiO_2) was alloyed with HA to deposit composite coat to promote the growth of the cell [19]. The surface film prevents the metal ion from being expelled from the substratum. Therefore, the size of the covering of particles influences the properties of the paint in the substrate [20] significantly. Through increasing the particle size, the properties boost. In recent developments in nanotechnology, nanocomposite coatings were developed [12].

Nonetheless, thermal plasma sprays have several drawbacks, such as mechanical properties modification, peeling and surface degradation, which further reduce the metallurgical bond strength between the coating and the substrate [21]. As a consequence, surface and subsurface defects in the coated substratum surface developed due to these various types. Researchers have made considerable strides in solving the problem of plasma deposition [22]. Among the different process investigated, the recent advance in nanotechnology have to lead to the development of composite coating knows as nanoporous composite coating. The application of micro-size powder particle the performance of the layer and effectively reduces surface defects by depositing biocompatible composite coating on the substrate's surface [23]. Several studies have shown the wide use of Ti and its alloys due to its good mechanical and biological characteristics based on the current literature [24]. In contrast, to date, no reports have been reported focusing on biomaterial Ti–6Al–4V surface modifications in 50–50 wt of HA/TiO_2 nanoporous composite bioceramics. Through incorporating TiO_2, the crystalline of the polymer surface is effectively strengthened. In the human body implant, the biomaterial was in direct contact with muscle tissues so, the initial response of these tissues to the implant depends on its surface properties of

implants. Longevity is a must for orthopedic implants. Although medical orthopedic implants have excellent properties such as strength, elasticity, and biocompatibility [9]. Surface modification of the surface was one of the best solutions for the longevity of the orthopedic implants. The needs of an alternative medical solution have not only demanded better biomedical devices but also more diverse functionality and bioactivity [17].

The success of the implantation depends on the biocompatibility, mechnaical properties, and surface integrity and also the response of the living tissues around the implant during the healing process [25]. There are many other factors that depend on the biocompatibility of implant biomaterials such as material composition, surface wettability, and surface roughness. Therefore, the present investigation attempts have been used to produce bioactive and biomimetic ceramics coating layer that boosts biocompatibility, microhardness, stiffness, and wear resistance of the Ti–6Al–4V alloy by means of nanoporous HA–TiO₂ composite coating using a plasma spray technology. A study was conducted to evaluate the effect of the plasma deposition as a technique of surface modification on biomaterials preparation for biomedical applications on microstructure, morphological studies, coating thickness, microhardness, and surface roughness of the modified surface.

2   Materials and Method

Ti–6Al–4V grade-V well-known biomedical alloy was used as a substrate/workpiece in this research. Ti–6Al–4V alloy having the composition with weight percentage was 0.02% N, 0.05% C, 0.01% H, 0.20% Fe, 0.16% O, 6.10% Al, 3.95% V, and Ti was balanced. Triangular shaped Ti–6Al–4V specimen was prepared for the investigation. High purity (99.9%) powders such as hydroxyapatite (HA) and titania (TiO₂) were used for the coating on the Ti–6Al–4V. The HA and TiO₂ powders of size 10–20 μm irregular in shape was used as coating materials in this study. Both the powder was mixed in the 50–50 wt%. The plasma spray deposition technique was used for the coating of HA–TiO₂ on the Ti–6Al–4V substrate. The spraying parameter used in HA/TiO₂ composite coating is given in Table 1.

Table 1 Plasma spray process parameters

Spraying parameters	Value
Primary gas flow (Argon)	38.5 NLPM
Secondary gas flow (Hydrogen)	2.0 NLPM
Carrier gas flow (Argon)	5.0 NLPM
Voltage	64 V
Current	500 A
Feed rate	32 gm/min
Spray distance	120 mm

The coated surface morphology and surface integrity were investigated by scanning electron microscope (SEM; JEOL JSM-6500) and elemental composition was investigated by energy-dispersive Spectroscopy (EDS). The coating thickness was measured at the cross section of the specimen and mounted in mold analyses. The mounted sample substrate was polished with emery paper with a different grade and etched with Kroll's reagent. X-ray diffractometer (XRD) with Cu Kα radiation analyzed the phase composition of the substratum coating. The XRD angle 2θ was used for scanning from 10° to 90°. The microhardness, surface topology, surface roughness, and chemical composition of coating in the substrate were important parameters for implanting biomaterial interaction with living tissue and affect the biocompatibility of orthopedic application. Vickers hardness tester with a dent load of 0.2 N was utilized to measure the microhardness of the HA/TiO_2-coated substrate. The surface roughness of a plasma-sprayed HA/TiO_2 nanoporous composite coating was measured by Talysurf CCI lite, this is a noncontact 3D surface profile.

3   Results and Discussions

3.1   Microstructural and Elemental Composition Analysis

Figure 1a shows the SEM morphology and EDS spectrum of biomimetic nanoporous composite coating of HA/TiO_2 on coated Ti–6Al–4V alloy by plasma spray deposition technique. Figure 1a shows the SEM micrograph and it can be seen that the deposited surface contains splat like morphology, globules, and characters at a magnification of 500×. This may be because of the impact of molten material on the substrate during the PSD process occurs. During the PSD process, the large amount of thermal energy, produced from the plasma jet, melts the mixture of nanoporous composite powder HA/TiO_2. The mixture of 50–50% HA/TiO_2 was in a molten state. The deposition of HA was presented by yellow color and TiO_2 was presented by red color. The rutile TiO_2 was deposited in the form of splats and globules, whereas HA was deposited in the form of brittle agglomerated structure. The HA deposited layer has a porous structure which enhances the bioactivity of the surface and accelerates the tissue growth or osseointegration in the host body. At higher magnification (500×), porous microstructure and small void on the surface of coated Ti–6Al–4V were observed.

The cross-sectional morphology of plasma-sprayed HA/TiO_2 nanoporous composite coating on the Ti–6Al–4V substrate is shown in Fig. 1b. From the cross section, a micrograph was measured the average value of coating thickness was 250 μm. HA/TiO_2 nanoporous composite coating appears to be well adhered and metallurgically bonded with the Ti–6Al–4V substrate. The coated surface has high adhesion strength (~25 Mpa), which resists the delamination of the coating. The EDS spectrum shows the elemental composition of HA/TiO_2 composite coating and confirmed the presence of rich content of Titanium (Ti), calcium (Ca), phosphorus (P), and oxygen
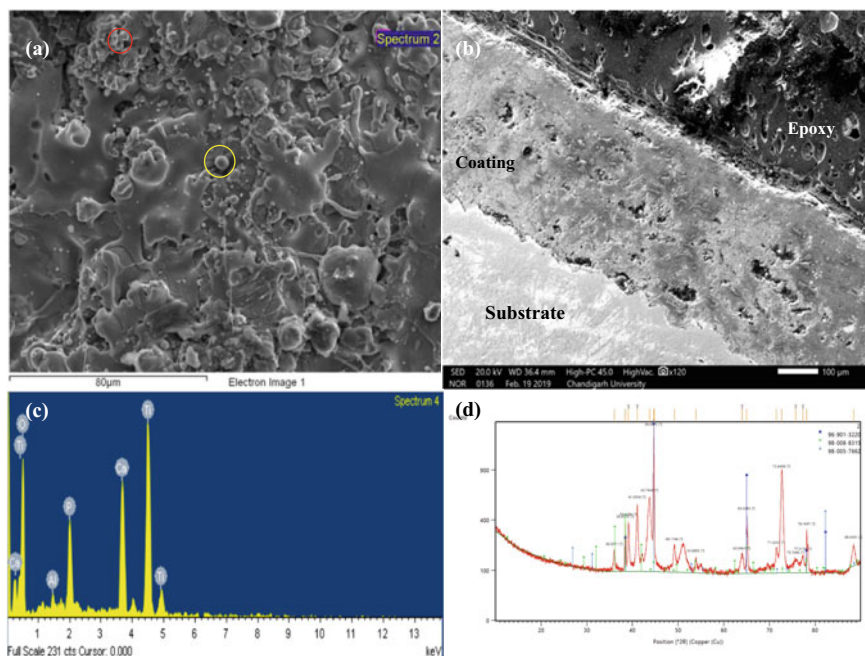
Fig. 1 **a** SEM morphology, **b** cross-sectional SEM morphology, **c** EDS spectrum of HA/TiO$_2$ coating, **d** XRD patterns of Ti–6Al–4V coated surface

(O) elements in the coating, which further conferred the deposition of HA and TiO$_2$ layer, as can be seen in Fig. 1c. The presence of elements revealed the development of biomimetic phases on the coated surface, which enhances the corrosion resistance and bioactivity of the surface. The Ca/P ratio of the nanoporous composite coating observed the presence of other additional phases rather than HA in the coating. The ratio of Ca/P was calculated from the EDS spectrum for the HA/TiO$_2$ nanoporous composite coating ratio 1.68. If the Ca/P ratio was in the range between 1.5 and 2.2, which indicates the presence of tricalcium phosphate (TCP), tetracalcium phosphate (TTCP), and HA compounds on the coating form during decomposition of nanoporous composite powder [26].

The XRD analysis of the sprayed HA/TiO$_2$ nanoporous composite coating on the Ti–6Al–4V substrate is shown in Fig. 1d. The sharp peaks in the XRD pattern clearly show the nanoporous coating of HA/TiO$_2$ was in crystalline in nature. The major hump around 40°–45° range of 2θ. The peaks were fitted within JCPDS reference for Ti–6Al–4V coated surface were 9–169 (β-TCP), 25–1137 (TTCP), and 9–432 (HA). By these results, it is confirmed the formation of Ca$_3$(PO$_4$)$_2$, Ca$_4$(PO$_4$)$_2$O, and rutile on the surface of the substrate. These phases indicate that the coated surface of Ti–6Al–4V was enhanced the biomechanical properties, biocompatibility and bioactive, which has potential applications in orthopedics [27].
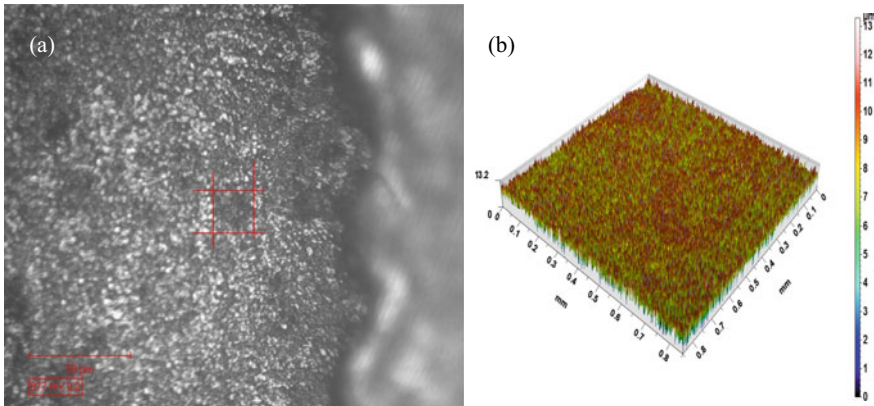
Fig. 2 **a** Microhardness of coating, **b** 3D plot of surface roughness

3.2 Microhardness and Surface Roughness

Figure 2a shows the microhardness measurement of plasma spray deposition of HA/TiO$_2$ nanocomposite coating on Ti–6Al–4V substrate along the polished cross section. The HA/TiO$_2$ nanocomposite coating exhibited a hardness of 277 HV. The value of microhardness shows the good crystallinity form in the nanocomposite coating. Comparison with other research studies showed that coating hardness value has been a significant enhancement. From the indented image, it was clear that the coating developed in the Ti–6Al–4V substrate has excellent metallurgical bonding. Also, the hard surface of the coating has to resist abrasive wear. The surface roughness of the implanted surface beneficial for both bone anchoring and biomechanical stability. The surface roughness was measured by 3D optical measurement system for the coated surface of Ti–6Al–4V substrate and the average value was used as roughness value (Fig. 2b. The average value for coated Ti-substrate was 3.59 μm. This roughness value due to the presence of TiO$_2$ in the nanoporous composite coating.

4 Conclusions

In this research work, HA/TiO$_2$ nanoporous composite coating was successfully deposited by the plasma spray technique on the Ti–6Al–4V substrate. The HA/TiO$_2$ composite powder was prepared by mixing HA and TiO$_2$ powder in 50:50 wt%. The salient conclusions from the present investigation were summarized as the following:

- The composite coating of the HA/TiO$_2$ layer and interface analysis confirmed that there was a strong metallurgical bonding of coating with the Ti–6Al–4V substrate.

- The surface morphology analysis confirmed that nanoporous biomimetic coating has been deposited, which enhanced the bioactivity of the alloy. The thickness of the coating was measured around 250 µm.
- The HA/TiO$_2$ coating exhibits good microhardness ~277 HV, which enhanced the wear resistance of Ti–6Al–4V alloy.
- The surface roughness was measured ~3.59 µm, which helped in cell adhesion and growth of tissues.
- The phase analysis shows the different phases such as TTCP, TCP, etc., on the HA/TiO$_2$-coated surface Ti–6Al–4V, which increase corrosion resistance and biocompatibility of substrate.

References

1. Rocha, R.C., Galdino, A.G.D.S., Silva, S.N.D., Machado, M.L.P.: Surface, microstructural, and adhesion strength investigations of a bioactive hydroxyapatite-titanium oxide ceramic coating applied to Ti–6Al–4V alloys by plasma thermal spraying. Mater. Res. **21**(4) (2018)
2. Prakash, C., Kansal, H.K., Pabla, B.S., Puri, S., Aggarwal, A.: Electric discharge machining–A potential choice for surface modification of metallic implants for orthopedic applications: a review. Proc. Inst. Mech. Eng. Part B J. Eng. Manuf. **230**(2), 331–353 (2016)
3. Chen, Q., Thouas, G.A.: Metallic implant biomaterials. Mater. Sci. Eng. R Rep. **87**, 1–57 (2015)
4. Rautray, T.R., Narayanan, R., Kwon, T.Y., Kim, K.H.: Surface modification of titanium and titanium alloys by ion implantation. J. Biomed. Mater. Res. B Appl. Biomater. **93**(2), 581–591 (2010)
5. Zhao, X., Liu, X., Ding, C., Chu, P.K.: In vitro bioactivity of plasma-sprayed TiO$_2$ coating after sodium hydroxide treatment. Surf. Coat. Technol. **200**(18–19), 5487–5492 (2006)
6. Prakash, C., Kansal, H.K., Pabla, B.S., Puri, S.: Experimental investigations in powder mixed electric discharge machining of Ti–35Nb–7Ta–5Zrβ-titanium alloy. Mater. Manuf. Process. **32**(3), 274–285 (2017)
7. Rosu, R.A., Serban, V.A., Bucur, A.I., Dragos, U.: Deposition of titanium nitride and hydroxyapatite-based biocompatible composite by reactive plasma spraying. Appl. Surf. Sci. **258**(8), 3871–3876 (2012)
8. Kumar, M., Kumar, R., Kumar, S., Prakash, C.: Biomechanical properties of orthopedic and dental implants: a comprehensive review. In: Handbook of Research on Green Engineering Techniques for Modern Manufacturing, pp. 1–13. IGI Global (2019)
9. Prakash, C., Kansal, H.K., Pabla, B.S., Puri, S.: Processing and characterization of novel biomimetic nanoporous bioceramic surface on β-Ti implant by powder mixed electric discharge machining. J. Mater. Eng. Perform. **24**(9), 3622–3633 (2015)
10. Milella, E., Cosentino, F., Licciulli, A., Massaro, C.: Preparation and characterisation of titania/hydroxyapatite composite coatings obtained by sol–gel process. Biomaterials **22**(11), 1425–1431 (2001)
11. Chang, M.C., Ko, C.C., Douglas, W.H.: Preparation of hydroxyapatite-gelatin nanocomposite. Biomaterials **24**(17), 2853–2862 (2003)
12. Lee, C.K.: Fabrication, characterization and wear corrosion testing of bioactive hydroxyapatite/nano-TiO$_2$ composite coatings on anodic Ti–6Al–4V substrate for biomedical applications. Mater. Sci. Eng. B **177**(11), 810–818 (2012)

13. Harun, W.S.W., Asri, R.I.M., Alias, J., Zulkifli, F.H., Kadirgama, K., Ghani, S.A.C., Shariffuddin, J.H.M.: A comprehensive review of hydroxyapatite-based coatings adhesion on metallic biomaterials. Ceram. Int. **44**(2), 1250–1268 (2018)
14. Rahmati, B., Sarhan, A.A., Zalnezhad, E., Kamiab, Z., Dabbagh, A., Choudhury, D., Abas, W.A.B.W.: Development of tantalum oxide (Ta-O) thin film coating on biomedical Ti–6Al–4V alloy to enhance mechanical properties and biocompatibility. Ceram. Int. **42**(1), 466–480 (2016)
15. Gan, J.A., Berndt, C.C.: Plasma surface modification of metallic biomaterials. In: Surface Coating and Modification of Metallic Biomaterials, pp. 103–157. Woodhead Publishing (2015)
16. Tsui, Y.C., Doyle, C., Clyne, T.W.: Plasma sprayed hydroxyapatite coatings on titanium substrates Part 1: Mechanical properties and residual stress levels. Biomaterials **19**(22), 2015–2029 (1998)
17. Prakash, C., Uddin, M.S.: Surface modification of β-phase Ti implant by hydroaxyapatite mixed electric discharge machining to enhance the corrosion resistance and in-vitro bioactivity. Surf. Coat. Technol. **326**, 134–145 (2017)
18. Prakash, C., Singh, S., Pabla, B.S., Uddin, M.S.: Synthesis, characterization, corrosion and bioactivity investigation of nano-HA coating deposited on biodegradable Mg-Zn-Mn alloy. Surf. Coat. Technol. **346**, 9–18 (2018)
19. Ramires, P.A., Romito, A., Cosentino, F., Milella, E.: The influence of titania/hydroxyapatite composite coatings on in vitro osteoblasts behaviour. Biomaterials **22**(12), 1467–1474 (2001)
20. Prakash, C., Singh, S., Singh, M., Verma, K., Chaudhary, B., Singh, S.: Multi-objective particle swarm optimization of EDM parameters to deposit HA-coating on biodegradable Mg-alloy. Vacuum **158**, 180–190 (2018)
21. Fauchais, P., Vardelle, M., Vardelle, A., Goutier, S.: What do we know, what are the current limitations of suspension plasma spraying? J. Therm. Spray Technol. **24**(7), 1120–1129 (2015)
22. Singh, G., Singh, H., Sidhu, B.S.: Characterization and corrosion resistance of plasma sprayed HA and HA–SiO$_2$ coatings on Ti–6Al–4V. Surf. Coat. Technol. **228**, 242–247 (2013)
23. Su, Y., Li, K., Zhang, L., Wang, C., Zhang, Y.: Effect of the hydroxyapatite particle size on the properties of sprayed coating. Surf. Coat. Technol. **352**, 619–626 (2018)
24. Van Noort, R.: Titanium: the implant material of today. J. Mater. Sci. **22**(11), 3801–3811 (1987)
25. Oshida, Y., Guven, Y.: Biocompatible coatings for metallic biomaterials. In: Surface Coating and Modification of Metallic Biomaterials, pp. 287–343. Woodhead Publishing (2015)
26. Sarao, T.P.S., Singh, H., Singh, H.: Enhancing biocompatibility and corrosion resistance of Ti–6Al–4V alloy by surface modification route. J. Therm. Spray Technol. **27**(8), 1388–1400 (2018)
27. Yao, H.L., Hu, X.Z., Bai, X.B., Wang, H.T., Chen, Q.Y., Ji, G.C.: Comparative study of HA/TiO$_2$ and HA/ZrO$_2$ composite coatings deposited by high-velocity suspension flame spray (HVSFS). Surf. Coat. Technol. **351**, 177–187 (2018)

Review on Surface Modifications of the Workpiece by Electric Discharge Machining

Vipin Handa, Parveen Goyal, and Rajesh Kumar

1 Introduction

Electric discharge machining (EDM) is conceivably productive to machine extremely hard materials that cannot be machined by a traditional machining process. Despite the fact that EDM is a machining operation, yet some interesting facts have come out in researches which show that there is an impressive material exchange from cathode to the workpiece amid electric discharge machining, a meager layer of the material of electrodes gets deposited on the machined surface of the workpiece. Because of this alteration, properties of the workpiece get changed giving a decent abrasion-resistant area and smaller scale hardness to the surface. This marvel is known as surface alloying and it delivers another region of research by which the surface properties of the workpiece can be improved deliberately for a given reason utilizing this unpredictable strategy for machining.

Electric discharge machining is an unconventional machining method. Even today the exact scenario of the mechanism of EDM remains unclear still the most favorable theory is that in EDM two electrodes are connected to the electric power supply and current is passed through them when they are sufficiently close to produce a spark. Following this phenomenon when the electric spark is produced between the workpiece and the tool, this electric spark produces plasma of electrons. This plasma collides with the surface of the workpiece with great coerce and some of the material vaporizes from the tool as well as the workpiece.

In EDM, dielectric also plays a significant role. Both the electrodes remain dipped inside the dielectric at the time of spark generation. Dielectric is basically an insulator that breaks down into ions and allows the current to pass through only for that particular instant when such a huge amount of voltage is applied across the electrodes. This voltage is known as breakdown voltage and depends upon the type of dielectric

V. Handa · P. Goyal (✉) · R. Kumar
Mechanical Engineering Department, UIET, Panjab University, Chandigarh, India
e-mail: pgoyal@pu.ac.in

used in the process. The selection of dielectric also plays a very important role. Chen et al. used Ti–6Al–4V alloy, with low thermal conductivity and high melting point temperature [1]. In this study, it was found that the material removal rate (MRR) increases and the relative tool wear ratio decreases with distilled water as dielectric rather than kerosene oil.

Electric discharge machining is adequate to machine material regardless of its hardness, but the only requirement is that the tool as well as the workpiece should be electrically conductive. Figure 1 shows a schematic diagram of the basic elements of EDM [2].

The examination of the machined surface reveals that there is a formation of three different types of layers as shown in Fig. 2. Besides the workpiece being machined some of the material from the tool migrates to the workpiece and this leads to the

Fig. 1 Basic components of the EDM [2]
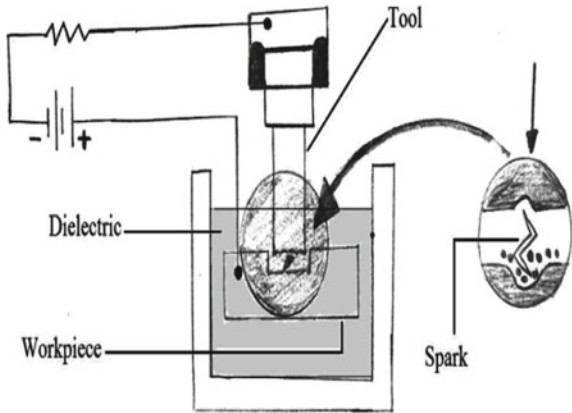
Fig. 2 Different layers after EDM
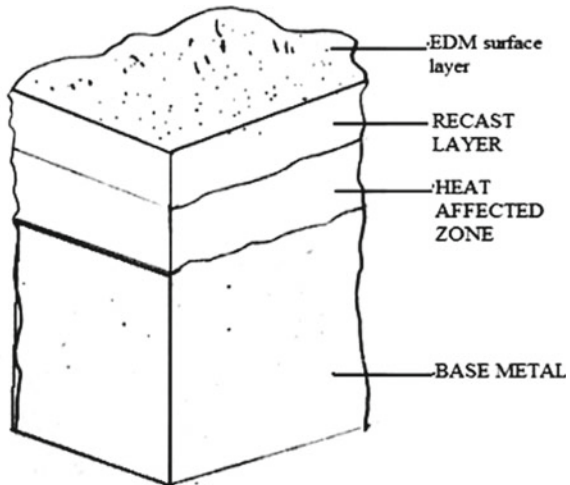
formation of the very first layer. The surface of the workpiece as well as substrate both are modified during the EDM process [3]. The second layer is the recast layer which is of the workpiece material itself. Recast layer is formed when the workpiece material is converted into the molten state but is not expelled away by the dielectric and hence solidifies on the surface of the workpiece due to quenching by the dielectric. Quenching phenomenon always leads to hardening so this recast layer is also very hard and brittle which can form micro-cracks.

Properties of surface and the subsurface differ from the base material and sometimes these properties are induced intentionally due to their better response in the environment in which the workpiece is to be used. For example, better resistance to corrosion and abrasion is obtained during the electric discharge machining of a steel workpiece due to the formation of white layers [4]. This is because some carbon is released during the breakdown of the dielectric.

Tan and Yeo [4] observed that with different machining conditions, there are significant changes in the recast layer whose thickness varies with the amount of powder mixed in the dielectric.

2 Literature Review

It was in 1943 when it was discovered for the first time that if the impact of the spark is controlled by any dielectric medium then the erosion effect of the spark can be used effectively to perform machining. Since then, continuous efforts have been made by the researchers in the surface modification of the workpiece during the EDM process. Simao et al. [5] concluded from their research that the use of WC/Co resulted in the creation of a modified surface layer having fewer micro-cracks.

Chen and Lin [6] discussed the feasibility of surface modification using TiC particles into the dielectric which is used in EDM coupled with ultrasonic machining (USM). Aspinwall et al. [7] used sintered TiC/WC/Co electrodes and WC/Co and results showed that there was a creation of a white layer with Ti and W. Prakash et al. [8] found that titanium (Ti) alloy can be used in a better way for the long-term hard body tissue, and the surface of the alloy is of main concern for its respective use, so they worked on the surface modification of the Ti alloy.

Kumar and Batra [9] concluded that a considerable amount of material can be transferred to the workpiece from the dielectric medium having mixed tungsten powder during the EDM surface modification process. Furutani et al. [10] observed the X-ray diffraction analysis of titanium and a layer of titanium carbide. He concluded that carbon was given out by the dielectric's breakdown.

Gangadhar et al. [11] found that surface topology of steel was changed when it was machined by sintered electrodes made up of 90% Copper and 10% tin. the electrodes were used in Reverse polarity and surface topology was detected. It was observed that the surface of Steel contained Cu_3Sn and some other phases were also there.

Lin et al. [12] explore surface alloying by means of a novel consolidated procedure of EDM utilizing the Taguchi method. Results demonstrated that the consolidated procedure successfully improves the surface harshness and wipes out the micropores brought about by EDM.

Marafona and Wykes [13] found that a layer of carbon, black in color was deposited on the tool. This carbon layer further stopped the erosion of electrode which allowed the use of high current intensity and hence increased amount of material removal rate.

Mohri et al. [14] used Cu, Al, WC, and Ti as electrodes with hydrocarbon oil as a dielectric. The EDM was carried out on carbon steel and aluminum. It was found that the surface characteristics were changed to a great extent.

Gangadhar et al. [11] used tungsten carbide sintered electrodes made up of 60% Fe and 40% WC and observed by energy dispersive analysis that tungsten carbide got transferred to the machined surface. Along with tungsten carbide, iron carbide was also deposited on the surface layer. Surface wear resistance was improved by 25–60%. Tsai et al. [15] reported a transfer of chromium and copper particles from the electrode to the workpiece using negative polarity.

Tsunekawa et al. [16] explored surface modification of aluminum using compact electrodes of 64% Ti and 36% of Al. In this study, fine dendritic particles of titanium carbide were observed on the workpiece. Dielectric used was kerosene and the negative polarity was used for the tool.

Yan et al. [17] used a mixture of urea and water dielectric to get TiN on the work surface. Improved wear characteristics were observed. The pulse duration was increased. Microhardness of the value of 250Hk was achieved. The significant work carried out recently by many researchers related to surface modification has been summarized in Table 1.

Recently, the effect of optimized parameters on EDM performance and surface modification investigations has been explored [28–36]. This results in a modified grain structure of the machined surface [37–44].

3 Applications

EDM finds its application in many processes such as micromachining using EDM. As the size of the product starts decreasing, its machining becomes more difficult. But with the help of EDM, machining up to microlevel is also possible such as drilling of micro-holes known as micro-electric discharge drilling [45].

Another application of EDM can be found while machining ceramic materials. These days ceramic materials have found their application in various industrial applications. EDM is very useful in machining very hard materials and geometrically complex shapes [46].

EDM is employed in the machining of very difficult to be machined materials and has replaced traditional manufacturing processes. We use EDM to process these materials using electrodes manufactured by powder metallurgy.

Table 1 Summary of significant work carried out recently related to surface modification

S no.	Author/year and journal	Research work	Conclusion
1.	Zhang et al. [18] Applied Surface Science (2011)	'Investigations on the surface recast layer machined by sinking EDM'	More surface roughness, higher thickness, and better microhardness was observed when the recast layer was created in W/O emulsion
2.	Kumar et al. [19] Journal of Materials Processing Technology (2009)	'A review on the surface modification by electrical discharge machining'	Considerable improvements in surface properties were observed
3.	Hirao et al. [20] International Journal of Electrical Machining (2016)	'A study about deposition machining with reciprocating rotation in air gap using EDM'	The deposition machining characteristics depend on the capacitor and electrode diameter. Amount of deposition increases when the capacitance is large and the diameter of the electrode is small
4.	Kuo et al. [21] Journal of Materials Processing Technology (2017)	'Effect of electrodes design on surface modification'	Surface modification was achieved with a depth of about six microns
5.	Batish and Bhattacharya [22] Materials Science Forum (2011)	'Effect of powder metallurgy electrodes on surface modification of Die-Steels'	Better microhardness was obtained with tungsten-copper electrode showing the transfer mechanisms on the workpiece surface
6.	Bains et al. [23] Silicon (2019)	'Effect of magnetic field on surface alloying in powder mixed electrical discharge machining'	The following observations were made: • Microhardness value decreases • Recast layer thickness decreases
7.	Chen et al. [24] Applied Surface Science (2014)	'Investigations of recast layer on implant surface in powder mixed EDM'	As the input parameters like pulse duration concentration and current increases, recast layer thickness also increases
8.	Trauth et al. [25] International Journal of Material Forming (2016)	'Effect of the fatigue strength of Inconel 718 workpiece'	Machine hammer peening was found to be suitable to enhance the fatigue strength of Inconel 718

<div align="right">(continued)</div>

Table 1 (continued)

S no.	Author/year and journal	Research work	Conclusion
9.	Mohanty et al. [26] IOP Conference Series (2018)	'Effect of tungsten disulphide powder on Ti–6Al–4V workpiece in powder mixed EDM'	Recast layer was found to be formed on the workpiece (Ti–6Al–4V)
10.	Gill and Kumar [27] The International Journal of Advanced Manufacturing Technology (2015)	'Effect of copper tungsten electrode on surface alloying of H11 workpiece'	Tungsten carbide was present on the workpiece surface and it was concluded that surface modification took place resulting in the transfer of material from the copper-tungsten electrode

4 Conclusion

The industrial revolution has led to the invention of very important and different types of material, which cannot be machined by traditional machining methods due to their properties which are quite different from the metals or other materials used before. So to overcome this problem, nonconventional machining methods like EDM had to be developed and for these nontraditional methods, electrodes had to be made with some special properties like hardness, good thermal properties, ease of manufacturing, less cost, etc. The utilization of EDM is developing quickly. After a detailed examination of the literature work on surface adjustment by this procedure, these inferences can be made:

1. The area of surface alloying utilizing EDM is still at the exploratory stage. Various research contemplates have been completed; noteworthy upgrades in surface properties have been accounted for and the plausibility of the procedure is settled. In any case, a lot more issues should be tended to before the strategy can be well acknowledged.
2. The exchange of material from powder metallurgy based electrodes offer a reasonable option in contrast to the next presently utilized costly techniques for surface alteration. However, the use of regular electrodes has not been achieved successfully for this application.
3. The impact of input parameters, i.e., pulse duration and discharge current has been thought about in different research works yet variety in pulse interim has not been examined. There is a need to autonomously examine the impact of this significant information on surface modification.
4. The vast majority of the accessible research takes a shot at powder-mixed dielectric and has contemplated the effect of such machining on performance measures.

5. A near examination of the two techniques for surface alteration, that is, material exchange from powders suspended in the dielectric medium and material exchange from electrodes is absent in the accessible literature.

References

1. Chen, S.L., Yan, B.H., Huang, F.Y.: Influence of kerosene and distilled water as dielectrics on the electric discharge machining characteristics of Ti–6A1–4V. J. Mater. Process. Technol. **87**(1–3), 107–111 (1999)
2. Abu Zeid, O.A.: On the effect of electro discharge machining parameters on the fatigue life of AISI D6 tool steel. J. Mater. Process. **68**(1), 27–32 (1997)
3. Leuven, K.U., Integrity, S.: Study of the white layer of a surface machined by die-sinking electro-discharge machining. **44**(1), 169–172 (1995)
4. Tan, P.C., Yeo, S.H.: Investigation of recast layers generated by a powder-mixed dielectric micro electrical discharge machining process. Proc. Inst. Mech. Eng. Part B J. Eng. Manuf. **225**(7), 1051–1062 (2011)
5. Simao, J., Lee, H., Aspinwall, D., Dewes, R., Aspinwall, E.: Workpiece surface modification using electrical discharge machining. Int. J. Mach. Tools Manuf. **43**(2), 121–128 (2003)
6. Chen, Y.F., Lin, Y.C.: Surface modifications of Al–Zn–Mg alloy using combined EDM with ultrasonic machining and addition of TiC particles into the dielectric. J. Mater. Process. Technol. **209**(9), 4343–4350 (2009)
7. Aspinwall, D., El-menshawy, F., Meadows, K., Sima, J.: Surface alloying using PM composite electrode materials when electrical discharge texturing hardened AISI D2. J. Mater. Process. Technol. **127**, 211–216 (2002)
8. Prakash, C., Kansal, H.K., Pabla, B.S., Puri, S., Aggarwal, A.: Electric discharge machining: a potential choice for surface modification of metallic implants for orthopedic applications: a review. Proc. Inst. Mech. Eng. Part B J. Eng. Manuf. **230**(2), 331–353 (2016)
9. Kumar, S., Batra, U.: Surface modification of die steel materials by EDM method using tungsten powder-mixed dielectric. J. Manuf. Process. **14**(1), 35–40 (2012)
10. Furutani, K., Saneto, A., Takezawa, H., Mohri, N., Miyake, H.: Accretion of titanium carbide by electrical discharge machining with powder suspended in working fluid. Precis. Eng. **25**, 138–144 (2001)
11. Gangadhar, A., Shunmugam, M.S., Philip, P.K.: Surface modification in electro discharge processing with a powder compact tool electrode. Wear **143**(1), 45–55 (1991)
12. Lin, Y.C., Yan, B.H., Huang, F.Y.: Surface improvement using a combination of electrical discharge machining with ball burnish machining based on the Taguchi method. Int. J. Adv. Manuf. Technol. **18**, 673–682 (2001)
13. Marafona, J., Wykes, C.: New method of optimizing material removal rate using EDM with copper-tungsten electrodes. Int. J. Mach. Tools Manuf. **40**(2), 153–164 (2000)
14. Mohri, N., Saito, N., Tsunekawa, Y., Technological, T., Kinoshita, N.: Metal surface modification by electrical discharge machining with composite electrode. CIRP Ann. **42**(1), 219–222 (1993)
15. Tsai, H.C., Yan, B.H., Huang, F.Y.: EDM performance of Cr/Cu-based composite electrodes. Int. J. Mach. Tools Manuf. **43**(3), 245–252 (2003)
16. Tsunekawa, Y., Okumiya, M., Mohri, N.: Surface modification of aluminum by electrical discharge alloying. Mater. Sci. Eng. A **174**, 193–198 (1994)
17. Yan, B.H., Tsai, H.C., Huang, F.Y.: The effect in EDM of a dielectric of a urea solution in water on modifying the surface of titanium. Int. J. Mach. Tools Manuf. **45**(2), 194–200 (2005)
18. Zhang, Y., Liu, Y., Ji, R., Cai, B.: Study of the recast layer of a surface machined by sinking electrical discharge machining using water-in-oil emulsion as dielectric. Appl. Surf. Sci. **257**(14), 5989–5997 (2011)

19. Kumar, S., Singh, R., Singh, T.P., Sethi, B.L.: Surface modification by electrical discharge machining: a review. J. Mater. Process. Technol. **209**(8), 3675–3687 (2009)
20. Hirao, A., Tani, T., Gotoh, H., Aoshima, S., Mohri, N.: Study of deposition machining using electrical discharge with reciprocating rotation in air gap. Int. J. Electr. Mach. **21**, 2–7 (2016)
21. Kuo, C., Kao, H., Wang, H.: Novel design and characterization of surface modification in wire electrical discharge machining using assisting electrodes. J. Mater. Process. Tech. **244**, 136–149 (2017)
22. Batish, A., Bhattacharya, A.: Mechanism of material deposition from powder, electrode and dielectric for surface modification of H11 and H13 die steels in EDM process. Mater. Sci. Forum **701**, 61–75 (2011)
23. Bains, P.S., Sidhu, S.S., Payal, H.S., Kaur, S.: Magnetic field influence on surface modifications in powder mixed EDM. Silicon **11**(1), 415–423 (2019)
24. Chen, S.L., Lin, M.H., Huang, G.X., Wang, C.C.: Research of the recast layer on implant surface modified by micro-current electrical discharge machining using deionized water mixed with titanium powder as dielectric solvent. Appl. Surf. Sci. **311**, 47–53 (2014)
25. Trauth, D., Klocke, F., Welling, D., Terhorst, M., Mattfeld, P., Klink, A.: Investigation of the surface integrity and fatigue strength of Inconel 718 after wire EDM and machine hammer peening. Int. J. Mater. Form. **9**(5), 635–651 (2016)
26. Mohanty, S., Kumar, V., Tyagi, R., Kumar, S., Bhushan, B., Das, A.K., Dixit, A.R.: Surface alloying using tungsten disulphide powder mixed in dielectric in micro-EDM on Ti–6Al–4V. IOP Conf. Ser. Mater. Sci. Eng. **377**(1), 012040 (2018)
27. Gill, A.S., Kumar, S.: Surface alloying of H11 die steel by tungsten using EDM process. Int. J. Adv. Manuf. Technol. **78** (9–12), 1585–1593 (2015)
28. Goyal, P., Suri, N.M., Kumar, S., Kumar, R.: Investigating the surface properties of EN-31 die-steel after machining with powder metallurgy EDM electrodes. Mater. Today: Proc. **4**(2), 3694–3700 (2017)
29. Goyal, P., Kumar, S., Kumar, R.: Effect of high chromium platinum steel with composite copper-tin material electrode on electric discharge machining performance. Mater. Today: Proc. **5**(14), 27726–27731 (2018)
30. Antil, P., Singh, S., Singh, S., Prakash, C., Pruncu, C.: Metaheuristic approach in machinability evaluation of SiCp/glass fiber reinforced PMCs during electrochemical discharge machining process. Meas Control (2019)
31. Basak, A., Pramanik, A., Prakash, C.: Surface, kerf width and material removal rate of Ti–6Al–4V titanium alloy generated by wire electrical discharge machining. Heliyon **5**(4), 01473 (2019)
32. Prakash, C., Singh, S., Pruncu, C.I., Mishra, V., Królczyk, G., Pimenov, D.Y., Pramanik, A.: Surface modification of Ti–6Al–4V alloy by electrical discharge coating process using partially sintered Ti–Nb electrode. Materials **12**(7), 1006 (2019)
33. Prakash, C., Singh, S., Pabla, B.S.: Multi-objective optimization of EDM parameters to deposit HA-containing coating on Mg-Zn-Mn alloy using particle swarm optimization. Vacuum **158**, 180–190 (2018)
34. Prakash, C., Singh, S., Pabla, B.S., Uddin, M.S.: Synthesis, characterization, corrosion and bioactivity investigation of nano-HA coating deposited on biodegradable Mg-Zn–Mn alloy. Surf. Coat. Technol. **346**, 9–18 (2018)
35. Prakash, C., Uddin, M.S.: Surface modification of β-phase Ti implant by hydroxyapatite mixed electric discharge machining to enhance the corrosion resistance and in-vitro bioactivity. Surf. Coat. Technol. **236**, 134–145 (2017)
36. Aliyu, A.A., Abdul-Rani, A.M., Ginta, T.L., Prakash, C., Axinte, E., Razak, M.A., Ali, S.: A review of additive-mixed electric discharge machining: current status and future perspectives for surface modification of biomedical implants. Adv. Mater. Sci. Eng. (2017)
37. Aliyu, A.A., Abdul-Rani, A.M., Ginta, T.L., Prakash, C., Axinte, E., Fua-Nizan, R.: Fabrication of nanoporosities on metallic glass surface by hydroxyapatite mixed EDM for orthopedic application. Accepted in Malaysian J. Fundam. Appl. Sci. (2017)

38. Prakash, C., Kansal, H.K., Pabla, B.S., Puri, S., Aggarwal, A.: Electric discharge machining—a potential choice for surface modification of metallic implants for orthopedic applications: a review. Proc. Inst. Mech. Eng. Part B J. Eng. Manuf. **230**(2), 231–253 (2016)
39. Prakash, C., Kansal, H.K., Pabla, B.S., Puri, S.: Processing and characterization of novel biomimetic nanoporous bioceramic surface on β-Ti implant by powder mixed electric discharge machining. J. Mater. Eng. Perform. **24**, 3622–3633 (2015)
40. Prakash, C., Kansal, H.K., Pabla, B.S., Puri, S.: Experimental investigations in powder mixed electrical discharge machining of Ti–35Nb–7Ta–5Zr β-Ti alloy. Mater. Manuf. Process **32**(3), 274–285 (2017)
41. Prakash, C., Kansal, H.K., Pabla, B.S., Puri, S.: Effect of surface nano-porosities fabricated by powder mixed electric discharge machining on bone-implant interface: an experimental and finite element study. Nanosci. Nanotechnol. Lett. **8**(10), 815–826 (2016)
42. Prakash, C., Kansal, H.K., Pabla, B.S., Puri, S.: Multi-objective optimization of powder mixed electric discharge machining parameters for fabrication of biocompatible layer on β-Ti alloy using NSGA-II coupled with Taguchi based response surface methodology. J. Mech. Sci. Technol. **30**(9), 4195–4204 (2016)
43. Prakash, C., Kansal, H.K., Pabla, B.S., Puri, S.: Powder mixed electric discharge machining an innovative surface modification technique to enhance fatigue performance and bioactivity of β-Ti implant for orthopaedics application. J. Comput. Inf. Sci. Eng. **14**(4), 1–9 (2016)
44. Prakash, C., Kansal, H.K., Pabla, B.S., Puri, S.: Potential of powder mixed electric discharge machining to enhance the wear and tribological performance of β-Ti implant for orthopedic applications. J. Nanoeng. Nanomanufa. **5**(4), 261–269 (2015)
45. Beri, N., Maheshwari, S., Sharma, C., Kumar, A.: Technological advancement in electrical discharge machining with powder metallurgy processed electrodes: a review. Mater. Manuf. Process. **25**(10), 1186–1197 (2010)
46. Lauwers, B., Kruth, J.P., Liu, W., Eeraerts, W., Schacht, B., Bleys, P.: Investigation of material removal mechanisms in EDM of composite ceramic materials. J. Mater. Process. Technol. **149**(1–3), 347–352 (2004)

Experimental Investigations on Heat Generation and Surface Roughness During Orthogonal Machining of Stainless Steel Using Bio-based Oil MQL

Gurpreet Singh, Vivek Aggarwal, Jujhar Singh, Amoljit Singh Gill, and Shubham Sharma

1 Introduction

Mass production of steel parts generates high cutting zone temperature. Such a hot temperature affects both the tool and the workpiece. Higher cutting temperature ends up in fast tool wear, loss of type stability, poor surface finish, dimensional quality deviation, and microstructure changes. These issues will be decreased by using lubricants in numerous ways like wet and flooded conditions. However, this way of lubrication typically creates a range of issues like environmental pollution health hazards, wastage disposal, and ultimately proves to become uneconomical [1]. The work of cutting liquid decreases the cutting temperature, device wear, and surface unpleasantness, whenever connected in an ideal amount and is the best technique. The quality of cutting fluid and the nature of selected lubricators put an imperative job in decreasing ecological contamination and upgrading the machining execution. Anyway today flood cooling strategy has turned out to be tricky, because of exacting principles associated with the bar of ecological contamination. In this procedure, a high progression of cutting liquids brings about ecological debasement like soil contamination, well-being risks and the most critical wastage transfer of cutting liquids [2]. Ointment volume, if there should be an occurrence of flood grease conjointly, needs optional set up that includes the cooling estimation of flood oil. Many creating nations have denied the work of flood grease and hence dry machining is of

G. Singh (✉) · V. Aggarwal · J. Singh · A. S. Gill
Department of Mechanical Engineering, I.K.G.P.T.U Main Campus, Kapurthala, Punjab, India
e-mail: gssingh410@gmail.com

G. Singh
Department of Mechanical Engineering, Chandigarh University, Gharuan, Mohali, Punjab, India

S. Sharma
C.S.I.R-CLRI, Regional Centre for Extension and Development, Jalandhar, Punjab, India

real worry due to ecologically agreeable conduct. Numerous investigations demonstrated that dry machining has conjointly been restricted limited cutting velocity due to hardness of material which could bring about higher cutting temperature that affects the instrument life and item quality [3]. Finally, the inquiry emerges about the application of cooling strategies like flood, MQL, and cryogenic treatment or machining without lubricant (dry machining) due to limitation of each approach. Shokrani et al. [4] studied the machining of harder and other materials like titanium, nickel-based alloy, ferrous alloy, composite ceramics, elastomer, magnesium alloys, cobalt-chromium alloys using coolant such as water-soluble cutting oil, nascent oils and gas-based coolant. The machining was performed under situations of dry, MQL, air, and cryogenic cooling. It was found that while cutting harder materials lesser tool life, high cutting temperature, poor surface finish, dimensional deviation, and undesirable form of chip formation was resulted contrary to other materials. Vishnu et al. [5] revealed that the best possible variable levels for less machining temperature were observed at cutting speed of 1100 rpm, feed rate at 0.2 mm/rev, at 0.5 mm depth of cut and tool consisting of PVD coating. It was also examined that flood cooling outperformed the other cooling system during numbers of observation by a minute margin than MQL. However, from overall analysis, it can be stated that MQL can be cheaper and beneficial over conventional flooded case cooling. ANOVA results showed that the cooling environment had an impact in descending order on process parameters such as temperature, DOC, rate of feed, tool type, and speed. Gunda et al. [6] performed turning operation on STAVAX ESR at a cutting speed of 100 m/min under machining environments like wet machining using soluble cutting oil, dry, and HPMQSL. While applying high-pressure minimum quantity lubrication with solid lubricant (HPMQLSL), the flow rate was fixed as 43.2 ml/h at 0.6 MPa pressure. The solid lubricant was 20% of MoS_2 having particle size 20 μm and base oil for wet machining was SAE-40. The experimental results indicated that the performance of HPMQSL in terms of tool and surface impairment was superior to the condition of machining without cutting fluid and flooding environment. So, outcomes indicted that such machining leads toward sustainability manufacturing due to its economical and ecological nature. Goindi and Saini [7] conducted a research on the modeling of heat accumulation and distribution in orthogonal cutting operation and revealed that temperature is dependent upon time variation. It was emphasized that the 2D FEMA model along with the reverse transient heat conduction equation calculated the temperature distribution on tool profile with significant accuracy. Sharma et al. [8] examined the effects of process parameters on machining assisted with MQL using various cutting fluids, such as mineral oil, vegetable oils, and nanofluid mixed with cutting oil in drilling, turning, milling, and grinding operations. Analysis exhibited that MQL machining performed better than the traditional way of cooling in terms of product quality, tool wear, Temperature and coefficient of friction. This methodology has gained popularity due to the aforementioned benefits and seems to be a substitute for the traditional way of heat absorption. In addition to this, MQL machining assisted with nanofluid is further enhancing the performance during turning, milling, and grinding operation [19, 20]. Furthermore, the supercritical cryogenic least lubrication system enhanced the tool life by twofold and raised the MRR to 1.4 times than

conventional cooling. Sadik et al. [9] investigated the effects of coolant discharge on tool life and wear rate during cryo-treated and wet face milling operation of titanium alloy. Experimental observation revealed that flow rate did not influence the flank wear much but on the other hand the low-temperature cooling aided with CO_2 reduced the frequency of thermal hot spots propagation in the tool. Tunca et al. [10] evaluated the significance of MQL on the surface quality of austenitic steel using robotics milling. The oil flow rate during machining was set at 75, 140, 280, and 600 ml/h while the nozzle was set at 30 mm. The investigation results revealed that the oil discharge influenced the surface residual stress, but on the other hand the airflow rate did not. The flank wears and HAZ was appreciably influenced by the volume of lubricant.

Jamaludin et al. [11] studied on FEMA to investigate the impact of least quantity lubrication methodology during turning of JIS S45C steel using TiCN-coated cermet tool exhibited that model applied in the study evaluated the tool force and machining temperature effectively as well as influenced by utilizing MQL. Tebaldo et al. [12] examined eco-friendliness and sustainability during machining of Inconel-718 with cemented carbide tool at different levels of machining parameters using characterization and economical criteria aspects. Results confirmed that abrasion and diffusion were the main wear mechanism in this study, maximum wear resistance was observed during wet cooling at a speed of 50 m/min. As far as MQL is concerned, it was found to be economical and eco-friendly as compared to dry and wet cooling due to its better lubrication action. Finally, it was evaluated that the uses of cutting fluid add cost to the manufacturing process per unit material removed than dry machining.

Suhaimi et al. [13] investigated the effect of cryogenic treatment and MQL during machining of advanced velocity ranges milling of compacted graphite iron using internal MQL. Experimental results confirmed that the combined strategy (Indirect Cryogenic treatment + MQL) enhanced the tool life by 26% compared to older wet cooling. The results were also examined in all other cooling methodologies for analyzing cutting force as well as acoustic pressure. Sivaiah and Chakradhar [14] analyzed that on increasing doc, the temperature increases. The least temperature was recorded in cryogenic followed by MQL, wet and dry environment. For selected material and machining conditions, the cryogenic cooling was superior to dry, wet, and MQL in terms of tool wear, surface finish and chip formation. Goindi et al. [15] investigated the utility of ionic fluids as a coolant and its performance during milling operation conducted on AISI-1055 steel. The investigation evaluated that F_2-containing ionic liquids enhanced the performance outcomes at advanced velocities ranges and hence can be utilized for accelerated velocity cases of machining application. Also, the ionic liquid emits F_2 while targeted at the chip and provides healing action and hence controls the chip formation effectively. Haq [16] analyzed the effects of Al_2O_3-assisted NMQL and MQL during face milling operation of D_2 Steel. The flow rate of cooling media was varied from 200 to 400 ml/hr during different machining conditions. The comparative analysis showed that the NFMQL condition reduced tempera-ture more efficiently up to 25% as compared to normal MQL. Mia et al. [21, 22] analyzed the performance of AISI 4140 steel by using modeling and optimization by RSM and Taguchi method during MQL-assisted milling.

The major parameter was a variation of MQL flow rate which was set in the range from 50 to 150 mL/h. The research observation revealed that specific cutting energy was affected by the velocity of cutting, feed rate, and as well as by the MQL flow rate. ANOVA results confirmed that the surface roughness was remarkably enhanced by the MQL flow rate than velocity of cutting. Muaz [17] optimized the different intentions of MQL milling during machining of AISI-4340 Steel with TiN CVD coated tungsten carbide inserts. During the investigation, the cutting fluid was changed and its influence on the machining performance was analyzed with a genetic algorithm approach. It was found that the low viscosity fluids provide better results in MQL application because of greater piercing characteristics exhibited by tiny droplet size enabling cleaner and sustainable production. Additionally, the reduction of waste leads to environment friendly process. Further, the genetic algorithm revealed that the high spindle speed and low feed rate machining conditions were optimum. As far as the different fluid efficiency was concerned, it was found that the performance of boric acid mixed emulsion was superior to graphite powder suspended in MQL. However, the mixing of graphite powder and boric acid during hybrid cooling was also not effective. Sen et al. [18] optimized MQL milling parameters during machining of Inconel 690 assisted with castor oil. The two different approaches like NSGA-II and TOPSIS were compared with experimental results. It was revealed that there was almost less than one percent error in two methodologies. Literature survey revealed that Minimum Quantity Lubrication aided machining extended numerous positive influences in metal machining and would be the future of the lubrication system (Fig. 1).
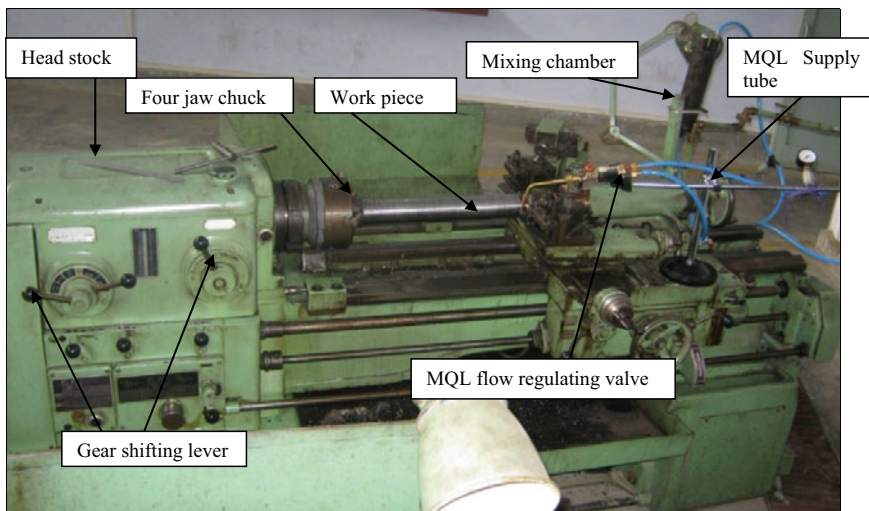
Fig. 1 Snapshot of the experimental setup

2   Experimental Investigation and Methodology of Work

Experimentation investigations were carried out by orthogonal machining of stainless steel (AISI-202) rod having diameter 80 mm and length 800 mm, utilizing lathe machine of 7.5 KW. The machining was performed at specified parameter levels under dry and MQL situations. The experimental investigation was specially attended to the evaluation of heat generation, work texture, and chip reduction coefficient in separate conditions of dry and MQL machining. The lubrication nozzle was placed at the gap of 30 mm from tool–chip coherence having a 160 ml/hr lubricant flow rate. The parametric levels were opted as per the tool manufacturer guidelines, expert suggestions, and on the basis of the literature survey. The surface characteristic (Ra Values) was evaluated using a Talysurf surface roughness meter. The chip reduction coefficient was evaluated from the sample of a chip collected during turning operation by using the standard ratio formula of uncut and cut chip thickness. The same variable was also reviewed by length formula for a few samples to check the accuracy of measurement during experimentation. The result of the chip reduction coefficient was approximately identical in both cases of evaluation. For the accuracy of measuring heat evolution during turning operation, the pilot experiments were conducted to find out the spot of higher cutting temperature. From the literature survey, it was pointed out that the greatest temperature was evolved at the interface of chip and insert. Further, the utility of infrared thermometer was practiced to confirm the spot of maximum heat generation. Finally, the heat generation (temperature) at tool work linkage was measured using a calibrated K-Type thermocouple. The special arrangement was made on the cutting insert to measure temperature by drilling hole near to nose radius. The blind hole of 0.8 mm diameter was drilled by EDM drilling at a 1 mm gap from the nose radius (Fig. 2).

3   Results and Discussions

During turning of tough materials, heat is evolved at a different zone of machining due to plastic deformation, sliding and rubbing at primary, secondary and tool–chip coherence section. Due to these heat sources, the huge amount of heat is generated and consequently, the tool sharpness, product quality, and environment get influenced. The majority of heat is taken away by chip, little portion of this transferred to workpiece due to conduction and the further remaining part is radiated to the surrounding. So, it is of prime importance to control this heat for better performance of machining operation. In this connection, to reduce the quantity of heat the MQL was applied in the present investigation and its role in terms of chip reduction coefficient, surface roughness, and cutting temperature was investigated. The results of experimental observation were presented in the form of graphs shown in Figs. 3, 4, 5, 6 and 7 (Table 1).
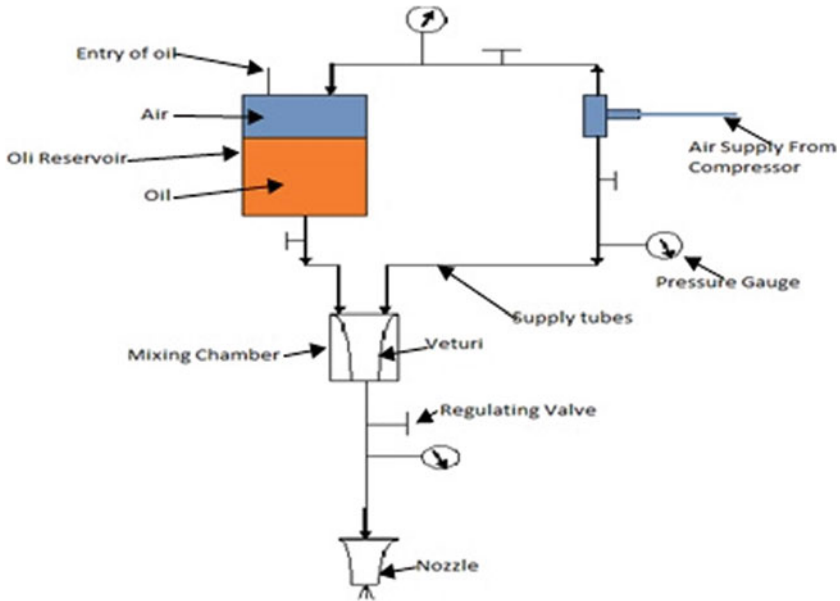
Fig. 2 Schematic diagram of MQL set up
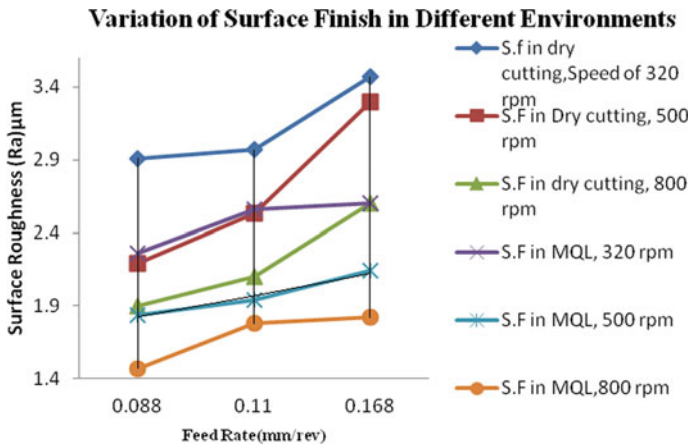
Fig. 3 Influence of feed rate on surface roughness at 0.5 mm DOC

The results of first phase machining shown in Fig. 3 indicates the effects of feed rate on surface roughness during dry and MQL environments at different levels of process parameters.

It was depicted that surface roughness reduces as the feed rate was advanced. The maximum surface roughness was reported at 0.168 mm/rev feed rate and 320 rpm. Also, it was examined that as the cutting speed increases the surface roughness
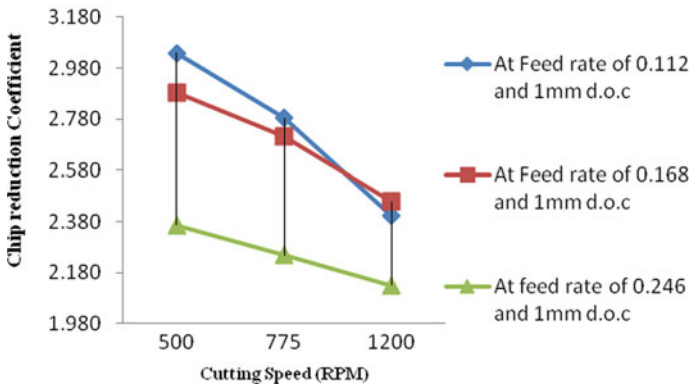
Fig. 4 Influence of speed on chip reduction coefficient in dry machining
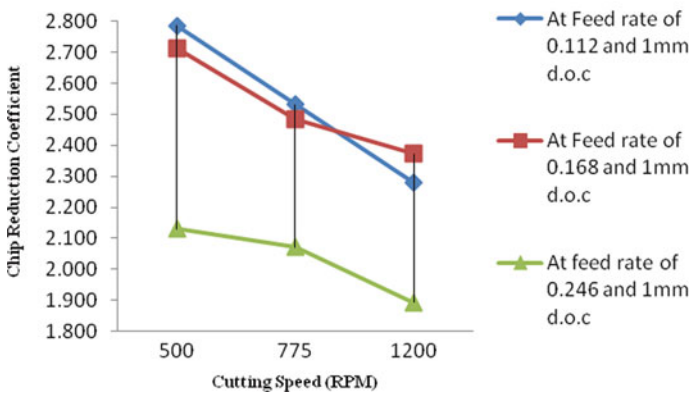
Fig. 5 Influence of speed on chip reduction coefficient in MQL

gets reduced due to the effect of high heat generation which further softens the material ahead of the tool. Consequently, surface quality got enhanced at higher cutting speeds in all machining environments. The best surface finish was noted in the MQL environment at 800 rpm and 0.088 mm/rev feed rate followed by MQL at 500 rpm having the same feed rate. During dry machining environment, a better surface finish was reported at 800 rpm along with 0.088 mm/rev fed rate. Hence from the parametric point of view, the experiment results concluded that the best surface finish was evaluated at 0.088 mm/rev feed rate and 800 rpm.

The outcomes of second phase machining are shown in Figs. 4 and 5, indicated the effect of cutting speed on chip reduction coefficient. The acceleration of cutting

Influence of Cutting speed in different machining conditions at 1mm doc
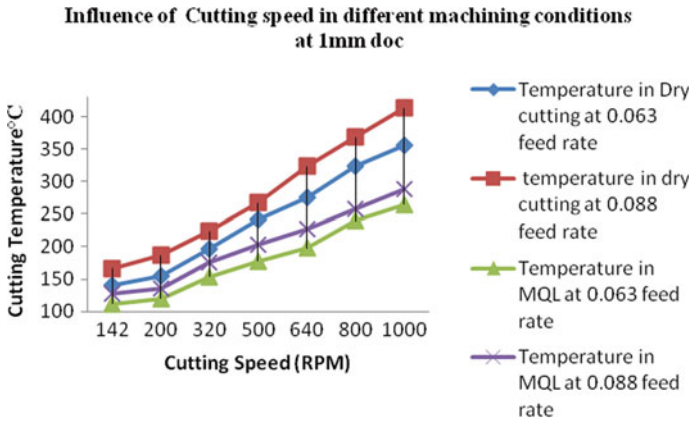
Fig. 6 Temperature variations at 1 mm DOC

Influence of Cutting speed in different machining conditions at at 0.5mm doc
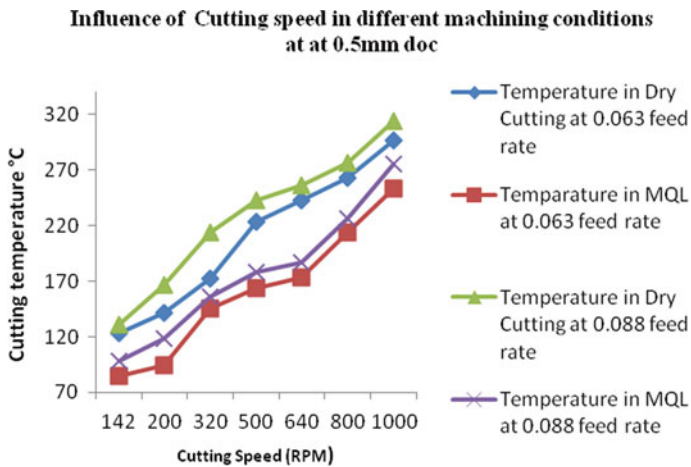
Fig. 7 Temperature variations at 0.5 mm DOC

speed lowers the chip reduction coefficient due to the softness of work material prior to the cutting tool. The chip reduction coefficient is a significant parameter, which shows the intensity of plastic deformation in the cutting zone. Cutting forces are directly concerned with plastic deformation in various machining sections. Higher the plastic deformation, the greater the magnitude of cutting forces involved during the machining operation. From experimental investigation, it was pointed out that the chip reduction coefficient was reduced during conditions of MQL as compared to dry machining situations. Finally, it was deduced that MQL significantly minimized the degree of plastic deformation by reducing the chip reduction coefficient in present machining trials. The extreme values of the chip reduction coefficient were recorded at 500 rpm and 0.112 mm/rev feed rate during dry and MQL machining.

Table 1 Experimental data

S. no.	Item	Description
1	Machine used	Lathe machine (HMT, INDIA) 7.5 kW
2	Work material	Stainless steel AISI-202 of 80 mm diameter and 1000 mm length
3	Type of insert	SNMG-120408
4	Tool designation	PSDNN 2525M12
5	Tool signature	−7°, −7°, 7°, 7°, 45°, 45°, 0.8 mm
6	Cutting speed (Rpm)	142–1200
7	Rate of feed	0.063–0.246 mm/rev
8	Depth of cut (d.o.c)	0.5 and 1 mm
9	MQL details	Bio-oil (Soybean oil) flow rate 160 ml/h at 5 bar
10	Nozzle distance (mm)	30 mm, 45°
11	Air compressor	Single-phase motor driven
12	Roughness tester	Mitutoyo—Japan
13	Thermocouple	Standard K-type thermocouple

The lower magnitude of chip reduction coefficient points out toward lower intensity of cutting forces, which further signifies that lower cutting forces require less power requirement for cutting operation and hence productivity of machining got enhanced in terms of lower power requirement. Investigation results obtained during the third phase of machining are expressed in graphs shown in Figs. 6 and 7 pointed out that while increasing the cutting speed the heat generation becomes intense, consequently, the product quality gets effected due to rapid tool wear, further leads to a shortened span of tool life. Figure 6 explored the intensity of cutting temperature in different machining conditions having 1 mm depth of cut. The results revealed that cutting speed variation influenced the temperature because of larger friction at accelerated levels of machining process parameters. The maximum temperature was examined at 1000 rpm and 0.08 mm/rev feed rate during MQL and dry cutting. It was also observed temperature rises quickly in case of higher depth of cut and speed rate as compared to lower levels of the aforementioned parameters. Furthermore, it was revealed that a notable reduction in temperature was recorded due to the cooling and lubrication effect of MQL. Finally, experimental results concluded that there was an approximately 10–25% reduction in temperature using MQL than dry machining. From experimental observation, the reduction in cutting temperature, surface roughness, and chip reduction coefficient during MQL machining indicated better machining performance than dry cutting environment because all three parameters are evaluators of the machinability index. Even such an apparently minor reduction in the surface roughness and chip reduction coefficient is expected to have a significant influence on the machinability index. Also the main cause of temperature variation, while leveling up the depth of cut and feed was due to the addition of cutting area and chip load at tool–chip interface.

4 Conclusion

From experimental results, the following conclusion was made.

1. Cutting temperature was reduced in the MQL machining environment as compared to dry cutting because of the cooling and lubrication action of amalgamated air-bio-based oil jet utilized during machining.
2. Surface roughness was enhanced due to lubrication property as well as cutting and healing action of vegetable oil jet focused on tool–chip interface area of machining zone.
3. Chip reduction coefficient was also reduced during MQL machining as compared to dry machining which indicated the lower friction at the tool–chip interface in MQL. These observation results confirmed the better lubrication and cooling action of vegetable oil.
4. During experimentation, it was observed that there was fewer fumes, environmental pollution as well as maintenance of ecological balance, which indicates environmental friendly and economical machining is possible with MQL.
5. Future work can be conducted by mixing nanofluids with bio-based oil to check its effects on heat generation, surface roughness, and cutting forces in various operations like milling, grinding, and hobbing.
6. The present work can be further extended by utilizing internal MQL system in drilling, milling and turning using

5 Future Scope

The futuristic work possibilities are listed below.

- Application of ionic fluid MQL during orthogonal machining.
- Hybrid-cryogenic nitrogen + bio-based MQL system while machining difficult to cut materials.
- Hybrid subcritical carbon dioxide mixed with oil-based MQL during machining of harder materials.
- Ultrasonic-assisted MQL machining using nanofluids in turning and grinding.
- Evaluation of exact size, volume flow rate and concentration of nanofluids with other additives oils, etc.

References

1. Byrne, G., Scholta, E.: Environmental clean machining processes a strategic approach. Ann. CIRP **42**(1), 471–474 (1993)

2. U.S Department of Health and Human Services. Occupational Exposure to Metal Working Fluid. NIOSH Publication, No. 98–102 (1998)
3. Dhar, N.R., Islam, S., Kamruzzaman, M.: Effect of minimum quantity lubrication (MQL) on tool wear, surface roughness and dimensional deviation in turning AISI-4340 steel. G.U. J. Sci. **20**(2), 23–32 (2007)
4. Shokrania, V.D., Newmana, S.T., Imani-Asraia, R.: An initial study of the effect of using liquid nitrogen coolant on the surface roughness of Inconel 718 nickel-based alloy in CNC milling. In: 45th CIRP Conference on Manufacturing Systems 2012, Procedia CIRP **3**, 121–125 (2012)
5. Vishnu, V.A., Naidu, G.G., Tilak, K.B., Ramakrishna, J.: Application of Taguchi method in the optimization of turning parameters for material removal rate of En-36 material. Int. J. Adv. Eng. Res. Dev. **2**(8), 54–62 (2015)
6. Gunda, R.K., Reddy, N.S.K., Kishawy, H.A.: A novel technique to achieve sustainable machining system. In: 13th Global Conference on Sustainable Manufacturing—Decoupling Growth from Resource Use, Procedia CIRP **40**, 30–34 (2016)
7. Goindi, G.S., Saini, K.: Thermal modelling of heat flux and tool-chip interfacial temperature distribution in orthogonal machining. Indian J. Sci. Technol. **9**(36) (2016)
8. Sharma, A.K., Singh, R.K., Dixit, A.R., Tiwar, A.K.: Characterization and experimental investigation of Al_2O_3 nanoparticle based cutting fluid in turning of AISI 1040 steel under minimum quantity lubrication (MQL). Mater. Today Proc. **3**(6), 1899–1906 (2016)
9. Ibrahim Sadika, M., Isaksonb, S., Malakizadib, A., Nyborgb, L.: Influence of coolant flow rate on tool life and wear development in cryogenic and wet milling of Ti-6Al-4V. In: 7th HPC 2016—CIRP Conference on High Performance Cutting, Procedia CIRP **46**, 91–94 (2016)
10. Tunca, L.T., Gub, Y., Burkeb, M.G.: Effects of minimal quantity lubrication (MQL) on surface integrity in robotic milling of austenitic stainless steel. In: 3rd CIRP Conference on Surface Integrity (CIRP CSI), Procedia CIRP **45**, 215–218 (2016)
11. Jamaludin, A.S., Hosokawa, A., Furumoto, T., Koyano, T., Hashimoto, Y.: Evaluation of the minimum quantity lubrication in orthogonal cutting with the application of finite element method. Int. J. Mech. Mech. Eng. IJMME-IJENS **17**(01), 104–109 (2017)
12. Tebaldo, V., di Confiengo, G.G., Faga, M.G.: Sustainability in machining: "Ecofriendly" turning of Inconel 718. Surface characterisation and economic analysis. J. Clean. Prod. **140**(Part 3, 1), 1567–1577 (2017)
13. Suhaimi, M.A., Park, K.-H., Gi-Dong, Y., Sharif, S.: Effect of cryogenic high-speed milling of compacted graphite iron using indirect spray system. Int. J. Adv. Manuf. Technol. **99**(1) (2018)
14. Sivaiah, P., Chakradhar, D.: Effect of cryogenic coolant on turning performance characteristics during machining of 17-4 PH stainless steel: a comparison with MQL, wet, dry machining. CIRP J. Manufact. Sci. Technol. **21**(2018), 86–96 (2018)
15. Goindi, G.S., Sarkar, P., Jayal, A.D., Chavan, S.N., Mandal, D.: Investigation of ionic liquids as additives to canola oil in minimum quantity lubrication milling of plain medium carbon steel. Int. J. Adv. Manuf. Technol. **94**, 881–896 (2018)
16. Haq, M.A.U., Khan, A.M., Gong, L., Xu, T., Meng, L., Hussain, S.: A comparative study of face milling of D2 steel using Al_2O_3 based nanofluid minimum quantity lubrication and minimum quantity lubrication. Adv. Sci. Technol. Res. J. **12**(1), 99–105 (2018)
17. Muaz, M., Choudhury, S.K.: Experimental investigations and multi-objective optimization of MQL-assisted milling process for finishing of AISI 4340 steel. Measurement **138**, 557–569 (2019)
18. Sen, B., Mia, M., Hussain, S.A.I., Mandel, U.K.: Selection of an ideal MQL assisted milling condition: a NSGA-II coupled TOPSIS approach for improving machinability of Inconel 690. Int. J. Adv. Manuf. Technol. **103**, 1811–1829 (2019)
19. Dhar, N.R., Khan, M.M.A.: A study of effects of MQL on temperature, force, tool wear and product quality in turning AISI 9310 steel. In: Net Fieldwise Seminar on Manufacturing and Material Processing, pp. 30–35 (2006)
20. Dhar, N.R., Islam, M.W.: The influence of minimum quantity of lubrication (MQL) by vegetable oil-based cutting fluid on machinability of steel. In: International Conference on Mechanical Engineering, pp. 1–5, Dec 2005

21. Mia, M., Bashir, M.A., Khan, M.A., Dhar, N.R.: Optimization of MQL flow rate for minimum cutting force and surface roughness in end milling of hardened steel (HRC 40). Int. J. Adv. Manuf. Technol. **89**(1), 675–690 (2018)
22. Mia, M., Razi, M.H., Ahmad, I., Mostafa, R., Rahman, S.M.S., Ahmed, D.H., Dey, P.R., Dhar, N.R.: Effect of time-controlled MQL pulsing on surface roughness in hard turning by statistical analysis and artificial neural network. Int. J. Adv. Manuf. Technol. **91**(9), 3211–3223 (2017)
23. Su, Y., Gong, L., Chen, D.: An investigation on tribological properties and lubrication mechanism of graphite nanoparticles as vegetable based oil additive. J. Nano-Mater. **7** (2015), Article ID 276753

Performance of Composite Coating on Cutting Tools: Coating Technologies, Performance Optimization, and Their Characterization: A Review

Vivek Mehta, Rajesh Kumar, and Harmesh Kumar

1 Introduction

Demand and challenges in the manufacturing industry are increasing rapidly. Industry requires high-speed cutting, dry cutting, and machining of hard materials that lead to strong demand for super hard cutting tools.

Materials like cemented carbide, cubic boron nitride (CBN)/polycrystalline CBN (PCBN), etc., are considerably exploited to manufacture tool materials for manufacturing processes. These materials have peculiar qualities: high melting point, toughness, chemical inertness, and wear resistance [1]. New age tools must be able to endure harsh performing conditions. Therefore, continuous attempts have been made to increase the tool life by using cutting fluids, ideal specifications, low-temperature treatment [2] using coated tools and heat treatment [3].

Many researchers have increased the performance of the materials above their prescribed limits to obtain enhanced results [4]. It is witnessed that MRR, surface finish, low cutting forces, accurate workpiece geometrical features, and lesser wear of tool exhibit superior machinability [5]. The machinability of hard materials can be increased by the use of coated cutting tools. Characteristics of coatings are superior microhardness and superior adhesion to the substrate [6].

When changing the properties of the raw materials is difficult, properties of cutting tool materials can be improved by surface coating, especially for tools working in extreme conditions [7]. The coating creates a blanket on the substrate which is applied to the surface of an object. Surface coating changes the key properties of parent material like wettability, corrosion, wear, etc. Coating also helps to develop properties to the substrate like a magnetic response, conductivity, etc., that becomes

V. Mehta (✉)
Govt. ITI Jubbal Distt., Shimla, HP 171205, India
e-mail: vivekbhauta@gmail.com

R. Kumar · H. Kumar
Mechanical Engineering Department, U.I.E.T. Panjab University, Chandigarh 160014, India

Table 1 Various coating techniques and coated material recently used by the different researchers for the coating of cutting tools

S. no.	Author and year	Coating technique	Material used for coating	Tool on which coating is done (Substrate)	Workpiece	Inferences	References
1	Halil Çaliskan et al. 2012	PVD	Nanolayer AlTiN/TiN, multilayer nanocomposite TiAlSiN/TiSiN/TiAlN, commercial TiN/TiAlN	Carbide tool	Tool steel (~61 HRC)	The result shows that during the machining by coated tools the least wear occurs on coated tools, but severe wear occurred on the uncoated tool	[6]
2	Kedong Zhang et al. 2015	Cathode arc-evaporation technique (PVD)	Ti55Al45N and nano-texture (CNT)	WC/Co carbide tools	AISI 1045 hardened steel (HRC 35–45)	The result shows that the firstly coated, then nanoscale-textured tools were much fruitful in reducing the tool wear as compared with the firstly nano-scale textured and then coated tools.	[34]

(continued)

Table 1 (continued)

S. no.	Author and year	Coating technique	Material used for coating	Tool on which coating is done (Substrate)	Workpiece	Inferences	References
3	K.-D. Bouzakis et al. 2013	Cathode arc-evaporation technique (PVD)	TiAlSiN, TiSiN, and TiAlN/TiSiN	Cemented carbide inserts	Stainless steel 304 L and nano-indentation test	Based on the acquired results the addition of Si into the TiN with Si contents of 7% and 14%, gives the improved strength, and nano- and macro-impact properties.	[36]
4	W. Henderer et al. 2013	Cathode arc-evaporation technique (PVD)	TiSiN base layer with low-friction CrC/a-C:H top layer	Cemented carbide substrates	A390 aluminum	The result showed that the coating enhances the wear resistance and cuts down friction.	[45]
5	Weiwei Wu et al. 2015	Cathodic arc ion plating (PVD)	AlCrN and AlCrSiN	HSS	40CrNiMo alloy steel(average hardness of 260 HB)	The life of the AlCrSiN coated tool was 40% more as compared to AlCrN-coated tools	[46]
6	Kedong Zhang et al. 2015	Cathodic arc-evaporation (PVD)	TiAlN	Tungsten carbide	AISI 316 austenitic stainless	Micro/nanoscale structure on cutting tools increases the adhesive properties of TiAlN-coated tool	[37]

Table 1 (continued)

S. no.	Author and year	Coating technique	Material used for coating	Tool on which coating is done (Substrate)	Workpiece	Inferences	References
7	Yin-Yu Chang et al. 2014	Cathodic arc-evaporation (PVD)	TiAlN, CrAlSiN, and TiAlSiN	Polished tungsten carbide (WC/Co)	Ti–6Al–4 V alloy	The CrAlSiN-coated tools have better wear resistances properties for the machining of Ti–6Al–4 V, when compared with TiAlN and TiAlSiN	[38]
8	Ai-HueiChiou et al. 2015	Direct current (DC) magnetron sputtering	TiCN, Al$_2$O$_3$ and TiN	Carbide tool and uncoated CBN	Hardened AISI H11 steel (48–49HRC)	Results revealed that the life of carbide inserts tool decreases at high cutting speeds	[30]
9	Manu Dograet al.2011	CVD	Al O, TiN, and Ti (C, N) Al$_2$O$_3$	TNMG 160412-23 and TNMG 160412-MF2	MMCs	The wear characteristics of TiN-coated tool were very lower than that of the Al O-coated tool during the machining of composites	[5]

Table 1 (continued)

S. no.	Author and year	Coating technique	Material used for coating	Tool on which coating is done (Substrate)	Workpiece	Inferences	References
10	A. A. Vereschaka et al. 2014	Filtered cathodic vacuum arc deposition (FCVAD)	Titanium nitride (TiN)	Coated and uncoated CBN tools	Inconel 718	Coated tools give better tool life than uncoated tools at a cutting speed less than 300 m/min	[47]
11	Y. Sahin et al. 2004	Chemical Vapor Deposition (CVD)	CNT	Copper (For EDM)	Stainless steel	It is observed that the wear rate of Cu-based CNT tools reduced 50–72% in comparison to those of electrolytic Cu tools	[31]
12	Jinming Zhou et al. 2012	CVD	Ti55Al45N and nano-texture (CNT)	WC/Co carbide tools	AISI 1045 hardened steel (HRC 35–45)	The result shows that the firstly coated, then nanoscale-textured tools were much fruitful in reducing the tool wear as compared with the firstly nanoscale textured and then coated tools	[34]

Table 1 (continued)

S. no.	Author and year	Coating technique	Material used for coating	Tool on which coating is done (Substrate)	Workpiece	Inferences	References
13	Tsunehisa SUZUKI et al. (2011)	Electroplating	TiAlSiN, TiSiN, and TiAlN/TiSiN	Cemented carbide inserts	Stainless steel 304 L and nano-indentation test	Based on the acquired results, the addition of Si into the TiN with Si contents of 7 and 14%, gives the improved strength, and nano- and macro-impact properties	[24]
14	M. Manjaiah Et al. 2015	–	TiSiN base layer with low-friction CrC/a-C:H top layer	Cemented carbide substrates	A390 aluminum	The result showed that the coating enhances the wear resistance and cuts down friction	[48]

a vital part of the end product. Coating provides high-performance tools that are ready to meet the increasing needs of modern manufacturing. Usage of coating tools at higher cutting speeds and feeds lowers machining time and cost. Also, the tool changing cost can be reduced due to the longer service [8–12].

Coated cutting tools have complex material configuration, in which the substrate is shielded with a stiff, abrasion resistant, chemically inactive and insulating layer having a micron range thickness. Coated tools, as compared to uncoated tools, increase load-bearing capacity(mechanical and thermal) and improve wear resistance over extensive cutting temperature range [13].

It has been observed that coating is widely applicable to enhance functioning of cutting tools even in conventional machining. A lot of the literature is available for the coated tools in conventional machining. Recently, the demand for hard machining and micromachining has been increased, due to the demand for products having lighter weight [14]. Every conductive material can be machined with electrical discharge machining (EDM). It can be used to manufacture small components, such as dies' injections, molds, tools, and nozzles [15]. Materials like copper (Cu), cemented carbide, tungsten carbide (WC), or tungsten copper (CuW), are prime selection to synthesize tools. These materials exhibit superior wear properties and capability to machine hard and conductive material [16–18]. Particularly, WC exhibits superior hardness and wear resistance that allows elevated current supply from the pulse generator during the EDM process [19]. Another preferred choice for EDM tool material is Cu. Cu has a drawback of the low melting point that prompts to increase electrode wear rate (EWR) while machining. To overcome this problem, lots of researchers have used CuW as electrode material for EDM, with hard WC and die-steels [20–22]. A very few researchers [15, 23, 24] have used coated electrode in EDM machining and it has been observed that these coated electrodes in EDM give the better surface finish, low tool wear rate, and higher material removal rate.

The present study follows the following structure. The first section gives information about the different deposition techniques; coated materials used in the cutting tools and related manufacturing methods. After that, suitable substrate and coating, treatments that enhance the performance, are presented. Later section highlights applications of cutting tools with renovating procedures are explained. The conclusion is presented in the end.

2 Manufacturing of Coating for Cutting Tools

2.1 Coating Techniques

There are different methods of coating of cutting tools such as electroplating [15, 24–26], electroless plating [27], vapor deposition(chemical CVD and physical PVD) [5, 28–38]. Some other methods as cold spray and thermal spray can also be used

for the coating of cutting tools. Each of the methods has its own advantages and drawbacks.

Electroplating is one of the electrodeposition processes for making a strong, and uniform coating, upon a surface by the use of electric current [23]. Chemical reduction plating is used in electroless plating. Process depends upon the reduction of nickel ions in solution containing reducing agents. [27, 39]

Chemical vapour deposition (CVD) coatings work on chemical activity of gaseous reactants primarily near to the heated substrate surface. This deposition process produces an atomic level layer having pure deposition of material. [40]. The degree contact between solid substrate base and gaseous ion phase influences the quality of the coating [40].

Usage of PVD hard coatings has, in industries, can be traced since the year 1980s. Earlier, the HSS tool was coated with PVD, both by electron-beam and arc deposition techniques. Apart from this, other important PVD deposition methods are high-voltage electron beam and magnetron sputtering [41].

A variety of production processes can be performed using PVD enhanced tool materials. Various coating for tool material is available these days like TiN, (Ti, Al)N, and Ti(C, N). [42].

There are various phases in the PVD process [43]. The new method of PVD has been developed known as a filtered cathodic vacuum arc deposition (FCVAD). FCVAD can also be used for the coating on carbide inserts. In this technique, an electric arc is used to vaporize material from a cathode target [44] (Table 1).

Essence drawn from the above table

From the above table, it is witnessed that coating improves the mechanical and tribological behavior of the substrate. It has been observed that a lot of literature is available for the coating of conventional cutting tools, which increases the cutting tool's performance during machining. Electrical discharge machining (EDM) is the nonconventional and widely used machining process for machining of difficult to machine materials, that are costly to machine using conventional methods. Apart from being cost-effective, nonconventional machining processes like EDM and micro-EDM are quite helpful to generate dimensional accuracy and difficult geometry that are vital parts of tool performance. EDM or micro-EDM uses electrothermal process to remove materials from workpiece. Electrothermal does not reply on hardness tool material and force between workpiece and tool is negligible too. It is also observed that a lot of literature is available for the manufacturing of cutting tool (electrode) of the EDM for the machining processes in order to increase the MRR, decreasing tool wear, and increasing surficial smoothness. Still, the elevated temperature used in EDM promotes tool wear. Tool wear and surface finish still remains a challenging task and further research work can be done in this area.

It is also observed that it is difficult to machine hard alloys and biomedical implants. Also, a very few literature is available for the coating of advanced materials on the cutting tool (electrode) of the EDM. So further research can be carried out using advanced material coating such as carbon nanotubes (CNTs) [49, 50]/graphene [51–56] and WC. These materials are potential reinforcement of the EMD tool too.

3 Characterization of Coating of the Cutting Tools

In this section, various characterization methods for the coating is discussed. Characterization can be explained as a process by which properties and structures of the materials can be gauged. Characterization is the basic tool by which researchers create understanding about materials and processes. Characterization enables researchers to measure elemental properties, morphological properties, physical and chemical properties, compositions, and strength. Characterization of coating properties, along with reproducibility, helps to understand coating performance [30, 57].

3.1 Strength of the Cutting Tool at Ambient and Elevated Temperatures

The new age nanoindentation technique is capable to determine mechanical properties of materials, especially coated materials [55, 58, 59]. At high temperatures, nanoindentation can characterize elevated temperature properties too [60–62]. Nanoindentation also enables researchers to measure "in situ" properties of materials. During the EDM process, nanoindentation can measure properties at actual working conditions [44, 63].

Fateh et al. [64] have studied the characterization of TiN and VN coatings. Coating has been produced using magnetron sputtering with respect to their oxidation behavior at high temperatures. Tribometer testing has been performed to characterize. X-ray diffraction (XRD) and Raman spectroscopy have been used to characterize various phases in material.

3.2 Coating Thickness Distribution on the Tool

Several strategies have been adopted to reduce wear in the EDM tool. These two strategies are most preferred first, wear-resistant materials and second, improving wear properties by reinforcing with other materials. A thin film of hard nitride coatings has been successfully enhanced wear properties and enhances life substantially too [13]. Rodriguez et al. [65] have studied the mechanical behavior of the most used hard coatings like TiN, TiCN, TiAlN, CrN, and ZrN. Microhardness tests were performed using micro-indenter. Pin-on-disk tribometer and an optical profilometer were used to measure frictional wear. All types of coatings show smooth topography, because of small droplets on the coated surface. On the other hand, friction characterization indicated a dip in friction coefficient on all types of coatings. TiCN (0.2–0.4), and for the ZrN (0.3–0.35) coatings showed optimized results.

Wagner et al. [66] have done the coatings of TiN by thermal CVD and studied the characterization of their microstructure, mechanical and tribological properties.

It is observed that texture influences hardness coating. Oriented films show lesser hardness as compared to non-textured coatings.

Shtansky et al. [67] have performed a comparative analysis of various Ti-based coating. Coatings were synthesized by DC magnetron sputtering and ion implantation assisted magnetron sputtering in an Ar atmosphere. The Ti–Si–B–N and Ti–Cr–B–N surfaces on substrate show batter machining performance against stainless steel.

3.3 Wear Resistance of the Coated Tools

Different researchers studied wear behavior of titanium nitride [68]. The effects of different parameters [69], thickness [70], and methods of coating synthesis [71, 72] have been investigated.

Tanno et al. [73] have investigated influence grain orientation, on friction coefficient of TiN coatings. The investigation showed that TiN coatings with (111) orientation deposited at 200 V had the lowest friction coefficient. Aihua et al. [68] found that reinforcement of Al increases friction coefficient (TiAlN$_4$–TiN).

TiN/TaN [68], TiN/CrN, TiN/MoN, TiN/NbN [74] multilayers developed by electron beam PVD on HSS and cemented carbide were investigated. Micro-abrasive analyzes examined by 'crater grinder test' [75] presented that the tribological properties of the TiN/TaN coatings were excellent than what was recommended by the properties of the two homogenous materials (rule of the mixture). TiN/TaN coating was the best choice for machining applications and abrasive wear is the main reason for wear [76].

Luo et al. [77] investigated the mechanical properties and wear characteristics of TiAlN/VN and TiAlCrYN coatings developed on a low alloy cold-mold steel P20. The study revealed that nanostructured multilayer TiAlN/VN coatings had excellent wear resistance with friction coefficients between 0.43 and 0.55 subjected to the applied load.

4 Conclusions

Machining is the key parameter for the manufacturing of products. A coating is used to increase the life of the tool and to improve the mechanical properties and increase wear resistance. This paper presents the existing trends of coated tools manufacturing, gives details for different techniques of thin film deposition, and coating materials. Here coated tools wear mechanisms are also represented by different methods. The exact substrate, coating material, and mechanical treatments for enhancing the tool performance and reducing the tool wear, is also presented. It is also explained in machining industry coated tools will play a major role in the future.

The overall behavior, performance, and its wear resistance of the coating are affected by many factors. The critical analysis presented in this study is related to the

manufacturing and application of coated cutting tools. Study shows that researchers are able to deal effectively the challenge of productivity improvement requirements while keeping high standards of quality.

5 Future Scope

In the present study it is observed that the hard coating can improve the overall performance of conventional machining. Also the above-explained deposition techniques require further testing and study. Results achieved so far indicate a good future for coated cutting tools. Further, some researchers have done the coating on EDM electrode especially copper. Using the hard coating in the EDM electrode, difficult to machine materials and biomedical implants can also be machined easily and also the tools wear rate of the coated electrode decreases. But a very few literature is available regarding the coated EDM electrode. So further research and testing can also be done for the coating of the EDM electrode in order to further improve the overall EDM performance.

References

1. López de Lacalle, L.N., Lamikiz, A., Fernández De Larrinoa, J., Azkona, I.: Advanced cutting tools. In: Machining of Hard Materials, pp. 33–86. Springer London, London (2011). https://doi.org/10.1007/978-1-84996-450-0_2
2. Özbek, N.A., Çiçek, A., Gülesin, M., Özbek, O.: Investigation of the effects of cryogenic treatment applied at different holding times to cemented carbide inserts on tool wear. Int. J. Mach. Tools Manuf. **86**, 34–43 (2014). https://doi.org/10.1016/j.ijmachtools.2014.06.007
3. Serdyuk, Y.D., Semizhon, O.A., Prokopiv, N.M., Petasyuk, G.A., Kharchenko, O.V., Omel'chuk, T.V.: The influence of thermal compression treatment parameters on quality characteristics and wear mechanisms of T5K10 carbide inserts in rough turning. J. Superhard Mater. **33**, 120–128 (2011). https://doi.org/10.3103/S1063457611020055
4. Bushlya, V., Zhou, J., Avdovic, P., Ståhl, J.-E.: Performance and wear mechanisms of whisker-reinforced alumina, coated and uncoated PCBN tools when high-speed turning aged Inconel 718. Int. J. Adv. Manuf. Technol. **66**, 2013–2021 (2013). https://doi.org/10.1007/s00170-012-4477-5
5. Dogra, M., Sharma, V.S., Sachdeva, A., Suri, N.M., Dureja, J.S.: Performance evaluation of CBN, coated carbide, cryogenically treated uncoated/coated carbide inserts in finish-turning of hardened steel. Int. J. Adv. Manuf. Technol. **57**, 541–553 (2011). https://doi.org/10.1007/s00170-011-3320-8
6. Çalışkan, H., Kurbanoğlu, C., Panjan, P., Kramar, D.: Investigation of the performance of carbide cutting tools with hard coatings in hard milling based on the response surface methodology. Int. J. Adv. Manuf. Technol. **66**, 883–893 (2013). https://doi.org/10.1007/s00170-012-4374-y
7. Chen, N., Shen, B., Yang, G., Sun, F.: Tribological and cutting behavior of silicon nitride tools coated with monolayer- and multilayer-microcrystalline HFCVD diamond films. Appl. Surf. Sci. **265**, 850–859 (2013). https://doi.org/10.1016/j.apsusc.2012.11.133
8. Kumar, C.H.R.V., Nair, P.K., Ramamoorthy, B.: Characterization of multilayer PVD nanocoatings deposited on tungsten carbide cutting tools. Int. J. Adv. Manuf. Technol. **38**, 622–629 (2008). https://doi.org/10.1007/s00170-007-1059-z

9. Minevich, A.A., Eizner, B.A., Gick, L.A., Popok, N.N.: Case studies on tribological behavior of coated cutting tools. Tribol. Trans. **43**, 740–748 (2000). https://doi.org/10.1080/10402000008982403

10. Stein, C., Keunecke, M., Bewilogua, K., Chudoba, T., Kölker, W., van den Berg, H.: Cubic boron nitride based coating systems with different interlayers for cutting inserts. Surf. Coatings Technol. **205**, S103–S106 (2011). https://doi.org/10.1016/j.surfcoat.2011.03.016

11. Siow, P.C., A. Ghani, J., Ghazali, M.J., Jaafar, T.R., Selamat, M.A., Che Haron, C.H.: Characterization of TiCN and TiCN/ZrN coatings for cutting tool application. Ceram. Int. **39**, 1293–1298 (2013). https://doi.org/10.1016/j.ceramint.2012.07.061

12. Xing, Y., Deng, J., Li, S., Yue, H., Meng, R., Gao, P.: Cutting performance and wear characteristics of Al$_2$O$_3$/TiC ceramic cutting tools with WS2/Zr soft-coatings and nano-textures in dry cutting. Wear **318**, 12–26 (2014). https://doi.org/10.1016/j.wear.2014.06.001

13. Santecchia, E., Hamouda, A.M.S., Musharavati, F., Zalnezhad, E., Cabibbo, M., Spigarelli, S.: Wear resistance investigation of titanium nitride-based coatings. Ceram. Int. **41**, 10349–10379 (2015). https://doi.org/10.1016/j.ceramint.2015.04.152

14. Jahan, M.P., Wong, Y.S., Rahman, M.: A comparative experimental investigation of deep-hole micro-EDM drilling capability for cemented carbide (WC-Co) against austenitic stainless steel (SUS 304). Int. J. Adv. Manuf. Technol. **46**, 1145–1160 (2010). https://doi.org/10.1007/s00170-009-2167-8

15. Uhlmann, E., Rosiwal, S., Bayerlein, K., Röhner, M.: Influence of grain size on the wear behavior of CVD diamond coatings in micro-EDM. Int. J. Adv. Manuf. Technol. **47**, 919–922 (2010). https://doi.org/10.1007/s00170-009-2131-7

16. Uhlmann, E., Roehner, M.: Investigations on reduction of tool electrode wear in micro-EDM using novel electrode materials. CIRP J. Manuf. Sci. Technol. **1**, 92–96 (2008). https://doi.org/10.1016/j.cirpj.2008.09.011

17. Jahan, M.P., Rahman, M., Wong, Y.S.: A review on the conventional and micro-electrodischarge machining of tungsten carbide. Int. J. Mach. Tools Manuf. **51**, 837–858 (2011). https://doi.org/10.1016/j.ijmachtools.2011.08.016

18. Kibria, G., Sarkar, B.R., Pradhan, B.B., Bhattacharyya, B.: Comparative study of different dielectrics for micro-EDM performance during microhole machining of Ti–6Al–4V alloy. Int. J. Adv. Manuf. Technol. **48**, 557–570 (2010). https://doi.org/10.1007/s00170-009-2298-y

19. Klocke, F.: Using ultra thin electrodes to produce micro-parts with wire-EDM. J. Mater. Process. Technol. (2004). https://doi.org/10.1016/S0924-0136(04)00214-6

20. Lee, S.H.H., Li, X.P.P.: Study of the effect of machining parameters on the machining characteristics in electrical discharge machining of tungsten carbide. J. Mater. Process. Technol. **115**, 344–358 (2001). https://doi.org/10.1016/S0924-0136(01)00992-X

21. Jahan, M.P., Wong, Y.S., Rahman, M.: A study on the fine-finish die-sinking micro-EDM of tungsten carbide using different electrode materials. J. Mater. Process. Technol. **209**, 3956–3967 (2009). https://doi.org/10.1016/j.jmatprotec.2008.09.015

22. Yu, Z.: Dry electrical discharge machining of cemented carbide. J. Mater. Process. Technol. (2004). https://doi.org/10.1016/S0924-0136(04)00179-7

23. Kim, C., Kang, M.C., Kim, J.S., Kim, K.H., Shin, B.S., Je, T.J.: Mechanical properties and cutting performance of nanocomposite Cr–Si–N coated tool for green machining. Curr. Appl. Phys. **9**, S145–S148 (2009). https://doi.org/10.1016/j.cap.2008.08.054

24. Suzuki, T., Kato, M., Saito, H., Iizuka, H.: Effect of carbon nanotube (CNT) size on wear properties of Cu-based CNT composite electrodes in electrical discharge machining. J. Solid Mech. Mater. Eng. **5**, 348–359 (2011). https://doi.org/10.1299/jmmp.5.348

25. Suzuki, T., Konno, T.: Improvement in tool life of electroplated diamond tools by Ni-based carbon nanotube composite coatings. Precis. Eng. **38**, 659–665 (2014). https://doi.org/10.1016/j.precisioneng.2014.03.003

26. Soltanieh, M., Aghajani, H., Mahboubi, F., Nekouee, K.A.: Surface characterization of multiple coated H11 hot work tool steel by plasma nitriding and hard chromium electroplating processes. Vacuum **86**, 1470–1476 (2012). https://doi.org/10.1016/j.vacuum.2012.01.003

27. Kurahashi, K., Yanagihara, K., Tani, Y., Sato, H.: Repeatable on-the-machine cutting-edge-forming technology applying composite electroplating and anodic electrolysis. CIRP Ann. Manuf. Technol. **53**, 53–56 (2004). https://doi.org/10.1016/S0007-8506(07)60643-X

28. Park, H.K., Onikura, H., Ohnishi, O., Sharifuddin, A.: Development of micro-diamond tools through electroless composite plating and investigation into micro-machining characteristics. Precis. Eng. **34**, 376–386 (2010). https://doi.org/10.1016/j.precisioneng.2009.09.001

29. Li, H.Y., He, H.B., Han, W.Q., Yang, J., Gu, T., Li, Y.M., Lyu, S.K.: A study on cutting and tribology performances of TiN and TiAlN coated tools. Int. J. Precis. Eng. Manuf. **16**, 781–786 (2015). https://doi.org/10.1007/s12541-015-0103-4

30. Chiou, A.H., Tsao, C.C., Hsu, C.Y.: A study of the machining characteristics of micro EDM milling and its improvement by electrode coating. Int. J. Adv. Manuf. Technol. **78**, 1857–1864 (2015). https://doi.org/10.1007/s00170-014-6778-3

31. Sahin, Y., Sur, G.: The effect of Al_2O_3, TiN and Ti (C, N) based CVD coatings on tool wear in machining metal matrix composites. Surf. Coatings Technol. **179**, 349–355 (2004). https://doi.org/10.1016/S0257-8972(03)00802-8

32. More, A.S., Jiang, W., Brown, W.D., Malshe, A.P.: Tool wear and machining performance of cBN-TiN coated carbide inserts and PCBN compact inserts in turning AISI 4340 hardened steel. J. Mater. Process. Technol. **180**, 253–262 (2006). https://doi.org/10.1016/j.jmatprotec.2006.06.013

33. Dosbaeva, G.K., El Hakim, M.A., Shalaby, M.A., Krzanowski, J.E., Veldhuis, S.C.: Cutting temperature effect on PCBN and CVD coated carbide tools in hard turning of D2 tool steel. Int. J. Refract. Met. Hard Mater. **50**, 1–8 (2015). https://doi.org/10.1016/j.ijrmhm.2014.11.001

34. Zhang, K., Deng, J., Meng, R., Gao, P., Yue, H.: Effect of nano-scale textures on cutting performance of WC/Co-based Ti55Al45N coated tools in dry cutting. Int. J. Refract. Met. Hard Mater. **51**, 35–49 (2015). https://doi.org/10.1016/j.ijrmhm.2015.02.011

35. Sidorenko, D., Mishnaevsky, L., Levashov, E., Loginov, P., Petrzhik, M.: Carbon nanotube reinforced metal binder for diamond cutting tools. Mater. Des. **83**, 536–544 (2015). https://doi.org/10.1016/j.matdes.2015.06.056

36. Bouzakis, K.D., Bouzakis, E., Kombogiannis, S., Paraskevopoulou, R., Skordaris, G., Makrimallakis, S., Katirtzoglou, G., Pappa, M., Gerardis, S., M'Saoubi, R., Andersson, J.M.: Effect of silicon content on PVD film mechanical properties and cutting performance of coated cemented carbide inserts. Surf. Coatings Technol. **237**, 379–389 (2013). https://doi.org/10.1016/j.surfcoat.2013.06.044

37. Zhang, K., Deng, J., Sun, J., Jiang, C., Liu, Y., Chen, S.: Effect of micro/nano-scale textures on anti-adhesive wear properties of WC/Co-based TiAlN coated tools in AISI 316 austenitic stainless steel cutting. Appl. Surf. Sci. **355**, 602–614 (2015). https://doi.org/10.1016/j.apsusc.2015.07.132

38. Chang, Y.Y., Lai, H.M.: Wear behavior and cutting performance of CrAlSiN and TiAlSiN hard coatings on cemented carbide cutting tools for Ti alloys. Surf. Coatings Technol. **259**, 152–158 (2014). https://doi.org/10.1016/j.surfcoat.2014.02.015

39. Kim, M., Chang, D.Y., Jeong, Y.S., Ro, B.H., Lee, K.H.: The wear resistance of electroless nickel and electroless composite (Ni-PX, X: SiC, Al_2O_3, diamond) coating layers. J. Korean Inst. Surf. Eng. **27**, 193–206 (1994)

40. Choy, K.L.: Chemical vapour deposition of coatings (2003). https://doi.org/10.1016/S0079-6425(01)00009-3

41. Vahlas, C., Caussat, B., Serp, P., Angelopoulos, G.N.: Principles and applications of CVD powder technology (2006). https://doi.org/10.1016/j.mser.2006.05.001

42. Sproul, W.D.: Physical vapor deposition tool coatings. Surf. Coatings Technol. **81**, 1–7 (1996). https://doi.org/10.1016/0257-8972(95)02616-9

43. König, W., Fritsch, R., Kammermeier, D.: Physically vapor deposited coatings on tools: performance and wear phenomena. Surf. Coatings Technol. **49**, 316–324 (1991). https://doi.org/10.1016/0257-8972(91)90076-9

44. Bouzakis, K.D., Michailidis, N., Skordaris, G., Bouzakis, E., Biermann, D., M'Saoubi, R.: Cutting with coated tools: coating technologies, characterization methods and performance

optimization. CIRP Ann. Manuf. Technol. **61**, 703–723 (2012). https://doi.org/10.1016/j.cirp.2012.05.006

45. Henderer, W., Xu, F.: Hybrid TiSiN, CrC/C PVD coatings applied to cutting tools. Surf. Coatings Technol. **215**, 381–385 (2013). https://doi.org/10.1016/j.surfcoat.2012.06.092

46. Wu, W., Chen, W., Yang, S., Lin, Y., Zhang, S., Cho, T.Y., Lee, G.H., Kwon, S.C.: Design of AlCrSiN multilayers and nanocomposite coating for HSS cutting tools. Appl. Surf. Sci. **351**, 803–810 (2015). https://doi.org/10.1016/j.apsusc.2015.05.191

47. Vereschaka, A.A., Grigoriev, S.N., Vereschaka, A.S., Popov, A.Y., Batako, A.D.: Nano-scale multilayered composite coatings for cutting tools operating under heavy cutting conditions. In: Procedia CIRP, pp. 239–244. Elsevier (2014). https://doi.org/10.1016/j.procir.2014.03.070

48. Manjaiah, M., Narendranath, S., Basavarajappa, S., Gaitonde, V.N.: Effect of electrode material in wire electro discharge machining characteristics of Ti50Ni50-xCux shape memory alloy. Precis. Eng. **41**, 68–77 (2015). https://doi.org/10.1016/j.precisioneng.2015.01.008

49. Bansal, S.A., Singh, A.P., Kumar, S.: Synergistic effect of graphene and carbon nanotubes on mechanical and thermal performance of polystyrene. Mater. Res. Express. **5**, 075602 (2018). https://doi.org/10.1088/2053-1591/aacfc0

50. Raj, S.O.N., Prabhu, S.: Analysis of multi objective optimisation using TOPSIS method in EDM process with CNT infused copper electrode. Int. J. Mach. Mach. Mater. **19**, 76–94 (2017). https://doi.org/10.1504/IJMMM.2017.081190

51. Bansal, S.A., Singh, A.P., Kumar, S.: High strain rate behavior of epoxy graphene oxide nanocomposites. Int. J. Appl. Mech. **10**, 1850072 (2018). https://doi.org/10.1142/S1758825118500722

52. Bansal, S.A., Singh, A.P., Kumar, S.: Reinforcing graphene oxide nanoparticles to enhance viscoelastic performance of epoxy nanocomposites. J. Nanosci. Nanotechnol. **19**, 4000–4006 (2019). https://doi.org/10.1166/jnn.2019.16336

53. Twinkle, Singh, K., Bansal, S.A., Kumar, S.: Graphene oxide (GO)/copper doped hematite (α-Fe_2O_3) nanoparticles for organic pollutants degradation applications at room temperature and neutral pH. Mater. Res. Express. **6**, 115026 (2019). https://doi.org/10.1088/2053-1591/ab4459

54. Zeller, F., Müller, C., Miranzo, P., Belmonte, M.: Exceptional micromachining performance of silicon carbide ceramics by adding graphene nanoplatelets. J. Eur. Ceram. Soc. **37**, 3813–3821 (2017)

55. Bansal, S.A., Singh, A.P., Kumar, A., Kumar, S., Kumar, N., Goswamy, J.K.: Improved mechanical performance of bisphenol-A graphene-oxide nano-composites. J. Compos. Mater. **52**, 2179–2188 (2018). https://doi.org/10.1177/0021998317741952

56. Bansal, S.A., Singh, A.P., Kumar, S.: 2D materials: graphene and others. In: AIP Conference Proceedings, p. 020459 (2016). https://doi.org/10.1063/1.4946510

57. Benninghoven, A.: Characterization of coatings. Thin Solid Films **39**, 3–23 (1976). https://doi.org/10.1016/0040-6090(76)90620-9

58. Bouzakis, K.D., Michailidis, N., Hadjiyiannis, S., Skordaris, G., Erkens, G.: The effect of specimen roughness and indenter tip geometry on the determination accuracy of thin hard coatings stress-strain laws by nanoindentation. Mater. Charact. **49**, 149–156 (2002). https://doi.org/10.1016/S1044-5803(02)00361-3

59. Bansal, S.A., Singh, A.P., Kumar, S., Bansal, S.A.: Reinforcing graphene oxide nano particles to enhance. J. Nanosci. Nanotechnol. **19**, 1–7 (2019). https://doi.org/10.1166/jnn.2019.16336

60. Bouzakis, K.D., Michailidis, N., Skordaris, G.: Hardness determination by means of a FEM-supported simulation of nanoindentation and applications in thin hard coatings. Surf. Coatings Technol. **200**, 867–871 (2005). https://doi.org/10.1016/j.surfcoat.2005.02.122

61. Beake, B.D.: Evaluation of the fracture resistance of DLC coatings on tool steel under dynamic loading. Surf. Coatings Technol. **198**, 90–93 (2005). https://doi.org/10.1016/j.surfcoat.2004.10.048

62. Beake, B.D., Smith, J.F., Gray, A., Fox-Rabinovich, G.S., Veldhuis, S.C., Endrino, J.L.: Investigating the correlation between nano-impact fracture resistance and hardness/modulus ratio from nanoindentation at 25–500 °C and the fracture resistance and lifetime of cutting tools with

Ti1-xAlxN (x = 0.5 and 0.67) PVD coatings in milling operations. Surf. Coatings Technol. **201**, 4585–4593 (2007). https://doi.org/10.1016/j.surfcoat.2006.09.118

63. Beake, B.D., Fox-Rabinovich, G.S., Veldhuis, S.C., Goodes, S.R.: Coating optimisation for high speed machining with advanced nanomechanical test methods. Surf. Coatings Technol. **203**, 1919–1925 (2009). https://doi.org/10.1016/j.surfcoat.2009.01.025

64. Fateh, N., Fontalvo, G.A., Gassner, G., Mitterer, C.: Influence of high-temperature oxide formation on the tribological behaviour of TiN and VN coatings. Wear **262**, 1152–1158 (2007). https://doi.org/10.1016/j.wear.2006.11.006

65. Rodríguez, R.J., García, J.A., Medrano, A., Rico, M., Sánchez, R., Martínez, R., Labrugère, C., Lahaye, M., Guette, A.: Tribological behaviour of hard coatings deposited by arc-evaporation PVD. In: Vacuum, pp. 559–566 (2002). https://doi.org/10.1016/S0042-207X(02)00248-8

66. Wagner, J., Mitterer, C., Penoy, M., Michotte, C., Wallgram, W., Kathrein, M.: The effect of deposition temperature on microstructure and properties of thermal CVD TiN coatings. Int. J. Refract. Met. Hard Mater. **26**, 120–126 (2008). https://doi.org/10.1016/j.ijrmhm.2007.01.010

67. SPIE, Proceedings of: Front Matter: Volume 6606. In: Advanced Laser Technologies 2006, pp. 660601-660601–14. SPIE (2007). https://doi.org/10.1117/12.739509

68. Liu, A., Deng, J., Cui, H., Chen, Y., Zhao, J.: Friction and wear properties of TiN, TiAlN, AlTiN and CrAlN PVD nitride coatings. Int. J. Refract. Met. Hard Mater. **31**, 82–88 (2012). https://doi.org/10.1016/j.ijrmhm.2011.09.010

69. Lin, J.F., Horng, J.H.: Analysis of the tribological behaviour and wear mechanisms of titanium nitride coating. Wear. **171**, 59–69 (1994). https://doi.org/10.1016/0043-1648(94)90348-4

70. Hainsworth, S.V., Soh, W.C.: The effect of the substrate on the mechanical properties of TiN coatings. Surf. Coatings Technol. **163–164**, 515–520 (2003). https://doi.org/10.1016/S0257-8972(02)00652-7

71. Guu, Y.Y., Lin, J.F., Ai, C.F.: The tribological characteristics of titanium nitride coatings part I. Coating thickness effects. Wear **194**, 12–21 (1996). https://doi.org/10.1016/0043-1648(95)06630-6

72. Guu, Y.Y., Lin, J.F.: The tribological characteristics of titanium nitride coatings Part II. Comparisons of two deposition processes. Wear **194**, 22–29 (1996). https://doi.org/10.1016/0043-1648(95)06631-4

73. Azushima, A., Tanno, Y., Iwata, H., Aoki, K.: Coefficients of friction of TiN coatings with preferred grain orientations under dry condition. Wear **265**, 1017–1022 (2008). https://doi.org/10.1016/j.wear.2008.02.019

74. Nordin, M., Larsson, M., Hogmark, S.: Wear resistance of multilayered PVD TiN/TaN on HSS. In: Surface and Coatings Technology, pp. 528–534 (1999). https://doi.org/10.1016/S0257-8972(99)00493-4

75. Nordin, M., Larsson, M., Hogmark, S.: Mechanical and tribological properties of multilayered PVD TiN/CrN, TiN/MoN, TiN/NbN and TiN/TaN coatings on cemented carbide. Surf. Coatings Technol. **106**, 234–241 (1998). https://doi.org/10.1016/S0257-8972(98)00544-1

76. Gåhlin, R., Larsson, M., Hedenqvist, P., Jacobson, S., Hogmark, S.: The crater grinder method as a means for coating wear evaluation—an update. Surf. Coatings Technol. **90**, 107–114 (1997). https://doi.org/10.1016/S0257-8972(96)03101-5

77. Luo, Q., Hovsepian, P.E., Lewis, D.B., Münz, W.D., Kok, Y.N., Cockrem, J., Bolton, M., Farinotti, A.: Tribological properties of unbalanced magnetron sputtered nano-scale multilayer coatings TiAlN/VN and TiAlCrYN deposited on plasma nitrided steels. Surf. Coatings Technol. **193**, 39–45 (2005). https://doi.org/10.1016/j.surfcoat.2004.07.058

Transient Analysis of GTA-Welded Austenitic and Ferritic Stainless Steel

Chetan Tembhurkar, Ravinder Kataria, Sachin Ambade, and Jagesvar Verma

1 Introduction

Welding with dissimilar metals with proper selection of filler material gives better strength and corrosion properties in the metal. However, the welding affects the nonuniform temperature distribution in the joint, and these results in residual stresses in the material [1]. The finite element method is a technique that gives the solution for boundary value engineering, temperature, and stress distribution of the material during welding processes [2, 3]. The transient thermal analysis to find out the temperature distribution gives better results. The different welding conditions are taken, and the simulation of these welding processes is conducted in ANSYS [4, 5]. The welding with GTAW is carried out with 316L ASS and 430 FSS with filler 309, 316 and without filler material. The process parameters are arc voltage (V) 20–23, welding current (amps) 90–100, welding speed (mm/s) 1.7–2.7 and nonconsumable tungsten electrode having a diameter (mm) 1.6 for the welding process.

The assumptions pertaining to this work are as follows:

 (i) Material properties are assumed to be isotropic;
 (ii) Heat flux is constant at the welding zone;
 (iii) Convective and radiative heat losses occur at all free surfaces;
 (iv) GTA welding with and without filler material is modeled.

C. Tembhurkar (✉) · R. Kataria
School of Mechanical Engineering, LPU, Jalandhar, Punjab, India
e-mail: chetantembhurkar@gmail.com

S. Ambade
Department of Mechanical Engineering, YCCE, Nagpur, Maharashtra, India

J. Verma
National Institute of Foundry & Forge Technology (NIFFT), Hatia, Ranchi, Jharkhand, India

2 Finite Element Analysis

2.1 Heat Source and Boundary Conditions

Heat source during welding is considered when welding torch comes near the two dissimilar plates. The heat is created at the interface within the torch and plate due to the current passing through the welding torch. The heat inputs (Q) in KJ/mm for weld are calculated by considering the arc efficiency of 0.7.

$$Q = \left(\eta \frac{VI}{v} \right) \tag{1}$$

where V is arc voltage (V), I is welding current (A), and v is speed (mm/s).

Heat conduction in three dimensions is carried out using Fourier's law.

According to it, the transient equation of temperature becomes

$$\rho Cp \frac{\partial T}{\partial t} = \frac{\partial}{\partial x}\left(k \frac{\partial T}{\partial x} \right) + \frac{\partial}{\partial y}\left(k \frac{\partial T}{\partial y} \right) + \frac{\partial}{\partial z}\left(k \frac{\partial T}{\partial z} \right) + Qv \tag{2}$$

where T is temperature, Cp is heat capacity, ρ is density, and k is heat conductivity that changes with temperature in the computations.

The boundary conditions are summed up as follows:

$$q_{\text{rad}} = \varepsilon \sigma \left((T - Tz)^4 - (T_0 - Tz)^4 \right) \tag{3}$$

where q_{rad} is the radiative heat losses, ε is emissivity, σ is Stefan Boltzmann's constant, which 5.67×10^{-8} W/m^2 K^4, T_0 is the temperature throughout the body at time zero at the staring of the weld, Tz is the temperature at the weld zone.

2.2 Welding Model

The finite element model (FEM) of two plates having dimension $75 \times 100 \times 3$ mm is used. The two plates of 316L ASS and 430 FSS are welded by using GTAW, and these are modeled in ANSYS software. The 316 L ASS is used in chemical, petrochemical, and shipbuilding industries [6–8]. It has excellent strength and corrosion-resistant properties. While 316L ASS welded with 430 FSS with filler material can be used in various industries due to the cost phenomenon. The chemical composition of 316L ASS and 430 FSS are given in Table 1 and the mechanical properties are given in Table 2 [4, 8–13].

In the present analysis, the single-pass butt welding is performed having constant heat flux. The current thermal analysis is conducted having element type SOLID183,

Table 1 Chemical composition (wt%) of AISI 316L ASS and AISI 430 FSS

Materials	C	Si	Mn	P	S	Cr	Mo	Ni	Al	Co	Cu
AISI 316L	0.02	0.52	1.30	0.031	0.003	16.86	2.00	10.06	0.003	0.17	0.272
AISI 430	0.012	0.165	0.70	0.030	0.008	16.30	0.030	0.110	0.001	0.01	0.018

Table 2 Mechanical properties of 316L ASS and 430 FSS (19) [14]

Material	Tensile strength (MPa)	Density (kg/m^3)	Thermal conductivity (W/m k)	Yield strength (MPa)	Melting point (°C)	% elongation
316L ASS	485	8000	21.5	170	1390–1440	40
430 FSS	488	7700	26.0	380	1425–1510	28

Fig. 1 Welding model
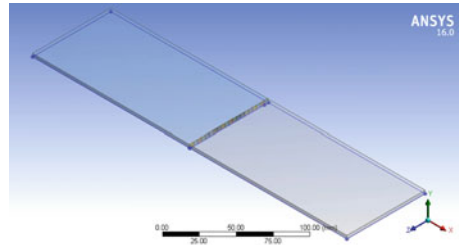
Fig. 2 Meshed model
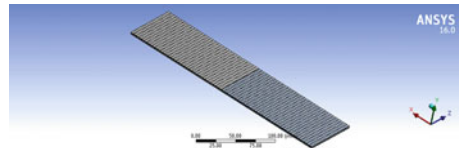
which is having three-dimensional conduction capacity including 8 nodes and having a single degree of freedom at each node.

The element is capable of three-dimensional, steady-state, and transient analysis [2, 13–18]. Welding model is shown in Fig. 1. The meshing is done, and the meshed model is developed as shown in Fig. 2.

3   Results and Discussion

3.1   Thermal Profile of Welding Using ANSYS

The distribution of temperature across the welding zone is carried out by ER 309 filler, ER 316 filler and without filler. At time t equal to 0 s, welding starts with heat rate (Q) given as the input parameter for the surface on the weld zone. Figures 3, 4 and 5 give the distribution of temperature across the welding zone at time t equal to 20 s [2]. The temperature across the welding zone is calculated using ANSYS 16.0. Figure 3 shows the temperature from 604 to 4440 °C for the input welding parameters. Figure 4 shows the temperature distribution which ranges from 602 to 3980 °C.
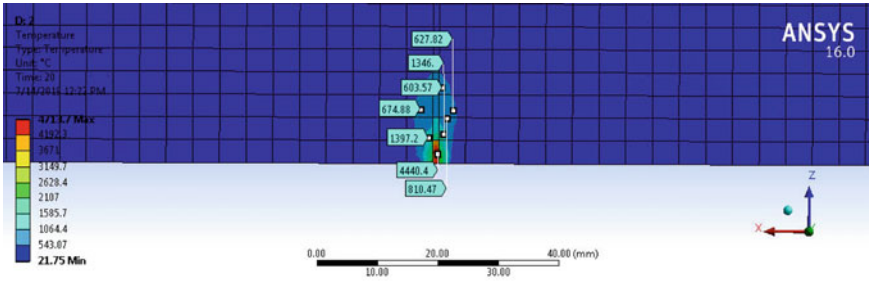
Fig. 3 Distribution of temperature using 309L filler material for 20 s
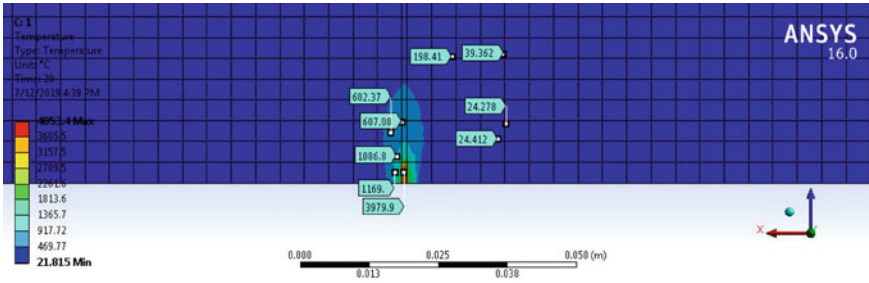
Fig. 4 Distribution of temperature using 316L filler material for 20 s
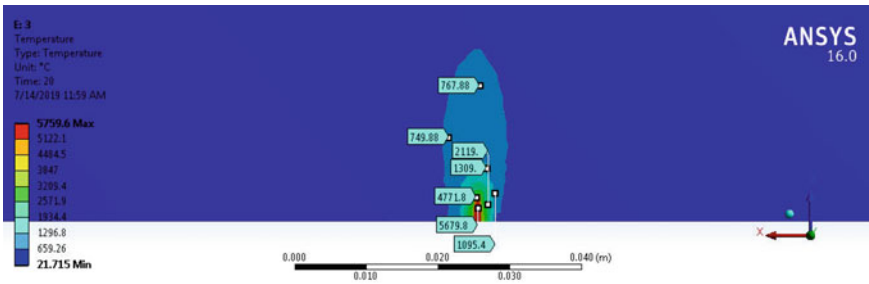
Fig. 5 Distribution of temperature using without filler material for 20 s

Figure 5 shows the temperature distribution across the welding zone that found to vary from 750 to 5680 °C. The maximum temperature across the welding zone is compared and found that autogenous welding (without filler) is having maximum temperature distribution across the weld zone.

4 Conclusion

The Finite Element Model simulation is conducted for 309 filler, 316 filler, and without filler material is compared and found that:

 (i) It is ascertained that the most temperature across the weld zone will increase because the tool holding time will increase.
(ii) For GTAW of 316L ASS and 430 FSS with ER316 filler material, the heat-affected zone is less as compared to the other two filler materials.
(iii) A procedure is developed for evaluating the maximum temperature distribution across the welding zone with a concerning time with a single pass.
(iv) This prediction of analysis can be useful to predict the heat input parameters, which can be used for experimentation.

References

 1. Stamenkovic, D., Vasovic, I.: Finite element analysis of residual stress in butt welding two similar plates. Specif. Tech. Rev. **LIX**(1) (2009)
 2. Vemanaboina, H., Akella, S., Buddu, R.K.: Welding process simulation model for temperature and residual stress analysis. Procedia Mater. Sci. **6**, 1539–1546 (2014)
 3. Kıra, B.G., Tabanoglu, M., Tarık Serindag, H.: Finite element modeling of friction stir welding in aluminum alloys joint. Math. Comput. Appl. **18**(2), 122–131 (2013)
 4. Barsoum, Z., Lundback, A.: Simplified FE welding simulation of fillet welds—3D effects on the formation residual stresses. Eng. Fail. Anal. **16**, 2281–2289 (2009)
 5. Deogade, S.R., Ambade, S.P., Patil, A.: Finite element analysis of residual stresses on ferritic stainless steel using shield metal arc welding. Int. J. Eng. Res. Gener. Sci. **3**(2) (2015)
 6. Peckner, D.: Bernstein. In: Hand Book of Stainless Steels, pp. 5–44. McGraw Hill, New York (1977)
 7. Madhusudhan Reddy, G., Mohandas, T., Sambasiva Rao, A., Satyanarayana, V.V.: Influence of welding processes on microstructure and mechanical properties of dissimilar of austenitic-ferritic stainless steel welds. Mater. Manuf. Process. **20**, 147–173 (2005)
 8. Atlas Steels, Stainless Steels Grade Datasheet, Atlas Steel Technical Department (2013)
 9. Capriccioli, A., Frosi, P.: Multipurpose ANSYS FE procedure for welding processes simulation. Fusion Eng. Des. **84**, 546–553 (2009)
10. Fenggui, L., Yao, S., Lou, S., Li, Y.: Modeling and finite element analysis on GTAW arc and weld pool. Comput. Mater. Sci. **29**, 371–378 (2004)
11. Kuddus, A.I., Ambade, S.P., Bansod, A.V., Patil, A.P.: Microstructural, mechanical and corrosion behaviour of dissimilar welding of Cr-Mn ASS and AISI 304 ASS by using 316L electrode. Mater. Today Proc. **5**(2) (2018)
12. Carmignani, C., Mares, R., Toselli, G.: Transient finite element analysis of deep penetration laser welding process in a single pass butt-welded thick steel plate. Comput. Methods Appl. Mech. Engrg. **179**, 197–214 (1999)
13. Chen, C.M., Kovacevic, R.: Finite element modeling of friction stir welding thermal and thermomechanical analysis. Int. J. Mach. Tools Manuf. **43**, 1319–1326 (2003)
14. Stainless Steel Grade Datasheets, Atlas Steels Technical Department, August (2013)
15. Mahiskar, G.I., Chadge, R.B., Ambade, S.P., Patil, A.P.: Thermo-mechanical analysis of multi-pass bead-on-plate welding. Procedia Mater. Sci. **5**, 2522–2531 (2014)

16. Wang, F., Hou, W.K., Hu, S.J., Kannatey-Asibu, E., Schultz, W., Wang, P.C.: Modelling and analysis of metal transfer in gas metal arc welding. J. Phys. D Appl. Phys. **36**, 1143–1152 (2003)
17. del Coz Díaz, J.J., Menéndez Rodríguez, P., García Nieto, P.J., Castro-Fresno, D.: Comparative analysis of TIG welding distortions between austenitic and duplex stainless steels by FEM. Appl. Therm. Eng. **30**, 2448–2459 (2010)
18. Song, J.L., Lin, S.B., Yang, C.L., Fan, C.L., Ma, G.C.: Analysis of intermetallic layer in dissimilar TIG welding–brazing butt joint of aluminum alloy to stainless steel. Sci. Technol. Weld. Join. **15**, 213–218 (2010)

Electrodeposition and Corrosion Analysis of Ni-Mo Alloy Coatings

Vandana V. Iragar, Shailashree Mendon, Shraddha Acharya, Sujaya, Sujana, V. Anjana Pai, D. Rashmi, and G. P. Pavithra

1   Introduction

Electrodeposition of an alloy is commonly used in the fabrication of nanostructured materials for specific mechanical, chemical, and physical properties in various applications. Corrosion resistance and electrocatalytic properties are of great importance in evaluating the future applications of electrodeposited nanostructured alloy materials [1]. Research has been carried out on Ni and its alloy electrodeposition to determine the ability of these alloys to show their properties at room temperature. Binary alloys of Ni with Mo, W, or V have been found to have good resistance to corrosion and electrocatalytic properties. With this regard, Ni-Mo alloy electrodeposition was widely employed in recent years mainly because of its corrosion protection, electrocatalytic and magnetic properties [2]. It is agreed that, from an aqueous solution, Mo cannot be electrodeposited, but it can electrodeposit by alloying with Fe-group metals. Apparently, the codeposition of Mo can be caused by Fe-group metals, Ni-Mo system is an example for induced electrodeposition [3]. Further, the literature shows that several hypotheses were suggested to explain the characteristics of the codeposition conduct induced, and the impact of electrolyte composition on alloy deposition was not properly predicted. It is assumed that the possible many-fold decrease of chemical Mo species is not completely explained. Therefore, the Ni-Mo alloy induced codeposition mechanism requires a more quantitative and systematic approach [4]. Yagi et al. [5] showed that Mo can be deposited with aqueous Mo (IV) electrolyte on Ni substrate using alternating pulse electrodeposition. With regard to the corrosion resistance of Ni-Mo deposits, Huang et al. [6] reported that 20% Mo deposited from an electrolytic bath without any additive resulted in significant corrosion resistance in 3.5% of saline water. Although, reports of Ahmad et al. [7] say elevated corrosion resistance was acquired at ~13% Mo content when monolayers

V. V. Iragar · S. Mendon · S. Acharya · Sujaya · Sujana · V. Anjana Pai · D. Rashmi ·
G. P. Pavithra (✉)
Alva's Institute of Engineering and Technology, Mijar, Mangaluru 574225, Moodbidri, India
e-mail: pavithra.gp2008@gmail.com

were produced from glycinate and saccharin-solution baths [8]. Laszczynska et al. [9] in his recent work reported the extreme corrosion resistance behavior obtained at 12% Mo for small exposure time in 0.5 M saline water, while for large exposure 17% Mo coatings showed the highest corrosion resistance in the same environment. The function of Mo in the corrosion conduct in the monolayer electrodeposited Ni-Mo alloy is, therefore, not supporting after considering the large Mo content with distinct corrosion experiment outcomes.

Citrate has been selected to deposit the variable composition of homogeneous Ni-Mo deposits, allowing the scope to investigate. The function of citrate in electrolytes during the deposition phase is to retain a stable pH. The data rendering from the literature shows citrate-based adsorbing intermediate helps with Ni ions in the deposition of Mo, which follows an independent path to reduce on electrode [10]. Further, in most cases, Ni-Mo alloy with high corrosion protection, low overpotential for hydrogen evolution reactions, less thermal expansion coefficient, and good hardness was obtained from electrodeposition with citrate baths containing ammonia. Only a few papers were dedicated to the complete characterization and its properties. The purpose of the present work is, therefore, to develop electrodeposited Ni-Mo monolayer alloy coatings and their surface structural interpretation at varying applied current density.

2 Experimental Setup

The deposition bath solution was prepared in distilled water from analytical-grade chemicals. Copperplate electroplating was performed at 9.5 ± 0.3 pH and $30\,°C \pm 2\,°C$ temperature. The polished copper plates with $5.0\,cm^2$, served as a cathode and the anode was pure Ni with the same exposed area. Metal salt, additives contents in an electrolytic solution, and operating parameter are shown in Table 1. The optimized content of the bath, pH, and applied c.d. was acquired by the conventional

Table 1 Composition and operating parameters of the Ni-Mo electrolyte

Chemicals	Composition in g/L
Nickel Sulfate ($NiSO_4.6H_2O$)	30.95
Sodium Molybdate ($Na_2MoO_4.2H_2O$)	4.839
Boric acid (H_3BO_3)	9.274
Trisodium Citrate ($Na_3C_6H_5O_7.2H_2O$)	77.42
Sodium dodecyl sulfate ($NaC_{12}H_{25}SO_4$)	0.0288
Sulfanilic acid ($C_6H_7NO_3S$)	1
Operating parameters	
Current density	1–5 A/dm^2
pH	9.5
Temperature	28 °C

Hull cell technique. Mechanically polished samples of copper were cleaned with deionized water and dipped in the electrolytic solution for electrodeposition. The electrodeposition was performed for 10 min of constant time.

From the optimized bath, thin Ni-Mo coatings were developed in rectangular 250 cm^3 polyvinyl chloride cell maintaining at a distance of 8 cm between parallely placed the anode and cathode. At constant applied c.d.'s, electrodeposition was performed at 1.0–5.0 A dm^{-2} using a direct current power source (N 6705C, Keysight Technologies). The bath solution pH was evaluated before and after each deposition (μ pH System-362, Systronics) and adapted to 9.5, using either H_2SO_4 or NaOH. Potentiodynamic Tafel studies and Electrochemical Impedance Spectroscopy (EIS) techniques (CHI Instruments, Electrochemical Analyzer, Austin, USA) were conducted to study corrosion behaviors of the monolayer coatings in 0.5 M H_2SO_4. Tafel and EIS studies were performed using the three-electrode arrangement system where the reference electrode was a saturated calomel electrode (SCE). EIS signals were recorded with a 10 mV amplitude AC signal. Scanning Electron Microscopy (SEM, ZEISS model) has examined the surface morphological structure of the electrodeposited Ni-Mo monolayer alloy coatings, and individual metal content in the developed coatings was obtained by SEM coupled Energy Dispersive X-ray Spectroscopy (EDX). The coatings phase structures were studied using an X-ray diffractometer (XRD, Rigaku) using Cu Kα radiation in continuous scanning mode at 2° min^{-1} scanning speed.

3 Results and Discussion

3.1 EDS and SEM

Ni-Mo alloy composition in the developed electrodeposits was evaluated by EDX using surface area analysis as shown in Fig. 1a. Figure 1b shows the variation in the Mo content in the coatings at various applied c.d.'s. The strong effect of c.d. was noted in deposits on the wt% of Mo. From Fig. 1, the composition of Mo increased greatly from 1 A dm^{-2} to 3 A dm^{-2} (3.48–23.89 wt%), from 1 A dm^{-2} to 3 A dm^{-2} there was a minor increase in Mo wt% (23.89–26.27 wt%). This is because higher c.d. has a minute effect on the wt% of Mo [11]. This insignificant increase in Mo at greater c.d. is a characteristic induced deposition property of Ni-Mo deposit layer owing to the lesser degree of transportation of Mo^{+2} ions compared to its parent electroactive metal ion species [12].

Figure 2 displays the surface structure of Ni-Mo alloy electrodeposits obtained at various c.d.'s. There was a distinct variation in the coatings' surface morphology indicating the greater influence of c.d. on the morphology of Ni-Mo electrodeposits. At low c.d.'s the deposit is finer and regular. As shown in Fig. 2. the Ni-Mo coatings obtained at 1 A dm^{-2} was homogeneous, compact, and crack free due to the lesser Mo content [13]. On further increasing the c.d., at 3.0 A dm^{-2}, micro-holes were
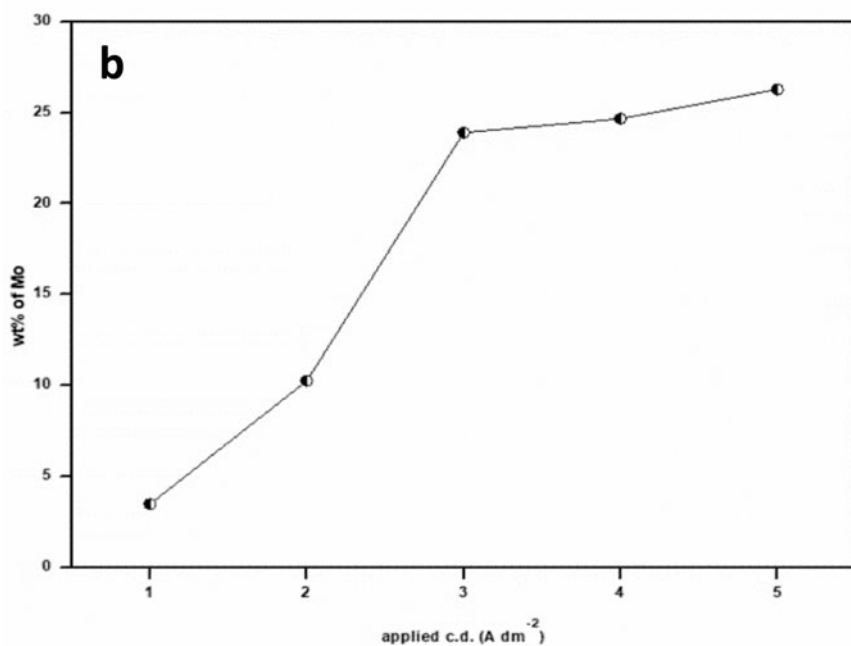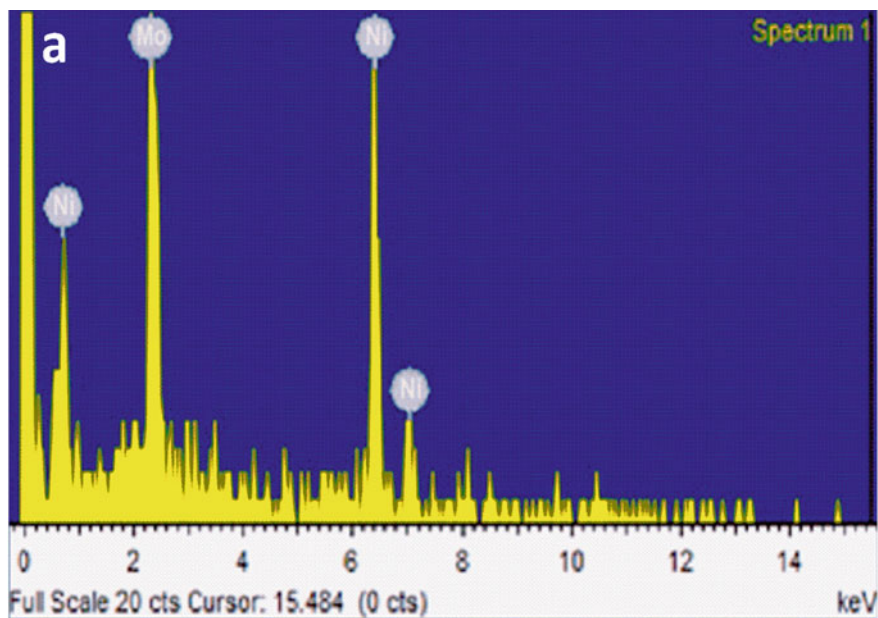
Fig. 1 a Surface EDX of Ni-Mo electrodeposits deposited at 3.0 A dm^{-2} b wt% of Mo at various applied current density
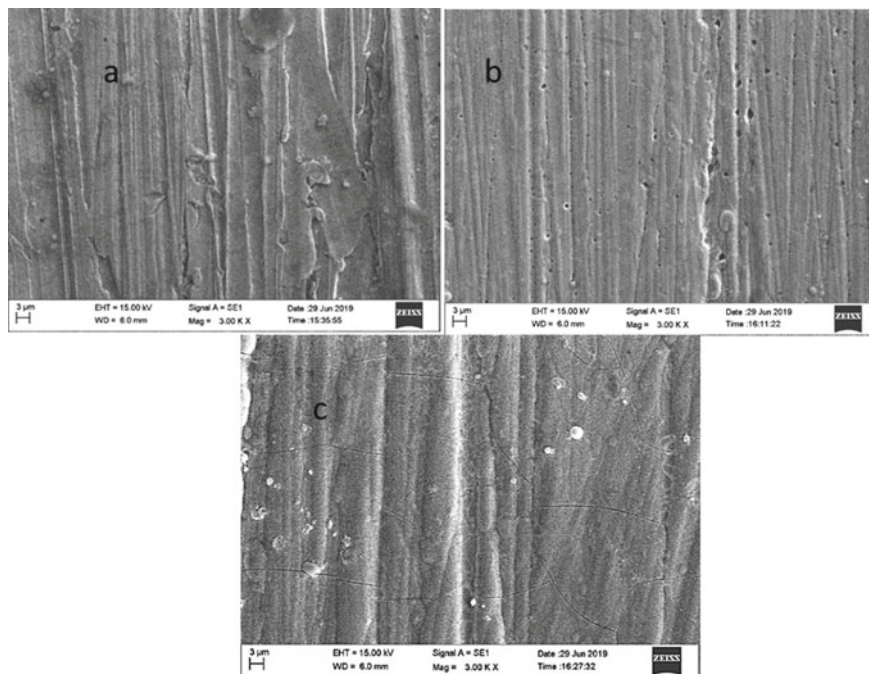
Fig. 2 SEM micrographs of developed Ni-Mo alloy electrodeposits developed using **a** 1 A dm^{-2}, **b** 3 A dm^{-2} and **c** 4 A dm^{-2}

detected on the surface of the coatings, this was due to the hydrogen bubbles produced during codeposition [14]. At 5 A dm^{-2}, the formation of the cracks on the Ni-Mo surface was noted with 26.27 wt% of Mo as a consequence of elevated residual stress during deposition in other wards of hydrogen embrittlement. Thus, an SEM image of Ni-Mo coatings evidenced with deposits developed with a wide range of c.d. It can also be observed to greater c.d. with high Mo content with tiny pinholes that indicate powerful HER/OER electrocatalytic coating.

3.2 Structural Studies

Phase morphology of the developed Ni-Mo alloys was acquired by the XRD technique. Figure 3 displays the XRD peaks of Ni-Mo alloy electrodeposits at 1 A dm^{-2}, 3 A dm^{-2}, and 5 A dm^{-2}. The narrow peaks obtained are the indication of the crystalline nature of the electrodeposits. The Ni-Mo crystallites are tetragonal MoNi$_4$ structure as all the resulting XRD peaks correspond to the tetragonal MoNi$_4$ phase (JCPDS No. 03-065-1533) [15]. From Fig. 3, the variations in the intensity of the peaks were witnessed indicating the vital role of c.d. in the coatings' structural properties. The deposits developed at 1 A dm^{-2}, maximum peak intensity was observed
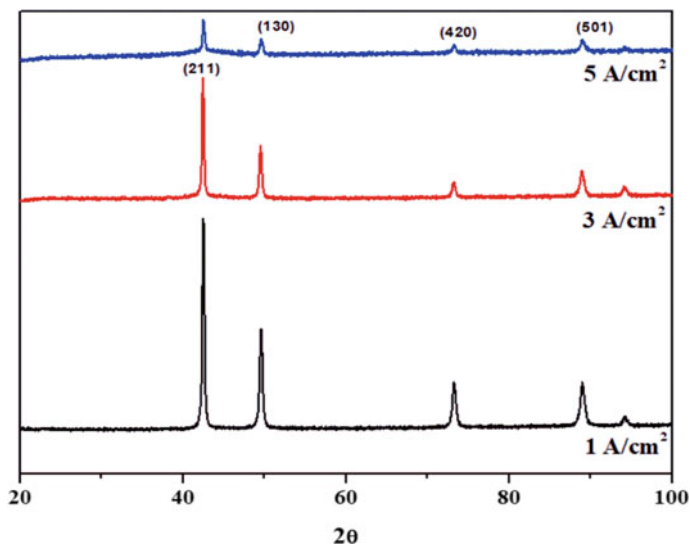
Fig. 3 XRD patterns for Ni-Mo electrodeposits at 1 A dm^{-2}, 3 A dm^{-2} and 5 A dm^{-2}

for (211). However, at higher c.d.'s, 3 A dm^{-2} and 5 A dm^{-2}, the peak intensities of all the major peaks, i.e., (211), (130), (420), and (501) decreased. This was attributed to the coatings with increasing c.d. to increasing wt% of Mo.

3.3 Corrosion Studies

To the study, the corrosion behavior of developed Ni-Mo monolayer alloy coatings at various c.d.'s, the potentiodynamic polarization method and impedance studies were evaluated in 0.5 M H$_2$SO$_4$. Figures 4 and 5 show the Nyquist plot and potentiodynamic polarization curves of the developed coatings, respectively. The corrosion parameter results like E_{corr}, i_{corr}, and Corrosion Rate (CR) obtained by the potentiodynamic polarization method, and the EIS technique informs charge-transfer resistance (R_{ct}) which are given in Table 2.

The corrosion behavior of the coatings depends upon the wt% of Mo and surface morphology of the coatings. From Table 2, it can be seen that i_{corr} increases with an increase in wt% of Mo in the coatings with almost the same E_{corr} value. The minimum CR was observed for the deposit at 1 A dm^{-2} with the least Mo content. Further decrease in CR at low c.d. shows that the coatings' corrosion stability is due to their greater Ni content [2]. The decrease in CR of low c.d. Ni-Mo coatings is due to an increase in coatings uniformity attributed by increasing Ni content in the deposit, as evident by SEM. The maximum CR was observed for the deposits at high c.d.'s with increased wt% of Mo. At high c.d., coatings were witnessed to have
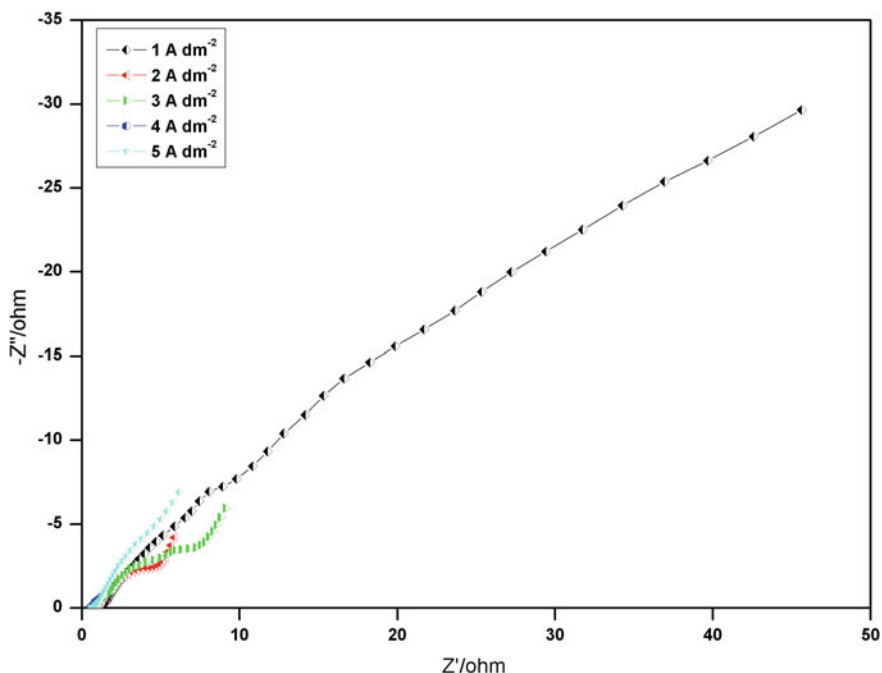
Fig. 4 Nyquist plots for Ni-Mo electrodeposits

micropores and cracks in their surface. Overall corrosion studies reveal that high Mo content in the deposit is unfavorable to corrosion resistance of the coatings in 0.5 M H_2SO_4. This makes them more susceptible to undergo corrosion but on contrary high c.d. Ni-Mo coatings testify the fact that it is more favorable for HER/OER.

The pattern of the Nyquist curves in Fig. 4 clearly shows double-layer capacitance at the metal and solution interface. From Table 2, it can be seen that charge-transfer resistance (R_{ct}) decreases with an increase in applied c.d.'s, in turn increase in wt% of Ni. The R_{ct} value of the Ni-Mo coatings is less than the value reported for pure Ni. It indicates Ni-Mo coatings are more prone to hydrogen or oxygen evolution reactions when compared to pure Ni [16].

4 Conclusions

In this study, Ni-Mo alloy electrodeposition was investigated using a sulfate bath and sulfanilic acid as an additive. Optimization of the bath was carried out for the bright, adherent appearance, and best performance of the coatings against corrosion in 0.5 M H_2SO_4 medium. Experimental results direct toward the lowest CR and the highest R_{ct} value of Ni-Mo coatings at low c.d. The ability of Ni-Mo coatings to
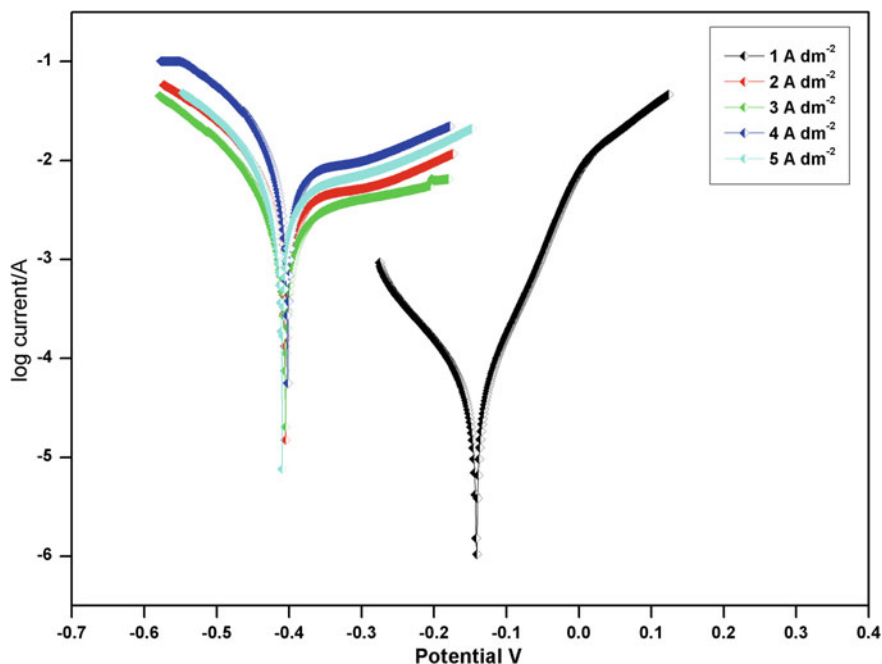
Fig. 5 Potentiodynamic polarization curves for Ni-Mo electrodeposits

Table 2 Corrosion data of Ni-Mo electrodeposits

Cathode c.d. (A dm^{-2})	$-E_{corr}$ (V vs. SCE)	i_{corr} (μA cm^{-2})	β_a (V/dec)	β_c (V/dec)	C.R. (mmy^{-1})	R$_{ct}$
1.0	0.141	50.71	15.379	8.587	0.6682	120
2.0	0.407	64.30	1.753	8.217	51.0286	52
3.0	0.405	1180	1.216	8.562	84.709	38
4.0	0.410	4046	1.829	8.485	96.0374	32
5.0	0.401	7289	1.517	10.216	155.498	29

resist corrosion was dependent on their composition, surface morphology, and phase structure, supported by EDS, SEM, and XRD analyses.

References

1. Bockris, J.O.M., Potter, E.C.: The mechanism of hydrogen evolution at nickel cathodes in aqueous solutions. J. Chem. Phys. **20**, 614–628 (1952)
2. Casciano, P.N.S., Benevides, R.L., de Lima-Neto, P., Correia, A.N.: Corrosion resistance of electrodeposited Ni-Mo-W coatings. Int. J. Electrochem. Sci. **9**, 4413–4428 (2014)
3. Chassaing, E., Portail, N., Levy, A.F., Wang, G.: Characterisation of electrodeposited nanocrystalline Ni-Mo alloys. J. Appl. Electrochem. **34**(11), 1085–1091 (2004)
4. Podlaha, E.J., Landolt, D.: Induced codeposition-II. A mathematical model describing the electrodeposition of Ni-Mo alloys. J. Electrochem. Soc. **143**(3), 893–899 (1996)
5. Yagi, S., Kawakami, A., Murase, K., Awakura, Y.: Ni–Mo alloying of nickel surface by alternating pulsed electrolysis using molybdenum(VI) baths. Electrochim. Acta **52**(19), 6041–6051 (2007)
6. Huang, P.-C., Hou, K.-H., Wang, G.-L., Chen, M.-L., Wang, J.-R.: Corrosion resistance of the Ni-Mo alloy coatings related to coating's electroplating parameters. Int. J. Electrochem. Sci. **10**, 4972–4984 (2015)
7. Ahmad, Y.H., Mohamed, A.M.A., Golden, T.D., D'Souza, N.: Electrodeposition of nanocrystalline Ni-Mo alloys from alkaline glycinate solutions. Int. J. Electrochem. Sci. **9**, 6438–6450 (2014)
8. Halim, J., Abdel-Karim, R., El-Raghy, S., Nabil, M., Waheed, A.: Electrodeposition and characterization of nanocrystalline Ni-Mo catalysts for hydrogen production. J. Nanomater. Article ID 84567 (2012). https://doi.org/10.1155/2012/845673
9. Laszczyńska, A., Tylus, W., Winiarski, J., Szczygieł, I.: Evolution of corrosion resistance and passive film properties of Ni-Mo alloy coatings during exposure to 0.5 M NaCl solution. Surf. Coat. Technol. **317,** 26–37 (2017)
10. Podlaha E.J., Landolt, D.: Induced codeposition-I. An experimental investigation of Ni-Mo alloys. J. Electrochem. Soc. **143**(3), 885–892 (1996)
11. Conway, B.E.: Theory and principles of electrode processes. The Ronald Press Company, New York (1965)
12. Bratoeva, M., Atanasov, N.: Effect of sulfamate-citrate electrolyte pH on the Ni-W alloy electrodeposition. J. Electrochem. Soc. **36**, 60–63 (2000)
13. Halim, J., Abdel-Karim, R., El-Raghy, S., Nabil, M., Waheed, A.: Electrodeposition and characterization of nanocrystalline Ni-Mo catalysts for hydrogen production. J. Nanomater. **18**, 1–9 (2012)
14. Sanches, L.S., Domingues, S.H., Carubelli, A., Mascaro, L.H.: Electrodeposition of Ni-Mo and Fe-Mo alloys from sulfate-citrate acid solutions. J. Braz. Chem. Soc. **14**(4), 556–563 (2003)
15. Shetty, A.R., Hegde, A.C.: Electrodeposition of Ni-Mo alloy coatings for water splitting reaction. In: AIP Conference Proceedings, vol. 1943, no. 1, pp. 020108-1–020108-8 (2018)
16. Xu, C., Zhou, J.-B., Zeng, M., Fu, X.-L., Liu, X.-J., Li, J.-M.: Electrodeposition mechanism and characterization of Ni-Mo alloy and its electrocatalytic performance for hydrogen evolution. Int. J. Hydrogen Energy 1–9 (2016)

Review on Microwave Cladding: A New Approach

Nalin Somani, Kamal Kumar, and Nitin Gupta

1 Introduction

The composite material can be formed by various techniques, i.e., mixing one material to the other material having different properties and resulting material being having a mixture of both material properties. This is known as a composite material. Now when the reinforcing of the material to the metals, ceramic, or polymer is done then it will show excellent properties like strength, porosity, hardness, etc. [1] As the composite material shows various properties so they can also be used in the thermal and electrical field. They are also used in various mechanical industrial components and more expensive to use. MMCs can be produced by various methods like powder metallurgy [2], forging, casting, microwave sintering, etc. Besides all the methods, microwave sintering has the advantage of volumetric heating which gives the formation of the MMCs with superior properties than the other processes. The basic fundamental of the composite material is that it shows desirable properties which cannot be seen in any other materials and various mechanical properties of this material can be varied increasing or decreasing the content of reinforced material or by varying thickness.

In this paper, a study has been done on the various efforts done by researchers in the field of microwave cladding by using the different materials and reinforcements.

N. Somani (✉) · K. Kumar · N. Gupta
Department of Mechanical Engineering, DIT University, Dehradun, India
e-mail: nalin.somani41@gmail.com

2 Literature Review

Prasad et al. [3] In this paper, the investigations of Ni/La$_2$O$_3$ composite powder has been done through microwave irradiation on AISI 1040 steel. This had been done to improve material properties. By using the microwave, the volumetric heating of material result in uniform gradient and thus improve material properties. The clad of composite powder was developed on the surface of AISI 1040 steel to get uniform material properties. The clad thickness was observed to be about 500 μm and a good metallurgical bond between Ni/La$_2$O$_3$ and AISI 1040 steel. The developed clad had more microhardness than the base metal without clad (Fig. 1).

Bansal et al. [4] By the help of microwave heating the nickel with tungsten carbide clad was introduced on the mild steel. Due to volumetric heating, there is a partial dilution of the clad material with the base metal which shows good metallurgical bonding between them and the developed clad improves wear resistance and microstructure of the base metal. It was observed that tungsten carbide was uniformly distributed over the clad region and the microhardness of the developed clad is more than base metal. The nickel with tungsten carbide clad had more wear resistance than the base metal that is mild steel.

Gupta et al. [5] By using the microwave heating, the tungsten carbide cobalt and nickel-based powder clad was introduced on the austenitic steel (SS-316). Due to volumetric heating, there is a partial dilution of clad material with the base metal which shows good metallurgical bonding between them and developed clad is free from any type of cracks. The tungsten carbide particle was uniformly distributed over the clad region and the developed clad is having high microhardness and less porosity. It was observed that the developed clad had good wear resistance properties than the base metal. The developed clad exhibits microhardness of 1064 Hv (Figs. 2 and 3).

Gupta et al. [6] By using microwave heating the nickel-based powder clad was introduced on the austenitic stainless steel (SS-316). Due to volumetric heating, there is a partial dilution of clad material with the base metal which shows good metallurgical bonding between them and various intermediate phase forms during the process like nickel silicate, etc. It was observed that at the cell boundary chromium is found and within the cell, the nickel is found and the shape of the clad microstructure is cellular. During the process at the cell boundary reaction takes place in which chromium reacts with carbon to form chromium carbide (Fig. 4).

Gupta et al. [7] By the help of microwave heating the nickel-based powder with 20% chromium carbide clad was formed on the austenitic stainless steel. Due to volumetric heating, there is a partial dilution of clad material with base metal which shows good metallurgical bonding between them. The clad shows the reinforced of chromium carbide in the Ni-based matrix and particles are uniformly distributed. The developed clad has less porosity and free from solidification cracks. It was observed that formed clad having more microhardness than without clad and this clad is very useful in the wear-resistant industrial components (Fig. 5).
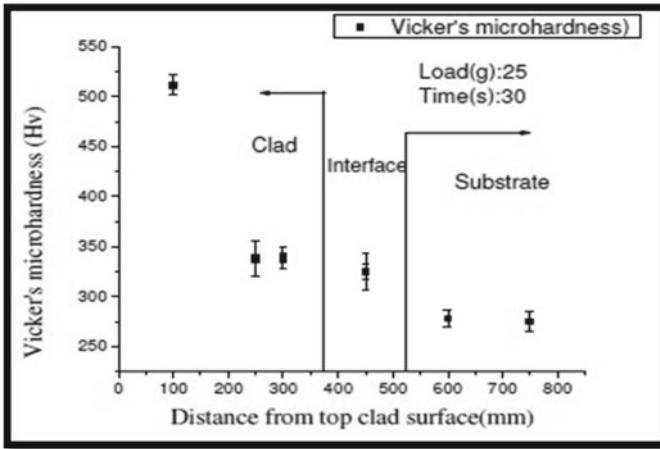
Fig. 1 This figure shows the distribution of microhardness [3]
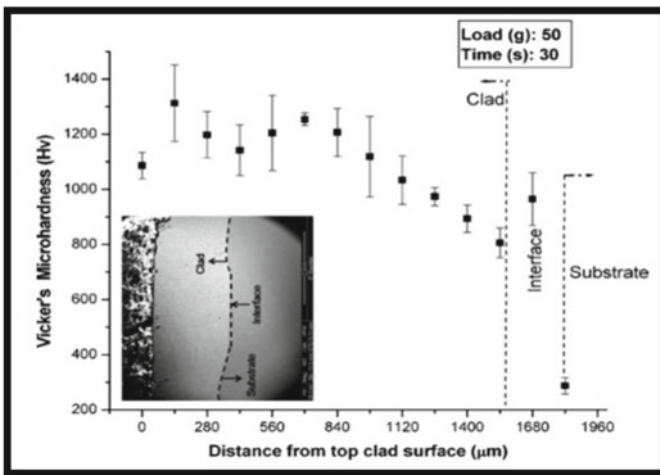
Fig. 2 This figure shows the microhardness distribution of the developed clad [5]

Gupta et al. [8] By using the microwave heating the tungsten carbide cobalt-nickel clad was introduced on the base metal that is austenitic stainless steel. Since volumetric heating dilution of the base metal with the clad material shows good metallurgical bonding and there are various carbides formed which uniformly distributed on the clad region and tungsten particle are also distributed over the clad region. Dilution of metal varies with dilution percentage. It was observed that as the dilution of the clad material increases the microhardness increases.
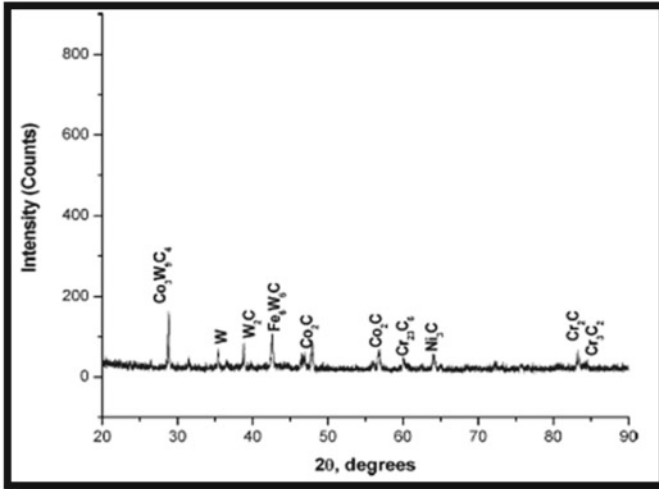
Fig. 3 This figure shows the XRD pattern of the developed clad [5]
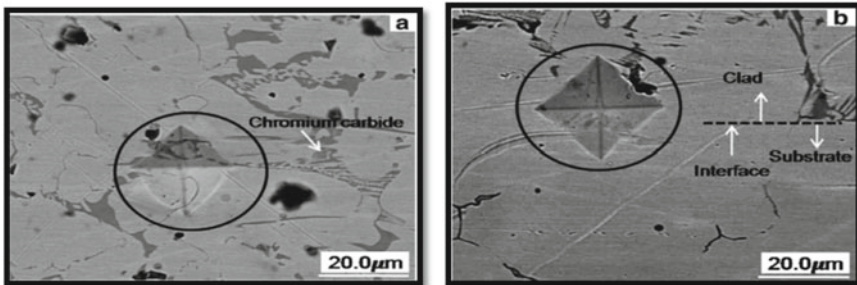
Fig. 4 This figure shows the indentations **a** developed clad region **b** at the interface [6]

Hebbale et al. [9] By the help of microwave heating the nickel-based clad was introduced on the high-speed steel (SS-304). It was observed that dilution of the metal occurs on the base metal and good metallurgical bond was formed between clad and SS-304. Due to volumetric heating of microwave, the intermediate of carbide of chromium is formed. The various phases are also formed like NiSi and FeNi3. Due to the formation of various carbides and intermetallic phases the microhardness is more as compared to the base metal. According to the analysis, at the boundary of the cell chromium was found and within the cell nickel and iron was found (Figs. 6 and 7).

Kaushal et al. [10] By the help of microwave heating nickel with silicon carbide was introduced on the austenitic stainless steel. Due to volumetric heating, the developed clad was free from any cracks and there is a uniform distribution of silicon carbide into the nickel powder. It was observed that there are many intermediate
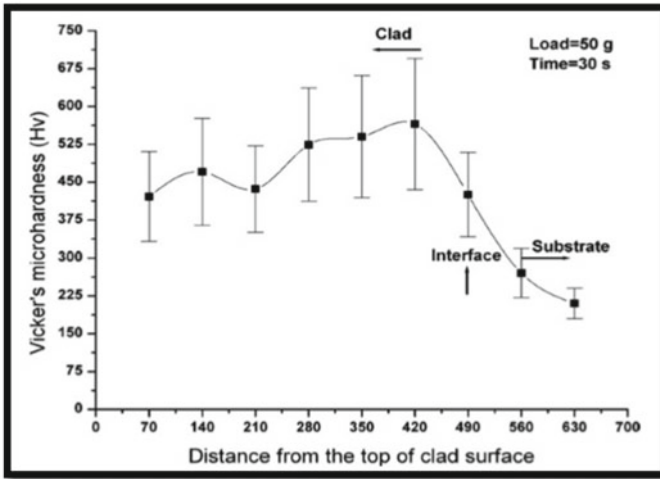
Fig. 5 This figure shows the microhardness distribution on the developed clad [7]
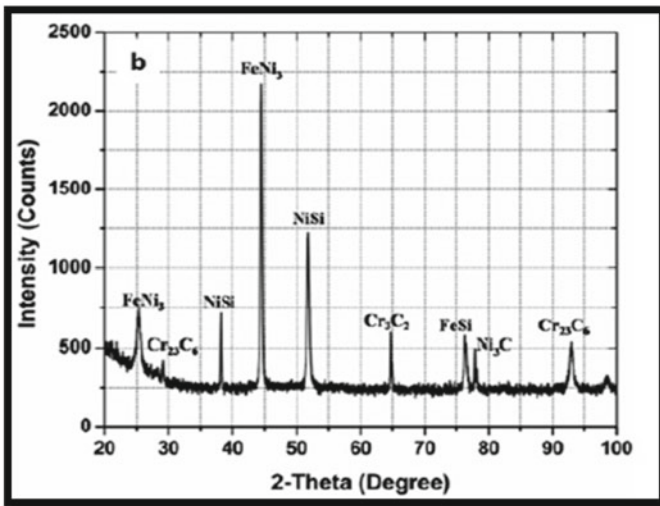
Fig. 6 This figure shows the XRD pattern of the formed clad on nickel-based powder [9]

forms during volumetric heating like nickel silicate, nickel carbide, etc. As the silicon carbide content increases into the nickel powder the microhardness increases and nickel-based powder with 30% silicon carbide have maximum microhardness (Fig. 8).

Kaushal et al. [11] By the help of microwave heating, the nickel based with silicon carbide powder clad was introduced on the base metal, that is, martensitic steel. It was
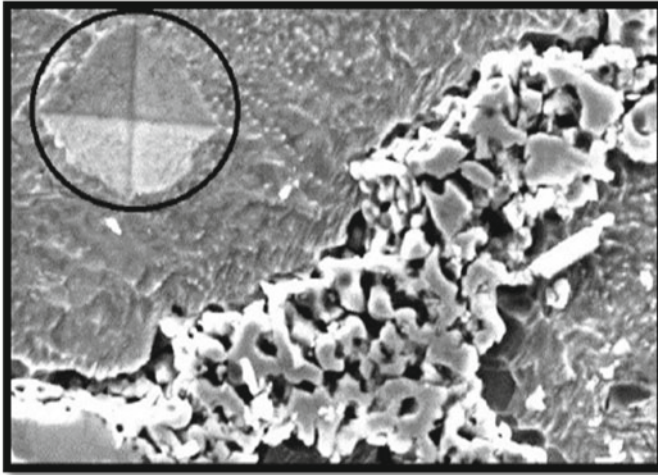
Fig. 7 This figure shows the image of indentations on the developed clad [9]
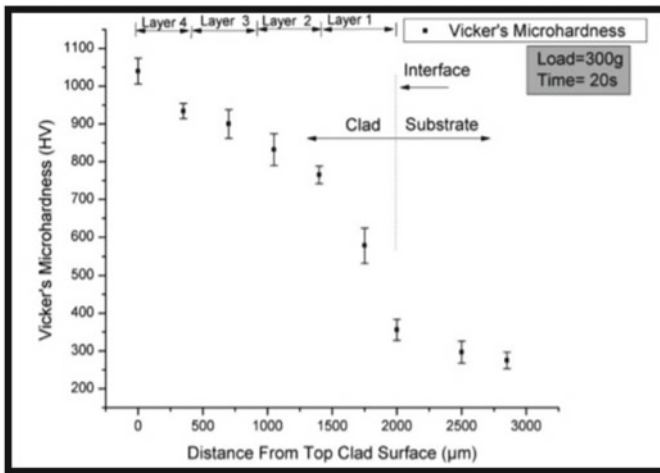
Fig. 8 This figure shows the microhardness distribution across the developed clad [10]

that due to proper mixing of base metal with clad material the microstructure of the formed clad was very uniform and shows good metallurgical bonding with the base metal. During volumetric heating, various phases and intermediate are formed like iron, nickel, etc. The microhardness of the formed clad was higher as a comparison to the base material, which can be used in various applications where antiwear properties are needed (Fig. 9).
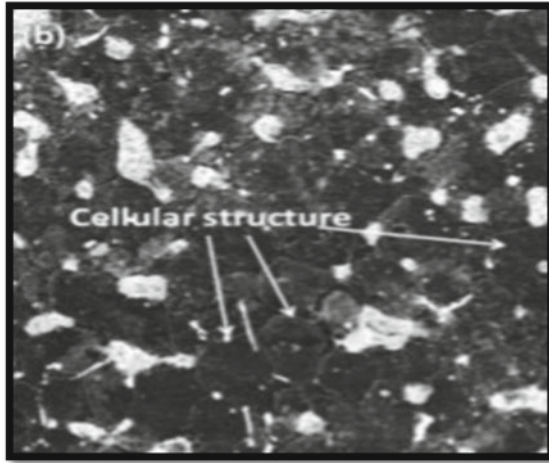
Fig. 9 This figure shows magnified image of formed clad [11]

Kaushal et al. [12] The cladding of Ni-20WC-10Mo based composite was developed on the austenitic steel by the help of microwave hybrid heating technique. In the clad region the phases like Ni_2Mo_4C, Co_7Mo_6, Fe_3W_3C, W_2C, $FeNi_3$, Mo_3Co_3 and $NiSi_2$ were observed. The presence of Fe element confirmed that substrate dilution in the clad region produce good metallurgical bonding between them. The microhardness of the formed clad was approximately seven hundred Hv (Figs. 10 and 11).

Liu et al. [13] By using the laser beam for heating, the cladding was introduced on the magnesium alloy. It was observed that to use this technique on the magnesium material, the magnesium must be oxidised or suitable atmosphere must be needed. For this technique to be used the laser of shorter wavelength must be used to enhance the heating. After the formation of cladding, it was observed that laser cladding
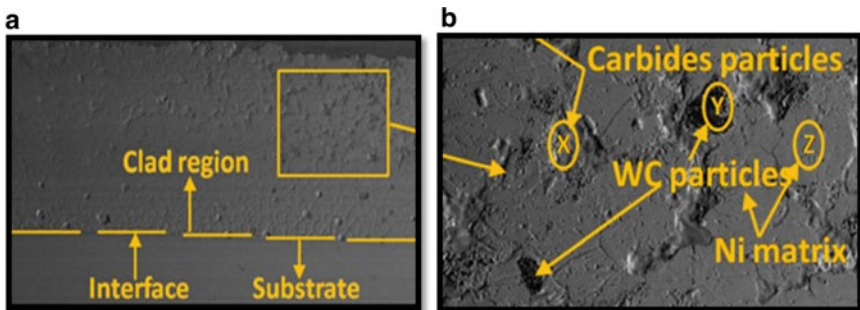
Fig. 10 This figure shows the **a** interface section of the clad **b** carbide particle in the mixture [12]
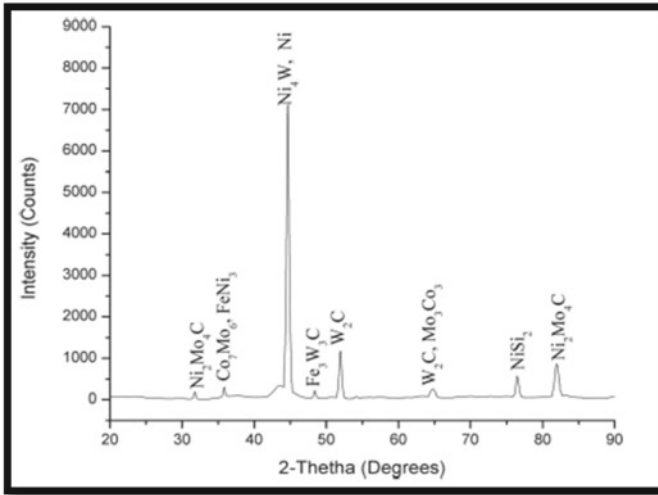
Fig. 11 This figure shows the XRD spectrum of the formed clad [12]

increases the metallurgical bonding between the base metal and clad material and also improved the wear and corrosion resistance properties of the alloy (Fig. 12).

Sharma et al. [14] By using the microwave heating the cladding of tungsten-based metal was introduced on the base metal (austenitic stainless steel). The developed cladding was free from interface cracking, defects, etc. During microwave heating, various phase transformations take place like tungsten carbide, etc. The carbide particle was uniformly distributed in the mixture. Due to volumetric heating of microwave developed clad has structure like cellular. The microhardness of the formed surface was $416 + 20$ Hv and also the strength was high after the formation of the clad surface.
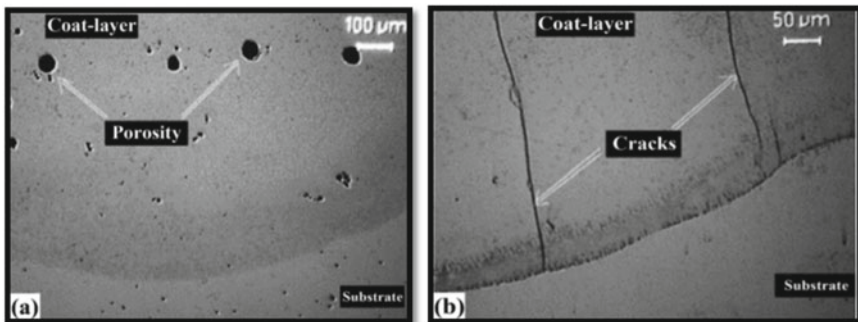
Fig. 12 This figure shows the microstructure of the clad with aluminium powder **a** pores **b** cracks [13]

Kratochviloval et al. [15] Polycrystalline diamond cladding was introduced on the zirconium. According to the concept of heat transfer, cladding prevents it from heat loss and its functionality. Cladding was also subjected to corrosion test to protect the material under nuclear reaction conditions. It was observed that after the formation of cladding the material was able to protect from oxidation and polycrystalline diamond layer can be used in a sensing device.

Wang et al. [16] By using laser cladding, the molybdenum with different contents was introduced with stainless steel powder. The iron-type martensite decreases with increases in molybdenum content while the iron-type ferrite increases with increases in molybdenum content. With the increases of distance from fusion line, the microstructure of coatings is changed from one crystal structure to another crystal structure. As the molybdenum content increases, microhardness decreases and wear resistance increases. By the help of this type of cladding, the corrosion resistance and wear resistance of the base metal is improved (Fig. 13).

Hebbale et al. [17] By the help of microwave heating, the nickel-based clad was introduced on the austenitic stainless steel (SS-304). It was observed that due to proper mixing of the nickel powder with austenitic stainless steel the developed clad is not having any cracks and to control the mass loss it depends upon two factors, that is, speed and impingement angle. It was also observed that with the developed clad surface the wear rate ranges between 0.03363 and 0.03570 g of mass loss (Fig. 14).

Singh et al. [18] By using the microwave heating, the Ni-based and CeO_2 modified coatings was introduced on the P20 steel material. With the addition of 1 wt% CeO_2, the microstructure was more refined and presence of chromium silicate and hard carbides which enhances the wear resistance and hardness properties of developed
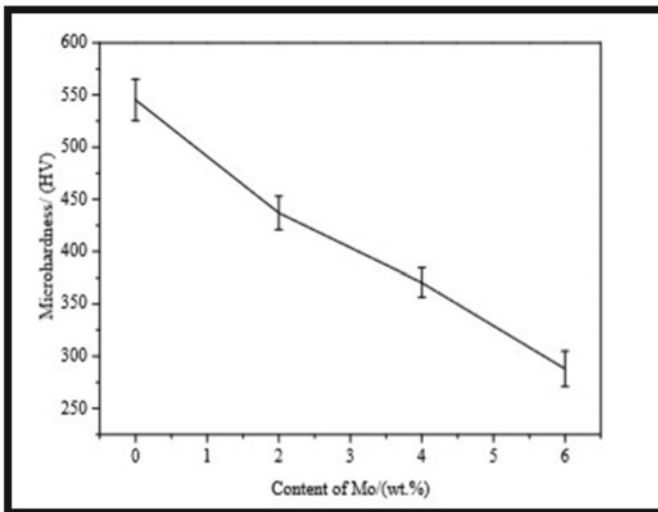
Fig. 13 This figure shows the effect of Molybdenum on the microhardness of the clad [16]
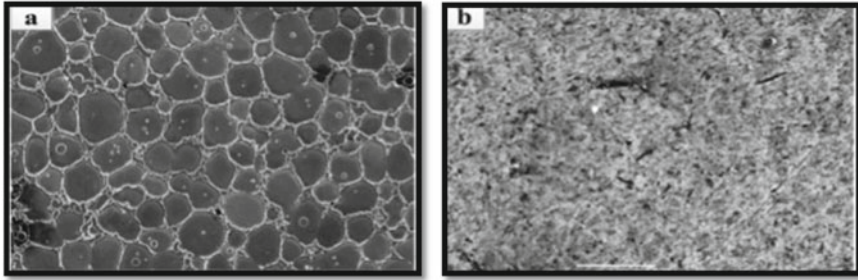
Fig. 14 This figures shows **a** developed clad structure **b** worn clad structure [17]

clad. With the optimal addition of CeO_2, the hardness is 30% higher as compared to unmodified coatings.

Zafar et al. [19] With the help of microwave heating, the nanostructured tungsten cobalt-based clad was introduced on the stainless steel. It was observed that due to proper mixing of clad material to base material there is good metallurgical bonding between clad material, and base metal and also clad is not having any cracks. Due to the dilution of carbide particle, microhardness also increases. Due to microwave heating, various intermediate carbides were also formed. The microhardness of nanostructured tungsten cobalt clad is five times the base material that is $1760 + 128$ Hv.

Zafar et al. [20] With the help of microwave heating the cladding of Inconel 718 was introduced on the austenitic steel. It was observed that due to proper mixing of Inconel 718 with base metal forms good metallurgical bonding and having less porosity due to the presence of fewer voids and cracks and the clad exhibit cellular dendritic morphology. Hardening in Inconel along with intermetallic Ni3Ti due to the formation of chromium carbides.

Singh et al. [21] The aluminum oxide with Ni-based metallic powder was introduced on the stainless steel (AISI 304) as the base material. The developed shows fewer cracks and strong metallurgical bonding due to the proper dilution of the aluminium oxide with the base metal. During the microwave heating, the intermetallic is formed like $FeNi_3$ and NiSi. The microhardness of Nickel with 10% aluminium oxide was then the base metal and more wear resistance than the base metal (Fig. 15).

Akshata et al. [22] In the automobile industry, hydropower plant, and gas power plant, the component's failure is the most common problem due to their complex geometry. By the help of microwave heating, the tungsten cobalt-based clad was introduced on the stainless steel. Due to proper mixing of clad material with the base material, the developed clad shows good metallurgical bonding between clad and the base metal. For the wear test, the Taguchi orthogonal array was successfully developed.

Prasad et al. [23] By using the microwave heating, the cobalt-based mixture was introduced in the titanium material. It was observed that with the addition of carbides
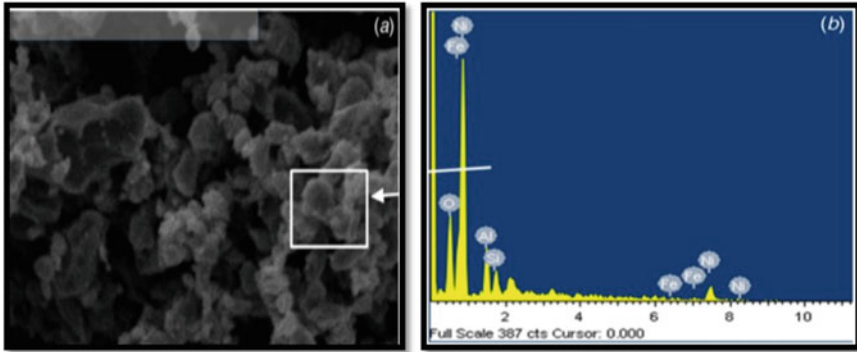
Fig. 15 This figures shows **a** wear debris image **b** wear debris analysis [21]

to the cobalt-based powder increases thermal conductivity than other cladding composition. The development of the thermal layer cobalt-based clad protects cladding and titanium material from higher temperature and shocks due to high temperature.

Singh et al. [24] With the help of microwave heating, Co-based powder with neodymium oxide was introduced. As from the observation with the increment of neodymium oxide, the microstructure of the coatings is more uniform. The presence of hard carbides enhanced the wear resistance and hardness of the developed coatings. It was observed that with the addition of impurity to Co-based increases more microhardness as compared to without impurity (Figs. 16 and 17).

Kaushal et al. [25] By the help of microwave heating, the Ni-WC-Cr3C$_2$-based powder mixture was introduced on the base metal that is austenitic stainless steel. The developed clad having less porosity due to the presence of fewer voids and cracks. The presence of iron nickel, iron tungsten carbide, and iron carbide confirms that the

Fig. 16 This figure shows the microhardness with or without impurities in the co-based coatings [24]

	1006	1006 + 1%Nd2O3	1006 + 2%Nd2O3	1006 + 3%Nd2O3
Section 1	760	846	897	926
Section 2	762	820	880	901
Section 3	763	866	879	910
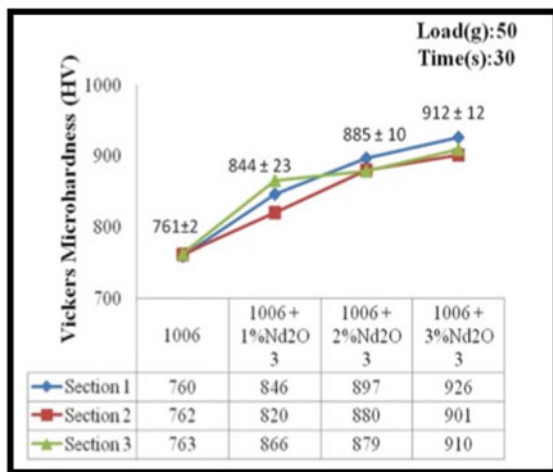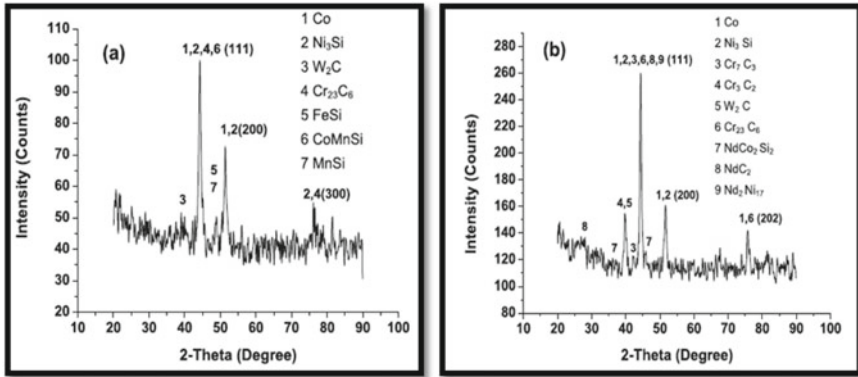
Fig. 17 This pattern shows **a** Co-based **b** Co-based with some impurities coatings [24]

iron element mixed with clad material and thus forms good metallurgical bonding between them. The microhardness of the developed clad was more as compared to the austenitic stainless steel (Fig. 18).

Singh et al. [26] By using the microwave heating, the clad of nickel with 20% tungsten cobalt and nickel with 30% tungsten cobalt was introduced on the austenitic stainless steel. According to microstructural analysis, it was observed that the carbides particle were uniformly distributed at the interface of the base metal and clad material. The hardness of nickel with 20% tungsten cobalt and 30% tungsten cobalt was formed strong bonding with austenitic stainless steel.

Guo et al. [27] In the present work, the cladding was done by using a laser on the iron base alloy to improve the properties like wear resistance, etc. It was observed that by the process of heat treatment the microstructure of base metal is more uniform and dense in nature and properties like wear also improved. Therefore, by the process of heat treatment, the wear resistance properties cab be enhanced using laser cladding to the base metal.

Fig. 18 This image shows the indentation morphology [25]
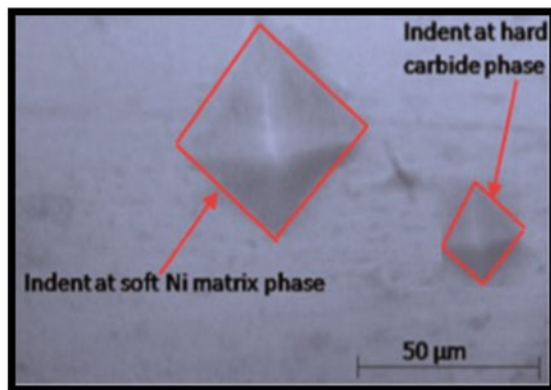
3   Results and Discussions

In the above review of different research papers, we find that the microhardness of the metal matrix composite increases by the formation of microwave cladding. Also, at different temperatures and dilution of metal on base metal forms the uniform structure, less porosity, and more hardness due to volumetric heating. As from the above study, we had seen that in the mechanical industries use of the composite material are having more advantage because of their mechanical properties due to adding of different materials to the base metal and used in many mechanical and electrical devices like heat exchangers, electrical wires, automobile and aviation industries, etc.

4   Conclusion

By studying the above papers, we concluded that by adding different metals which can improve properties like tensile strength, hardness, impact strength, wear strength, and corrosion resistance can be added to the working metal/material and also microhardness and microstructure are more uniform with cracks free interface and moreover there is also improvement in the wear and corrosion resistance of the material. Metallic properties like electrical conductivity and thermal conductivity also can be improved by adding conductive material to the working metal.

References

1. Gautam, Y.K., Somani, N., Kumar, M., Sharma, S.K.: A review on fabrication and characterization of copper metal matrix composite. In: AIP Conference Proceedings, p. 020017 (2018)
2. Somani, N., Tyagi, Y.K., Kumar, P., Srivastava, V., Bhowmick, H.: Enhanced tribological properties of SiC reinforced copper metal matrix composites. Mater. Res. Express **6**, 016549 (2019)
3. Prasad, A., Gupta, D., Sankar, M.R., Reddy, A.N.: Experimental investigations of Ni/La$_2$O$_3$ composite micro-cladding on AISI 1040 steel through microwave irradiation. In: 5th International & 26th All India Manufacturing Technology, Design and Research Conference (AIMTDR 2014), 12–14 December 2014
4. Bansal, A., Zafar, S., Sharma, A.K.: Microstructure and abrasive wear performance of Ni-WC composite microwave clad. ASM International, JMEPEG **24**, 3708–3716 (2015). https://doi.org/10.1007/s11665-015-1657-0
5. Gupta, D., Sharma, A.K.: Investigation on sliding wear performance of WC-10Co-2Ni cladding through microwave irradiation. Wear **271**, 1642–1650 (2011)
6. Gupta, D., Sharma, A.K.: Development and microstructural characterization of microwave facing on solid solution stainless steel. Surf. Coat. Technol. **205**, 5147–5155 (2011)
7. Gupta, D., Sharma, A.K., Bhovi, P.M., Sharma, A.K., Dutta, S.: Development and characterization of microwave composite cladding. J. Manuf. Proc. **14**, 243–249 (2012)

8. Gupta, D., Sharma, A.K.: Microwave cladding: a new approach in surface engineering. J. Manuf. Proc. **16**, 176–182 (2014)
9. Hebbale, A.M., Srinath, M.S.: Microstructural characterization of ni based cladding on SS-304 developed through microwave energy. In: Materials Today: Proceedings, vol. 2, pp. 1414–1420 (2015)
10. Kaushal, S., Gupta, D., Bhowmick, H.: An approach for functionally graded cladding of composite material on austenitic stainless-steel substrate through microwave heating. J. Compos. Mater. **0**(0), 1–12 (2018). https://doi.org/10.1177/0021998317705977
11. Kaushal, S., Sirohi, V., Gupta, D., Bhowmick, H., Singh, S.: Process and characterization of composite protective cover through microwave heating on martensitic steel. J. Mater.: Style Appl. **0**(0), 1–7 (2015). https://doi.org/10.1177/1464420715616139
12. Kaushal, S., Singh, D., Gupta, D., Bhowmick, H., Jain, V.: Processing of Ni-20WC-10Mo based composite clads on austenitic stainless steel through microwave hybrid heating. Mater. Res. Express **5**, 036401 (2018)
13. Liu, J., Yua, H., Chenb, C., Weng, F., Dai, J.: Research and development status of laser cladding on magnesium alloys: a review. Opt. Lasers Eng. **93**, 95–210 (2017)
14. Sharma, A.K., Gupta, D.: On microstructure and flexural strength of metal—ceramic composite cladding developed through microwave heating. Appl. Surf. Sci. **258**, 5583–5592 (2012)
15. Kratochviloval, I., Skoda, R., Skarohlid, J., Ashcheulov, P., Jager, A., Racek, J., Taylor, A., Shao, L.: Nano sized polycrystalline diamond cladding for surface protection of zirconium nuclear fuel tubes. J. Mater. Process. Technol. **S0924-0136**, 00176-9 (2014)
16. Wang, K., Chang, B., Chen, J., Fu, H., Lin, Y., Lei, Y.: Effect of molybdenum on the microstructures and properties of stainless-steel coatings by laser cladding. Appl. Sci. **7**, 1065 (2017). https://doi.org/10.3390/app7101065
17. Hebbale, A.M., Srinath, M.S.: Microstructure and experimental design analysis of nickel based clad developed through microwave energy. Perspect. Sci. **S2213-0209**(16), 30066-0 (2016)
18. Singh, K., Sharma, S.: Development of Ni-based and CeO_2 modified coatings by microwave heating. J. Mater. Manuf. Proc. **33** (2018)
19. Zafar, S., Sharma, A.K.: Structure-property correlations in nanostructured WC-12Co microwave clad. Appl. Surf. Sci. **S0169–4332**, 30292–30296 (2016)
20. Zafar, S., Sharma, A.K., Arora, N.: Development and microstructural characterisation of Inconel cladding on stainless steel through microwave irradiation. I-manager's J. Mech. Eng. **3**(1) (2013)
21. Singh, B., Kaushal, S., Gupta, D., Bhowmick, H.: On development and dry sliding wear behaviour of microwave processed Ni/Al_2O_3 composite clad. J. Tribol. **140**, 061603-1 (2018)
22. Akshata, M.K., Hebbale, A.M., Srinath, M.S.: Sliding wear studies of microwave clad versus unclad surface of stainless steel 304. MATEC Web Conf. **144**, 02010 (2018)
23. Prasad, C.D., Joladarashi, S., Ramesh, M.R., Sarkar, A.: High temperature gradient cobalt based clad developed using microwave hybrid heating, advances in mechanical design, materials and manufacture. In: AIP Conference Proceedings, vol. 1943, pp. 020111-1–020111-13 (2018)
24. Singh, K., Sharma, S.: Effect of neodymium oxide on microstructure, hardness and abrasive wear behaviour of microwave clads. Mater. Res. Express **6**, 086599 (2019)
25. Kaushal, S., Singh, D., Gupta, D., Jain, V.: Processing of Ni–WC–Cr_3C_2-based metal matrix composite cladding on SS-316L substrate through microwave irradiation. J. Compos. Mater. **0**(0), 1–10 (2018). https://doi.org/10.1177/0021998318794846
26. Singh, D., Kaushal, S., Gupta, D., Bhowmick, H.L., Jain, V.: On processing of Ni–WC_8Co-based composite clads on austenitic stainless steel through microwave energy, Advances in Manufacturing Processes, Lecture Notes in Mechanical Engineering (2019). https://doi.org/10.1007/978-981-13-1724-8_15
27. Guo, W., Zhang, L., Xu, C., Chai, R., Gao, Z., Kogo, B., Chizari, M., Zhang, C., Wang, B.: Study on the wear resistance of laser cladding iron-base alloy by heat treatment, Author Submitted Manuscript—MRX-110000.R1 (2018)

Characterization of Hemp Fibre-Reinforced Gypsum Panels for Building Insulation

Kanishka Jha, Syam Kumar Degala, and Akeshawar Singh Yadav

1 Introduction

In the present scenario in order to conserve the natural resources and for being eco-friendly, rather than using the conventional materials, it was necessary for the researchers to develop a new material having the properties of conventional materials and to meet the required properties of existing needs. A lot of research is carrying out in the field of materials which leads to the newly developed materials. A composite material is developed which consists of reinforcement phase and matrix phase. Combining of these, a newly developed material is formed which exhibits the properties greater than the parental materials. S. Gassita et al. discussed that by adding water to the gypsum, calcium sulphate $CaSO_4$ with H_2O forms a strong bond and that the hydric transfer property of water with gypsum and also carried out the investigation on sorbivity and hydraulic diffusivity [1]. A. korjenic et al. presented the use of naturally available flax, hemp and jute fibres and compared the physical and mechanical properties with currently using insulating materials in building structures and also compared the properties of the natural materials with conventional materials [2]. F. Iucolano et al. state that in order to restore the historical buildings and design the reinforcement materials fibreglass, basalt fibre with mortar of better characteristics and also converted the brittle structure into ductile structure [3]. F. Iucolano et al. in another article discussed that because of high latent heat dehydrate into hemi-hydrates gypsum is used for to cut down the fire and the impact of hemp fibre on the thermal behaviour, properties under isothermal conditions are studied in [4]. S. Verma says, however, the cellulose, hemicellulose, lignin weight percentages are

K. Jha · S. K. Degala (✉)
School of Mechanical Engineering, Lovely Professional University, Phagwara, Punjab, India
e-mail: syamdegala@gmail.com

A. S. Yadav
Department of Metallurgical and Materials Engineering, Indian Institute of Technology, Roorkee, Uttarakhand, India

57–77, 14–22.4, 3.7–13, respectively, which shows the strength of the fibre is found good compared to banana, flax, cotton fibres in [5]. Q. L Yu et al. elaborated that gypsum boards formed from β-hemihydrate, its dehydration was determined at the micro and macro levels, the thermal properties such as enthalpy of reaction, specific heat capacity were studied in the thermal properties of gypsum boards caused not only by the void fraction but also considerably with the particle system [6]. Kanishka jha et al. fabricated the jute/E-glass hybrid composites which can withstand at different environment conditions by taking the wear property as a parameter [7]. H.arikan et al. discussed gypsum-based composite materials for the strong bonding to concrete and brick as well as to improve the mechanical properties it needs chemical admixtures and chemical additives such as air-entraining admixture, super-plasticizer in [8]. Hari Om Maurya et al. discussed the wear property of the short sisal fibre reinforced with the epoxy composite. [9]. R. A. Kurtz discussed, the effect of water vapour on the formation of $CaSO_4 \cdot \frac{1}{2} H_2O$ by the three types of dehydration methods, i.e., atmospheric pressure, digesting in salt and autoclaving in lump form forms α, β-hemi-hydrates at different temperatures, where 75% α-hemihydrate and 25% β-hemihydrate are obtained by dehydration in atmosphere nearly saturated with water vapour is explained in [10]. K. Ghazi et al. states that the amount of calcium sulphate is essential for the response to fire of gypsum plaster boards in the first 30 min of the standard fire of ISO 834. The percentage of calcium carbonate with a strong endothermic decomposition was found to influence the temperature rise of the board only at higher temperatures [11]. O. Gencal et al. in his paper explained that vermiculite and polypropylene fibres are added to powder gypsum to reduce the thermal conductivity and also a mathematical model has been developed to study and optimise the fibre ratio of gypsum composites in [12]. S. Seufert et al. discussed that similarly, the calcium sulphates in gypsum was influenced by dehydration temperature and XRD analysis of bassanite and iso-structural anhydrite III was clearly distinguished in [13]. In Yasemin et al. [14], the author tested the gypsum boards used in the USA and Japan at room and elevated temperatures and found that not significant at particularly elevated temperatures. N. L. Moigne et al. say that the polypropylene composites with fibres, flax, sisal and wheat straw fibres discussed that no significant effect on the concentration of length and aspect ratio distributions was detected, and it states that the fibre type plays an important role influencing size and shape distributions [15]. Panyakaew et al. in [16] state that binderless bagasse insulation boards are compared with coconut husk boards which show that bagasse insulation boards compete with the coconut and also met the requirements of the conventional insulation materials. Kanishka jha et al. fabricated biodegradable polymer composites which are eco friendly by polycaprolactone as matrix with pine cone particle shows that decomposition temperature of the specimen decreases from 250 to 233 °C [17].

2   Materials and Methods

Gypsum is a soft sulphate mineral composed of calcium sulphate bi-hydrate, with the chemical formula $CaSO_4 \cdot 2H_2O$. It can be used as fertiliser. For binding various layers of fibre, the resin-hardener mixture is used. Gypsum ($CaSO_4 \cdot 2H_2O$) gives the best binding property under standard room temperature. The properties of Gypsum are as follows:

Compressive strength 8.4 Mpa
Density   1.2 gm/cc
Specific gravity   2.3
Thermal conductivity   0.449 w/mk

Hemp fibre typically found in the northern hemisphere is a variety of the Cannabis sativa plant species that is grown specifically for the industrial uses of its derived products. Properties of hemp fibre are as follows:

Tensile strength   550–900 Mpa
Young's modulus   70 Gpa
Density   0.86 gm/cc
Water absorption   8–30%
Compressive strength 26.4 Mpa
Thermal conductivity   0.048 w/mk

2.1   Composites Fabrication

The samples are fabricated with five different volume fractions of 0, 3, 6, 9, and 12% of hemp fibre, and mechanical and thermal characteristics. The samples are prepared by: (i) mixing of gypsum powder and water with a water/gypsum ratio of 0.6–0.8 in the automatic Perrier blender, in the laboratory environment (at room temperature and air humidity of 75%) during 5 min. (ii) Fibres are added to the mixture and mixed during 5 min. (iii) The blending is done quickly in the mould. The physical, mechanical, and thermal experiments were performed using samples of dimensions 40 mm × 40 mm × 160 mm and 100 mm × 100 mm × 40 mm and 120 mm × 120 mm × 40 mm, respectively.

2.2   Method of Fabrication

Hand lay-up technique (HLUT)
In this paper, a hand lay-up technique was used as the fabrication method. It was the easiest method of composite processing. The material requirement and cost associated with this method are also very minimal. Composite materials can be prepared

Table 1 Designation of composites

Sample	Composition
K1.	Gypsum 100%
K2.	Gypsum 7% + Hemp 3%
K3.	Gypsum 94% + Hemp 6%
K4.	Gypsum 91% + Hemp 9%
K5.	Gypsum 88% + Hemp 12%

by different methods. However, due to many reasons such as part size and shape, cost, familiarity with the technique and availability of tools, composite is fabricated using hand lay-up technique. The hand lay-up was one of the oldest composite fabrication techniques and it belongs to the open mould category. The operator places the reinforcement and the resin mix manually on a mould and thereafter the resin reinforcement mixture is compressed with a hand roller.

2.3 Designation of Composite Samples

See Table 1.

3 Results and Discussions

3.1 Physical and Mechanical Characteristics

The theoretical and experimental densities, volume fraction of voids of composites are plotted in the graph Figs. 1 and 3, in which the specimen based on the BS standards are shaped and are observed for every 24 h. It is observed that calculated density and theoretical densities are approximately nearer to each other. The volume fraction % of voids present in compositions are increased with increase in the hemp fibre content (Fig. 2).

$$\text{Actual Density}, \rho_{ct} = \frac{1}{\left(\frac{W_{fh}}{\rho_{fh}}\right) + \left(\frac{W_m}{\rho_m}\right)}$$

$$\text{Void content}, v_v = \frac{\rho_{ct} - \rho_{ce}}{\rho_{ct}}$$

The observed rise of water absorption in the sample is due to the increase in the percent of number of fibres, however, the void content percent also increases due to the formation of air gaps during the fabrication between the fibre and gypsum.

Fig. 1 Density
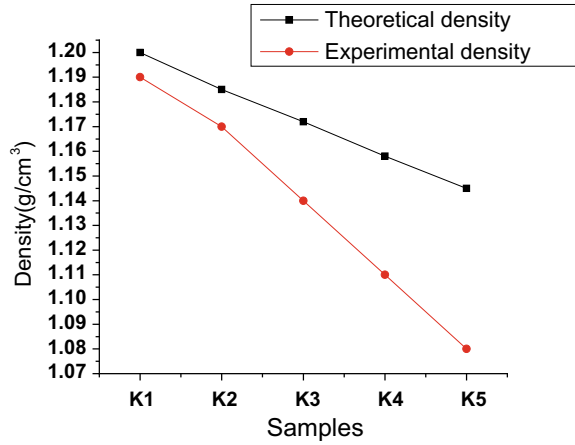
Fig. 2 Volume fraction of voids
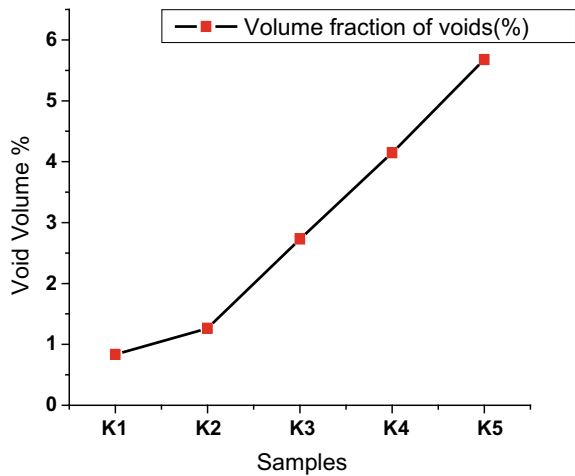
The compression test is carried out on fabrication of the different compositions of the specimens. The above graph gives the detailed values of the tests that have been carried out on the specimens. The compression strength substantially increases up to 9% of hemp fibre content and then decreased at 12%. due to an increase in the void contents, the compression strength is decreased. The flexural test was carried out in Universal Testing Machine in accordance with BS EN 13.279-2. The flexural strength was shown in Fig. 3, the values were observed that the composites having 6% fibre content has the highest value of flexural strength and then decreases due to the weak bonding of the matrix and reinforcement, i.e. voids present in the composition samples (Fig. 4).

In Fig. 5, the substantial decrease in the thermal conductivity can be observed due to the addition of hemp fibre in the composition samples. Here the composites

Fig. 3 Flexural strength
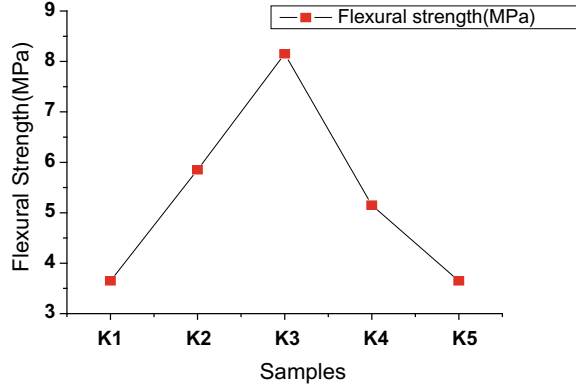
Fig. 4 Compression strength
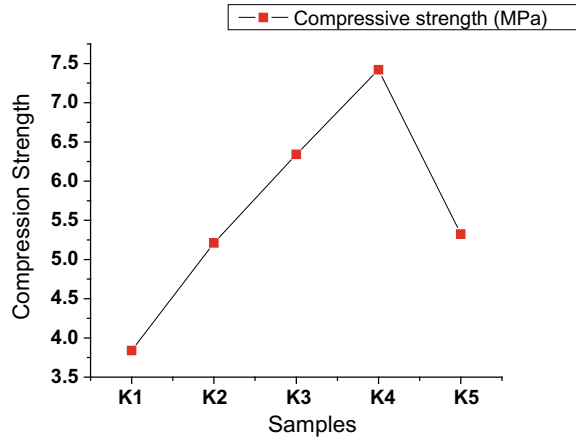
Fig. 5 Thermal conductivity
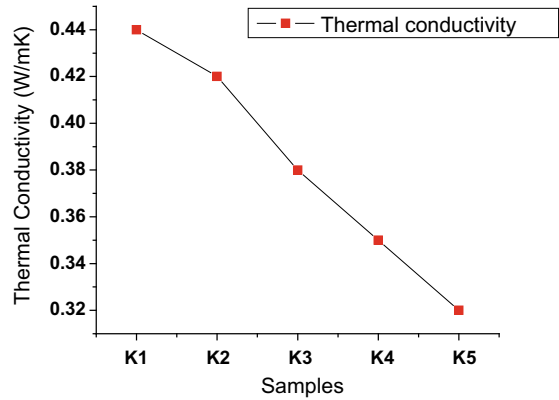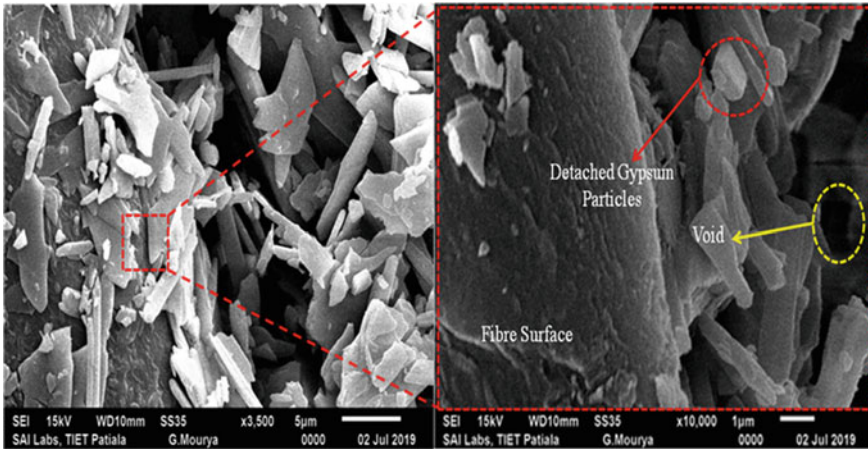
Fig. 6 Hemp fibre of 12% concentration

filled with hemp fibre of 12% having very less thermal conductivity than the pure gypsum. Hence, we can say that the hemp fibre has a tremendous impact on thermal performance.

3.2 Characterization

3.2.1 SEM Analysis

See Figs. 6 and 7.

3.2.2 XRD Analysis

See Figs. 8 and 9.

In Figs. 6 and 7, the scanning electron micrograph of 9%, 12% of hemp fibre has been characterised. At 6 the sample was at a magnification of 3500× which clearly shows that it consists of clearly crystals of hydrated gypsum along with fibre and Fig. 6 also shows at a magnification of 10000× shows the bonding of the fibre with the crystals of gypsum. As we calculated the volume of the fraction of void contents it gradually increases and that was clearly observed in Fig. 6 in the dark region which is the void formation between the hemp fibre and gypsum. At 12% concentration of hemp fibre, the gypsum is in the form of crystals and makes bond with reinforcement indicating the presence of anhydrite gypsum on the surface of fibre. The X-ray diffraction of the samples was characterized to determine the elements present in the mixture which can vary the 2θ from the 0 to 45°. In Fig. 8,
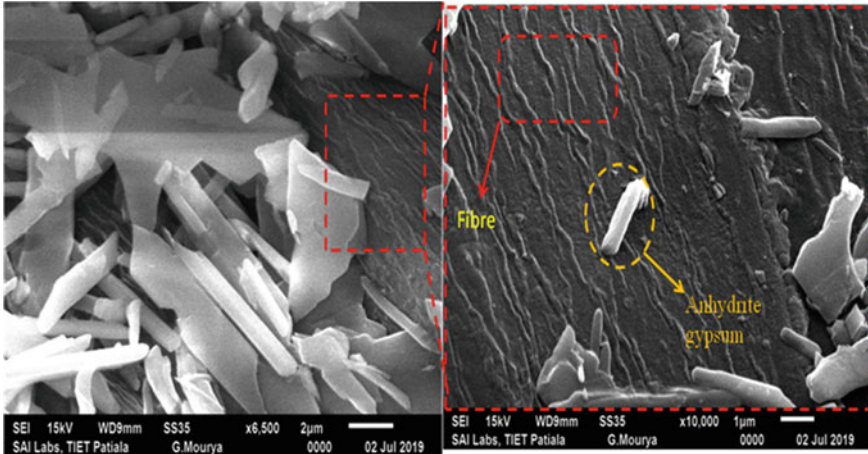
Fig. 7 Hemp fibre of 9% concentration
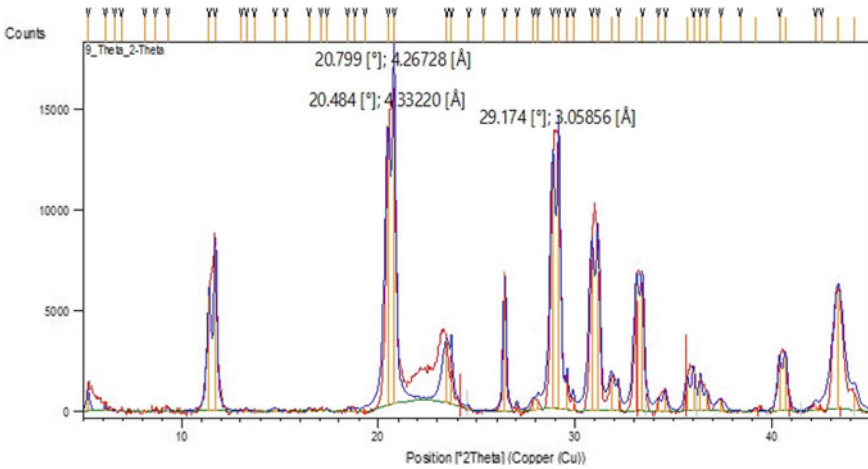
Fig. 8 XRD analysis of 9% hemp fibre

9% hemp fibre were characterised and the maximum peaks of the sample were obtained at an angle of 20.79°.20.48°,29.17° and at the reference code 00-033-0664 having a high score of 31 which consists of the burnt ochre Fe_2O_3. In Fig. 9, 12% hemp fibre were characterised and the maximum peaks of the sample were obtained at an angle of 11.53°.20.51°, 28.92° and at the reference code 00-005-0628 having a high score of 19 which consists of the element quartz.
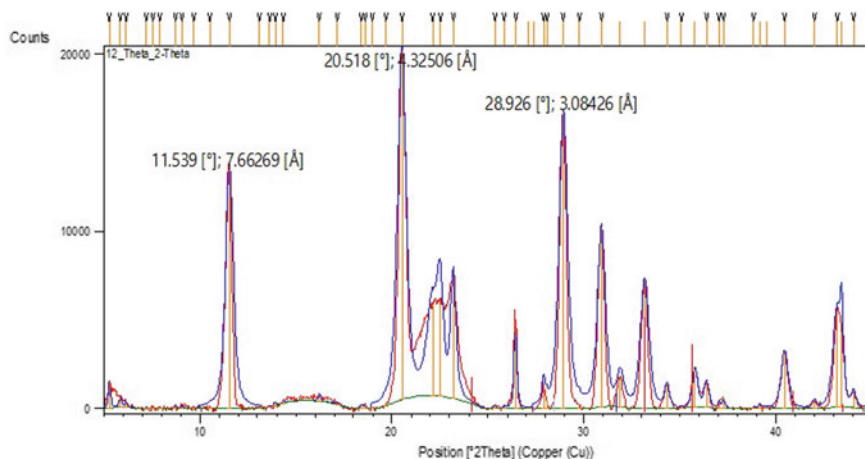
Fig. 9 XRD analysis of 12% hemp fibre

4 Conclusion

Although the use of air conditioning in buildings was necessary for the present scenario due to increase in global warming, the use of conventional materials for thermal insulation was increasing rapidly. It was then now possible to replace it with by the bio-compatible materials, i.e. gypsum with hemp fibre where the thermal conductivity value decreases from 0.44 to 0.32 W/mk with an increase in the hemp fibre content. The flexural and compression strength values are also enhanced due to the addition of hemp fibre. So, for thermal insulation of the buildings the use of gypsum with hemp fibre suits for better air conditioning.

References

1. Gassita, S., Marmoret, L., Ben Hamed, H., Beji, H.: Sorptivity and hydraulic diffusivity of coating gypsum and impact of hemp fibers addition. Defect Diffus. Forum **312–315**, 818–823 (2011)
2. Korjenic, A., Petránek, V., Zach, J., Hroudová, J.: Development and performance evaluation of natural thermal-insulation materials composed of renewable resources. Energy Build. **43**(9), 2518–2523 (2011)
3. Iucolano, F., Liguori, B., Colella, C.: Fibre-reinforced lime-based mortars: a possible resource for ancient masonry restoration. Constr. Build. Mater. **38**, 785–789 (2013)
4. Iucolano, F., Liguori, B., Aprea, P., Caputo, D.: Thermo-mechanical behaviour of hemp fibers-reinforced gypsum plasters. Constr. Build. Mater. **185**, 256–263 (2018)
5. Verma, S.: A Review on thermal behaviour of natural fiber reinforced composites. **8**(4), 251–255 (2017)
6. Yu, Q.L., Brouwers, H.J.H.: Thermal properties and microstructure of gypsum board and its dehydration products: a theoretical and experimental investigation. Fire Mater. **36**(7), 575–589 (2012)

7. Jha, K., Samantaray, B.B., Tamrakar, P.: A study on erosion and mechanical behavior of jute/E-Glass hybrid composite. Mater. Today Proc. **5**(2), 5601–5607 (2018)
8. Arikan, M., Sobolev, K.: The optimization of a gypsum-based composite material. Cem. Concr. Res. **32**(11), 1725–1728 (2002)
9. Maurya, H.O., Jha, K., Tyagi, Y.K.: Tribological behavior of short sisal fiber reinforced epoxy composite. Polym. Polym. Compos. **25**(3), 215–220 (2017)
10. Kuntze, R.A.: Effect of water vapor on formation of $CaSO_4$ H_2O modifications. **43**(6) (1965)
11. Ghazi Wakili, K., Hugi, E.: Four types of gypsum plaster boards and their thermophysical properties under fire condition. J. Fire Sci. **27**(1), 27–43 (2009)
12. Gencel, O., et al.: Properties of gypsum composites containing vermiculite and polypropylene fibers: numerical and experimental results. Energy Build. **70**, 135–144 (2014)
13. Seufert, S., Hesse, C., Goetz-Neunhoeffer, F., Neubauer, J.: Quantitative determination of anhydrite III from dehydrated gypsum by XRD. Cem. Concr. Res. **39**(10), 936–941 (2009)
14. Yasemin, A., Doğan, M., Bayramlı, E.: The effect of red phosphorus on the fire properties of intumescent pine wood flour – LDPE composites Yasemin. Finnish-Swedish Flame Days 2009 4B (2009)
15. Le Moigne, N., Van Den Oever, M., Budtova, T.: A statistical analysis of fibre size and shape distribution after compounding in composites reinforced by natural fibres. Compos. Part A Appl. Sci. Manuf. **42**(10), 1542–1550 (2011)
16. Panyakaew, S., Fotios, S.: New thermal insulation boards made from coconut husk and bagasse. Energy Build. **43**(7), 1732–1739 (2011)
17. Jha, K., Tyagi, Y. K., Singh Yadav, A.: Mechanical and thermal behaviour of biodegradable composites based on polycaprolactone with pine cone particle. Sadhana—Acad. Proc. Eng. Sci. **43**(9), 1–5 (2018)

A Short Note on the Processing of Materials Through Microwave Route

Gurbhej Singh, Hitesh Vasudev, and Hitesh Arora

1   Introduction

In the modern era of growing and developing technologies, the lots of advancements are being noticed in the field of engineering. The industries are looking forward for new and improved processing techniques. The wide range of advanced materials including ceramics, metals, non-metals and composites can be processed easily and effectively through these technologies. With the development of technology, new materials came into existence and, to process those materials, high energy-efficient methods were developed. But the problems associated with these technologies such as environmental degradations, high energy consumption, high manufacturing cost, etc., have lead the researchers to focus on all those processing techniques which can minimizes these losses up to an extent. Number of processing/sintering techniques was utilized for metal, ceramics and alloys for various industrial applications [1–8]. The microwave energy leads the researchers to explore the field of microwave processing towards different areas of materials manufacturing. Recently, lot of research has reported in the field of sintering, joining, cladding, etc.

1.1   Introduction of Microwaves

The microwaves are the part of the electromagnetic spectrum in which the electric and magnetic waves travels perpendicular to each other having frequency of range

G. Singh
Department of Mechanical Engineering, CT University, Ferozepur Road, Ludhiana Sidhwan Khurd-142024, India

H. Vasudev (✉) · H. Arora
Department of Mechanical Engineering, Lovely Professional University, Jalandhar—Delhi G.T. Road, Phagwara, Punjab 144411, India
e-mail: hitesh.24804@lpu.co.in

300 MHz–300 GHz. The wavelength in case of microwaves varies from 1 mm to 1 m as shown in Fig. 1, which represents the EM spectrum. The frequency range of microwaves is specific for different applications, which includes communication systems, food processing, medical purposes, industrial heating and material processing [8]. The primary applications of microwaves were noticed in the communication systems including RADAR, satellite communications and television broadcasting, etc. But the use of microwaves for heating purpose was discovered accidently by Spencer (1945) while he was eating ice cream on a highway and he noticed its melting and concentration of electromagnetic field towards heating and got first patent. Over the time, this energy became an important source of household product and used in food processing because of its advantages such as high heating rate, lower processing time and lower energy consumption. The frequency on which domestic microwave ovens operates is 2.45 GHz, which is primarily used for heating food items. The electromagnetic spectrum with various frequencies and wavelengths are shown in Fig. 1. The furnaces have been developed for material processing purposes which are used in many industrial applications and they work on higher frequencies ranging from 915 MHz to 18 GHz [9]. The use of microwave energy was further developed in the field of material processing to gain the advantages of higher heating rates with having lower processing time [10], i.e. used tires recycling, metallic materials and ceramic processing.
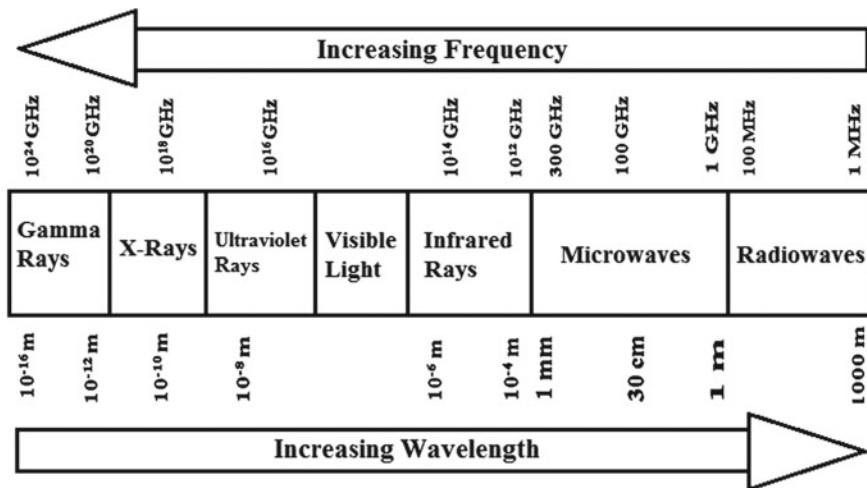
Fig. 1 Electromagnetic spectrum carrying frequencies and wavelength of microwave band [11]
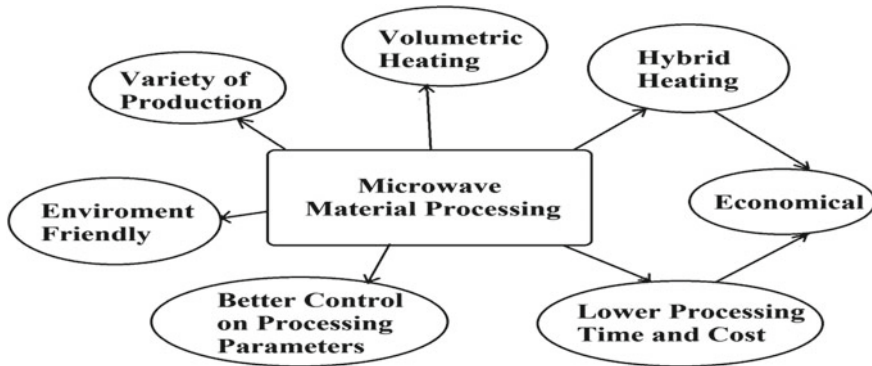
Fig. 2 Some common characteristics of material processing through microwaves

1.2 Characteristics of Microwave Processing

The microwave heating has various characteristics due to which it has become popular for heating low-temperature applications as well as high-temperature applications.

The microwave energy is utilized for the purpose of surface engineering. The substrate is placed over the insulation. The substrate is cleaned by using ultrasonic cleaner before the deposition of the material on its surface. The powder is then poured on the surface the substrate and further covered by the separator. Then, the separator is covered by the susceptor, where charcoal is preferred as the best charcoal material used for the absorption of heat. The radiations of the microwave are absorbed by the charcoal, as it is a good conductor of heat and has a good absorption capacity as compared to any other material used in microwave processing. The energy absorbed by the charcoal, is then converted into the heat energy, which in turns transferred to the separator by means of conduction [11]. The heat is absorbed by the separator, where the alumina or silicon carbides are the preferred materials used as separators. The heat is then transferred to the powder placed over the substrate, where the powder melts and gets deposited on the surface of the substrate. This process is known as 'microwave cladding', where the powder gets deposited to form a clad over the surface. This various characteristics of this process are presented in Fig. 2. This technique is now in process of its application in the industry.

1.3 Microwave/Material Interaction

Heating/melting is the most common process in each and every manufacturing industry but there are lots of methods to carry out these processes. As for as microwave heating is concerned, its commonly used for heating the food products as a kitchen

appliance and with passage of time the use of this technology is being noticed in different fields such as engineering as well as in chemical and textile industries. There are lots of electric-based heating technologies, which utilize the specific bands of electromagnetic spectrum such as induction, infrared, ultraviolet and microwave heating. Microwave technology is well known for food and rubber processing, but there is a growing interest towards the industries to properly utilize its potential for various manufacturing processes (dealing with metallic materials) as well as for the treatment of various waste streams, etc. The mechanism of microwave energy is different from the conventional heat. In case of conventional heat, the conducting body follows a Fourier's law for conduction. The section of a component that is in the contact of heat or flame gets heated initially, while the inner core of the material has somewhat lower temperature in comparison to the free surface exposed to the heat. The heat flows due to the temperature difference. As there is a difference between the temperatures, the heating is not uniform throughout the surface of a component. The utilization of the microwave energy has introduced a new concept of volumetric heating, where the heat is same throughout the component. This reduces the development of residual stresses in the components during fabrication. The various materials have different properties and the interaction of the various materials with the microwave is presented in Fig. 3.

The transparent materials such as glass does not have an ability to absorb microwaves and it directly allows them to pass through without having any type of loss and hence heating does not take place when rays are impacted on it. On the other hand, bulk metallic conductor materials do not allow microwaves to pass and neither absorbs but causes reflection when these opaque surfaces are exposed to microwaves. This leads to the plasma formation and causes surficial heating of the body. However, the third class of materials are known as dielectric materials, which tends to absorb the microwaves and heating is obtained by the conversion of

Fig. 3 Interaction of microwaves with **a** transparent materials, **b** conducting opaque and **c** dielectric materials
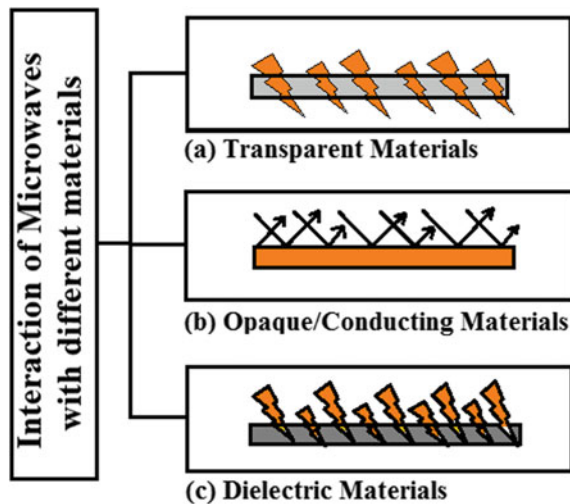
radiation into heat and this principle of heating is known as microwave heating. The dielectric property plays an important role in absorption of microwave and heating profile of the materials.

1.4 Concept of Conventional Heating and Microwave Heating

The generation of heat is a complex phenomenon which occurs mainly because of dipolar loss or re-orientation mechanism. When material is subjected to microwaves then electric and magnetic fields alternates 2.45 billion times in a second and this causes rotation of dipoles from the +ve to the −ve and travels from −ve to +ve. The presence of cohesive forces between the dipoles hinders the rapid reversals and causes frictional heating. The internal resistance of material also causes resistance heating on application of alternating electric fields. This process starts to take place instantaneously within the whole body and leads to the volumetric heating of whole mass subjected to microwaves. The main highlight of microwave heating is that heat is produced within the material and has inverted profile, i.e. from inward to outward surface; whereas, in conventional heating, surface (outer zone, closer to heat) is heated first and then heat travels inward [12, 13]. The difference between the heating phenomenon of conventional and microwave heating is shown in the following Fig. 4. As shown in Fig. 4, the concept of conventional heating states that the heating takes place from outside to inside (e.g. boiling water on commercial oven). Basically, in conventional heating, there is a large temperature gradient between the inside temperature and outside temperature of the material. This temperature difference leads to uneven heating profile of the product. Microwave heating overcomes this limitation of conventional heating, because the heating profile generates at the centre in this type of heating and moves towards outside area. Microwave heating is a
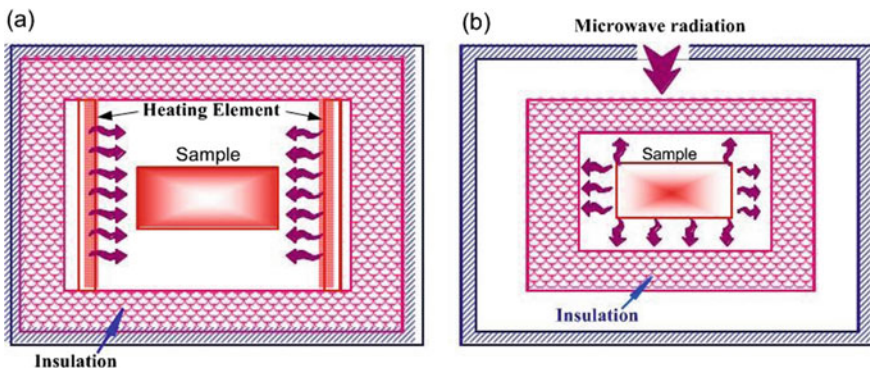
Fig. 4 Mechanism of heat transfer in a sample in case of **a** conventional heating and **b** microwave heating

volumetric heating that why in this type of heating temperature gradient is very less as comparative to conventional heating [14]. After understanding the concept of conventional heating and microwave heating, point comes to understand the concept of microwave hybrid heating (MHH).

1.5 Microwave Hybrid Heating

The processing of non-coupled materials through the microwave energy is really a challenging task. To deal such types of materials through the microwave energy, the research was carried out and microwave heating came out with a different form to process these materials, namely microwave hybrid heating [15, 16]. This type of heating phenomenon considers the concepts of conventional heating as well as the concept of microwave heating. The concept of microwave hybrid heating with its heating profile is shown in Fig. 5.

In conventional heating of materials, surfacial heating occurs first and then heat transfer takes place throughout the remaining material from the outer surface to the inner surface with having a varying temperature gradient, which corresponds to the microstructures having poor surfaces and it may lead to the overheating of the surface in contact or sometimes the metallic powder may get fused. In context of microwave heating, this type of heating mode may leads to the poor microstructure of core because of carbon content at the core surface, which can cause excessive brittleness and due to burning of core cracks may generate. It is because of heating from inside to outside of the material. To reduce the thermal gradient between the surface and
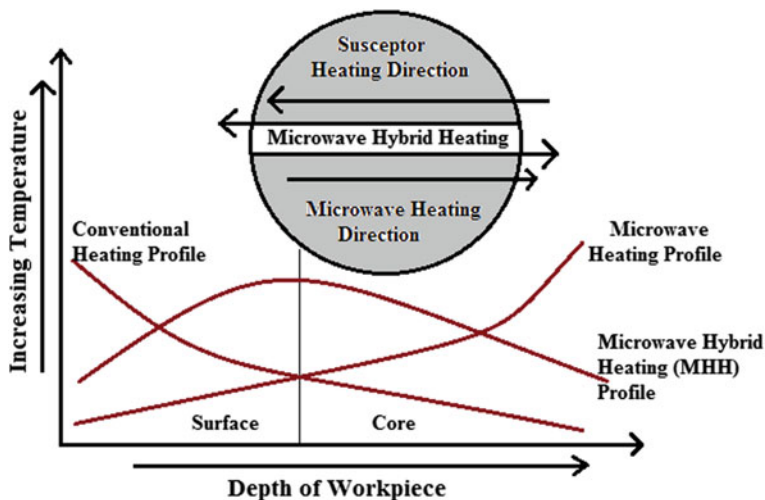
Fig. 5 Heating profiles for various types of heating method [17]

core and to make the limitations of these processes as an additional advantage, a new approach was introduced after lots of research in the field of material processing through microwave named it as two directional heating or microwave hybrid heating, such that heating can take place from the outside towards inside as well as from the inside towards outside during processing. The heating phenomenon leads to reduced temperature gradient and high rate of heating [16].

Basically, the microwave technology was firstly used for the purpose of telecommunication in the year of 1940 and it was well-known technology for the low-temperature application and after this in 1950–65, technology used for the processing of rubber curing, food processing, wood curing, etc. It was the time, when microwaves were used to treat the materials up having temperature of 450 °C. After the passage of time with the continuous research, the range of control was achieved up to 1000 °C and this technology was implemented in ceramic processing, processing of nitrides and glasses from the period of 1970 to 99. With the development of technology, the microwave technology used for material processing in the year of 2000 and after that claddings, sintering, melting and joining of metallic materials carried out. The chronological developments in the filed of microwave energy are presented in a schematic diagram as presented in Fig. 6.
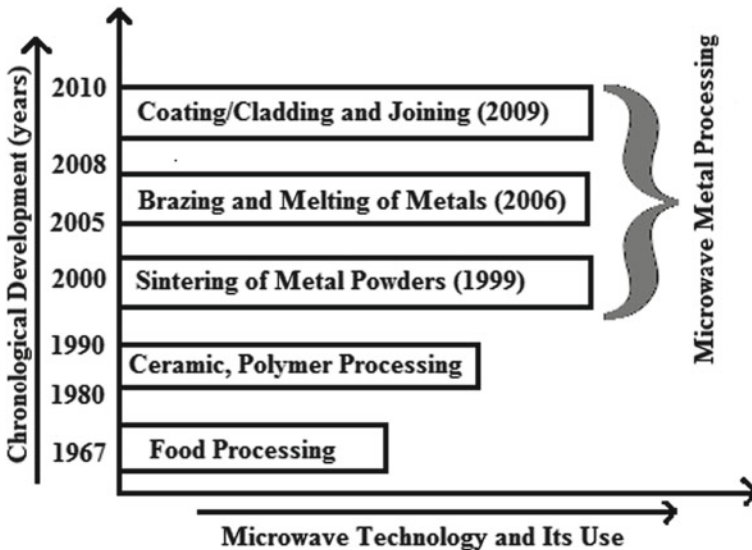
Fig. 6 Chronological developments in material processing through microwaves
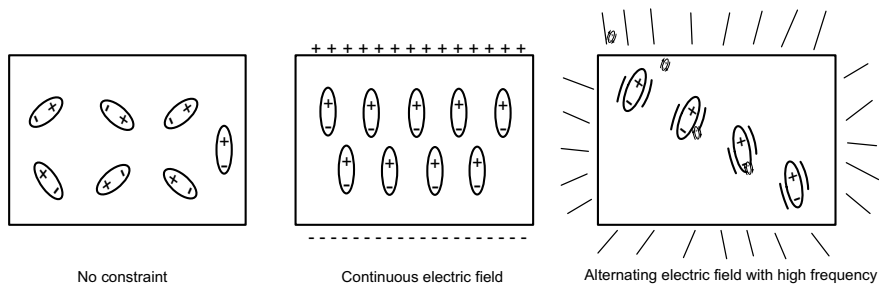
Fig. 7 Redistribution of charge under the influence of oscillating electromagnetic field

1.6 Microwave Material Interactions

The material permittivity is related to the level of absorption by the microwaves in the form of dielectric material and its relationship is defined as given below:

$$\varepsilon^* = \varepsilon' - j\varepsilon'' = \varepsilon_0(\varepsilon_r' - j\varepsilon_{eff}'') \tag{1}$$

where, ε'' is loss factor and ε' is permittivity.

The two mechanism are responsible for the interaction of a microwaves, which are ionic conduction and rotation of dipoles [17, 18]. The charge distribution in a given filed is presented in Fig. 7. The accumulation of a charge in composite materials occurs at interface and is a fundamental mechanism of hating [19].

The interaction of microwaves happens in different manner for different materials such as for metals and ceramics and so on. The classification of the interaction has been presented earlier by researchers [20, 21].

1.7 Microwave Cladding

The schematic of irradiation used for cladding is shown schematically in Fig. 8.

Gupta and Sharma analysed the wear resistance of the developed clads, the WC-Co is mixed with Ni to get a composite clad. The developed clad has been utilized for the wear-related application, where hardness is required to combat the abrasive wear. The clad depicted a very less porosity level in a range of 0.6–08. Therefore, the microstructure of a clad is sufficient to have a closed packed structure as compared to the composites fabricated by using some other techniques. The hardness of the clad was checked at ten locations to get an average value of a microhardness and it was found that the microhardness of the developed clad is 416 ± 20 HV, whereas the clad was developed on the surface of stainless steel, which showed a microhardness of 200 HV. The hard reinforced WC particles were responsible for the high wear resistance of clads [22]. Zafar et al. reported the cladding on the surface of a stainless steel
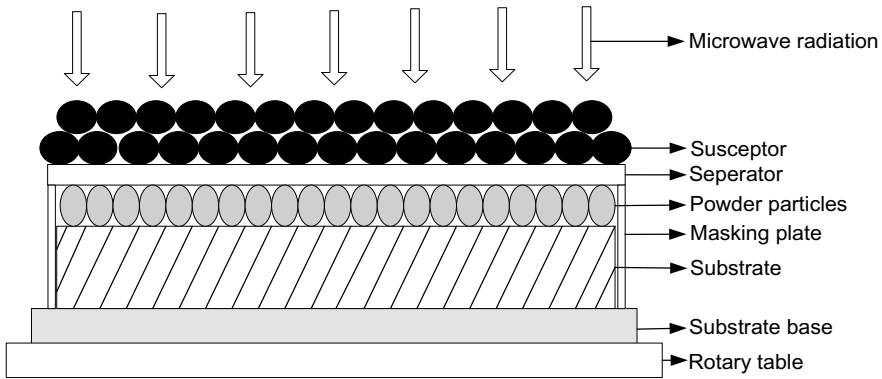
Fig. 8 Experimental set-up for microwave cladding

using microwave leads to the formation of well-bonded interface, that is, free from any kind of cracks and any other particles. The development of such interface is very important for having adhesion strength in the coatings. Therefore, the well-bonded interfaces resulted in the excellent bond strength. The tungsten carbide and cobalt were reinforced with Ni powder to have a composite coating. The composite clad showed a good tribological performance in terms of wear resistance under sliding wear conditions [23]. Prasad and Gupta reported the composite cladding using nickel with lanthanum oxide on the mild steel substrate. The size of the powder cladded on the surface of mild steel was around 40 μm. The thickness of the developed cladding was around 500 μm and showed a microhardness around 319 HV [24]. The various materials like superalloys can be cladded and joined by using microwave-processing route, which are very beneficial for high-temperature applications like structural joints, turbocharger and turbocharger casings [25–30]. Recently, the application of microwave for the sintering of titanium-based alloys has been reported [31–33]. It was reported that microwave technology can sinter titanium materials efficiently and consumes less time as compared with spark plasma sintering and other conventional technique.

2 Conclusion

The mechanical properties obtained from the microwave-processed technique (MHH) were significantly higher as compared to other techniques. The microstructure of the developed materials by using microwave-processing route is capable of producing crack-free surfaces with higher density and low porosity. The composite and metals can be processed at high temperature as they do not absorb microwaves at room temperature.

References

1. Prakash, C., Singh, S., Verma, K., Sidhu, S.S., Singh, S.: Synthesis and characterization of Mg-Zn-Mn-HA composite by spark plasma sintering process for orthopedic applications. Vacuum **155**, 578–584 (2018)
2. Prakash, C., Singh, S., Pabla, B.S., Sidhu, S.S., Uddin, M.S.: Bio-inspired low elastic biodegradable Mg-Zn-Mn-Si-HA alloy fabricated by spark plasma sintering. Mater. Manuf. Processes **34**(4), 357–368 (2019)
3. Prakash, C., Singh, S., Gupta, M.K., Mia, M., Królczyk, G., Khanna, N.: Synthesis, characterization, corrosion resistance and in-vitro bioactivity behavior of biodegradable Mg–Zn–Mn–(Si–HA) composite for orthopaedic applications. Materials **11**(9), 1602 (2018)
4. Bhushan, B., Singh, A., Singh, R., Mehta, J.S., Gupta, A., Prakash, C.: Fabrication and characterization of a new range of β-type Ti-Nb-Ta-Zr-xHaP (x = 0, 10) alloy by mechanical alloying and spark plasma sintering for biomedical applications. Mater. Today: Proc. **5**(14), 27749–27756 (2018)
5. Singh, B., Singh, R., Mehta, J.S., Gupta, A., Singh, M., Singh, S., Prakash, C.: Nano-mechanical characterization of Mg-Zn-Mn-Si alloy fabricated by spark plasma sintering for biomedical applications. Mater. Today: Proc. **5**(14), 27742–27748 (2018)
6. Singh, B.P., Singh, R., Mehta, J.S., Prakash, C.: Fabrication of biodegradable low elastic porous Mg-Zn-Mn-HA alloy by spark plasma sintering for orthopaedic applications. In: IOP Conference Series: Materials Science and Engineering, IOP Publishing, vol. 225, no. 1, p. 012050, Aug 2017
7. Singh, R., Singh, B.P., Gupta, A., Prakash, C.: Fabrication and characterization of Ti-Nb-HA alloy by mechanical alloying and spark plasma sintering for hard tissue replacements. In: IOP Conference Series: Materials Science and Engineering, IOP Publishing, vol. 225, no. 1, p. 012051, Aug 2017
8. Lauf, R.J., Bible, D.W., Johnson, A.C., Everliegh, C.A.: 2 to 18 GHz broadband microwave heating systems. Microwave J. **36**, 24–27 (1993)
9. Ku, H.S., Siores, E., Ball, J.A.R.: Review—microwave processing of materials: Part I. The Honking Institution of Engineers Transactions, **8**, 31–37 (2001)
10. Thostenson. E.T., Chou. T.: Microwave processing: fundamentals and applications. Composites: Part A **30**, 1055–1071 (1999)
11. Menendez, J.A., Arenillas, A., Fidalgo, B.: Microwave heating processes involving carbon materials. Fuel Process. Technol. **91**, 1–8 (2010)
12. Zhou. J., Shi, C., Mei, B.: Research on the technology and the mechanical properties of the microwave processing of polymer. J. Mater. Process. Technol. **137**, 156–158 (2003)
13. Bruce, R.W., Fliflet, A.W., Huey, H.E., Stephenson, C.: Microwave sintering and melting of titanium powder for low-cost processing. Key Eng. Mater. **436**, 131–140 (2010)
14. Ku. H.S., Siores, E., Ball, J.A.R., Review—microwave processing of materials: part I. The Honking Institution of Engineers Transactions, **8**, 31–37 (2011)
15. Leonelli, C., Veronesi, P., Denti, L., Gatto, A., Luliano, L.: Microwave assisted sintering of green metal parts. J. Mater. Process. Technol. **205**, 489–496 (2008)
16. Huang, Z., Gotoh, M., Hirose, Y.: Improving sinter-ability of ceramics using hybrid microwave heating. J. Mater. Process. Technol. **209**, 2446–2452 (2009)
17. Singh, S., Gupta, D., Jain, V., Sharma, A.K.: Microwave processing of materials and applications in manufacturing industries: a review, Mater. Manuf. Process. (2015)
18. Thostenson, E.T., Chou, T.W.: Microwave processing: fundamentals and applications. Compos. A **30**, 1055–1071 (1999)
19. Zhu, S., Fahrenholtz, W.G., Hilmas, G.E. et al.: Microwave sintering of a ZrB_2–B_4C particulate ceramic composite. Compos. A, **39**, 449–453 (2008); Mijovic, J., Wijaya, J.: Review of cure of polymers and composites by microwave energy. Polym. Compos. **11**(3), 184–191 (1990)
20. Mijovic, J., Wijaya, J.: Review of cure of polymers and composites by microwave energy. Polym. Compos. **11**(3), 184–191 (1990)

21. Agrawal, D.: Microwave sintering of ceramics, composites, metals, and transparent materials. J. Mater. Edu. **19**(4, 5 & 6), 49–58 (1999)
22. Gupta, D., Sharma, A.K.: Investigation on sliding wear performance of WC10Co2Ni cladding developed through microwave irradiation. Wear **271**(9), 1642–1650 (2011)
23. Zafar, S., Sharma, A.K.: On friction and wear behaviour of WC-12Co microwave clad. Tribol. Trans. **58**, 584–591 (2015)
24. Prasad, A., Gupta, D.: Microwave cladding: Emerging innovative cladding process. Emerg. Trends Eng. Technol. **271** (2013)
25. Oghbaei, M., Mirzaee, O.: Microwave versus conventional sintering: a review of fundamentals, advantages and applications. J. Alloys. Compd. **494**, 175–189 (2010)
26. Vasudev, H., Thakur, L., Singh, H.: A review on tribo-corrosion of coatings in glass manufacturing industry and performance of coating techniques against high temperature corrosion and wear. i-Manager's J. Materi. Sci. **5**, 38–48 (2017)
27. Vasudev, H., Thakur, L., Bansal, A., Singh, H., Zafar, S.: High temperature oxidation and erosion behaviour of HVOF sprayed bilayer Alloy-718/NiCrAlY coating. Surf. Coat. Technol. **362**, 366–380 (2019)
28. Vasudev, H., Thakur, L., Bansal, A., Singh, H.: Mechanical and microstructural behaviour of wear resistant coatings on cast iron lathe machine beds and slides. Kovove Mater. **56**(1), 55–63 (2018)
29. Bansal, A., Vasudev, H., Sharma, A.K., Kumar, P.: Investigation on the effect of post weld heat treatment on microwave joining of the Alloy-718 weldment. Mater. Res. Express **6**(8), 086554 (2019)
30. Vasudev, H., Singh, G., Bansal, A., Vardhan, S., Thakur, L.: Microwave heating and its applications in surface engineering: a review. Mater. Res. Express **6**(10), 102001 (2019)
31. Prakash, C., Singh, S., Ramakrishna, S., Królczyk, G., Le, C.H.: Microwave sintering of porous Ti–Nb-HA composite with high strength and enhanced bioactivity for implant applications. J. Alloy. Compd. **824**, 153774 (2020)
32. Prakash, C., Singh, S., Basak, A., Królczyk, G., Pramanik, A., Lamberti, L., Pruncu, C.I.: Processing of Ti50Nb50–xHAx composites by rapid microwave sintering technique for biomedical applications. J. Mater. Res. Technol. **9**(1), 242–252 (2020)
33. Prakash, C., Singh, S., Sharma, S., Singh, J., Singh, G., Mehta, M., Mittal, M., Kumar, H.: Fabrication of low elastic modulus Ti50Nb30HA20 alloy by rapid microwave sintering technique for biomedical applications. Mater. Today: Proc. **21**, 1713–1716 (2020)

Investigations for Improving Solid-State Weldability of Dissimilar Thermoplastic Composites Through Melt Processing

Ranvijay Kumar , **Rupinder Singh** , **and IPS Ahuja**

1 Introduction

Joining of thermoplastic composite structures is an important manufacturing step applied in aerospace, automobile, and civil engineering fields [1]. Since other techniques of welding processes are performed above the melting point or with use of arc or gases, the solid-state welding (like: adhesive bonding, solvent bonding, fusion bonding, and co-consolidation) processes are processed below melting points with no use of external additives and covers wide range of thermoplastic composite materials [2]. Most importantly, the solid-state welding processes eradicate requirements for introduction of hole, use of costly fasteners, loading pins, and use of filler or gases [3]. Friction stir welding (FSW) is one of the energy-efficient processes, which is adopted mostly for manufacturing with the edge of environment-friendly and economy prospects since there is insignificant emission of gases, fumes, and flames [4, 5]. The heat generation at the tool–work interface established the net material flow from retreating side to advancing side, so it is always be needed a smoothen material flow mechanism [6–9]. Also, it is reported that clamping mechanism plays an important role in stress concentration on weld bead. The numerical model defined that in

R. Kumar · R. Singh
Department of Production Engineering, GNDEC, Ludhiana, India
e-mail: ranvijayk12@gmail.com

R. Kumar
University Center for Research and Development, Chandigarh University, Mohali, India

R. Singh (✉)
Department of Mechanical Engineering, National Institute of Technical Teachers Training and Research, Chandigarh, India
e-mail: rupindersingh@nitttrchd.ac.in

I. Ahuja
Department of Mechanical Engineering, Punjabi University, Patiala, India
e-mail: ahujaips@gmail.com

longitudinal direction residual stresses are constant through depth and in traverse direction residual stresses are constant away from the bead [10–12]. The FSW of dissimilar thermoplastic composite materials is need of the hour and to be potentially applied in the gas/oil pipeline joining or crack refilling applications. Since dissimilar thermoplastic has different mechanical, thermal, rheological, and chemical morphological properties, there are number of issues during practical FSW process resulting into inferior weld quality [13–15]. It has been reported that melt flow index (MFI) is one of the rheological properties which can be used as a yardstick for establishing possibilities of joining reinforced metallic/nonmetallic thermoplastic matrix-based substrates [16, 17]. Fused deposition modeling (FDM) is one of the additive manufacturing and melt processing techniques which is applicable for manufacturing if multifunctional prototypes for various engineering applications [18].

The literature review reveals that FSW of dissimilar thermoplastics is feasible and a lot of studies on joining of dissimilar thermoplastics (with reinforcements of metallic fillers) have been reported. But hitherto, very little has been reported on crash applications of such FSW joints. The present study an extension of work reported by Kumar et al. [18] on FSW of Al-reinforced acrylonitrile butadiene styrene (ABS) and polyamide (PA6). The ABS being amorphous thermoplastic has wide range of applications in prototype fabrication, construction scaffolds, pipe fitting, etc. The PA6 is semicrystalline thermoplastic with high elastic modulus and thermal, chemical, and wears resistive. The welding application of ABS and PA6 includes repair and maintenance of leakages and cracks in oil/gas pipelines where rapid tool printed with FDM can be useful for mentioned applications. The present study deals with evaluation of modulus of toughness in tensile and flexural fracture for crash applications along with traverse force monitoring for decision-making of input process variables.

2 Materials and Methods

The pilot experimentation of FSW in form of trial run has been conducted for joining of FDM printed (without changing hardware/software) virgin ABS and PA6. The joining of these virgin thermoplastics was failed due to noncompatibility based upon melt flow properties, melting point, molecular weight, etc. The melting point of ABS and PA6 was monitored by differential scanning calorimetric (DSC) and found 190.0–193.49 °C for ABS and 223.29 °C for PA6. The MFI of ABS and PA6 was observed as 8.76, 23.27 g/10 min as per ASTM D1238. The dissimilar melting point and dissimilar melt flow characteristics may have contributed for infeasible joints. So, based upon these observations, a process chart has been developed to enhance the FSW compatibility of ABS and PA6 thermoplastic by reinforcement of 50-micron electrolytic Al metal particle reinforcement (Fig. 1). Some of reasons for selecting the Al metal particle for reinforcement over other metals particles are corrosive resistance, good ductility, and low melting point. The electrolytic Al metal particles were blended with ABS and PA6 granules and the fed to MFI testing unit. The Al
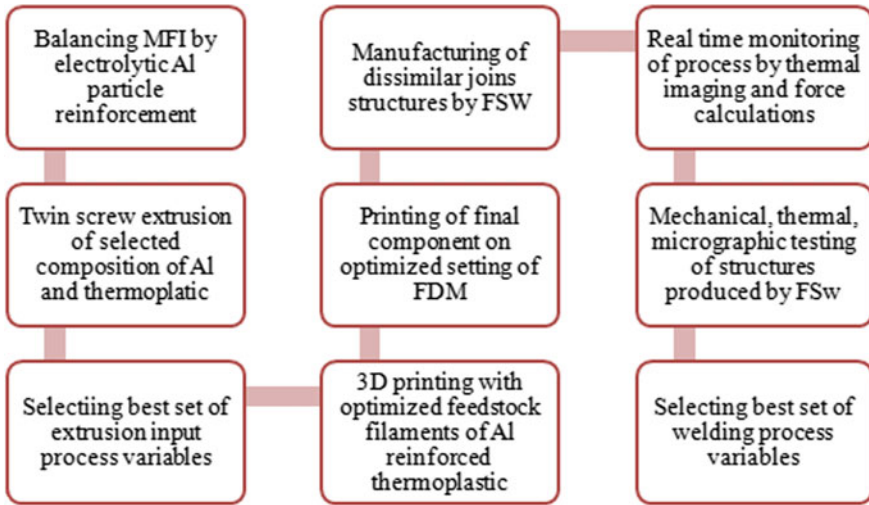
Fig. 1 Experimental procedure for FSW of 3D printed parts

Table 1 Tensile, thermal, and micrographic properties of ABS-15Al and PA6-50Al

Materials	Peak strength (MPa)	Break strength (MPa)	Percentage elongation at peak	Percentage elongation at break	MFI (g/10 min)	Melting point (°C)
ABS-15Al	224.30	202.07	11	12	11.57	203.20–223.59
PA6-50Al	220.20	198.19	14	14	11.97	221.06

particle proportions form 5–50% in the thermoplastic matrix have been varied by changing the MFI (Table 1). It should be noted that the reinforcement of 15% Al in ABS matrix resulted MFI of 11.57 g/10 min, whereas 50% Al in PA6 resulted MFI of 11.97 g/10 min.

So, ABS-15%Al and PA6-50%Al were selected as the processing compositions/proportions for twin screw extrusion (TSE), FDM, and FSW processes. The ABS-15%Al and PA6-50%Al were subjected to tensile, thermal and micrographic properties for evaluation of basic characteristics (Table 1).

It should be noted that changes in levels of input variables for both ABS-15%Al and PA6-50%Al was dependent upon the uniformity (e.g., diameter) in feedstock filaments. In the present study, a TSE with co-rotating screws was used for preparations of feedstock filaments. In the present study, open source FDM printer (Company: Accucraft, Model: 250D) under optimized input processing variable was used to fabricate the specimen for joining through FSW (Size: $60 \times 60 \times 4$ mm). FDM setup was operated at: 80% infill, $\Phi 1.75 \pm 0.05$ mm (feed stock filament), outer boundary layers 06, filling rectilinear, 30 mm/sec perimeter speed, 60 mm/sec printing speed, 250 °C extruder temperature, and 55 °C printing bed temperature.

Table 2 Experimental design

S. no.	Rotational speed (rpm)	Traverse speed (mm/min)	Plunge depth (mm)
1	1000	30	2
2	1000	40	3
3	1000	50	4
4	1200	30	3
5	1200	40	4
6	1200	50	2
7	1400	30	4
8	1400	40	2
9	1400	50	3

Fig. 2 3D printed parts of **a** PA6-50%Al, **b** ABS-15%Al and **c** joints by FSW process

3 Experimentation

Based upon the pilot experimentation for feasibility and physical appearance, rotational speed was selected between 1000 and 1400 rpm, traverse speed in between 30 and 50 mm/min and plunge depth of 2–4 mm. Table 2 shows experimental design for present study. Further, nine different sets of experiments have been performed under varying rotational speed, traverse speed, and plunge depth. Figure 2 shows the 3D printed parts and welded parts.

4 Results and Discussion

Table 3 shows the mechanical properties of FSW joints (average of three experiments). It should be noted that maximum tensile properties were possessed by joints in experiment no. 7 (break strength: 70.64 MPa and percentage elongation at break: 8%) which is the combination of input variables 1400 rpm (maximum rpm), 30 mm/min traverse speed (minimum traverse speed), and 4 mm plunge depth (maximum plunge depth). The minimum tensile properties were obtained at experiment no. 2 (break strength: 10.78 MPa and percentage elongation at beak: 2%), with input combination of 1000 rpm (minimum), 40 mm/min traverse speed, and 3 mm plunge depth (intermediate). It has been observed that flexural properties have

Table 3 Mechanical properties of joints prepared by friction stir welding

Exp no.	Tensile strength at break (MPa)	Percentage elongation at break	Flexural strength at break (MPa)	Percentage deflection at break	Transverse force (N)	Modulus of toughness of tensile properties(MPa) (1/2 × break strength × strain at break)	Modulus of toughness of flexural properties(MPa) (1/2 × break strength × strain at break)
1	30.49	5	50.04	11	75	0.76	2.75
2	10.78	2	40.41	3	79	0.10	0.60
3	60.19	7	60.17	14	45	2.31	4.21
4	20.85	3	80.37	12	64	0.31	4.82
5	40.64	8	150.89	8	38	1.62	6.03
6	40.5	5	50.27	5	52	1.01	1.25
7	70.93	9	160.29	4	26	3.19	3.20
8	70.64	8	100.58	8	34	2.82	4.02
9	30.88	8	90.23	11	36	1.23	4.96

been obtained in-line with the tensile properties. However, the modulus of toughness for tensile and flexural properties was not obtained analogous. The maximum modulus of toughness was obtained for S. no. 5 and minimum for S. no. 2. It was observed that that requirement of force (26 N) was minimum where most durable joints were obtained (at S. no. 7), similarly the maximum force (79 N) was required where minimum durability of the joints were resulted (at S. no. 2).

Figure 3 shows the stress vs. strain trends for tensile and flexural properties. It was observed that maximum tensile properties were possessed by joints at S. no. 7, which is the combination of input variables 1400 rpm (maximum rpm), 30 mm/min traverse speed (minimum traverse speed), and 4 mm plunge depth (4 mm). The minimum tensile properties were obtained at S. no. 2 with input combination of 1000 rpm (minimum), 40 mm/min traverse speed, and 3 mm plunge depth (intermediate). Here, it is interesting facts that keeping maximum rpm (rpm) and full plunge depth (4 mm) with maintaining minimum traverse speed (30 mm/min) resulted in maximum tensile properties. The flexural testing of the joints were appeared analogous to the tensile testing and similar results were obtained. The micrographs of thermomechanical heat-affected zone (TMAZ) were taken at × 30 magnification (Fig. 4). The micrograph of experiment at S. no. 2 clearly shows non-blended layers of ABS and PA6 matrix, whereas comparison to this, micrograph with experiment at S. no. 7 shows uniformly blended layers of ABS and PA6 matrix.

Figure 5 shows the results obtained from surface topology of joints for experiment as per S. no. 2 and S. no. 7 in the form of 3D rendered images and surface roughness plots at 0.04 mm cutoff length. It has been ascertained from the 3D rendered images that joint in experiment at S. no. 2 is not properly stirred and resulted into higher surface roughness as compared to joint prepared in S. no. 7.

(a) Stress vs. strain trends (while tensile testing)

(b) Stress vs. strain trendss (while flexural testing)
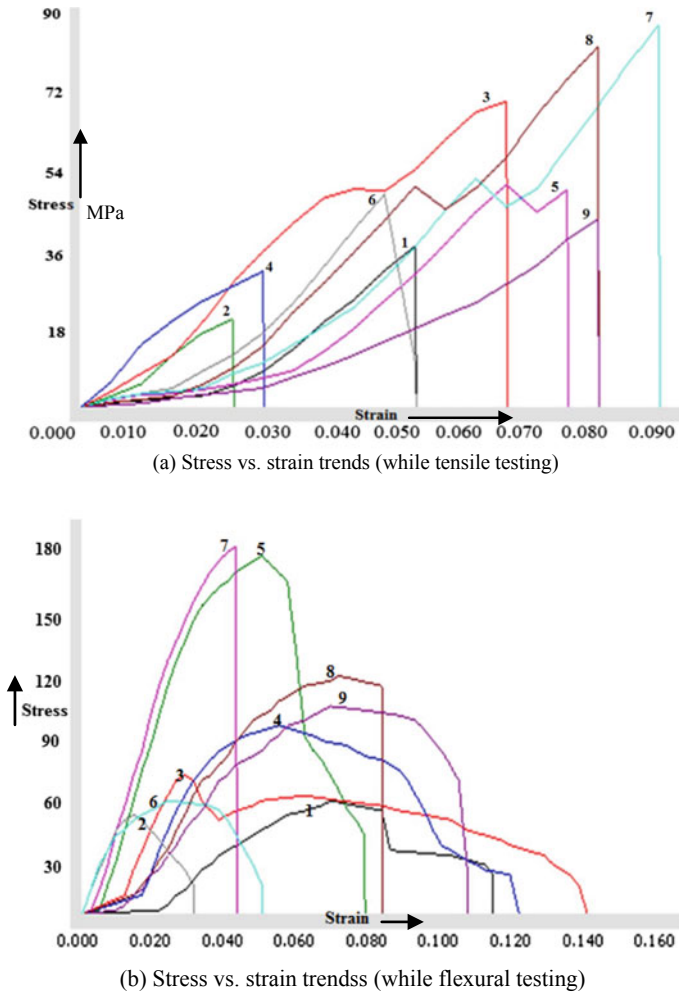
Fig. 3 Stress versus strain plots for **a** tensile and **b** flexural properties

5 Conclusions

The better tensile properties were observed for joint prepared as per S. no. 7 (break strength: 70.64 MPa and percentage elongation at break: 8%) which is the combination of input variables 1400 rpm (maximum rpm), 30 mm/min traverse speed (minimum traverse speed), and 4 mm plunge depth (maximum plunge depth). It has been ascertained that results for flexural strength, modulus of toughness, while tensile testing was in-line with the tensile properties. However, the modulus of toughness for flexural properties was better for experiment no. 5. Hence, for crash applications with tensile load, the experimental conditions reported in experiment no. 7 may be
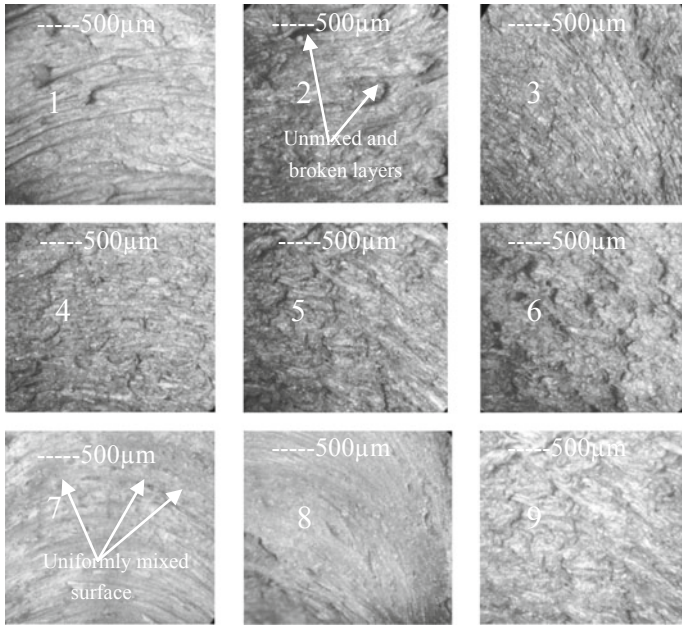
Fig. 4 Optical micrographs of joints at × 30 magnifications
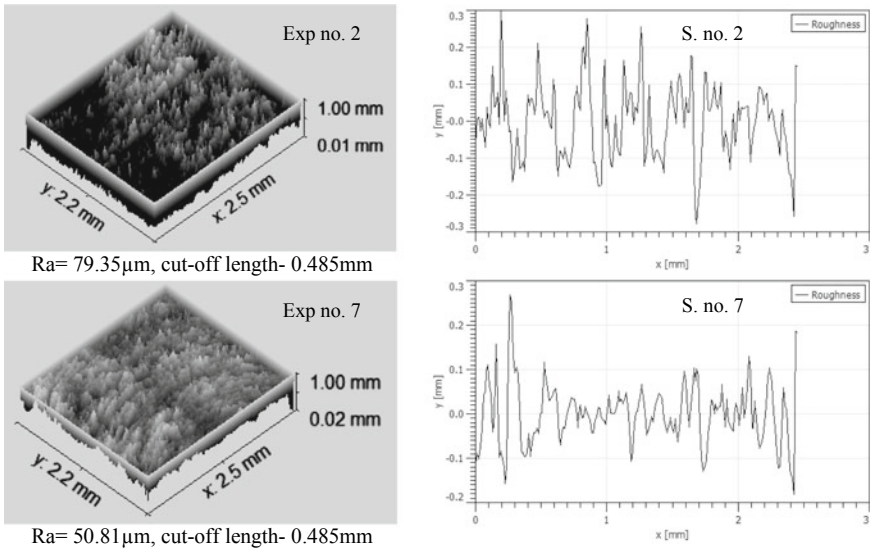
Fig. 5 Surface topology plots for joints for experiment at S. no. 2 and S. no. 7

followed, whereas for crash applications in flexural cases, experimental conditions mentioned in experiment no. 5 may be followed.

References

1. Yousefpour, A., Hojjati, M., Immarigeon, J.P.: Fusion bonding/welding of thermoplastic composites. J. Thermoplast. Compos. Mater. **17**(4), 303–341 (2004)
2. Kumar, R., Singh, R., Ahuja, I.P.S., Penna, R., Feo, L.: Weldability of thermoplastic materials for friction stir welding-a state of art review and future applications. Compos. B Eng. **137**, 1–15 (2018)
3. Ahmed, H., van Tooren, M.J.L., Justice, J., Harik, R., Kidane, A., Reynolds, A.P.: Investigation and development of friction stir welding process for unreinforced polyphenylene sulfide and reinforced polyetheretherketone. J. Thermoplast. Compos. Mater. (2016). https://doi.org/10.1177/0892705718785676
4. Shah, P.H., Badheka, V.J.: Friction stir welding of aluminium alloys: An overview of experimental findings–Process, variables, development and applications. Proc. Inst. Mech. Eng., Part L: J. Mater.: Des. Appl. (2017). https://doi.org/10.1177/1464420716689588
5. Yaduwanshi, D.K., Bag, S., Pal, S.: Heat transfer analyses in friction stir welding of aluminium alloy. Proc. Inst. Mech. Eng., Part B: J. Eng. Manuf. **229**(10), 1722–1733 (2015)
6. Pashazadeh, H., Masoumi, A., Teimournezhad, J.: A study on material flow pattern in friction stir welding using finite element method. Proc. Inst. Mech. Eng., Part B: J. Eng. Manuf. **227**(10), 1453–1466 (2013)
7. Ghorbanzade, T., Soltanipour, A., Dehghani, K., Chabok, A.: Microstructural evolutions and mechanical properties of friction stir welded AA2024-3. Proc. Inst. Mech. Eng., Part L: J. Mater.: Des. Appl. **230**(1), 75–87 (2016)
8. Gadakh, V.S., Kumar, A.: Friction stir welding window for AA6061-T6 aluminium alloy. Proc. Inst. Mech. Eng., Part B: J. Eng. Manuf. **228**(9), 1172–1181 (2014)
9. Akbari, M., Aliha, M.R.M., Keshavarz, S.M.E., Bonyadi, A.: Effect of tool parameters on mechanical properties, temperature, and force generation during FSW. Proc. Inst. Mech. Eng., Part L: J. Mater.: Des. Appl. (2016). https://doi.org/10.1177/1464420716681591
10. Casavola, C., Cazzato, A., Moramarco, V., Pappalettere, C.: Influence of the clamps configuration on residual stresses field in friction stir welding process. J. Strain Anal. Eng. Des. **50**(4), 232–242 (2015)
11. Azhiri, R.B., Tekiyeh, R.M., Zeynali, E., Ahmadnia, M., Javidpour, F.: Measurement and evaluation of joint properties in friction stir welding of ABS sheets reinforced by nanosilica addition. Measurement **127**, 198–204 (2018)
12. Kumar, R., Singh, R., Ahuja, I.P.S.: Friction stir welding of ABS-15Al sheets by introducing compatible semi-consumable shoulder-less pin of PA6-50 Al. Measurement **131**, 461–472 (2019)
13. Singh, R.K.R., Rathod, D.W., Pandey, S.: Friction stir welding of nuclear grade SA508Gr. 3Cl. 1 and SS304LN dissimilar steels. Proc. Inst. Mech. Eng., Part C: J. Mech. Eng. Sci. **232**(21), 3814–3822 (2018)
14. Doniavi, A., Babazadeh, S., Azdast, T., Hasanzadeh, R.: An investigation on the mechanical properties of friction stir welded polycarbonate/aluminium oxide nanocomposite sheets. J. Elastomers Plast. **49**(6), 498–512 (2017)
15. Singh, R., Kumar, R., Feo, L., Fraternali, F.: Friction welding of dissimilar plastic/polymer materials with metal powder reinforcement for engineering applications. Compos. B Eng. **101**, 77–86 (2016)

16. Singh, R., Kumar, R., Ranjan, N.: Sustainability of recycled ABS and PA6 by banana fiber reinforcement: thermal, mechanical and morphological properties. J. Inst. Eng. (India): Series C 1–10 (2018)
17. Kumar, R., Singh, R., Ahuja, I.P.S., Amendola, A., Penna, R.: Friction welding for the manufacturing of PA6 and ABS structures reinforced with Fe particles. Compos. B Eng. **132**, 244–257 (2018)
18. Kumar, R., Singh, R., Ahuja, I.P.: Mechanical, thermal and micrographic investigations of friction stir welded: 3D printed melt flow compatible dissimilar thermoplastics. J. Manuf. Process. **38**, 387–395 (2019)

A Short Note on the Friction Stir Welding of the Aluminum Alloys

Yogita Sharma and Hitesh Vasudev

1 Introduction

In FSW, the job parts are joined without the base metals being melted. This process' development was a important shift from standard rotary motion and linear reciprocating procedures of friction welding [1]. The FSW's primary characteristic is to join materials without achieving the temperature of fusion [2]. Special tool with proper parameters is used for friction welding process to creating the heating zone between two mating plates. Various types of alloys which are not welded by any process are best suited with this process. In friction stir welding, there is use of nonconsumable electrode which gives the defect free joining of aluminum alloys. From the study of various researchers, there is lots of optimization techniques are used to control the various parameters to enhance the quality of this process.

In automated sectors, friction stir welding is commonly used to substitute the aluminum sheet resistance spot welding method for better and better quality production. FSW's main advantages are a solid-state technique, low distortion area unit, lack of melt-related defects, and high joint strength, even in those alloys the unit of thought-about un-welded region ready by typical methods.

Y. Sharma
Mechanical Engineering, Guru Kashi Univesrity, Talwandi Sabho, Bathinda, Punjab, India

H. Vasudev (✉)
School of Mechanical Engineering, Lovely Professional University, Jalandhar - Delhi G.T. Road, Phagwara, Punjab 144411, India
e-mail: hitesh.24804@lpu.co.in
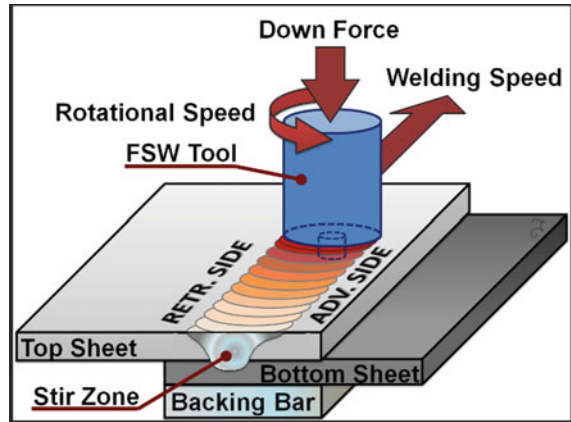
1.1 Working of FSW

This welding technique can be used to join butt and lap joints and having a flexible range of dimensioning for the parts to be joined. This is now widely accepted process of welding, which is used in some typical engineering application like aeronautical parts, etc. The aluminum and magnesium alloys are widely accepted by the structure, power, and automobile sector due to its lightweight. The reduction the weight of the component enhances the efficiency of the system. Moreover, these materials can be fabricated by using this welding technique. The process uses nonconsumable tool for welding the parts. The tool is bring into with the contact in the work piece, where heat is generated by means of friction and volumetric heating takes place, as the tool progressed over the length of the weld. The tool is made of two parts, where top part is known as probe [4, 5]. The second part of the tool is known as shoulder and it has a large diameter as compare to the probe. The tool rotates over the workpiece and produces friction at the interface. The schematic arrangement of the welded joint processed through FSW is shown in Fig. 1. The figure shows the rotating tool over the substrate. The downward force is the intensity of force required to weld the parts.

1.2 Process Parameters of FSW

Friction stir welding means that the parameters can be regulated and the energy input to the scheme can be controlled. The two main process parameters are the TRS and the WS. The geometry of the instrument (size and profile) and the process parameters influence the generation of heat, the material flow, the evolution of the microstructure, and the joint properties. In this method, the tool life is a very significant variable depending on the process parameter and obtaining a parameter that is more appropriate for the characteristics of the friction stir welding process as well as knowing

the effects of the impact of these parameters on the welding microstructural conduct to be performed.

It has been explored the impact of some of the significant parameters such as axial stress force, rotation velocity, tool tilt angle, shoulder and pin diameter, welding velocity affecting welding characteristics. Therefore, an attempt was produced in this inquiry to know the impact of tool parameters and process parameters on the formation of FSP area and associated friction tensile strength characteristics. Important parameters were explored on welding characteristics such as axial tool stress (F), rotational velocity (N), and traverse velocity (S). However, few investigations [6] on formulating and optimizing the impacts of FSW parameters on mechanical and metallurgical characteristics have been carried out.

The Taguchi technique is a very significant technique used to optimize metallurgical conduct in the past to define friction stir welding by the highest possible process parameter of approx. 1150–1200 rpm rotational speed, 7 KN axial pressure, 75 mm min welding velocity, 225 MPa yield strength, and 247 MPa tensile strength. Approximately 35% more than other welding joints and the microstructure contains very good grain and equiaxial grain. Highly fine narrower grain was acquired that looked like elliptical onion ring in the middle of the weld and also increased the microhardness profile and began to descend in every 2 mm until the hardness was reached the same as the base material [7–9]. Fine and equiaxial grain was discovered around the nugget. It has been evaluated to increase the repeated fatigue life of failure.

2   Review of Literature

Colegrove and Shercliff [10] studied the flow of material during friction stir welding process using the model based on CFD. This model was used to obtain the flow of material to all around of Trivex as well as MX-Trivex tool. The result obtained was compared to the analysis result of Triflute tools. By using Trivex tool, the analysis was indicated that the downward force as well as transverse was decreased. To know the behavior of material flow, the stream lined around the tool was used. The force along the downward direction was found to be increased using Triflute tool.

Da Silva et al. [11] studied flow of material, microstructural behavior, mechanical properties like tensile strength and hardness based on the variation of process parameter and their effect on weld was done by friction stir welding joints of two dissimilar alloys between AA2024-T3 and AA7075-T6. Boundary of the base metal around the stir zone was clearly observed; no onion ring formation was observed.

Fratini et al. [12], in friction stir welding method of aluminum alloy 7075, also researched how material flow occurs. He followed the numerical simulation method as well as the experiment by taking the tool rotation velocity variation, welding traverse velocity, and altering the profiled pin shape. The bonding of the material to the forward side of the friction stir welding joints is to be established. When geometry of the instrument profile was conical, the material flow was discovered to

be uniform because it enabled the vertical material motion in order to prevent the defect formation. It is well known that the effect on the weld characteristics of some needed parameters, such as moving speed and fastening velocity, is that for scientists the main subjects.

Sadeesh et al. [13] The study of the fastening of dissimilar AA2024 and AA6061 5-mm-thick aluminum plates was also carried out using the method of friction stir welding (FSW). Optimum method parameters have been acquired for math approach applied to the victimization of joints. Sevvel P and Jai Ganesh V also outlined and examined the recent scenario of Tool Geometry's role in FSW along with its tooling components, kinds, forms, sizes, and harm mechanisms in association with various metals along with steels, aluminum, titanium, and their alloys.

Karimi et al. [14] studied in their research the effect of tool material and tool offset on tool erosion and metallurgical and mechanical properties of dissimilar friction stir fastening of Al alloy to steel area unit investigated. Different tool materials and offset were used in Al alloy friction stir welding to carbon steel with a steady tool velocity and feed rate of 710 rpm and 28 mm/min.

3   Function of Tool in FSW

When the button comes into touch with the workpiece, it produces heat that is deforming and frictional, softening the fabric of the workpiece. So, the material used for making tools for friction stir welding must have the following properties (Fig. 2)

- Good resistance
- Resistance to fracture
- Resistance to wear
- High temperature stability
- High temperature resistance
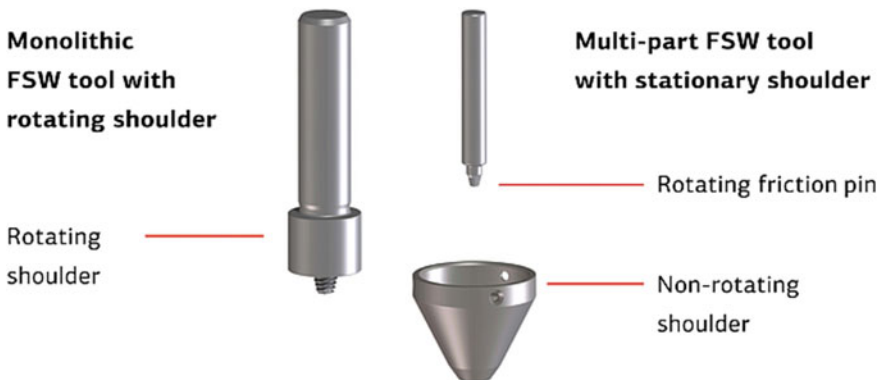
Fig. 2   Friction stir welding tool

- Total reactivity
- Thermal expansion co-efficient.

3.1 FSW in Industries

TWI originally patented FSW method in many industrialized countries. For many industrial applications, FSW and its numerous versions such as friction stir spot welding and friction stir welding are used.

- Used in the manufacturing industry
- Used in chemical sectors for connecting pipelines, thermal exchangers, etc.
- Used for welding wings, fuel tanks. and airplane structures in aviation sectors.

3.2 Advantages and Disadvantages of FSW

- In welded area, distortion is significantly small as well as residual stress.
- Higher mechanical characteristics.

Disadvantages

- The work piece should be very closely clamped to ensure that the weld is performed properly.
- Surface thickness is decreased marginally as no filler material is used during the method.

3.3 Typical Engineering Applications of FSW

- FSW is mainly used for welding wings, fuel tanks, airplane structure, and also for structural job in marine sectors.
- Used for the construction of railway tankers in marine sectors for structural job and railway sectors.
- Recently, began to use in automotive motor chassis and body frame.
- In the electronic sectors, friction stir welding is also used to connect bus bars, aluminum, copper, other electronic machinery and connectors.
- It is also used for welding the spacecraft fuel tank because of the strong state joining method [15–19] (Fig. 3).
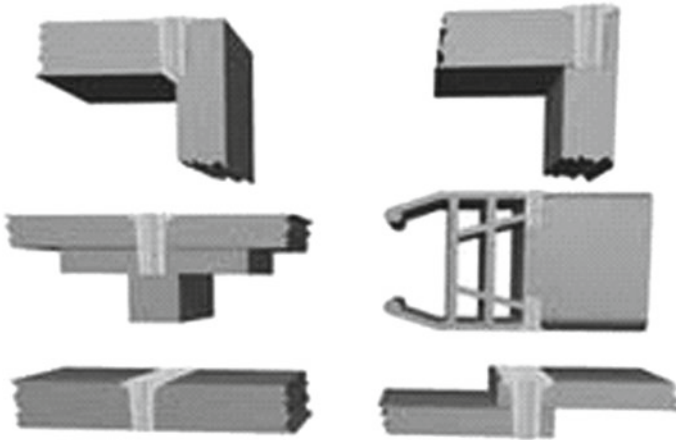
Fig. 3 Various joints by friction stir welding process

3.4 Experimental Review

AISI 1045 carbon steel and 3-mm-thick aluminum alloy A1100-H16 welded plates were welded [20, 21]. For welding purposes, AISI 4140 tool material steel with a cylindrical pin was used.

4 Friction Stir Welding of Similar and Dissimilar Materials

Recently, the focus has been on creating rapid, cost-effective procedures that make the area unit-friendly. The focus was turned on friction stir attachment as a link technology capable of delivering welds with no defects frequently associated with procedures of fusion attachment.

5 Conclusion

The present review has just given an introduction to FSW on aluminum alloys and how it works. The tool for FSW process must be designed taking into account numerous considerations such as material, surface quality, geometry of tools, tool and its design are the key parameters to meet the growing demands on the weld materials. A review of some previous works is done and what parameters are taken into account while analyzing the results when FSW technique used for aluminum alloys.

References

1. Sadeesh, P., Venkatesh Kannan, M., Rajkumar, V., Avinash, P., Arivazhagan, N., Devendranath Ramkumar, K., Narayanan, S.: Studies on friction stir welding of AA 2024 and AA 6061 dissimilar Metals. Procedia Eng. **75**, 145–149 (2014)
2. Muruganandam, D., Balasubramaniyan, C., Gokulachander, B.: Review paper on friction stir welding of aluminium and magnesium alloys. Indian J. Sci. Technol. **8**(35) (2015)
3. Sevvel, P, Jai Ganesh, V.: A detailed investigation on the role of different tool geometry in friction stir welding of various metals & their alloys. In: ICMMM 2014 August 8–9, 2014, IIT Madras, Chennai, India
4. Karimi, N., Nourouzi, S., Shakeri, M., Habibnia, M., Dehghani, A.: Effect of tool material and offset on friction stir welding of Al alloy to carbon steel. Adv. Mater. Res. **445**, 747–752 (2012)
5. Sajan, S.G., Meshram, M., Pankaj, P.S., Dey, S.R.: Friction Stir Welding of Aluminum 6082 with Mild Steel and its Joint Analyses. Int. J. Adv. Mater. Manufact. Charact. **3**. https://doi.org/10.11127/ijammc.2013.02.033. (March 2013)
6. Hussain, A.K, Quadri, S.A.P.: Evaluation of parameters of Friction Stir Welding For Aluminium Aa6351 Alloy. Int. J. Eng. Sci. Technol. **2**(10), 5977–5984 (2010)
7. Acerra, F., Buffa, G., Fratini, L., Troiano, G. On the FSW of AA2024-T4 and AA7075-T6 T-joints: an industrial case study. Int. J. Adv. Manuf. Technol. **48**, 1149–1157 (2010)
8. Buffa, G., Hua, J., Shivpuri, R., Fratini, L.: Design of the friction stir welding tool using the continuum based FEM model. Mater. Sci. Eng.: A **419**(1–2), 381–388 (2006)
9. Cavaliere, P., Cerri, E., Squillace, A.: Mechanical response of 2024–7075 aluminium alloys joined by Friction Stir Welding. J. Mater. Sci. **40**(14), 3669–3676 (2005)
10. Colegrove, P.A., Shercliff, H.R.: 3-Dimensional CFD modelling of flow round a threaded friction stir welding tool profile. J. Mater. Process. Technol. **169**, 320–327 (2005)
11. Da Silva, A.A.M., Arruti, E., Janeiro, G., Aldanondo, E., Alvarez, P., Echeverria, A.: Material flow and mechanical behavior of dissimilar AA2024-T3 and AA7075-T6 aluminium alloys friction stir welds. Mater. Des. **32**(4), 2021–2027 (2011)
12. Fratini, L., Buffa, G., Palmeri, D., Hua, J., Shivpuri, R.: Material flow in FSW of AA7075-T6 butt joints: numerical simulations and experimental verifications. Sci. Technol. Weld. Joining **11**, 413–421 (2006)
13. Khodir, S.A., Shibayanagi, T.: Friction stir welding of dissimilar AA2024 and AA7075 aluminium alloys. Mater. Sci. Eng.: B **148**(1–3), 82–87 (2008)
14. Mahoney, M., Rhodes, C., Flintoff, J., Bingel, W., Spurling, R.: Properties of friction-stir-welded 7075 T651 aluminium. Metall. Mater. Trans. A **29**(7), 1955–1964 (1998)
15. Rajakumar, S., Balasubramanian, V.: Establishing relationships between mechanical properties of aluminium alloys and optimized friction stir welding process parameters. Mater. Des. **40**(10), 17–35 (2012)
16. Rhodes, C.G., Mahoney, M. W., Bingel, W.H., Spurling, R.A., Bampton, C.C.: Effects of friction stir welding on microstructure of 7075 aluminium. Scripta Mater. **36**(1), 69–75 (1997)
17. Yan, J. and Reynolds, A. P. "Effect of initial base metal temper on mechanical properties in AA7050 friction stir welds", Science and Technology of Welding and Joining", Vol. 14, No. 4, pp. 282–287, 2009
18. Dawes, C.J., Thomas, W.M.: Friction stir process welds aluminum alloys. Weld. J. (3), 41–45 (1996)
19. Prado, R.A., Murr, L.E., Shindo, D.J., Soto, K.F.: Tool wear in the friction-stir welding of aluminum alloy 6061z20% Al_2O_3: a preliminary study. Scr. Mater. **45**(1), 75–80 (2001)
20. Fernandez, G.J., Murr, L.E.: Characterization of tool wear and weld optimization in the friction-stir welding of cast aluminum 359z20% SiC metal-matrix composite. Mater. Charact. **52**(1), 65–75 (2004)
21. Rodriguez, N.A., Almanza, E., Alvarez, C.J., Murr, L.E.: Study of friction stir welded A319 and A413 aluminum casting alloys. J. Mater. Sci. **40**(16), 4307–4312 (2005)

Pyrolysis System
for Environment-Friendly Conversion
of Plastic Waste into Fuel

S. N. Waghmare, S. D. Shelare, C. K. Tembhurkar, and S. B. Jawalekar

1 Introduction

The increase in plastic using up has been going on speedily since the last 5–6 decades because of lightweight and ability of plastic to form. Today, the principal interests are the requirement for energy and the degradation of the environment, which are because of expanding population and accelerated industrialization [1]. Actions are initiated to defeat the fossil fuel crisis by looking for options to replace gasoline and diesel. The development of alternative fuel technologies is created to give the alternative to fossil fuels [2]. The techniques focused are bioethanol, biodiesel, biodiesel derived from lipids, recycling the waste oils, pyrolysis, gasification, dimethyl ether, and biogas [3]. The use of plastic in a world was about 5 million tons annually in 1950s has enlarged to 20 times from about 100 million tons [4]. Currently, most plastic waste is disposed of in landfills or deposits, which involve our precious land spaces. The disposal methods, such as landfills, reuse, and combustion, can produce serious risks, particularly in human and environmental health [5]. Only a small percentage of plastic waste enters the reuse/recycling options, such as the use as a filler on asphalt roads or as a raw material for secondary product generation, such as recycled rubber, nonnatural barriers, or breakwaters [6].

Therefore, plastic waste can be deemed an energy resource. It has a sizeable calorific value, a high volatile content, and decreased ash content than coal and bio-ass [7]. Therefore, the residual plastic is the right suitor for the utilization of thermal elimination. These characteristics present it a perfect element for thermal processes like pyrolysis and gasification. Waste into the energy is designed to process potential materials into waste that are plastics, biomass, and rubber tires to oil [8]. The pyrolysis is growing as a substitute to give biofuel for compensation of the fossil fuel [9, 10]. Plastic waste is studied in the study as an accessible technology. The

S. N. Waghmare · S. D. Shelare (✉) · C. K. Tembhurkar · S. B. Jawalekar
Priyadarshini College of Engineering, Nagpur, MS 440019, India
e-mail: sagmech24@gmail.com

pre-treatment of the material is comfortable, as described in the article. The plastic is necessary to be classified and dried. Also, pyrolysis is neither toxic nor dangerous to an environment, unlike incineration [11]. Pyrolysis found enormously flexible procedure fit for large- and small-scale production [12].

2 Materials and Methods

2.1 Types of Plastics, Properties, and Its Uses

The different kinds of plastic have various features such as moisture content, heat resistant, chemical resistance, surface phenomenon, etc., which can be the prominent phenomenon for typical household uses [13]. The classification of plastic based on properties is listed in Table 1.

2.2 Principle of Pyrolysis

Pyrolysis is an endothermic process, an ecologically attractive method to treat plastic waste. The method practices average temperatures (300–700) °C and an oxygen-independent atmosphere for chemical decomposition of solid plastic waste into coal, oil, and gas, as per Fig. 3, which produces a minimal discharge of the nitrogen oxide and sulfur compared to incineration, the most popular method of industry [14]. Pyrolysis method consists of a collection of waste plastic, weighing and adding a waste plastic including catalyst into the reactor, pyrolysis of this waste plastic and collection, analyzing the extracted oil of a waste plastic [15]. The systematic flowchart of this process is presented within the Fig. 1.

The feedstocks utilized for the experiments were waste plastics having polyethylene terephthalate and high-density polyethylene and the same were obtained from the dumping place, and the little plastic recycling at Nagpur City, Maharashtra, India. The appearance of these feedstocks such as the collection of waste plastic, cleaning it, and shredding the waste plastics are shown in Fig. 2.

2.3 Experimentation on Pyrolysis Setup

Pyrolysis set-up as in Fig. 3 mainly comprises of reactor, GI coupling, GI pipe, condenser, water inlet, water outlet, RB flask, condenser, LPG gas cylinder, and iron stand.

The specification for material, top and bottom diameter, depth, volume, and weight of the reactor for pyrolysis setup is listed in Table 2.

Table 1 Plastic categorization depending upon properties and its uses

Type	Properties	General uses
1. Polyethylene terephthalate	Apparent, excellent gas properties, high heat resistance, hard, tough, microwave transparency, solvent resistant, unique moisture characteristics	Crystal liquid, fizzy liquid, and brew containers, pre-prepared meal platters and roasting cases, soft beverage and water containers, a string for clothes and carpetings, strapping, mouthwash bottles, shampoo bottles
2. Higher density polyethylene	Strong and semi-flexible, Perforable for gas, Smooth glassy cover, Superior chemical protection, HDPE films crinkle for touch	Surfactant, greenhouse fixtures, compost boxes, textile conditioning vessels, dolls, pots, thick pipes, roses containers, plastic timber, lunch box, drinks containers
3. Polyvinyl chloride	Excellent transparency, hard, rigid (flexible when plasticized), excellent drug immunity, extended time security, unique weathering capability, constant electrical characteristics, moderate vapor	ATM strips, carpeting lining, and different ground surfacing, windowpane and doorway frames, guttering, pipelines and fixtures, wiring, artificial skin goods
4. Low-density polyethylene	Robust and flexible, waxy surface, soft scratches quickly, good transparency, low melting point, stable electrical properties, excellent unique moisture characteristics	Films, fertilizers pockets, rejected pouches, packaging sheets, balloon cover, soft containers, watering troughs, compact purchasing handbags, wiring cord applications, any jar covers
5. Polypropylene	Hard and flexible, waxy surface, high melting point, translucent, sturdy	Larger-size bags/fabrics, bottle tips, bowls, short parcels, store containers, silages, joined food cases, refrigerated boxes, salsa and syrup bottles.
6. Polystyrene	Clear to the opaque, glassy surface, hard/foamed, brittle, great purity, influenced by lipids/solvents	Yogurt bowls, egg cases, ready meal dishes, video covers, trading containers including disposable cutlery, grain plates, clothes racks, low-cost brittle toys
7. Other	Other polymers have a broad scope to use, especially in manufacturing areas. These are recognized as number 7 and another	Multiple element-blended polymers, acrylonitrile butadiene styrene, nylon
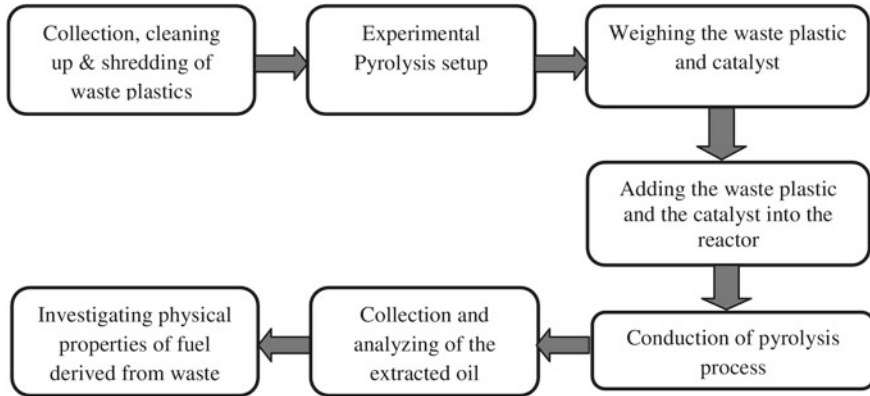
Fig. 1 Flowchart for pyrolysis process

Fig. 2 Typical pyrolysis process

In this process after the entire setup of pyrolysis was done, as it turned on and fired with the help of matchbox along with turning on the flow of cold water into a condenser and left for observation. The reactor gets consistently heated, which further raises a temperature of the reactor, causing the waste plastics to break and release vapors [16]. The air-packed manufacturing of reactor gives no leakage to the system and allows a vapor for flow through the outlet pipe, which then goes into the inner glass tube of the condenser [17, 18]. Meanwhile, the noncondensable vapors get out within the environment from the loosely tightened end of the condenser and the RB flask [19, 20]. The condensable vapor sticks to the inner wall of the tube and simultaneously forms droplets of oil as a result of heat exchanged with the cold water and get collected into the RB flask. After sometimes, it is seen that the flow of oil from the condenser stops, which shows that the number of plastics added into the reactor is pyrolyzed [21, 22]. Still to confirm that there are no leftover condensable vapors the reactor is heated for a few more minutes.
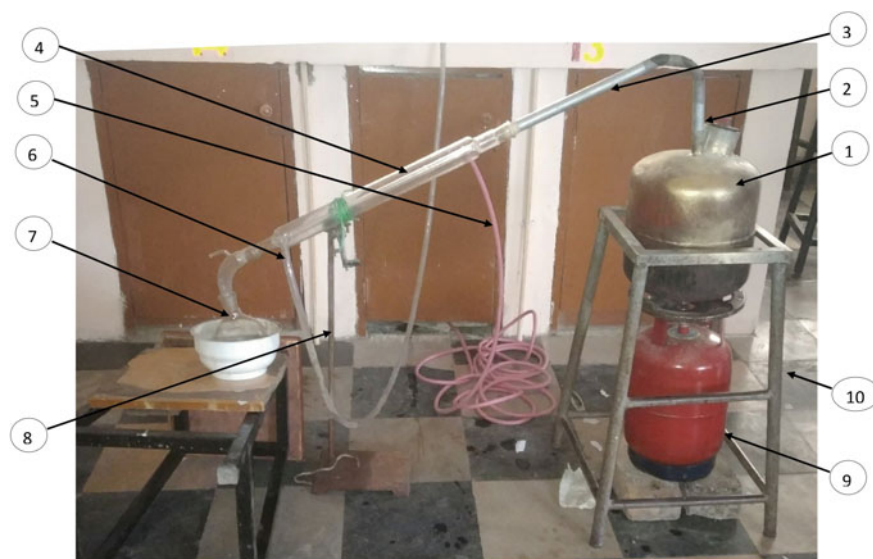
Fig. 3 Typical pyrolysis process, where 1—reactor, 2—GI coupling, 3—GI pipe, 4—condenser, 5—water inlet, 6—water outlet, 7—RB flask, 8—condenser, 9—LPG gas cylinder, and 10—iron stand

Table 2 Dimensions of different elements of the setup

S. No.	Particulars	Specification
1.	Material	Mild steel
2.	Top diameter	248 mm
3.	Bottom diameter	248 mm
4.	Depth	267.5 mm
5.	Volume	9 L (approx.)
6.	The diameter of the outlet GI pipe	15 mm
7.	The diameter of waste inlet GI coupling	59 mm
8.	Weight of reactor	5 kg

Subsequent cooling of reactor, remaining ash is there and plastic compressed like char, which needs to be separate using sieving. The char can be further utilized in road construction.

In the experimentation, 180–400 gm of the feedstock was supplied to a pyrolysis reactor. After this, pyrolyzer unit plus reformer was heated up to selected temperatures. Output obtained from a process in liquid form were got inside the RB flask

3 Results and Discussions

The amount of weight plastic 180 gm, 380 gm, 400 gm was tested for 1 h, 2 h, and 2 h 15 min, respectively. Amount of oil collected from waste plastic is, as presented in Table 3.

The amount of fuel getting collected in the RB flask and fuel collected at the end of the experimentation is as presented in Fig. 4.

Table 4 reflects the various properties of the liquid product for diesel grade.

Table 3 Observations during experimentations

Particulars	Observation stage		
	I	II	III
Weight of plastic waste	180 gm	380 gm	400 gm
Weight of catalyst (fly ash)	720 gm	1520 gm	1600 gm
Total time of heating	1 h	2 h	2 h, 15 min
Amount of oil collected	8 ml	25 ml	27 ml

(a)   (b)

Fig. 4 **a** Fuel getting collected in the RB flask, **b** Fuel collected at the end of the experiment

Table 4 Physical properties of fuel extracted

S. No.	Properties	Value
1.	Flashpoint	87 °C
2.	Density	800 kg/m^3
3.	Fire point	92 °C
4.	Calorific value	19 MJ/kg
5.	Viscosity	3.8 °C

4   Conclusions

The conclusions reached by experimentations are,

1. Pyrolysis method looks an efficient waste-to-energy converter which is considered reasonable to turn plastic into liquefied outputs and to enhance the waste plastics.
2. Pyrolysis could be carried under minimal expenses for small-scale waste plastic oil extraction, and 10–20 ml could be obtained by burning 180–380 gm of plastic.
3. Rather than direct burning of plastic into the atmosphere, converting into fuel decreases 80 percent of CO_2 emission in the atmosphere.
4. Fewer emissions of unburned hydrocarbons in plastic pyrolysis waste oil as comparing to diesel.
5. Obtained diesel oil or oil has better performance and, as compared, has 30–40% low production costs.
6. The waste plastic recycling will perform a crucial task in the transformation of a newer era.
7. The gas portion can be analyzed in the future with gas chromatography to know the contents of CO, CO_2, H_2, N_2, and others.

References

1. Syamsiro, M., Saptoadi, H., Norsujianto, T., Noviasri, P.: Fuel oil production from municipal plastic wastes in sequential pyrolysis and catalytic reforming reactors. Energy Procedia. **47**, 180–188 (2014)
2. Wong, S.L., Ngadi, N., Abdullah, T.A.T., Inuwa, I.M.: Current state and future prospects of plastic waste as source of fuel: a review. Renew. Sustain. Energy Rev. **50**, 1167–1180 (2015)
3. Dogan, O., Celik, M.B., Ozdalyan, B.: The effect of plastic derived fuel/diesel fuel blends utilization on diesel engine performance and emissions. Fuel **95**, 340–346 (2012)
4. UNEP. Converting waste plastics into resource: compendium of technologies. In: United Nations Environment Programme. Osaka (2009)
5. Siauw, H., Toc, C., Drive, O.P., Seoud, H., Stanciulescu, M.: Conversion of polyethylene to transportation fuels through pyrolysis and catalytic cracking, 30–33 (1995)
6. Kunwar, B., Cheng, H.N., Chandrashekaran, S.R., Sharma, B.K.: Plastics to fuel: a review. **54**, 421–428 (2016)
7. Al-Salem, S.M., Lettieri, P., Baeyens, J.: The valorization of plastic solid waste (PSW) by primary to quaternary routes: from re-use to energy and chemicals. Prog. Energy Combust. Sci. **36**(1), 103–129 (2010). https://doi.org/10.1016/j.pecs.2009.09.001
8. Murugan, S., Ramaswamy, M., Nagaranian, G.: The use of tyre pyrolysis oil in diesel engines. Waste Manag. **28**(12), 2743–2749 (2008)
9. Williams, P.T.: Pyrolysis of waste tyres: a review. Waste Manag. **33**(8), 1714–1728 (2013)

10. Leung, D., Wang, C.: Fluidized-bed gasification of waste plastic powders. Fuel Process. Technol. **84**(1–3), 175–196 (2003)
11. Bernardo, M., Lapa, N., Goncalves, M.: Toxicity of char residues produced in the co-pyrolysis of different wastes. Waste Manage. **30**, 628–635 (2010)
12. Chenier, P.J.: Survey of Industrial Chemistry, 3rd edn. Kluwer Academic/Plenum Publishers, New York (2002)
13. Thorat, P.V, Warulkar, S., Sathone, H.: Thermofuel—pyrolysis of waste plastic to produce liquid hydrocarbons. **3**, 14–18 (2013)
14. Karatas, H., Olgun, H., Engin, B., Akgun, F.: Experimental results of gasification of waste plastic with air in a bubbling fluidized bed gasifier. Fuel **105**, 566–571 (2013)
15. Nahid, M., Hamid, H.: Catalytic coprocessing of waste plastics and petroleum residue into liquid fuel oils. J. Anal. Appl. Pyrol. **86**, 141–147 (2009)
16. Portofino, S., Donatelli, A., Iovane, P., Innella, C., Civita, R., Martino, M., Matera, D.A., Russo, A., Cornacchina, G., Galvango, S.: Steam gasification of waste tyre: influence of process temperature on yield and product composition. Waste Manag **33**(3), 672–678 (2013)
17. Evans, A., Evans, R.: The composition of a plastic: typical components. The Waste Resour. Act. Programme, Banbury (2006)
18. Betancur, M., Martinez, J.D., Murillo, R.: Production of activated carbon by waste plastic thermochemical degradation with CO_2. J. Hazard. Mater. **168**(2–3), 882–887 (2009)
19. Malkow, T.: Novel and innovative pyrolysis and gasification technologies for energy efficient and environmentally sound MSW disposal. Waste Manag. **24**(1), 53–79 (2004)
20. Galvango, S., Casciaro, G., Casu, S., Martino, M., Mingazzini, C., Russo, A., Portofino, S.: Steam gasification of tyre waste, poplar, and refuse-derived fuel: a comparative analysis. Waste Manag. **2**, 678–689 (2009)
21. Islam, M.R., Tushar, M., Haniu, H.: Production of liquid fuels and chemicals from pyrolysis of Bangladeshi bicycle/rickshaw plastic wastes. J. Anal. Appl. Pyrol. **82**(1) (2008)
22. Murugan, S., Ramaswamy, M., Nagarajan, G.: A comparative study on the performance, emission and combustion studies of a DI diesel engine using distilled tyre pyrolysis oil-diesel blends. Fuel **87**(10–11), 2111–2121 (2008)

Experimental Investigation of Surface Integrity and Machining Characteristics of Ti–6Al–4V Alloy Machined by Wire-EDM Process

Sandeep Malik and Vineet Singla

1 Introduction

Titanium–Aluminium–Vanadium-based biomedical alloy (Ti–6Al–4V) was widely and commercially used biomaterial for medical applications like development of implants, screws, and plates, etc., owing to its desirable biocompatibility and excellent physiomechanical properties [1]. This particular grade of titanium (Ti) has been regarded as "wonder metal" as it possesses very low density and its strength could be enhanced, enormously, by using different types of alloying elements, which include tin, aluminum, chromium, manganese, vanadium, and molybdenum, etc. [2]. However, it has been classified as the "hard-to-cut" category of the materials, which means it is extremely difficult to machine Ti as results of its low thermal conductivity, elastic modulus, and high chemical reactivity [3]. The limited thermal conductivity of Ti restricts the distribution of the heat from the machining interface and causes high tool abrasive, adhesive, and diffusive wear mechanisms which further lead to catastrophic tool failures.

Likewise, during machining the obtainable surface finish is degraded by a small degree of elastic modulus. In addition, high chemical reactivity, especially at high temperatures, increases the adhesion between the tool and the workpiece and results in the cutting tool's wear/failure [4, 5]. Therefore, it has been observed that the efficacy of conventional machining methods for processing Ti alloys is marginal and, further, the potential of nonconventional machining methods, such as electric discharge machining (EDM), ultrasonic machining, magnetic abrasive machining, etc., could be explored. Reportedly, in case of EDM process, the material removal mechanism is governed by the rapid and repetitive spark discharges across the gap between electrode and workpiece [6]. Basically, EDM is a process of electrothermal machining that produces a large number of electrical sparks in a fraction of seconds,

S. Malik (✉) · V. Singla
Department of Mechanical Engineering, UIET, Maharshi Dayanand University, Rohtak, Haryana, India
e-mail: sandymalik0077@gmail.com

resulting in intense heat energy that is sufficient to remove the working material [7]. In addition, EDM could be used for electrically conductive materials irrespective of their hardness and strength. Prakash et al. have highlighted the potential of machining Ti-based alloy by using EDM process, for biomedical applications [8]. Previous investigations reported that EDM modifies the surface of Ti–6Al–4V alloy in order to yield a biocompatible coating of nanohydrides [9]. This is, in fact, mainly due to the electrothermal nature of the EDM system, the simultaneous action of thermal energy generation and process cycle quenching [10]. It affects the process and a variety of morphological disorders are usually developed on the machined surface, such as surface roughness, cracks, and pit/dimples that deteriorate the surface value [11, 12]. However, during the actual work scenario, the resulted morphological defects degrade the corrosion performance [13], and fatigue performance [14] of biomedical device.

Therefore, in order to overcome the above-mentioned disorders, number of advancements in EDM process has been suggested in the literature, such as wire-cut EDM [15], vibration assistance during EDM [16], rotational EDM [17], HyFlex[TM] EDM [18], coating of EDM tool [19], dry EDM [20], and powder mixed slurry EDM [21–28]. Rahman et al. outlined the morphological, chemical, and crystallographic characteristics of recast layer on wire-cut EDM processed Ti–6Al–4V alloy [29]. Kuriachen et al. studied tribological performance of wire-cut EDM surface and found an increase in the oxide layer formation that improved the tribological properties [30]. Similarly, other studies emphasized on the machining of magnesium (Mg) alloys by wire-cut EDM process [31, 32]. Wire-cut EDM showed excellent attributes toward the cell viability [33, 34].

Overall, it has been reviewed that a very limited research studies have been reported on machining/cutting of microholes in Ti–6Al–4V alloy, focusing biomedical applications. So, the scope of machining of Ti–6Al–4V alloy and investigating the obtainable surface and machining characteristics is huge with regards to wire-cut EDM process. The present study is focused perform an investigation onto the effect of wire-cut EDM (W-EDM) process parameters in response of the surface morphology, surface chemistry, and machining characteristics.

2 Materials and Method

The workpiece material is Ti–6Al–4V alloy as rectangular plate with dimensions as 15 mm × 10 mm × 50 mm. Experiments were performed using an Electronoca wire-electrical discharge machine (W-EDM) as shown in Fig. 1. Distilled water was used as the dielectric fluid in this experiment. The material removal rate (MRR) was calculated for all the included experimental runs, as suggested by design of experimentation, by observing the average amount of material removed with respect to the incurred cutting time. Further, surface roughness (SR) of the machined work samples has been recorded by using surface roughness tester (Talysurf: Mitutoyo). The selected input process parameters and their levels are given in Table 1.

Fig. 1 Schematic representation of WEDM machine

Table 1 Process parameters and their levels

Process parameters	Units	Parameter designation	Levels		
			L-1	L-2	L-3
Peak current	amp	I_p	80	120	160
Pulse duration	μs	T_{on}	100	150	200
Pulse interval	μs	T_{off}	50	100	150
Wire feed	mm/s	Wf	6	8	10

Taguchi-based design of experimental (DOE) technique is used to get information about interaction and main effects of parameters for experiments. The main objective of Taguchi design is to get best possible results with minimum variation. The statically design of the experimentation, design of experiment (DOE), has

been proved for providing best combination of the input parametric levels at minimum cost and time consumption. MINITAB-16-based statistical software package, as commercially available, has been employed for managing the raw data and to covert the same into responses, signal/noise (S/N) plots, and interaction plots. Here, MRR and SR have been processed at "larger the better" and "smaller the better" settings. The observed results in accordance of Taguchi L-27 orthogonal array are shown in Table 2.

3   Results and Discussion

3.1   Analysis of MRR

From Fig. 2, it has been seen that the MRR increased with peak current (I_p), mainly because of the fact that at higher level of I_p a large amount of heat is enlightened at the cutting interface and finally traveled into the workpiece. Owing to this, the size and shape of pits/craters on the machined surface increased, and finally affected the MRR. Specifically, the MRR value increased from 1.82 to 2.3 mm³/min as the level of the I_p increased from 80 to 160 A. Further, it has been observed that the MRR value also increased with the pulse duration. This is because of the proportionality of discharge energy and pulse duration that helped machining process in enlarging the craters [21]. In this case, the MRR value enhanced from 1.85 to 2.35 mm³/min as the pulse duration increased from 100 to 200 μs. The MRR value increased from 1.75 to 2.27 mm³/min, when pulse interval increased from 25 to 75 μs. The MRR deceases with wire feed and increased with gap voltage. These two parameters have a very lesst effect on the MRR. Figure 3 shows the effect of interactions of parameters on MRR. It can be clearly seen that interaction of parameters has large and high impact on the MRR. The MRR increased in higher proposition when peak current increased combination with pulse duration and pulse interval.

Overall, the best parametric setting suggested by Taguchi is peak current (A3), pulse duration (B3), duty cycle (C3), and spark gap (E3), and low value of wire feed rate (D1). Table 3, analysis of variance (ANOVA), highlighted that the peek current, pulse-on, and pulse-off time have a significant contribution toward increasing the MRR.

3.2   Analysis of SR

From the Fig. 4, It was noticed that the SR increased with peak current (I_p), as when the I_p was increased, an immense amount of heat was illuminated and sunk into the workpiece. As a result, on the regenerated layer, the pits/craters increased, which increased the SR further. The pulse duration increased the SR value. This may be

Table 2 Process parameters and their levels

| Sr. no. | I_p | T_{on} | T_{off} | F_d | V | Mean | | S/N ratio | |
						MRR	SR	MRR	SR
1	80	100	50	6	25	1.240	0.890	1.868	1.013
2	80	100	100	8	50	1.760	1.029	4.910	−0.251
3	80	100	150	10	75	2.286	1.155	7.182	−1.250
4	80	150	50	8	75	1.734	0.998	4.781	0.017
5	80	150	100	10	25	2.000	1.079	6.021	−0.661
6	80	150	150	6	50	1.780	1.022	5.008	−0.186
7	80	200	50	10	50	1.874	1.059	5.455	−0.500
8	80	200	100	6	75	1.314	0.910	2.372	0.822
9	80	200	150	8	25	2.274	1.166	7.136	−1.337
10	120	100	50	6	25	1.240	0.873	1.868	1.179
11	120	100	100	8	50	2.514	1.198	8.007	−1.568
12	120	100	150	10	75	1.874	1.063	5.455	−0.529
13	120	150	50	8	75	1.894	1.044	5.548	−0.375
14	120	150	100	10	25	2.760	1.262	8.818	−2.019
15	120	150	150	6	50	1.834	1.046	5.268	−0.388
16	120	200	50	10	50	1.906	1.059	5.602	−0.495
17	120	200	100	6	75	2.726	1.342	8.711	−2.555
18	120	200	150	8	25	2.660	1.280	8.498	−2.147
19	160	100	50	6	25	2.146	1.124	6.633	−1.012
20	160	100	100	8	50	1.560	0.957	3.862	0.380

Table 2 (continued)

Sr. no.	I_p	T_{on}	T_{off}	F_d	V	Mean		S/N ratio	
						MRR	SR	MRR	SR
21	160	100	150	10	75	1.914	1.060	5.639	−0.507
22	160	150	50	8	75	1.714	0.998	4.680	0.017
23	160	150	100	10	25	1.714	0.994	4.680	0.054
24	160	150	150	6	50	3.274	1.434	10.302	−3.133
25	160	200	50	10	50	2.074	1.114	6.336	−0.935
26	160	200	100	6	75	3.526	1.446	10.946	−3.201
27	160	200	150	8	25	2.394	1.202	7.582	−1.598
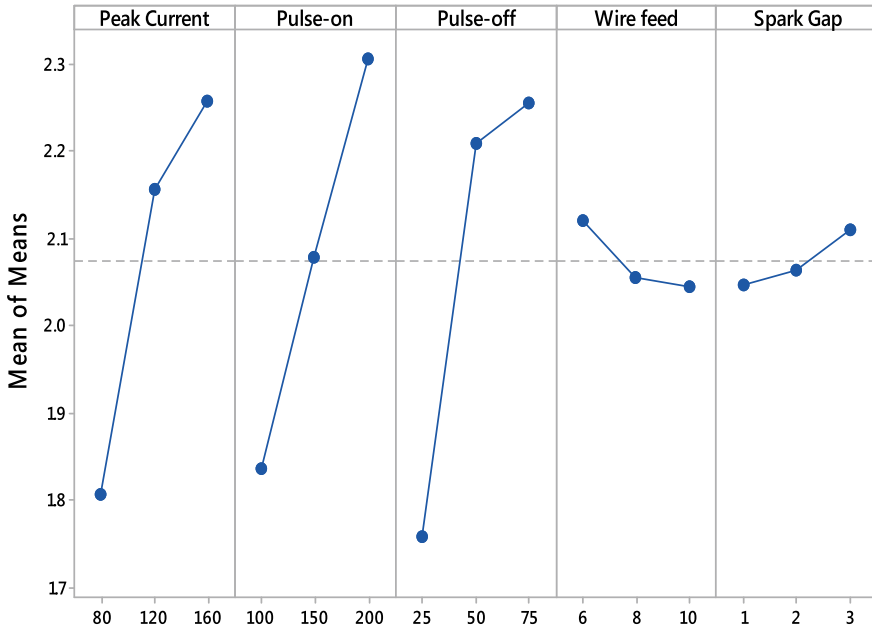
Fig. 2 Main effects plot of MRR

because discharge energy is a pulse duration feature that increases crater depth and width [21]. It is recorded that the SR value grew from 1,027 to 1,178 µm as the length of the pulse increased from 100 to 200 µs. The SR increases with the pulse interval because the discharge debris had sufficient time to flush out the machining with the increase in the pulse interval zone. The SR deceases with wire feed and increased with gap voltage. These two parameters have very least effect on the SR. Figure 5 shows the effect of interactions of parameters on SR. It can be clearly seen that interaction of parameters has large and high impact on the SR. The SR increased in higher proposition when peak current increased combination with pulse duration and pulse interval. The best parametric setting suggested by Taguchi is peak current (A3), pulse duration (B3), duty cycle (C3), spark gap (E1), wire feed rate (D3). Table 4 highlighted that all the input process parameters, in case of SR, have significant contribution toward increasing the SR except wire feed and spark gap. These two parameters were, therefore, pooled form the analysis.

3.3 Surface Morphology Analysis

Machined surface morphology investigation was conducted to evaluate the surface quality obtained through the WEDM process. Three samples were chosen for machined surface morphology investigation (Sample at low peak current, sample at
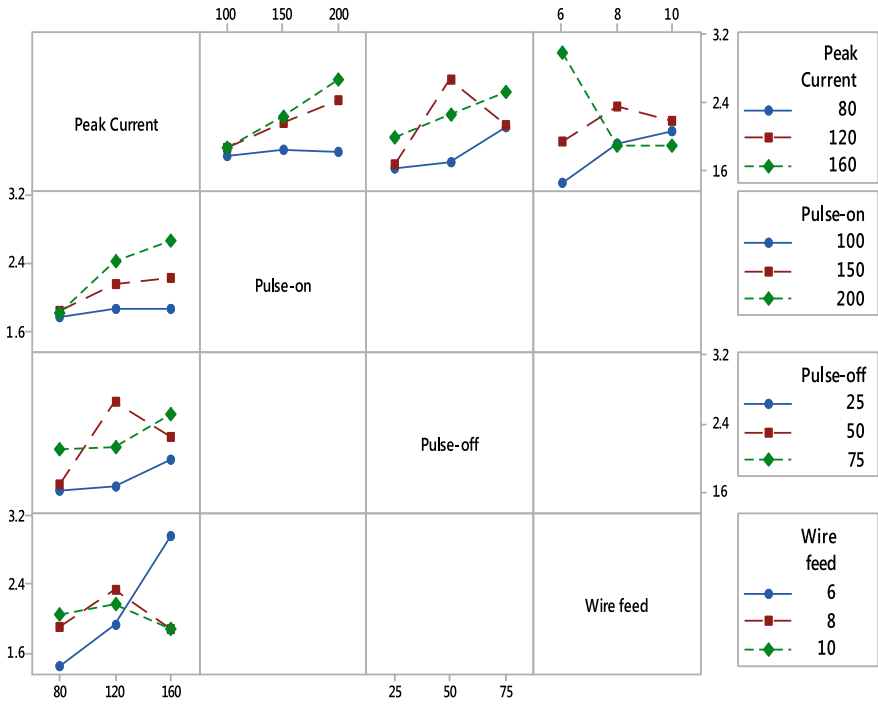
Fig. 3 Interaction effects plot of MRR

Table 3 Analysis of variance for MRR

Source	DF	Seq-SS	Adj-SS	Adj-MS	F	P	%
Peak current	2	1.006	1.006	0.503	12.640	0.019	0.123
Pulse-on	2	0.987	0.987	0.493	12.400	0.019	0.120
Pulse-off	2	1.354	1.354	0.677	17.010	0.011	0.165
Wire feed	2	0.030	0.030	0.015	0.370	0.710	0.004
Spark gap	2	0.018	0.018	0.009	0.230	0.805	0.002
Peak current*Pulse-on	4	0.426	0.426	0.107	2.680	0.182	0.052
Peak current*pulse-off	4	0.996	0.996	0.249	6.260	0.042	0.121
Peak current*wire feed	4	3.220	3.220	0.805	20.230	0.006	0.393
Residual error	4	0.159	0.159	0.040			0.019
Total	26	8.196					

* mean "x" (Multiplication)
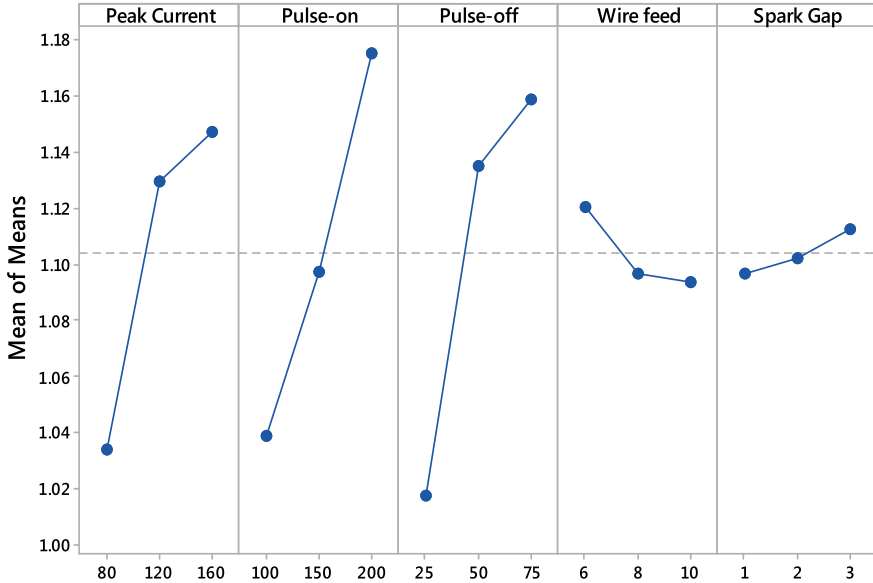
Fig. 4 Main effects plot of SR
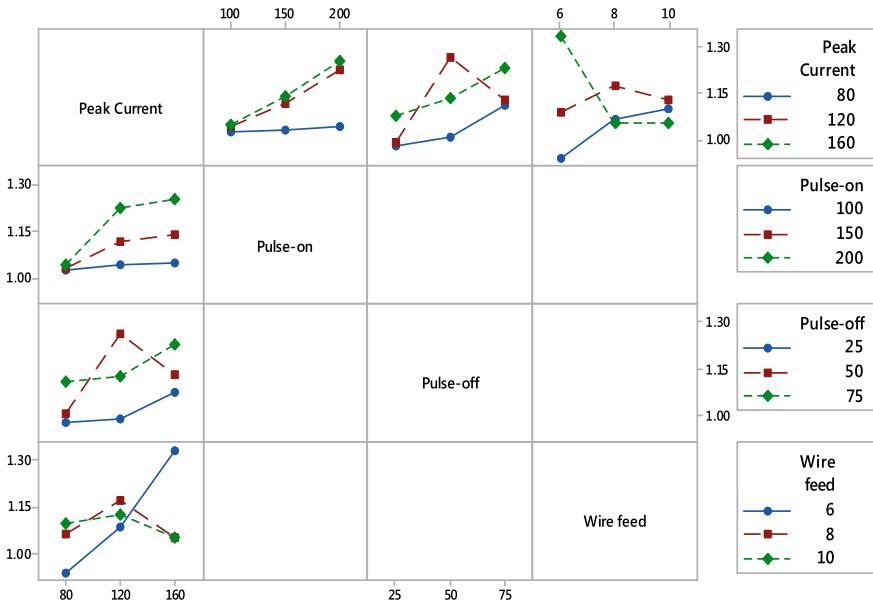
Fig. 5 Interaction effects plot of SR

Table 4 Analysis of variance for SR

Source	DF	Seq-SS	Adj-SS	Adj-MS	F	P	%
Peak current	2	1.006	1.006	0.503	12.640	0.019	0.123
Pulse-on	2	0.987	0.987	0.493	12.400	0.019	0.120
Pulse-off	2	1.354	1.354	0.677	17.010	0.011	0.165
Wire feed	2	0.030	0.030	0.015	0.370	0.710	0.004
Spark gap	2	0.018	0.018	0.009	0.230	0.805	0.002
Peak current*pulse-on	4	0.426	0.426	0.107	2.680	0.182	0.052
Peak current*pulse-off	4	0.996	0.996	0.249	6.260	0.052	0.121
Peak current*wire feed	4	3.220	3.220	0.805	20.230	0.006	0.393
Residual error	4	0.159	0.159	0.040			0.019
Total	26	8.196					

* mean "x" (Multiplication)

moderate peak current, and sample at high peak current). It can be clearly seen that at low peak current (80 A), the surface was very smooth and low degree of craters were found. Only scares during cutting due to wire travel were observed, as can be seen in Fig. 6a. The associated EDS spectrum of machined surface presents the significant availability of base material elements along with high content on oxygen (O) element, as can be seen in Fig. 6b. The element O reacts with Ti and formed rutile TiO_2, which is beneficial for the corrosion resistance and bioactivity. When the peak current was increased to 120 A, the machined surface become rough and craters were observed on the surface, as can be seen in Fig. 6c. The associated EDS spectrum of machined surface presents the significant availability of base material elements along with high content on oxygen (O) element, as can be seen in Fig. 6d. When the peak current was increased to 160 A, highly rough surface was observed. Deep and wide craters were formed on the machined surface results in poor surface finish and surface quality, as can be seen in Fig. 6e. The associated EDS spectrum of machined surface presents the significant availability of base material elements along with high content on oxygen (O) element, as can be seen in Fig. 6f. As the peak current increased the O content in the machined surface morphology increased, which increased the formation of formed rutile TiO_2. Thus results in good surface quality in terms of bioactivity.

4 Conclusions

Following conclusions could be drawn from this investigation:
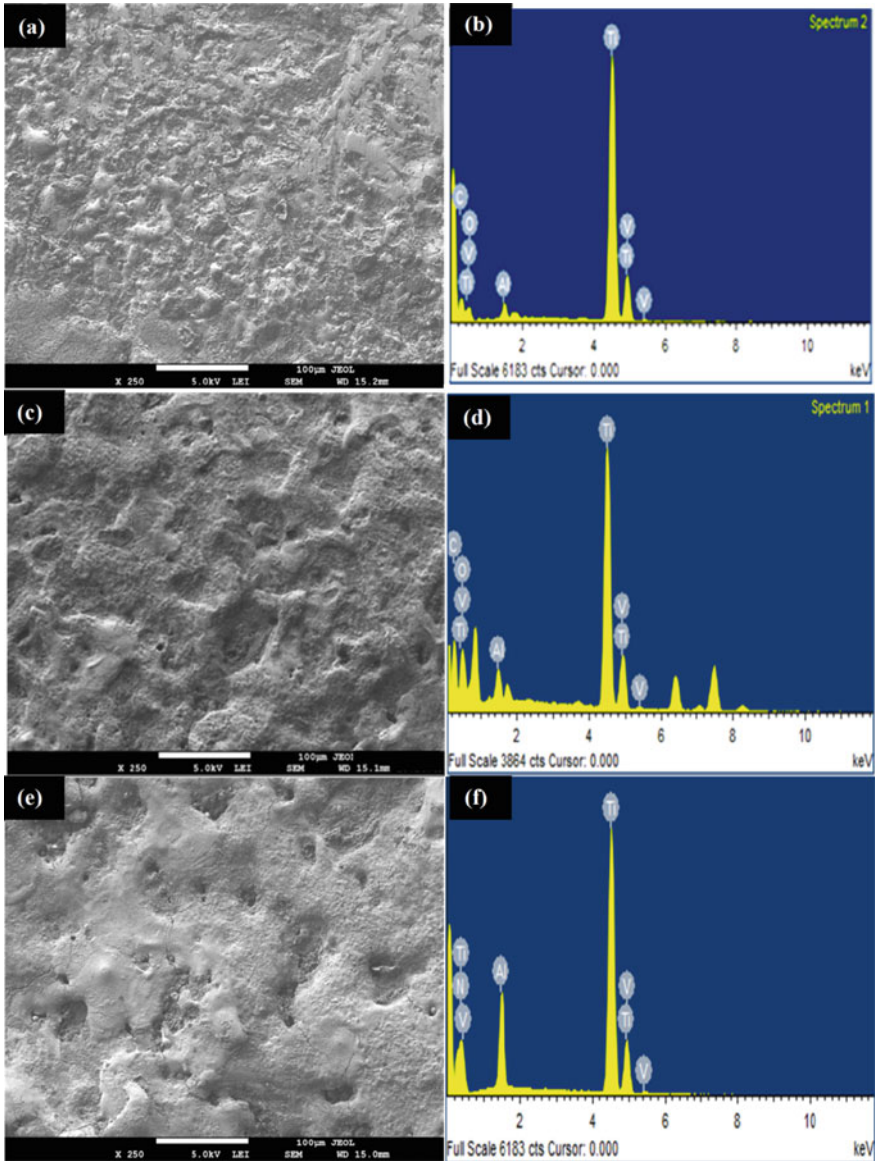
Fig. 6 Surface morphology of Ti–6Al–4V alloy by W-EDM process at different peak current levels: **a** 80 A, **b** 120 A, and **c** 180 A

- From the Taguchi-based design of experimentation, it has been found that peak current, pulse-on and pulse-off times have significantly affected the obtained MRR and SR results. In case of MRR, the optimized process parametric setting is A3, B3, C3, D1, and E3. The maximum MRR was obtained 3.69 mm^3/min, whereas in case of SR, the optimized process parametric setting is A1, B1, C1, D3, and E1. The maximum SR was obtained 1.02 μm.
- The machined surface morphology depicts that rutile TiO$_2$ were formed, which is beneficial to enhance the corrosion resistance and bioactivity of implant.
- From the present investigations, it can be concluded that W-EDM can be used as potential nonconventional machining/cutting technique to implants processing.

References

1. T Zaman, H.A., Safian, S., Idris, M.H., Kamarudin, A.: Metallic biomaterial for medical implant applications: a review. Appl. Mech. Mater. **735**, 19–25 (2015). www.scientific.net/AMM.735.19
2. Niinomi, M., Narushima, T., Naka, M. Advances in Metallic Biomaterials, p. 348. Springer Berlin Heidelberg, Berlin, Germany (2015)
3. Pramanik, A.: Problems and solutions in machining of titanium alloys. Int. J. Adv. Manuf. Technol. **70**(5), 919–928 (2014). https://doi.org/10.1007/s00170-013-5326-x
4. Klocke, F., Zeis, M., Klink, A., Veselovac, D.: Technological and economical comparison of roughing strategies via milling, EDM and ECM for titanium-and nickel-based blisks. Procedia CIRP **2**(1), 98–101 (2012). https://doi.org/10.1016/j.cirpj.2013.02.008
5. Andrew Y.C. Nee.: Handbook of Manufacturing Engineering and Technology, 3485 pp. Springer, London (2015)
6. Kumar, S.; Singh, R.; Batish, A,; Singh, T.P. Electric discharge machining of titanium and its alloys: a review. Int. J. Mach. Mach. Mater. **11**(1), 84–111 (2012). https://doi.org/10.1504/ijmmm.2012.044922
7. Prakash, C., Kansal, H.K., Pabla, B.S., Puri, S.: Experimental investigations in powder mixed electric discharge machining of Ti–35Nb–7Ta–5Zrβ-titanium alloy. Mater. Manuf. Processes **32**(3), 274–285 (2017)
8. Prakash, C., Kansal, H.K., Pabla, B.S., Puri, S., Aggarwal, A.: Electric discharge machining—a potential choice for surface modification of metallic implants for orthopedic applications: A review. Proc. Inst. Mech. Eng. Part B: J. Eng. Manuf. **230**(2), 331–353 (2016)
9. Peng, P.W., Ou, K.L., Lin, H.C., Pan, Y.N., Wang, C.H.: Effect of electrical-discharging on formation of nanoporous biocompatible layer on titanium. J. Alloy. Compd. **492**(1–2), 625–630 (2010). https://doi.org/10.1016/j.jallcom.2009.11.197
10. Yang, T.S., Huang, M.S., Wang, M.S., Lin, M.H., Tsai, M.Y., Wang, P.Y.: Effect of electrical discharging on formation of nanoporous biocompatible layer on Ti-6Al-4V alloys. Implant dentistry **22**(4), 374–379 (2013). https://doi.org/10.1097/ID.0b013e31829a170a
11. Bin, T.C., Xin, L.D., Zhan, W., Yang, G.: Electro-spark alloying using graphite electrode on titanium alloy surface for biomedical applications. Appl. Surf. Sci. **257**(15), 6364–6371 (2011). https://doi.org/10.1016/j.apsusc.2011.01.120
12. Harcuba, P., Bačakova, L., Strasky, J., Bačakova, M., Novotna, K., Janeček, M.: Surface treatment by electric discharge machining of Ti–6Al–4V alloy for potential application in orthopaedics. J. Mech. Behav. Biomed. Mater. **7**, 96–105 (2012). https://doi.org/10.1016/j.jmbbm.2011.07.001

13. Janecek, M., Novy, F., Strasky, J., Harcuba, P., Wagner, L.: Fatigue endurance of Ti-6Al-4V alloy with electro-eroded surface for improved bone in-growth. J. Mech. Behav. Biomed. Mater. **4**, 417–422 (2011). https://doi.org/10.1016/j.jmbbm.2010.12.001

14. Strasky, J., Janecek, M., Harcuba, P., et al.: The effect of microstructure on fatigue performance of Ti–6Al–4V alloy after EDM surface treatment for application in orthopaedics. J. Mech. Behav. Biomed. Mater. **4**, 1955–1962 (2011). https://doi.org/10.1016/j.jmbbm.2011.06.012

15. Goswami, A., Kumar, J.: Optimization in wire-cut EDM of nimonic-80A using Taguchi's approach and utility concept. Eng. Sci. Technol. Int. J. **17**(4), 236–246 (2014)

16. Shabgard, M.R., Alenabi, H.: Ultrasonic assisted electrical discharge machining of Ti–6Al–4V alloy. Mater. Manuf. Processes **30**(8), 991–1000 (2015). https://doi.org/10.1080/10426914.2015.1004686

17. Dwivedi, A.P., Choudhury, S.K.: Effect of tool rotation on MRR, TWR and surface integrity of AISI-D3 steel using rotary EDM process. Mater. Manuf. Processes (2016). https://doi.org/10.1080/10426914.2016.1140198

18. Pirani, C., Iacono, F., Generali, L., Sassatelli, P., Nucci, C., Lusvarghi, L., Gandolfi, M.G., Prati, C.: HyFlex EDM: superficial features, metallurgical analysis and fatigue resistance of innovative electro discharge machined NiTi rotary instruments. Int. Endod. J. (2015). https://doi.org/10.1111/iej.12470

19. Krishna, M.E., Patowari, P.K.: Parametric study of electric discharge coating using powder metallurgical green compact electrodes. Mater. Manuf. Processes **29**(9), 1131–1138 (2014). https://doi.org/10.1080/10426914.2014.930887

20. Dhakar, K., Dvivedi, A.: Parametric Evaluation on near-dry electric discharge machining. Mater. Manuf. Processes **31**(4), 413–421 (2016)

21. Prakash, C., Kansal, H.K., Pabla, B.S., Puri, S.: Processing and characterization of novel biomimetic nanoporous bioceramic surface on β-Ti implant by powder mixed electric discharge machining. J. Mater. Eng. Perform. (2015). https://doi.org/10.1007/s11665-015-1619-6

22. Chander Prakash, Sunpreet Singh, Pabla, B.S.: Multi-objective optimization of EDM parameters to deposit HA-containing coating on Mg–Zn–Mn alloy using particle swarm optimization. Vacuum **158**, 180–190 (2018)

23. Chander Prakash, Sunpreet Singh, Pabla, B.S., Uddin, M.S.: Synthesis, characterization, corrosion and bioactivity investigation of nano-HA coating deposited on biodegradable Mg–Zn–Mn alloy. Sur. Coat. Technol. **346**, 9–18 (2018)

24. Chander Prakash and M. S. Uddin, "Surface modification of β-phase Ti implant by hydroxyapatite mixed electric discharge machining to enhance the corrosion resistance and in-vitro bioactivity. Surf. Coat. Technol. Part A **236**, 134–145 (2017)

25. Chander Prakash, Kansal, H.K., Pabla, B.S., Sanjeev Puri: Effect of surface nano-porosities fabricated by powder mixed electric discharge machining on bone-implant interface: an experimental and finite element study. Nanosci. Nanotechnol. Lett. **8**(10), 815–826 (2016). https://doi.org/10.1166/nnl.2016.2255

26. Chander Prakash, Kansal, H.K., Pabla, B.S., Sanjeev Puri: Multi-objective optimization of powder mixed electric discharge machining parameters for fabrication of biocompatible layer on β-Ti alloy using NSGA-II coupled with Taguchi based response surface methodology. J. Mech. Sci. Technol. **30**(9), 4195–4204 (2016). https://doi.org/10.1007/s12206-016-0831-0

27. Chander Prakash, H.K. Kansal, B.S. Pabla, and Sanjeev Puri: Powder mixed electric discharge machining an innovative surface modification technique to enhance fatigue performance and bioactivity of β-Ti implant for orthopaedics application. J. Comput. Inf. Sci. Eng. **14**(4), 1–9, 2016. https://doi.org/10.1115/1.4033901

28. Chander Prakash, H.K. Kansal, B.S., Sanjeev Puri: Potential of powder mixed electric discharge machining to enhance the wear and tribological performance of β-Ti implant for orthopedic applications. J. Nanoeng. Nanomanuf. **5**(4), 261–269 (2015)

29. Kuriachen, B., Lijesh, K.P. and Kuppan, P.: Multi response optimization and experimental investigations into the impact of wire EDM on the tribological properties of Ti–Al–4V. Trans. Indian Inst. Met., 1–11 (2018)

30. Rahman, S.S., Ashraf, M.Z.I., Bashar, M.S., Kamruzzaman, M., Amin, A.N., Hossain, M.M.: Crystallinity, surface morphology, and chemical composition of the recast layer and rutile-TiO_2 formation on Ti–6Al–4V ELI by wire-EDM to enhance biocompatibility. Int. J. Adv. Manuf. Technol. **93**(9–12), 3285–3296 (2017)
31. Klocke, F., Schwade, M., Klink, A., Kopp, A.: EDM machining capabilities of magnesium (Mg) alloy WE43 for medical applications. Procedia Eng. **19**, 190–195 (2011). https://doi.org/10.1016/j.proeng.2011.11.100
32. Razak, M.A., Abdul-Rani, A.M.; Rao, T.V.V.L.N., Pedapati, S.R., Kamal, S.: Electrical discharge machining on biodegradable AZ31 magnesium alloy using taguchi method. Procedia Eng. **148**, 916–922 (2016). https://doi.org/10.1016/j.proeng.2016.06.501
33. Klocke, F., Schwade, M., Klink, A., Kopp, A.: Influence of electro discharge machining of biodegradable magnesium on the biocompatibility. Procedia CIRP **5**, 88–93 (2013). https://doi.org/10.1016/j.procir.2013.01.018
34. Ponappa, K., Aravindan, S., Rao, P.V., Ramkumar, J., Gupta, M.: The effect of process parameters on machining of magnesium nano alumina composites through EDM. Int. J. Adv. Manuf. Technol. **46**, 1035–1042 (2010). https://doi.org/10.1007/s00170-009-2158-9

Effect of Hard Chromium Coating on the Frictional Behavior of Piston Ring Material

Vipin Kumar Sharma, Vinayak Goel, and Mudit Shukla

1 Introduction

Low coefficient of friction, high melting point, high hardness, and resistance to wear and corrosion are some of the main properties which are required for the heavy-duty work. To achieve these, the coating of some elements is deposited on the components. Hard chromium coating has a wide application in the automotive and aerospace industry. The hard chromium coating is applied to the components which are used in the extreme operating conditions. The assembly of the piston and cylinder is such an assembly where the piston rings and cylinder walls are subjected to high-pressure and -temperature conditions. This makes the understanding of the hard chromium coating in these conditions as of great importance.

The mechanical behavior of hard chromium-coated stainless steel was evaluated by Almotairi et al. [1]. Excellent bonding between the chromium and steel was reported by the authors. With the increase in the thickness of the chromium coating, the residual stress induced in the steel specimens also gets increased which signifies more inherent crack generation capacity. The single and duplex layers of hard chromium coatings on mild steel substrate with the help of direct current and pulse current electroplating process. A detailed analysis of the corrosion resistance of the coating revealed that pulse current electroplated specimens resulted better as compared to the direct current electroplated coating in salt spray corrosion tests. However, direct current electroplated coating yielded better microhardness [2]. The generation of toxic fumes during the electroplating of the hard chromium coating on the components is a big concern in its usage. High-velocity oxy-fuel coating represents a possible alternative to the electroplating process. Picas et al. used the HVOF coating technique to deposit CrC75 (NiCr25) 25 coatings on the pistons rings and valve stems [3]. The hard chrome coating also has wide applications in the field of

V. K. Sharma · V. Goel (✉) · M. Shukla
Department of Mechanical and Automation Engineering, Maharaja Agrasen Institute of
Technology, Rohini, Delhi 110086, India
e-mail: vinayakgoel11@gmail.com

tool materials. The effects of chromium coating on the wear and friction behavior of several tooling materials like aluminum, brass, and mild steel was performed by Dave et al. Pin on disc wear tests was performed by the authors at 10, 15, and 20 N loads with 250, 350, and 450 rpm, respectively, of disc speeds. It was reported that the application of chromium coating helped in improving the wear resistance and hence the service lifespan of aluminum, brass, and steel materials [4].

Pin on disc tests has been performed by El-Amoush et al. to find out the effect of sliding distance on the tribological properties of chrome-coated mild steel [5]. With sliding distance, the wear rate tends to increase. An investigation to study and compare the behavior of electrolytic hard chrome and arc-PVD CrN coatings under reciprocating conditions with a base oil was conducted by Bozyazi et al. The study was conducted under different loads of 5, 10, and 30 N and two different temperatures of 60 °C and room temperature. Effects of these varying conditions on wear behavior of both the coatings were studied. The results indicated that under lubricating wear circumstances, CrN coating proved to be a better alternative than electrolytic hard chrome [6]. The density of cracks in the coatings and polishing process used to clean the surface also affects the tribological properties of the coating. To investigate this, Podgornik et al. performed a study to determine the effect of density of cracks in a coating as well as a postpolishing process on the friction and wear characteristics of hard chrome coatings. The study was performed with coatings of three distinct crack densities in a ball on disc apparatus in lubricated condition. It was found that size and density of cracks determine the friction and wear performance with the best performance obtained with medium density cracks [7]. Jang et al. used two coatings on a gray cast iron specimen to study the wear rate and friction coefficient between piston ring coatings and cylinder liner. One of the coatings was hard coating composed of chrome-aluminum oxide and the other coating was a soft coating of copper–aluminum alloy. The study was performed on Pin-On-Disk machine with different test parameters. The results indicated that the hard coating of chrome-aluminum oxide can be used to improve lifespan and its friction coefficient is less than that of soft coating. The results also indicated that the wear rate of soft coating is higher than the hard coating [8].

The wear behavior of cylinder liners and piston rings of different materials was studied by Wopelka et al. The investigation was conducted using a linear tribometer in boundary lubrication regime. Different materials that were considered were nitrided steel, diamond-like carbon, and chromium nitride. Many parameters such as wear, coefficient of friction, and Hertzian contact pressure were evaluated. It was found that the combination of PTWA-coated cylinder liners and CrN-coated piston ring performed the best with respect to friction and wear behavior [9]. The sliding wear performance of WC–(W,Cr)2C–Ni was investigated by Williamson et al. and compared it with the performance of a hard chromium plate. The experiment was carried out on a ball-on-flat reciprocating tribometer in three different conditions. It was found that wear performance of both the materials was comparable with hard chromium plate displaying lower maximum penetration depths [10].

Different varieties of coatings such as nano-structured cobalt–phosphor and tungsten/tungsten carbide wear deposited by Williamson et al. and wear and friction

behavior was evaluated using a pin-on-disk apparatus. The performance, mechanical resistance, and fatigue resistance of both the coatings were compared with hard chromium. It was reported that both the coatings displayed high resistance to wear and corrosion as well as better functional properties [11]. Chromium nitride and multilayer Cr/CrN coatings on a steel specimen were deposited by Polcar et al. Friction and wear analysis conducted at high temperatures of about 600–800 °C by a pin-on-disc apparatus led to a conclusion that multilayer Cr/CrN coatings displayed higher resistance to wear than CrN coating [12].

Based on the extensive literature review, it was observed that hard chromium coatings have been extensively used to enhance the tribological properties of piston ring material; however, very few studies have been conducted by considering the actual engine-working conditions. Based on this literature gap, attempts have been made in the present work to evaluate the effects of hard chrome coating on the wear and friction of the piston ring material. Reciprocating sliding tests were performed to investigate the tribological behavior of the hard chrome coating. In this work, three tribopairs by considering the hard chrome coating on the piston ring and cylinder liner material were considered.

2 Materials and Methods

2.1 Material Specifications

The material used for the pins was cast iron and that for the plate was complemented by Mild Steel. The pins and plates were fabricated from the raw material using the lathe machine, hand cutter, and surface grinder. Mild steel is strong and readily available and has relatively low carbon content. It has a high melting point of 1410 °C, encompassing its high utility. Cast iron has a carbon content of greater than 2% and the usefulness is derived from its low melting point around 1150 °C. It is known for its resistance to deformation and wear resistance; oxidation enables to resist the destruction and weakening. The elemental composition of the cast iron pins and mild steel plates was evaluated using chemical spectroscopy and presented in Table 1.

Cast iron pins and plates were plated with hard chrome over the surfaces for experimentation. It is performed through electroplating process. The thickness of the coating applied was 15 μm. Coating was successfully achieved over the plates by using the iron strings to hold plate from edges and dip the plate in the well. But there were some failures while coating the pins, it was hard to hold the pin with the

Table 1 Elemental composition of cast iron pins and mild steel plate

Element	C	Cr	Mn	Si	Fe
Cast iron (wt%)	3.52	1.05	0.58	2.96	92
Mild steel (wt%)	0.18	–	0.80	0.25	97

Table 2 Vickers hardness number for coated and uncoated samples

Specimen	Vickers hardness (HV)
Uncoated pin	450
Coated pin	1240
Uncoated plate	352
Coated plate	1249

strings therefore a drill of 2 mm was made along the pin to facilitate holding it with the iron string. Although the failure we faced was majorly because of the carbon content present in the cast iron pins due to which the plating got cracked a lot of times. An average Vickers hardness value achieved on the coated pin and plate was around 1240 HV. Table 2 presents the Vickers hardness number for the coated and uncoated samples. Chrome plating gives successful result in resistance to corrosion and wears in enhancement to its tribological properties.

2.2 Reciprocating Sliding Wear Testing

There are a number of different methods which has been used by researchers in the past for the determination of wear and friction like pin on disc, pin on cylinder, ball on flat [13, 14]; however, the selection of a particular type of tribometer depends on the type of contact and the relative motion between the two mating parts. In the current research work, the main focus is evaluation frictional behavior of the piston ring material, for modeling the actual piston and cylinder assembly, a reciprocating pin on flat-type tribometer was selected [15].

The reciprocating pin on flat tribometer consists of a procedure to hold the flat plate (representing the engine cylinder) in a static position and a pin (representing piston ring materials) reciprocates on the flat plate under the effect of applied loads. The loads were applied using the dead weights and a lever arm was used to transfer the load onto the pin. The flat plate chamber was connected with a heating coil, which heats the flat plate through conduction between the coil and flat plate chamber. A temperature sensor was installed on the testing area to continuous determine the temperature of the tribopair interface. A friction sensor was used to continuously measure the friction force between the tribopairs. Figure 1, presents the basic parts of the reciprocating pin on a flat tribometer.

The various input parameter selected to perform the tribo-testing are given in Table 3 and each experimental run was repeated three times and average of three was taken to draw the results. For the detailed examination of the frictional behavior of the piston ring materials, experiments were performed by using three different tribopairs. As (i) uncoated pin and plate, (ii) coated pin and plate and, and (iii) coated pin and uncoated plate.
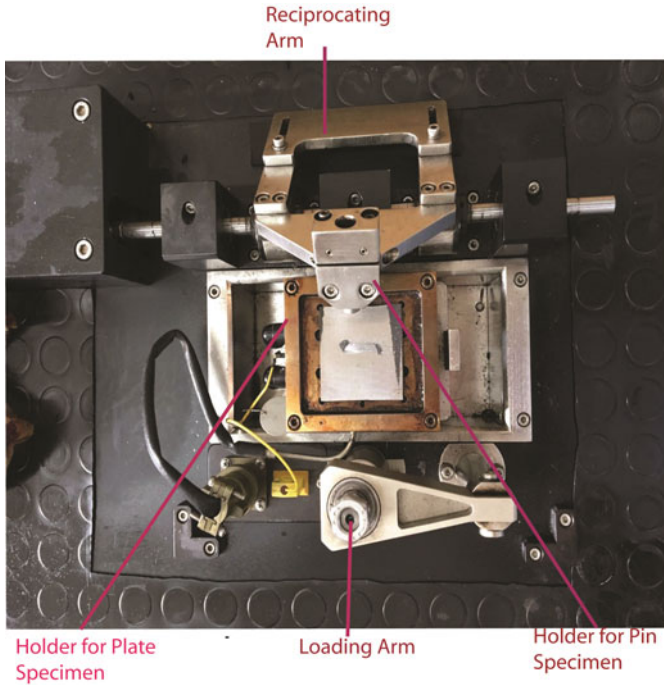
Fig. 1 Linear reciprocating tribometer setup

Table 3 Input parameter for the reciprocating wear test

Input parameter	Value
Stroke length	4 mm
Frequency	25, 30 Hz
Applied load	35, 40 N
Temperature of plate	180 °C
Pin diameter and length	12 and 15 mm
Plate height, length, thickness	50, 50, 5 mm

3 Results and Discussion

For evaluating the effects of hard chromium coating, the variation of friction force with applied load and frequency at 180 degree Celsius temperature is presented in Figs. 2, 3, and 4. Figure 2a, b presents the friction force for both the specimens coated, Fig. 3a, b for both the specimens uncoated, and Fig. 4a, b for the coated pin and uncoated plate. The general trend for all the three physical conditions supports that with an increase in frequency, the friction force decreases thereby decreasing the coefficient of friction, on the contrary, increase in load led to the increase in frictional
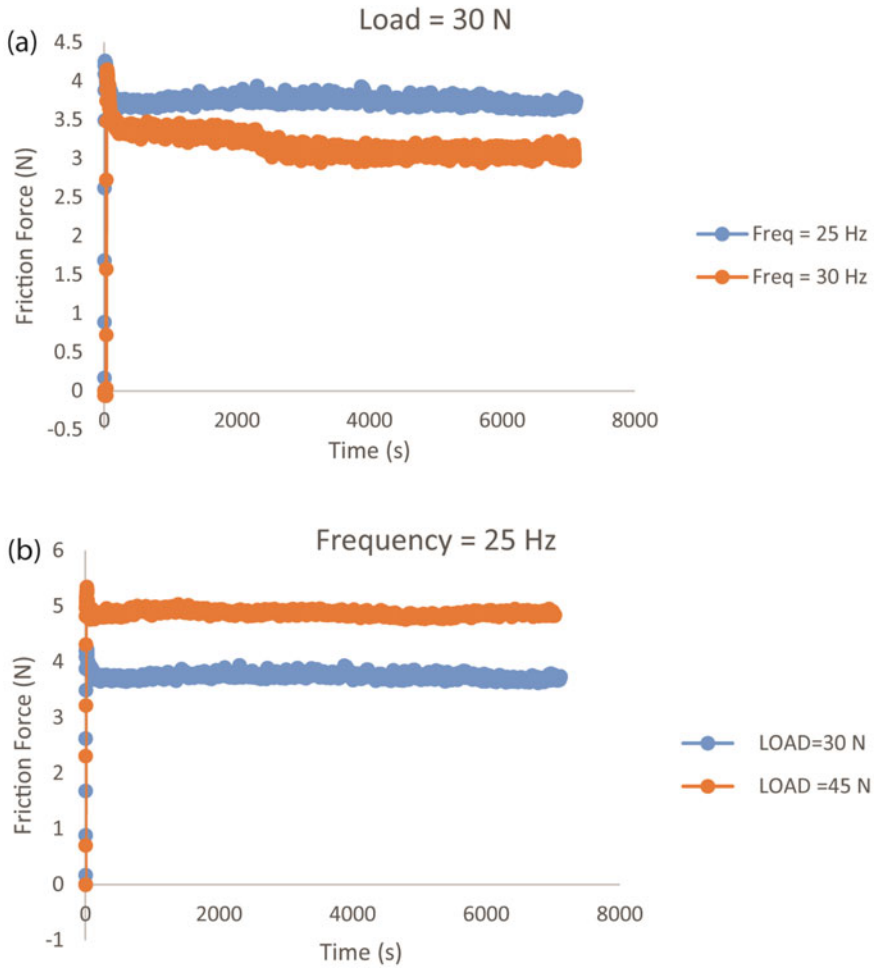
Fig. 2 **a**, **b** Friction force variation with time for coated pin and coated plate

force. It is observed that the friction force value increases very sharply for the initial few seconds and attained a maximum value. After this, the mixed zone starts where the friction force reduces to attain the near-constant value. This kind of pattern was observed for all the tribopairs.

It is seen from Fig. 2a that, with the increase in the frequency of the sliding, the friction force value tends to decrease. At 25 Hz frequency, the average friction force was 3.9 N and, for 30 Hz, it was 3.4 N. The reduction in the total contact area between the tribopairs and separation between the surfaces happened with the increase in frequency. Due to these two phenomena, the average friction force gets reduced with an increase in the frequency [16]. Similar trends were reported for the other tribopairs as well as indicated in Figs. 3a and 4a, and with an increase in load,
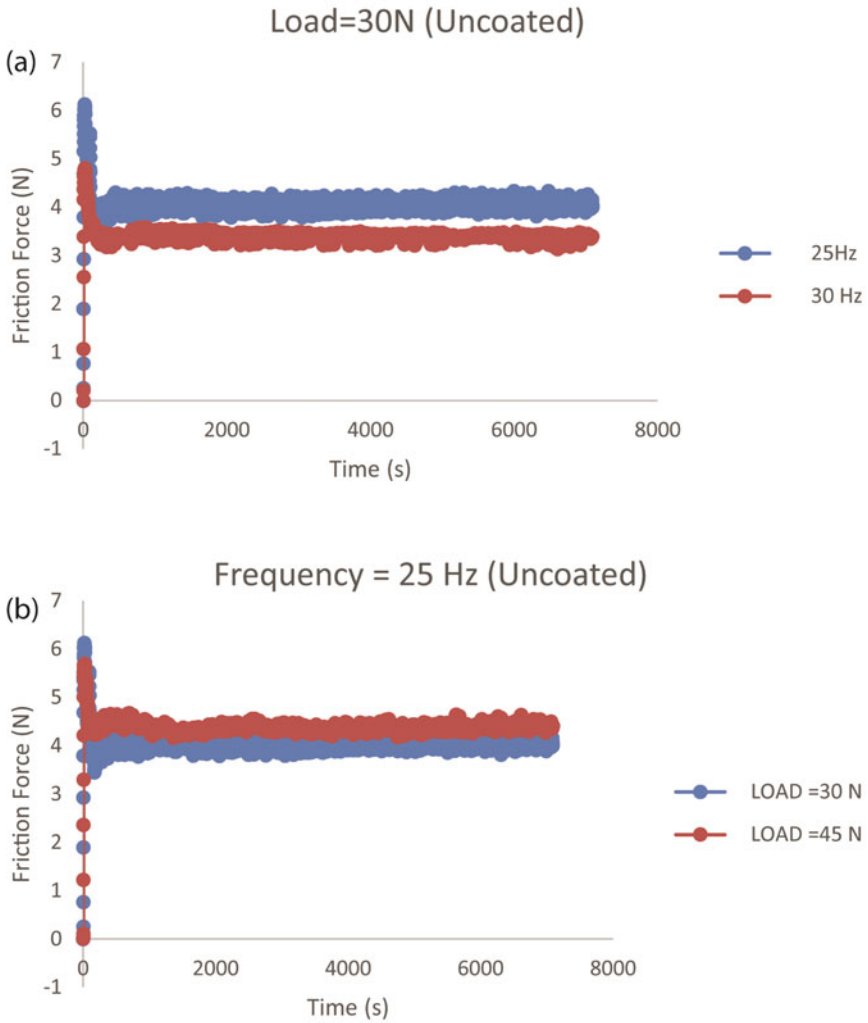
Fig. 3 a, b Variation of friction force for both uncoated condition

the friction force also increases. The increase in load, applies more pressure on the pin specimens, which increases the friction force.

Figure 5a, b depicts the dissimilarity among the three physical conditions with respect to the frictional force. All the samples run for 15 min at 180 °C gave comparative results in which both coated proved to be least efficient, while the other two situations with both samples uncoated, and the pin coated with plate uncoated provided lower friction force values. The tribopair of the coated pin and uncoated plate has resulted in the lowest friction force value. The tribopairs, where the pin and plate both the material are same resulted with high COF as compared to the
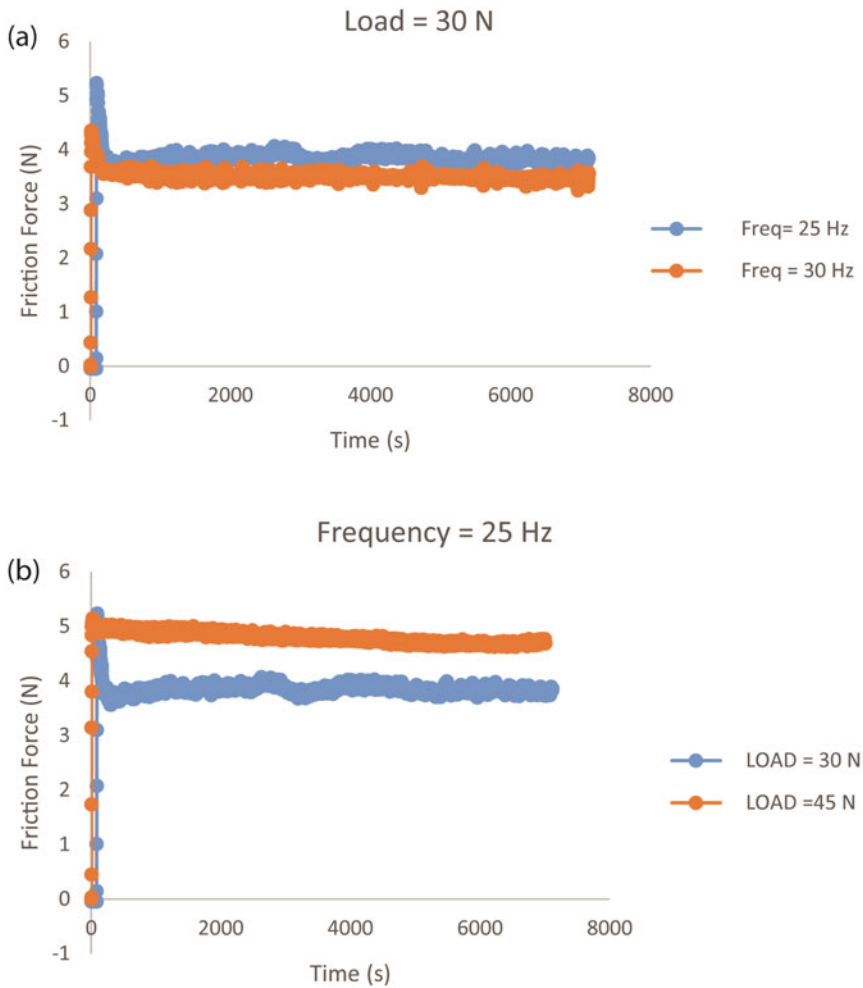
Fig. 4 a, b Variation of friction force for coated pin and uncoated plate

dissimilar tribopairs of coated pin and uncoated plate. The similar hardness values, roughness value, and nature of material removes the almost equal amount of materials from pin as well as plate specimens which in result increases the roughness value. With increase in surface roughness value the COF also gets increased. For the coated pin and uncoated plate tribopair, the chromium coating on the pin surface helped in reducing the friction force. The coefficient of friction was calculated as depicted in Table 4.
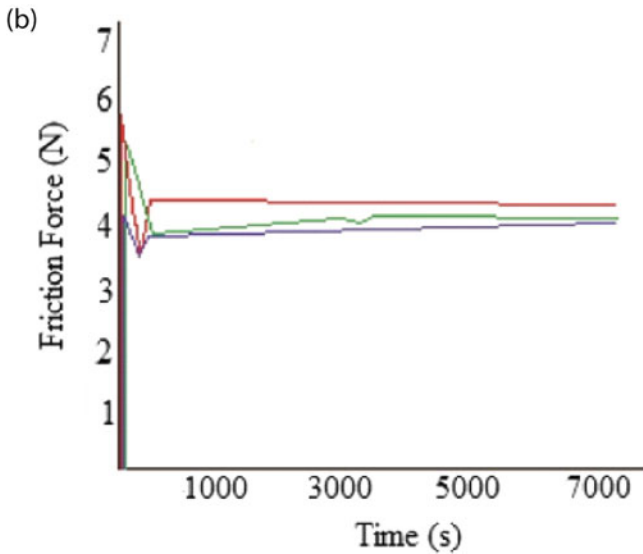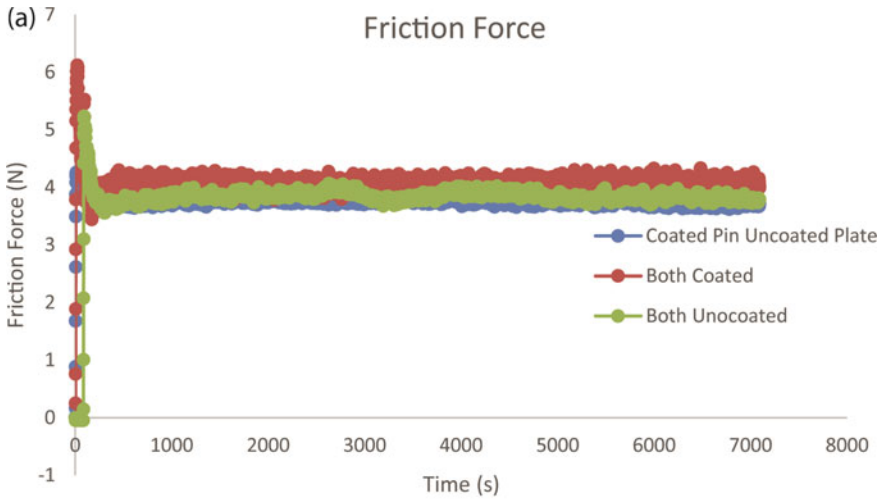
Fig. 5 **a** Variation of friction force for all the considered cases; **b** Line diagram for variation of friction force

4   Conclusions

In the present work, the effects of hard chromium coating on the friction behavior of piston ring material. Experiments were performed at different loading and frequency values at 180 °C temperature. Following conclusions could be drawn from this experimental study.

Table 4 Coefficient of friction values for all the considered conditions

Condition	Freq (Hz)	Load (N)	COF
Both condition	25	30	0.1352
	25	45	0.1097
	30	30	0.1137
	30	45	0.1334
Pin coated–plate uncoated	25	30	0.1268
	25	45	0.1063
	30	30	0.1173
	30	45	0.1102
Both coated	25	30	0.1247
	25	45	0.1083
	30	30	0.1058
	30	45	0.1247

- The hard chromium coating has been successfully coated on the piston ring material surface using the electroplating technique.
- It is observed that, with an increase in frequency, the friction force decreases thereby decreasing the coefficient of friction and, with an increase in load, the friction force value also increases.
- The chromium coating has proved to improve the friction behavior of the piston ring material; however, coating on both the mating parts (piston ring and cylinder) is not useful.

References

1. Almotairi, A., Warkentin, A., Farhat, Z.: Mechanical damage of hard chromium coatings on 416 stainless steel. Eng. Fail. Anal. **66**, 130–140 (2016)
2. SaghiBeyragh, M., KhamenehAsl, Sh, Norouzi, S.: A comparative research on corrosion behavior of a standard, crack-free and duplex hard chromium coatings. Surf. Coat. Technol. **205**(7), 2605–2610 (2010)
3. Picas, J., Forn, A., Matthäus, G.: HVOF coatings as an alternative to hard chrome for pistons and valves. Wear **261**(5–6), 477–484 (2006)
4. Dave, D., Chauhan, K., Chavda, M., Rawal, S.: Study of Tribological Behavior for Chromium Based Coatings Deposited on Conventional Materials. Procedia Technology **23**, 91–97 (2016)
5. El-Amoush, A., Abu-Rob, A., Edwan, H., Atrash, K., Igab, M.: Tribological properties of hard chromium coated 1010 mild steel under different sliding distances. Solid State Sci. **13**(3), 529–533 (2011)
6. Bozyazı, E., Ürgen, M., Çakır, A.: Comparison of reciprocating wear behaviour of electrolytic hard chrome and arc-PVD CrN coatings. Wear **256**(7–8), 832–839 (2004)
7. Podgornik, B., Massler, O., Kafexhiu, F., Sedlacek, M.: Crack density and tribological performance of hard-chrome coatings. Tribol. Int. **121**, 333–340 (2018)
8. Jang, J., Joo, B., Lee, J., Moon, Y.: Effect of hardness of the piston ring coating on the wear characteristics of rubbing surfaces. Met. Mater. Int. **15**(6), 903–908 (2009)

9. Wopelka, T., Cihak-Bayr, U., Lenauer, C., Ditrói, F., Takács, S., Sequard-Base, J., Jech, M.: Wear of different material pairings for the cylinder liner—piston ring contact. Ind. Lubr. Tribol. **70**(4), 687–699 (2018)

10. Williamson, E., Gee, M., Robertson, D., Watts, J., Whiting, M., Yeomans, J.: Wear performance and characterisation of coatings for nuclear applications: WC-(W, Cr)2C-Ni and hard chromium plate. Wear **430–431**, 169–182 (2019)

11. Vernhes, L., Azzi, M., Klemberg-Sapieha, J.: Alternatives for hard chromium plating: nanostructured coatings for severe-service valves. Mater. Chem. Phys. **140**(2–3), 522–528 (2013)

12. Polcar, T., Martinez, R., Vítů, T., Kopecký, L., Rodriguez, R., Cavaleiro, A.: High temperature tribology of CrN and multilayered Cr/CrN coatings. Sur. Coat. Technol. **203**(20–21), 3254–3259 (2009)

13. Sharma, V., Singh, R., Chaudhary, R.: Effect of flyash particles with aluminium melt on the wear of aluminium metal matrix composites. Eng. Sci. Technol. Int. J. **20**(4), 1318–1323 (2017). https://doi.org/10.1016/j.jestch.2017.08.004

14. Singh, R., Chaudhary, R., Sharma, V.: Fabrication and sliding wear behavior of some lead-free bearing materials. Mater. Res. Express **6**(6), 066533 (2019). https://doi.org/10.1088/2053-1591/ab0be4

15. Sharma, V., Singh, R., Chaudhary, R., Saxena, M., Anand, M.: Effects of flyash addition on the dry sliding tribological behavior of aluminum composites. Mater. Res. Express 6(8), 0865f4 (2019). https://doi.org/10.1088/2053-1591/ab24fd

16. Dhakar, B., Chatterjee, S., Sabiruddin, K.: Linear reciprocating wear behaviour of plasma-sprayed Al_2O_3–Cr_2O_3 coatings at different loading and sliding conditions. Sādhanā **42**(10), 1763–1772 (2017). https://doi.org/10.1007/s12046-017-0716-7

To Study the Effect of SLS Parameters for Dimensional Accuracy

Vishal Sharma and Sharanjit Singh

1 Introduction

Selective laser sintered (SLS) process is discovered by C. Deckard in Texas in mid-1980. The SLS setup consists of carbon dioxide laser, a powder chamber, and the nitrogen gas chamber. This process is generally used at economic level, for the generation of complete functional end use products from various materials (polymer and metallic etc.) [1]. SLS has capability to stand out and enhance developments, along with timely production of parts. Therefore, SLS is successfully utilized by diverse industries like aerospace, automotive, and medical applications. In this method, components are directly created from CAD data. Initial. STL file is converted into sliced layers, which generates contour info of every layer [2]. During the process, bed temperature is enhanced up to a little lower of the melting temperature of material to protect parts from thermal distortion and for the complete sintering/joining of the powder layer with respect of the present layer of sintered powder. Although, the parts created by this process are not according to dimensions, which leads to a variety of trial runs, for reducing the errors and to produce accurate parts [3].

In previous years, Raghunath and Panday [4] observed the effect of shrinkage on parts along X, Y, and Z direction. They examined that hatch length and laser power have effects on shrinkage along X direction; hatch spacing and bed temperature have effects along the Y direction; and Z direction is only effected by hatch speed. Senthilkumaran et al. [5] examined the shrinkage behavior of polymer made parts by changing part orientation, different compensations and exposure ways. It is noticed that shrinkage pattern was influenced by orientation, which kept shrinkage very uniform on the Y direction than on the X direction. Further, it is investigated that

V. Sharma (✉) · S. Singh
Department of Mechanical Engineering, DAV University, Jalandhar, India
e-mail: vishalsharma4071@gmail.com

S. Singh
e-mail: malhi.sharanjit@gmail.com

as the hatch length decreases, the shrinkage of parts increases. Singh et al. [6] investigated the accuracy of SLS components considering different parameters, along with Dura form polyamide as work material. It was discovered that dimensional accuracy enhanced at the peak level of laser power, hatch spacing, and bed temperature. Scan spacing is established as foremost important parameter; i.e., accuracy lowers with the rise in scan spacing. Guo et al. [7] studied that during post-processing of SLS parts by using PA12 material. The objective of this study is to improve tribology performance of SLS produced parts. They also studied the interrelation between process parameters and surface quality. Hamed et al. [8] examined that the mechanical properties of parts produced by SLS with glass-filled polyamide material. They used input parameters, namely bed temperature, laser power, hatch speed, hatch spacing, and hatch length to examined produced parts. Xiaoyong et al. [9] had done heat transfer analysis by using mathematical modeling of SLS process. The mathematical model had been used for numerical simulation. Hiren et al. [10] examined that the effect of the different parameters on the accuracy of parts produced by SLS process using metallic material. Raja et al. [11] investigated the hardness and tensile strength of the parts produced by polyamide material, using bed temperature, layer thickness, and orientation as process parameters.

2 Detail of Material, Method, and Experimentation

For analyzing dimensional accuracy, specimens are produced using Dura form polyamide powder. This is a semi-crystalline type of powder. The ratio of material used is 70% used powder and 30% fresh powder. In the current investigation, face-centered CCD of response surface methodology (RSM) has been used for the calculation of dimensional accuracy of parts (Eq. 1).

$$S = ([(A_1 - A_0)/A_0]) \times 100\% \tag{1}$$

A_0 = design size of cad drawing, A_1 = actual size measured from vernier caliper.

RSM approach, which is employed in the current study, was first popularized by Box and Wilisan in 1951. RSM basically involve a set of systematic and analytical approach to frame a relationship among an output and the different input parameters. It is helpful for the modeling and analysis of response variables, which are influenced by different variables. Its main aim is to optimize the response. The optimum condition has been obtained from regression Eq. (2) and by inspecting surface contours. In this study, total 50 experiments are conducted as shown in Table 1. There are five variable parameters (Table 1) and all other parameters are kept constant.

$$Y = \beta_0 + \sum_{j=1}^{k} \beta_j X_j + \sum_{j=1}^{k} \beta_{jj} X_j^2 + \sum_{i}\sum_{<j=1}^{k} \beta_{ij} X_i X_j + e_i \tag{2}$$

Table 1 The list of experiments for dim. accuracy

S No	Laser power	Bed temp.	Layer thickness	Scan spacing	Orientation	Dim. accuracy
1	1	1	1	−1	1	5.131
2	0	0	0	1	0	−0.85
3	−1	−1	1	−1	1	−1.592
4	0	0	1	0	0	−4.903
−5	−1	1	−1	−1	1	8.503
6	−1	−1	1	1	−1	−2.547
7	−1	1	−1	1	−1	−3.772
8	−1	1	−1	−1	−1	2.106
9	−1	0	0	0	0	−1.247
10	0	0	0	0	0	−0.836
11	0	0	0	0	0	−0.575
12	0	0	−1	0	0	−3.386
13	−1	1	1	1	−1	−3.2
14	1	−1	−1	−1	1	−0.169
15	1	−1	1	1	1	−3.114
16	0	1	0	0	0	−0.567
17	0	0	0	0	0	0.153
18	1	1	−1	1	−1	−2.764
19	1	−1	−1	1	−1	−0.456
20	0	0	0	0	0	−1.739
21	−1	−1	−1	−1	1	−0.742
22	−1	1	1	−1	1	5.703
23	1	0	0	0	0	−0.592
24	−1	−1	1	−1	−1	−2.822
25	0	0	0	0	0	−0.547
26	1	−1	−1	1	1	−1.939
27	−1	−1	−1	−1	−1	−0.392
28	1	1	−1	−1	−1	4.356
29	1	−1	1	−1	1	−0.081
30	−1	0	0	0	−1	−1.714
31	−1	1	1	−1	−1	0.064
32	0	0	0	0	1	0.828
33	1	1	−1	−1	1	9.017
34	0	0	0	0	0	−3.772
35	0	0	0	0	0	−0.747

(continued)

Table 1 (continued)

S No	Laser power	Bed temp.	Layer thickness	Scan spacing	Orientation	Dim. accuracy
36	0	0	0	−1	0	2.658
37	−1	1	−1	1	1	−0.547
38	1	−1	1	−1	−1	−1.469
39	1	1	1	1	−1	−4.036
40	0	0	0	0	0	0.142
41	1	−1	−1	−1	−1	−0.356
42	−1	−1	−1	1	−1	−2.392
43	−1	−1	1	1	1	−2.436
44	1	1	1	1	1	−2.239
45	1	−1	1	1	−1	−3.214
46	1	1	1	−1	−1	2.853
47	1	1	−1	1	1	−1.419
48	−1	−1	−1	1	1	−2.125
49	−1	1	1	1	1	−1.95
50	−1	−1	0	0	0	−3.136

3 Development of Model

The mathematical models developed for dimensional accuracy contains significant model terms. Based on result of the model created in present study for calculating dimensional accuracy is measured sensibly. With actual factors, an empirical connection between dimensional accuracy and input parameters can be presented by the Eq. 3 shown below, with A-Laser Power (35–41 W), B-Temperature (170–176 °C), C-layer Thickness (0.9–0.11 mm), D-Scan Spacing (0.15–0.25), and E-Orientation (0–90°), respectively. In this model, (Eq. 1) created for dimensional accuracy, the parameters such as B, C, D, E, C^2, D^2, BD, BE, DE are significant model terms.

Obtained eq. in terms of actual factors:

$$
\begin{aligned}
Dimentional\ Accuracy = {} & -523.90861 + 2.15208B + 4134.49696C + 1191.66537D \\
& - 0.94569E - 21016.23482C^2 + 1178.75061D^2 - 9.80417BD \\
& + 5.81991E - 003BE - 0.20581DE
\end{aligned}
\tag{3}
$$

4 Result and Discussion

4.1 Analysis of Variance

The importance and the significance of different selected process parameters are analyzed with the application of analysis of variance (ANOVA). The suggested model i.e. quadratic model is used because the data are best fitted to monitor the dimensional accuracy of SLS parts. A significant model F value (44.10) is presented in Table 2. There is only 0.01% chance that this value is obtained due to noise. Lower probability value (Prob > F < 0.0500) depicts that this generated model is significant for dimensional accuracy. The model terms having values >0.1000 are nonsignificant terms. The 0.52 value obtained for lack of fit is not significant in relation to pure error. So, there is a probability of 90.52% that this large value of lack of fit occurs due to the noise which is otherwise desirable. It is good if lack of fit is nonsignificant. The value of Predicted R^2 obtained 0.8577 is in realistic good in relation with the value of Adjusted R^2, which is 0.8889. The value obtained for the Adequate Precision ratio of the generated model is 26.992 (>4), this shows an ample signal for the model.

Table 2 ANOVA table for shrinkage/dimensional accuracy shows adequacy of the model

Source	SS	DF	Mean square	F value	Prob > F	
Model	386.28	9	42.92	44.1	<0.0001	significant
B	62.83	1	62.83	64.57	<0.0001	
C	16.07	1	16.07	16.51	0.0002	
D	151.49	1	151.49	155.66	<0.0001	
E	27.51	1	27.51	28.27	<0.0001	
C2	16.04	1	16.04	16.49	0.0002	
D2	31.54	1	31.54	32.41	<0.0001	
BD	69.21	1	69.21	71.11	<0.0001	
BE	19.75	1	19.75	20.3	<0.0001	
DE	6.86	1	6.86	7.05	0.0113	
Residual	38.93	40	0.97			
Lack of fit	27.59	33	0.84	0.52	0.9052	not significant
Pure error	11.34	7	1.62			
Cor total	425.2	49				

Std. Dev. = 0.99		$R^2 = 0.9084$
Mean = 0.58		Adj $R^2 = 0.8879$
C.V. = 170.85		Pred R-Squared = 0.8575
PRESS = 60.61		Adeq Precision = 26.992
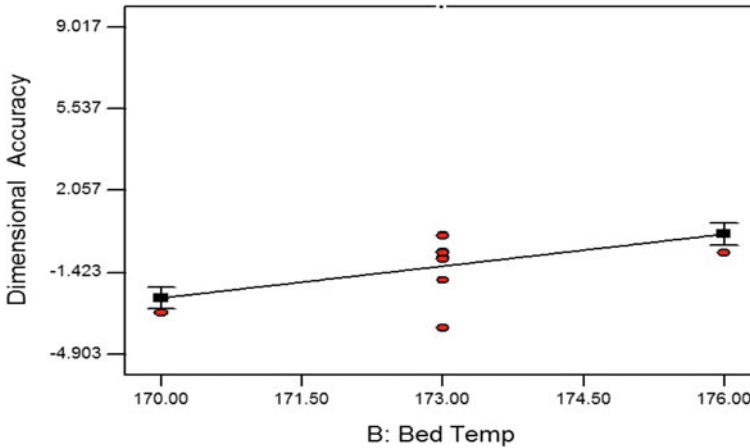
Fig. 1 Effect of bed temperature on dimensional accuracy

4.2 Influence of Input Variables on Dimensional Accuracy

In this section, the influence of various parameters has been analyzed for performance measures. From Figs. (1 to 4), it is clearly detected that the bed temperature, layer thickness, scan spacing, and orientation shows a major impact for dimensional accuracy.

Bed temperature The temperature has an additionally important impact on dimensional accuracy as shown in Fig. 1. This is visualized that with the rise in bed temperature from 170 to 176 °C, the shrinkage of the parts also increases. This is because laser sintering consist of heating of powder up to its melting temperature, and then a gentle re-crystallization of fused powder is desired. Speed of crystallization is a vital link, about determination its tendency to curl. This curling probability is highly concerned with dimension accuracy. Normally, the material particles are properly melted/sintered because high temperature causes swear shrinkage.

Layer thickness Layer thickness also shows the important impact for dimensional accuracy of parts as shown in Fig. 2. With the rise in layer thickness from 0.09 to 0.10 mm the accuracy of the parts are also enhanced and, with the further rise in layer thickness from 0.10 to 0.11 mm, there is regular decrease in accuracy of parts. As the layer thickness increases, a thick layer of powder spreads on machine bed which requires extra time and high energy to sinter each powder layer. Thus, temperature difference between different adjacent layers occurs, which results in irregular cooling rate and leads to further deformation and warpage in the parts. Additionally, fusion is also not appropriate at greater layer thickness, and if layer thickness is further enhanced above desired range, the degree of fusion tends to be stationary.
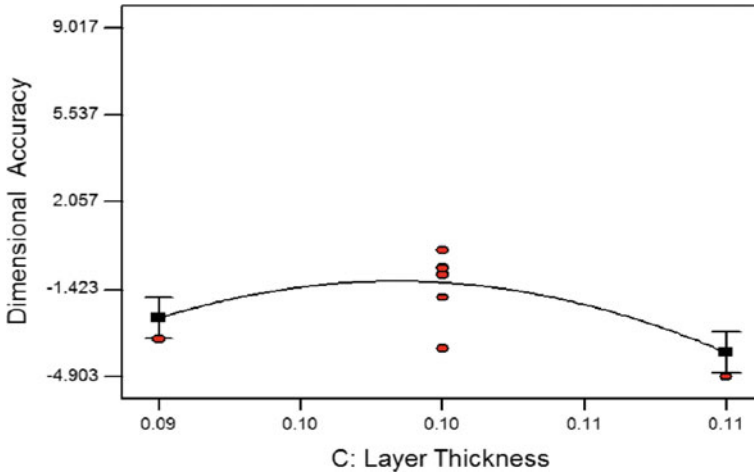
Fig. 2 Effect of layer thickness on dimensional accuracy

Scan spacing The rise in the level of this parameter from 0.15 to 0.2 mm the shrinkage is reduced as seen in Fig. 3, but the further rise in scan spacing from 0.2 to 0.25 mm the shrinkage is also increases. This is because, with the increase in scan spacing, the particle of powder is not packed properly. Normally, lower scan spacing confirms refine heat flow during sintering but it also overheat the layers/part and that requires cooling to preceding layer also. So, this grows a nonporous parts having less warpage. However, high scan spacing results poor packing of the powder particles.
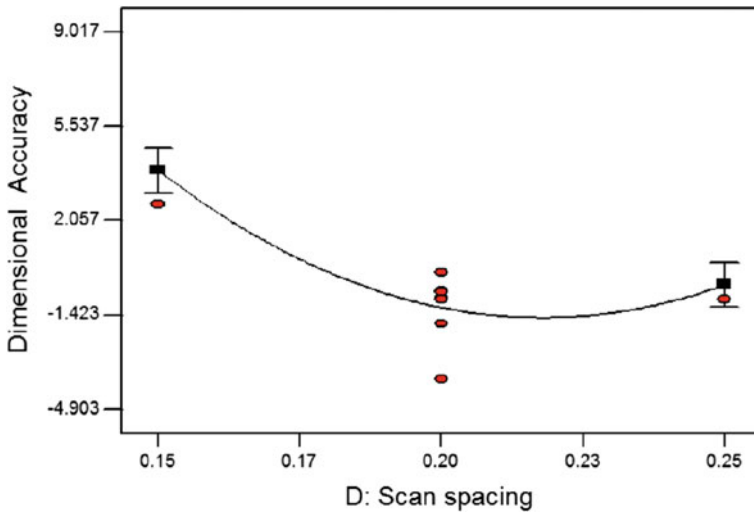
Fig. 3 Effect of scan spacing on dimensional accuracy
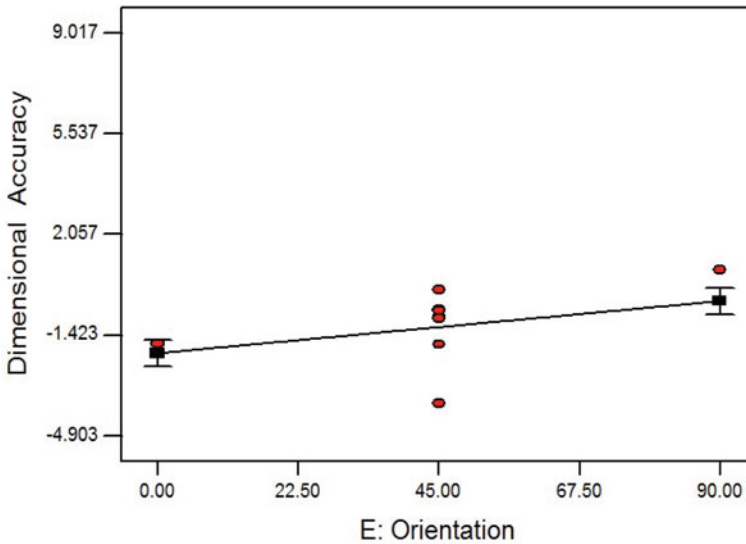
Fig. 4 Effect of orientation on dimensional accuracy

Which enhances the tendency of the powder layers to curl and to stick with roller. This effects fusion between the adjacent layers and effect dimensional accuracy.

Effect of orientation As shown in Fig. 4, with the increase in orientation of parts from 0° to 45° the accuracy of the parts also increases. With further increase in the orientation of part from 45° to 90° the accuracy of parts again increases. The parts at 90° orientation are more accurate than the parts having 0° orientations. This is due to that, the parts which are at 90° aligned in the bed got properly melted and sintered because of high energy density.

5 Conclusion

This study analyzed the impact of different parameters: laser power, bed temperature, thickness of layer, scan spacing, and orientations measured against the accuracy of sintered parts. The following observations have been obtained:

- A significant impact of bed temperature on dimensional accuracy is observed while rising bed temperature from 173 to 176 °C.
- Layer thickness also shows an impact on the accuracy of parts. Increase in layer thickness from middle level, i.e., 0.10–0.11 mm there is decline in accuracy.
- Scan spacing also shows its high significance over shrinkage. The increase in the scan spacing up to top level the shrinkage of part lowers.

- A dimensional accuracy of the parts also increased with increase an orientation from 0° to 90°.

References

1. Chua, C.K., Leong, K.F., Lim, CS.: Rapid prototyping: principles and applications, 4th edn. World Scientific, Singapore (2010)
2. Zhiwen, Z., Luc, L.: Adaptive direct slicing of the solid model for rapid prototyping. Int. J. Prod. Res. **38**(1), 69–83 (2000)
3. Hopkinson, N., Hague R.J.M., Dickens, P.M.: Rapid manufacturing: an industrial revolution for the digital age. Wiley (2006)
4. Raghunath, N., Pandey, P.M.: Improving accuracy through shrinkage modelling by using Taguchi method in selective laser sintering. Int. J. Mach. Tools Manuf **47**, 985–995 (2007)
5. Senthilkumaran, K., Pandey, P.M., Rao, P.V.M.: Influence of building strategies on the accuracy of parts in selective laser sinterin. Mater. Des. **30**(8), 2946–2954 (2009)
6. Singh, S., Sharma, V.S., Sachdeva, A.: Application of response surface methodology to analyze the effect of selective laser sintering parameters on dimensional accuracy. Prog. Addit. Manuf. **4**(1), 3–12 (2019)
7. Guo, J., Bai, J., Liu, K., Wei, J.: Surface quality improvement of selective laser sintered polyamide 12 by precision grinding and magnetic field-assisted finishing. Mater. Des. **138**, 39–45 (2017)
8. Hamed, S., Sushant, N., Hamed, S., Inam, U.A., Dermot, B.: Selecting optimal parameters on selective laser sintering process: a combined simulation and optimization approach. Optik **174**, 185–196 (2018)
9. Xiaoyong, T., Gang, P., Mengxue, Y., Shunwen, H., Ruijuan, Y.: Process prediction of selective laser sintering based on heat transfer analysis for polyamide composite powders. Int. J. Heat Mass Transfer. **120**, 379–386 (2018)
10. Hiren, M., Gajera, M.E., Komal, G.D., Veera J.: Experimental investigation and analysis of dimensional accuracy of laser-based powder bed fusion made specimen by application of response surface methodology. Prog. Addit. Manuf. 1–12 (2019)
11. Raja, B.K., Raja, R.J.P., Karan, K., Soundararajan, R., Ashokavarthanan, P.: Parameter optimization for polyamide in selective laser sintering based on mechanical behavior. 3D Printing and Additive Manufacturing Technologies, pp. 217–231 (2018)

Residual Stresses Analysis on Thermal Barrier Coatings—NDT Tool for Condition Assessment

V. R. Reghu, Souvik Ghosh, Akhil Prabhu, V. Shankar, and Parvati Ramaswamy

1 Introduction

Residual stresses are normally present in any engineering product as a consequence of fabrication and are removed prior to use [1, 2]. They are locked-in stresses within a large metal component or small product, even though no external forces may be acting on them. When one location gets stressed in any preferential orientation with the neighboring region in the component, either due to microstructural manifestations or macro features such as expansion or contraction, such stresses are most likely to occur. They can either be tensile or be compressive: they may even coexist, thereby balancing the many forces acting on the component to retain its structurally stable state. It is not easy to predict their presence or location without detailed analysis. Therefore, as a general manufacturing practice, the stresses are removed via thermal annealing process without compromising the other useful properties of the metal.

When in components, two or more types of configurations, for example, coatings or welded zones are involved, stresses of different nature, tensile, and/or compressive may be introduced into the interface of coating–substrate system or weld zones during processing due to the mismatch in the physical and thermal properties of the metal and/or ceramic materials [3]. Thermal contractions generate uneven stresses due to uneven cooling. Mechanical treatments or structural phase transformations also may generate stresses.

Residual stresses can be advantageous or damaging, and depend upon if the stress is tensile or compressive. Tensile residual stresses can be so high in magnitude that will promote defects in the component to eventually lead to ultimate failure. Furthermore, fatigue and stress corrosion cracking also get aggravated due to the presence of tensile stresses. Surface residual tensile stresses when get aided by the influence of

V. R. Reghu (✉) · S. Ghosh · A. Prabhu · V. Shankar · P. Ramaswamy
Department of Mechanical and Automobile Engineering, CHRIST (Deemed to Be University), Bangalore, India
e-mail: reghu.vr@christuniversity.in

an applied tensile stress in service, reliability of components can be highly compromised. Surface residual compressive stresses are generally supportive for component stability because they annihilate the effects of applied tensile stresses. Mostly, surface compressive stresses contribute to the enhancement of fatigue strength and resistance to stress-corrosion cracking.

Residual stresses remain dormant in normal conditions: however, their influence dominates when the components are put into service [4]. In the case of coatings, whenever the coated components are subjected to thermal treatment, the developed stresses will get added up or will be canceled with the already existing residual stresses. The combined stresses, both tensile and compressive, will cause the failure of the coating system much before the anticipated lifetime. X-rays can be used to sense the presence of residual stresses in an uncoated or coated system. A portable residual stress analyzer can be used to evaluate the stresses induced and precautionary measures can be taken to alleviate its effects during its service.

Predictions of these stresses are challenging and reliable measurement of their existence is extremely important. X-ray microdiffraction research instruments supported by 2D and 3D detectors facilitate their evaluation. X-ray detectors record residual elastic strain in areas with high spatial resolution in a material in a single measurement along a set of scattering vectors: therefore, the number of sample rotations required for determining the residual stress state is considerably reduced and, in some cases, totally eliminated. In the traditional "photographic film" techniques Debye Ring(s) from a polycrystalline sample were taken on X-ray-sensitive photographic film using portable stress analyzers and more recently digital images form the primary data for carrying out such analysis [5]. The utility of residual stress measurements has been fairly well documented in industrial components: however, the capability of this analysis technique when coatings with different compositions, such as metals and ceramics with distinctly different thermal expansion coefficients have not gained much attention. It is this aspect of nondestructive evaluation that has been addressed in this research work. The most popular thermal barrier coating (TBC) material studied for aerospace and automobile components is 6–8% Y_2O_3-stabilized ZrO_2 (6–8 YPSZ). Automobile applications (engine components, i.e., Al–Si alloy pistons) use the coatings to protect the substrate considering the melting point of Al–Si alloys (577 °C) used as piston materials.

2   Scope of the Present Work and Experimental Details

Understanding the state of residual stress after service at high temperature is important to improve the performance of TBC and its likelihood of failure in both: (a) as-deposited coatings and (b) changes in stress patterns after thermal cycling. This research work involves investigational determination of the residual stresses in plasma sprayed 8YPSZ TBCs on Al–11Si flat plates from diesel engine pistons.

8YPSZ Top coat (~250μm thick)
Ni-5Al Bond coat (50 - 75 μm thick)
Al-11Si substrate (~ 5 mm thick)

Table 1 Specimen configuration

Sl no.	Specimen configuration	Specimen designation
1.	5-mm-thick Al–11Si alloy flat plate/substrate (bare metal)	Uncoated Al–Si substrate
2.	250-μm-thick ceramic plasma spray-coated (on bond coated) Al–11Si alloy flat plate/substrate	Spray-coated Al–Si
3.	250-μm-thick ceramic-coated Al–11Si flat plate/substrate, thermal shock cycled between 500 °C and ambient at room temperature (1000 cycles)	Spray-coated and thermal shock cycled Al–Si

2.1 Coating Configuration

Plasma spray coatings of 250 to 400 μm-thick 8YPSZ were deposited on Al–11 Si alloy flat substrates. The coating configuration with Al–Si substrate (~5 mm thick), NiAl (AMDRY 956) bond coat (~50 μm), and 8YPSZ (METCO 204 NS) top coat (typically 250 μm thick) is shown in Fig. 1. The as sprayed coatings were subjected to thermal shock tests and oxidation stability tests ranging between 300 and 500 °C for 1000 h. Details of the process have been described elsewhere [6].

Table 1 shows the specimen configurations with the designation given alongside.

Residual stresses developed on three different samples were analyzed and compared. (1) Uncoated Al–Si alloy substrate (2) Al–Si substrate coated with 50-μm nickel aluminide (NiAl) bond coat and 250-μm yttria partially stabilized zirconia (YPSZ) as the top coat in as-sprayed condition (3) Thermal barrier-coated Ni–Al substrate, thermal shocked for 1000 cycles at 500 °C using oxy acetylene flame. Before and after the thermal treatment, cross-sectional metallographic sections were removed from all specimen, polished, examined by scanning electron microscopy (SEM) to study co relation, if any was present, between the residual stress analysis data and microstructure.

2.2 Residual Stress Analysis

The residual stress within the coatings and coating substrate interface were measured by X-ray diffraction (the Cos α method) for the as-sprayed coated and thermal cycled samples. Figure 2. shows (a) spray-coated Al–Si specimen with cross-sectional met-

■ Sample information

Item	Analyisis	Analysis
Name	Al(311)	Al(222)
Lattice constant(a)	4.0494 A	4.0494 A
Lattice constant(c)	---	---
Wavelength	K-Alpha	K-Alpha
Diffraction angle(2Theta)	139.497 d	156.986 d
Diffraction lattice angle(2Eta)	40.503 de	23.014 de
Interplanar spacing(d)	1.221	1.169
Diffraction plane(h,k,l)	3, 1, 1	2, 2, 2
Crystal structure	F.C.C	F.C.C
Young's modulus(E)	69.310 GI	72.470 GI
Poisson's ratio(v)	0.348	0.341
Sigma(x) stress constant(K)	-103.343	-180.445
Tau(xy) stress constant(K)	93.661 GI	163.539 C
Sigma(y) stress constant(K)	-214.572	-678.986

■ Measurement condition

Measurement area	All
	(5.000 - 40.500 [mm])
Pitch	100 [um]
X-ray irradiation time(Setup)	30 [sec]
X-ray irradiation time(Meas.)	10 [sec]
X-ray irradiation time(Max)	14 [sec]
X-ray tube current	1.50 [mA]
X-ray tube voltage	30.00 [kV]
Sample distance(Monitor)	39.000 [mm]
Sample distance(Analysis)	39.783 / 39.817 [mm]
X-ray incidence angle	25.0 [deg]
Offset of alpha angle	0 [deg]
X-ray wavelength (K-Alpha)	2.29003 [A] (Cr)
X-ray wavelength (K-Beta)	2.08480 [A] (Cr)
Total measurement count	6085
Oscillation count	300
X-ray tube total use time	59.13 [h] (212879 [sec])
Detection sensitivity	62.0 [%] (533339)
Peak strength (Ave)	160k / 65k
Level of ambient light	0.3 [%]
Temperature	37.19 [deg C]
K-Beta cut filter	Unused
Valid range of alpha angle	18.00 <---> 90.00 [deg]
Peak analysis method	Fitting Lorentz
Correction coefficient (Stress)	0.000α + 1.000x + 0.000
Correction coefficient (FWHM)	0.000α + 1.000x + 0.000
Correction coefficient (R.Gamma)	0.000α + 1.284x + 0.263
Austenite calculation method	Integrated intensity ratio
R-value (Alpha)	---
R-value (Gamma)	---
Collimator size	Phi1.0

Fig. 2 Photographs: coated Al–Si plate, Residual stress measurement instrument and conditions

allographic sections placed over the plates used and (b) typical specimen under residual stress analysis instrument.

Sample information used by the analysis instrument in analyzing the uncoated Al–Si substrate and measurement conditions used in the analysis is also shown in Fig. 2. The Debye rings in the analysis pattern are a function of microstructural features (grain orientation: texture, grain sizes, stress states) and automatic rapid calculation of the residual stress was carried out from the complete Debye ring measuring simultaneously from up to 500 data points on it. In this work, measurements were carried out on the metal side (at the back of the coated side).

Portable residual stress measurement system (micro-X360s, PULSTEC, Japan) was used in this work.

3 Results and Discussion

3.1 Uncoated Al–Si Substrate

The analysis data obtained from the residual stress analyzer is given in Fig. 3. (a) the 2D Debye ring, (b) the 3D Debye ring, and (c) the Distortion ring.

Diffraction rings from multiple (hkl) crystalline planes collected with area detectors allow for variation in d values and their relationship with the residual stresses generate the distortion rings. The detection in the different peak levels in the ring also indicates different grain orientations. Figure 3c shows the distortion ring which is a display of diffraction peak position and full width at half maximum (FWHM) position. In the process of analysis, the Debye rings are opened up in a linear form of presentation. They are shown in Fig. 4 which shows the images seen in Fig. 3
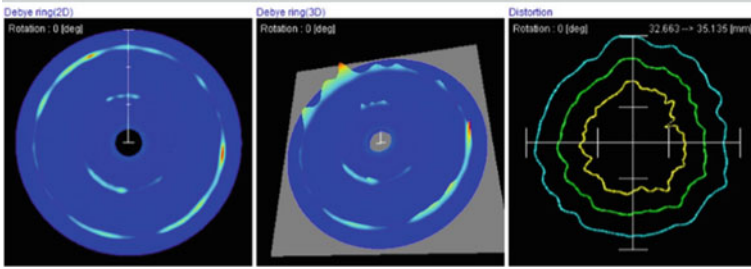
Fig. 3 Debye ring **a** 2D image **b** 3D image and **c** Distortion ring (uncoated Al–Si substrate)
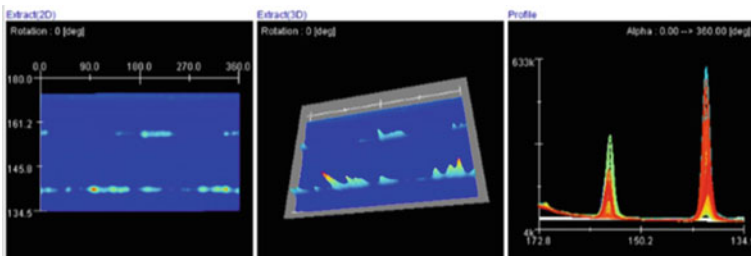
Fig. 4 Opened Debye ring (0 to 360^0) **a** 2D, **b** 3D, and **c** Intensity distribution of Distortion ring (uncoated Al–Si substrate)

in 2D image, 3D image, and the profile format of the Distortion ring, i.e., intensity distribution in the open Debye ring formation.

The residual stress and surface shear graph are given in Fig. 5.

In the residual stress graph, the graph going up toward the right indicates compressive stress and graph going down toward right indicates tensile stress: the net stress is compressive. The average values of the residual stresses at the top surface of uncoated Al–Si substrate are also shown in Fig. 5. A compressive residual stresses
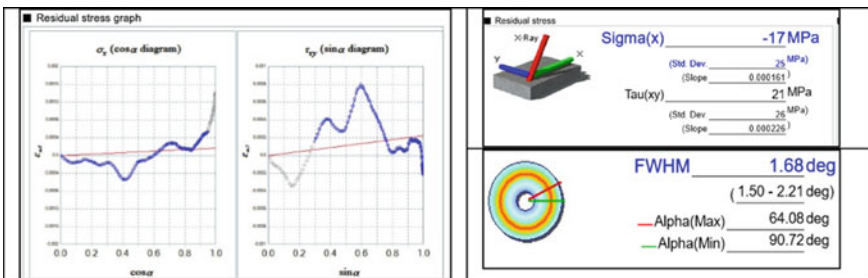
Fig. 5 Residual stress graph: residual stress and surface shear graph and average values of the residual stresses at the uncoated Al–Si substrate

for the machined uncoated surface is seen with a magnitude of 17 MPa (negative sign indicates compressive stress) which was marginal.

3.2 Spray Coated Al–Si

The specimen described in the configuration shown in Fig. 1 was subjected to the same analysis as described in detail in the previous Sect. (2.2) Fig. 6 shows the microstructure (SEM) from polished metallurgical cross section from the Al–Si substrate coated with TBC. The micrograph showed a smooth coating–substrate interface, and uniform microstructure without defects and minimum porosity. TBC coating thickness was between 250 and 300 µm. The results are presented in the same manner as shown in Sect. 3.1 for the uncoated Al–Si substrate. The residual stress measurements were carried out on the Al–Si substrate (metal side) at the back of the TBC. Figure 6 shows the Debye rings and Distortion rings.
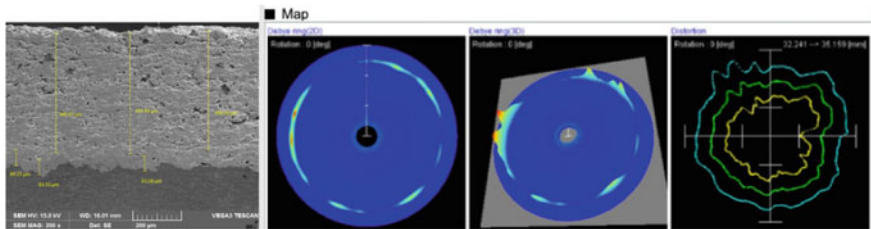
Fig. 6 SEM micrograph of the TBC configuration (polished cross-sectional metallograph): and Debye and Distortion Rings on coated Al–Si substrate
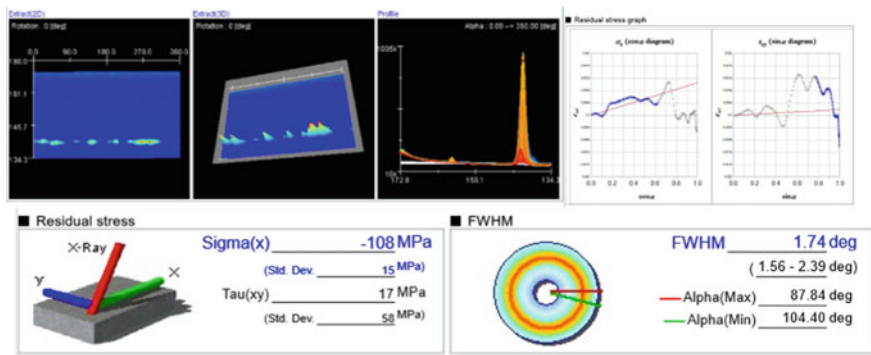
Fig. 7 Opened Debye/intensity distribution of distortion ring and Residual stress graph and average values of residual stresses (Coated Al–Si substrate)

Figure 7 shows the analysis results in opened Debye ring pattern for the coated Al–Si substrate and the residual stress graph and surface shear, respectively. The average value of the residual stresses at the back (metal side) is also shown.

The coating was attributed with the generation of additional stress on the substrate which was compressive in nature. The magnitude of compressive stress was 108 MPa. The orientation of the graph toward the positive stress direction is indicative of an increased stress state of the specimen and this was expected.

3.3   Spray-Coated and Thermal Shock Cycled Al–Si

The TBC was subjected to 1000 severe thermal shock cycles between 500 °C and ambient at room temperature. Results are presented in the same manner as has been done in the previous sections. Figure 8 shows the test results. The residual stress pattern becomes evident upon examination of the patterns depicted in Fig. 8 and by drawing comparison between the patterns shown for the uncoated Al–Si substrate and coated Al–Si. As already brought out, the sloping down pattern of the residual stress graph in the negative side is indicative of the presence of tensile stresses in the material under test. The magnitude of the tensile stress was 285 MPa (significantly +). In order to confirm if the positive residual stress values had any physical bearing with the thermal tests and to assess its status, cross-sectional metallographic section was removed from the specimen after the end of residual stress measurement. The SEM micrograph also is shown in Fig. 8.

The micrograph revealed a significant damage to the coating. 100–200 μm long cracks were observed in the coated layers. The interface was not affected. These defects were not noticeable on the specimen surface and there was no indication if
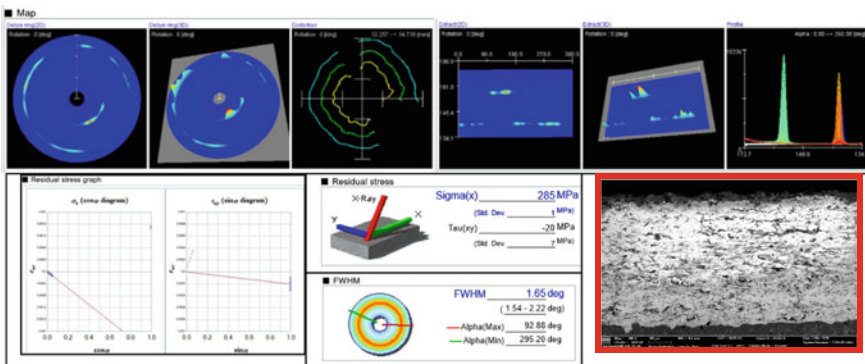
Fig. 8 Debye/distortion and opened Debye ring and Intensity distribution residual stress/surface shear graph, average values of residual stress and SEM Micrograph from polished metallographic cross section removed from coated and thermal shock cycled Al–Si

the specimen had undergone any damage during thermal shock cycling. The defective/cracked interlamellar layers were responsible for the generation of strong tensile stress patterns, a pattern also observed by other researchers [4].

4 Concluding Remarks

Among the three types of specimen analyzed for residual stress analysis, i.e., (a) uncoated Al–Si, (b) Spray-coated Al–Si, and (c) coated and thermal shock cycled Al–Si; the uncoated Al–Si specimen exhibited almost a residual stress-free status. The small compressive stress that was found to be present could be attributed to the machining process during sectioning of the substrate from the piston.

The analysis of as sprayed coating revealed a compressive stress at the interface. During the plasma spray coating process, the metal will expand significantly more than the metal substrate contract faster than the ceramic during cooling process. This process is expected to introduce an induced stress of compressive nature at the interface. This variation in heat–cool variation is attributable to the varied coefficient of thermal expansion characteristics of Al–Si alloy and the ceramic coating.

The ultimate goal of the analysis was to determine if residual stress measurements can detect the finer aspects of the coating condition before and after thermal stress treatments. The viability of this method of analysis was confirmed in the stress state analysis of the coated and thermal shock cycled Al–Si and thereafter co relation with the microstructural features. The tensile stresses within the coating were attributed to capability of the metal substrate to expand in a direction perpendicular to the coating–substrate interface.

Thus, the potential of using Residual Stresses Analysis as a Non-Destructive test tool to assess onset of failure of ceramic coatings on Al–Si Alloy castings after thermal treatments was explored and viability of the analysis tool was established.

References

1. Mishchenko, Andrii, Leonardo, Wu, da Silva, Vanessa K., Scotti, Americo: Analysis of residual stresses resulting from the surface preparation for X-ray diffraction measurement. J. Braz. Soc. Mech. Sci. Eng. **40**, 94 (2018)
2. Monine, V.I., Payao Filho, J.C., Gonzaga, R.S., Passos, E.K.D., Joaquim Teixeira de Assis, J.T.D.: X-Ray diffraction technique for residual stress measurement in NiCrMo Alloy Weld metal. Adv. Mater. Sci. Eng. **2018** (8986423) (2018)
3. Teixeira, V., Andritschky, M., Fischer, W., Buchkremer, H.P., Stover, D.: Analysis of residual stresses in thermal barrier coatings. J. Mater. Process. Technol. **92–93**, 209–216 (1999)

4. Lee, Gary, Atkinson, Alan, Selcuk, Ahmet: Development of residual stress and damage in thermal barrier coatings. Surf. Coat. Technol. **201**, 3931–3936 (2006)
5. Gelfi, M., Bontempi, E., Roberti, R., Depro, L.E.: X-ray diffraction Debye Ring Analysis for Stress measurement (DRAST): a new method to evaluate residual stresses., Acta Mater. **52**(2004), 583–589 (2004)
6. Reghu V.R., Lobo, K., Basha, A., Tilleti, P., Shankar, V., Ramaswamy, P.: Protection offered by thermal barrier coatings to Al-Si Alloys at high temperatures—a microstructural investigation, materials today: Proceedings, https://doi.org/10.1016/j.matpr.2019.07.752 (2019)

Wettability Analysis of Polyetheretherketone-Based Nanocomposites

Manjeet Kumar, Rajesh Kumar, and Sandeep Kumar

1 Introduction

Polyetheretherketone (PEEK) is thermoplastic polymer having semi-crystalline structure with linear polycyclic aromatic chain. Figure 1 shows the chemical structure of PEEK. The aromatic chain has combinations of ether and ketone functional groups between the aryl rings [1]. PEEK has high melting point, stiffness, strength, and also has high resistance to impact and fatigue. It has an excellent chemical and thermal stability. PEEK is a biocompatible material and used in bio implants, specially orthopedic and dental implants [2]. More significantly, the mechanical properties of PEEK are closer to that of human cortical bone [3, 4]. PEEK is radiolucent material; so, X-Rays easily pass through it and provide good image [5]. But PEEK is not a bioactive material, which limited its use in implantation [6].

Hydroxyapatite (HA) is calcium–phosphorus-based ceramic, extensively used in the field of bioimplants and tissue engineering. It is a main inorganic component of the bone matrix. The nanocrystals of HA are attached to collagen through non-collagenous proteins in bone matrix [7, 8]. The nanocrystals of HA forms roughly

Fig. 1 Chemical structure of PEEK
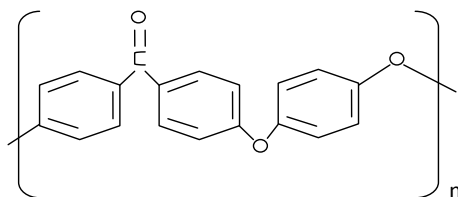
M. Kumar (✉) · R. Kumar
Department of Mechanical Engineering, UIET, Panjab University, Chandigarh, India
e-mail: dangi.manjeet@yahoo.com

S. Kumar
Department of Bio & Nanotechnology, Guru Jambheshwar University, Hissar, India

185

45% by volume of the cortical bone and make available active sites for biomineralization and cellular attachment [9]. HA is known for its bioactivity and widely used in bioactive coating on implants. It is also very decent filler in polymer matrix to make polymer-based bioactive composite for orthopaedic and dental applications. It is reported that the nano-HA (nHA) has more potential to improve the mechanical properties as well as bioactivity of PEEK-based composite compare to conventional HA [10]. Carbon nanotubes (CNTs) are the sheet of graphene rolled into a cylinder having diameter in nanometers and length in millimeters [11]. CNTs have excellent electrical, thermal, mechanical, and structural properties. CNTs have high strength to weight ratio and young modulus of 1 TPa range [12]. These are classified into two types, single-walled carbon nanotubes (SWCNTs) and multi-walled carbon nanotubes (MWCNTs), based on number of graphene sheet rolled. MWCNTs are easy to produce compare to SWCNTs, so cheaper in price.

The surface of bioimplants should be bioactive to allow the adhesion and growth of osteoblast cells [13]. Biological tissue growth on surface of implants depends upon bioactivity of material. Bioactivity of surface depends upon the adsorption of protein on surface [14]. Figure 2 shows the mechanism of protein adsorption and osteoblast adhesion on implant surface.

The adsorption of protein is governed by topographical entities like surface energy, pore size, and roughness [15]. Enhancement in surface energy is the typical way to alter the protein adsorption on surface of material [16]. High-energy surfaces are more
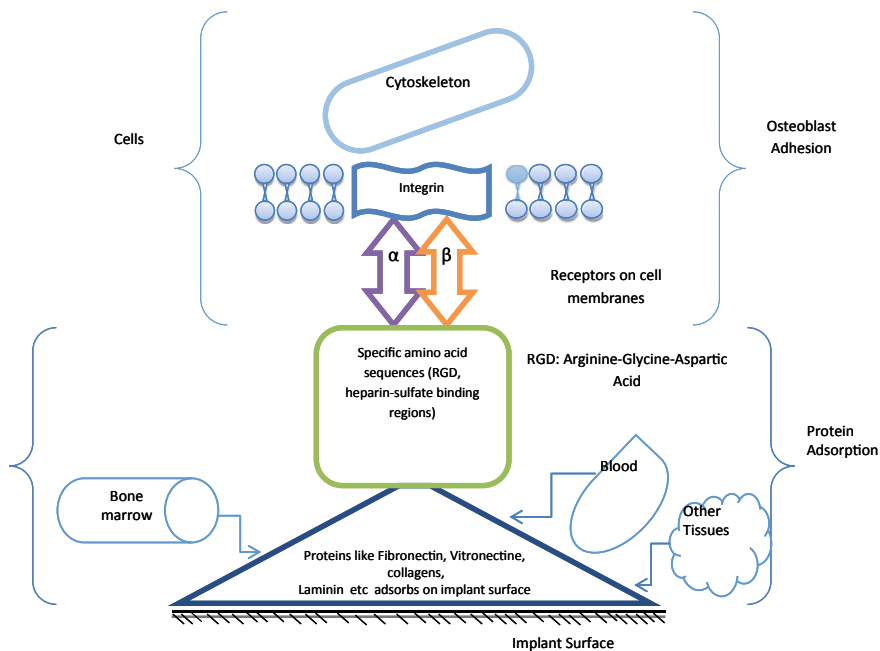
Fig. 2 Mechanism of protein adsorption and osteoblast adhesion (18)
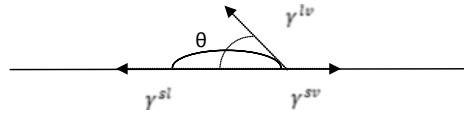
bioactive. The high-energy surfaces are complete wet by most of liquids. Surface energy depends upon the fluid contact angle of surface. As stated by young equation, the solid surface energy is indirectly proportional fluid contact angle. Equation 1 shows the young equation.

$$\gamma^{sv} = \gamma^{sl} + \gamma^{lv} \cos\theta \tag{1}$$

$\gamma\hat{}(sv)$ = Solid surface energy
$\gamma\hat{}(sl)$ = Solid–Liquid surface energy or interfacial tension
$\gamma\hat{}(lv)$ = Liquid surface energy or surface tension of liquid
θ = Water contact angle

According to young equation, small the fluid contact angle more is the solid surface energy. Figure 3 shows the contact angle and all three energies associated with liquid drop. It is clear from the Fig. 3 that lesser the contact angle, the liquid drop spread more and wettability increase. If the contact angle is acute, the surface is hydrophilic and if, it is obtuse, the surface is hydrophobic. Surface wettability depends upon the composition and roughness of surface. The nano topography enhanced the surface wettability and protein adsorption [16, 17]. Nano rough surfaces have more wettability and more capacity of protein adsorption compare to conventional rough surfaces [18]. So, the nano-structured surfaces increase the osteoblast adhesion and oseointegration and ultimately enhance the bioactivity of material.

Rui Ma et al. [19] put forward the ways for improving the bioactivity of PEEK by surface modification, coatings and making composite with bioactive materials. The nanomaterials as filler have potential to improve the surface energy and further bioactivity of PEEK. Wang et al. [20] reported the 14.3% decrement in water contact angle of PEEK/nanoflurohdroxyapatite (29.6% by vol.) composite compare to pristine PEEK. The functionalized MWCNTs are hydrophilic and improve the wettability of polymers. Majeed et al. [21] reported that hydroxyl functionalized MWCNTs improves the hydrophilicity of polyacrylonitrile (PAN) ultrafiltration membranes on blending at lower concentrations. While Choi et al. [22] observed the decreasing contact angle of surface of Polysulfone and carboxyl functionalized MWCNTs blended membrane with increasing MWCNTs concentration. The surface modification of PEEK composites is observed to be result in heavy decrement in contact angle, most probably due to impartment of micro/nano roughness on surface. Anxiu xu et al. [23] superimposed the micro/nano-topography on PEEK/nHA/carbon fiber composite by plasma treatment and sand blasting and observed that the contact angle reduced to 10° from 75°.

This work is summary of fabrication of PEEK/nHA (Nano hydroxyapatite) and PEEK/MWCNT nanocomposite, calculation of water contact angle of the surface of these nanocomposites and the analysis of the effect of microstructure of surface on water contact angle.

2 Material and Method

2.1 Material and Preparation

'VESTAKEEP 2000FP PEEK' powder having average particle size of approximate 50 μm was procured from M/S VESTAKEEP, Mumbai, India. It is unreinforced medium viscosity PEEK powder. The HA nanopowder having particle size 50–90 nm was procured from M/S Nano Labs, Jamshedpur, India. The MWCNTs of 50 nm in diameter and 3–8 μm in length was procured from M/S Nano Shell, Panchkula, India.

Round disk shaped samples were fabricated by powder mixing and melt and blending method. The particle size of PEEK powder was reduced to 10 μm from 50 μm using ball milling method. The materials in powder form were weighted precisely and mixed by ball mixing. The powder mixer was allowed to dehumidify for 1.5 h at 150 °C in vacuum oven. Compressing molding method was used to form the round disk shape of samples as shown in Fig. 4. Specially designed die and band heater setup as shown in Fig. 5 was used in compression molding to perform uniform heating and cooling. Total 7 samples were fabricated, one of pure PEEK, three samples of PEEK/MWCNT (3%, 5% and 7% weight of MWCNT) and three samples of PEEK/nHA (25%, 30%, and 35% weight of nHA). The composition of MWCNT and nHA in PEEK was decided by literature as well as pilot experiments.

Fig. 4 PEEK/nHA and PEEK/MWCNT's round disk shaped samples
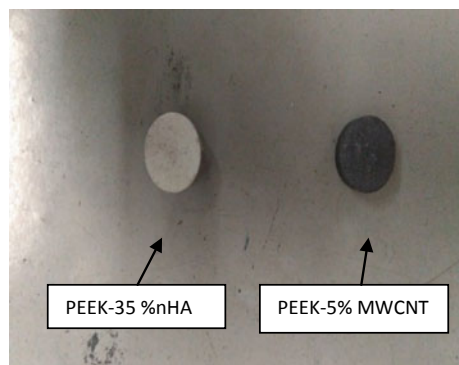
Fig. 5 Die-band heater setup for uniform heating and cooling in compression molding method
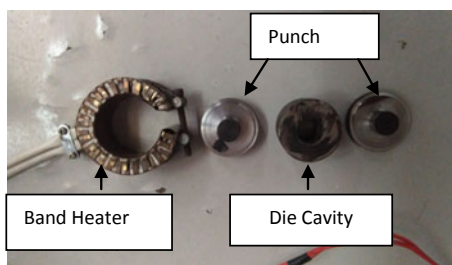
Fig. 6 Drop shape analyzer measuring the water contact angle

2.2 Characterization

2.2.1 Water Contact Angle Test

Wettability of samples was tested by performing the water contact angle test. ASTM D7334 standard for advancing contact angle measurement was used. Sessile drop method and ellipse fitting method was used to calculate the contact angle. Kruss made drop shape analyzer (DSA25) as shown in Fig. 6 was used to make and analyze the water drop on surface of samples. Plastic syringe of circular shape was used to make the drop of 0.5 mm diameter. Distilled water was used to make the drops. The angle which droplet made with surface of sample was recorded by high resolution cameras Fig. 7 shows the real time image of calculation of water contact angle on surface of PEEK and PEEK-5% MWCNT samples. Total 20 readings of angles on each surface were taken within 20 seconds and averages of these readings were considered as shown in Fig. 8 and Fig. 11.
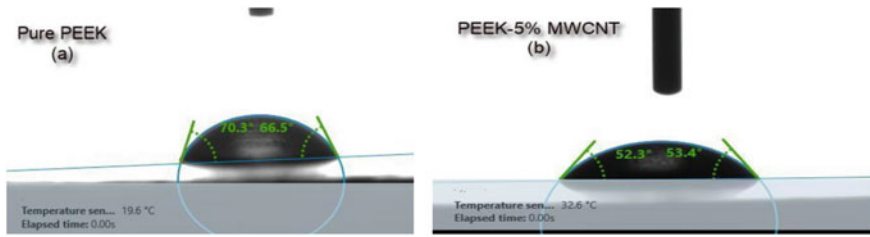
Fig. 7 Water contact angle of **(a)** pure and **(b)** PEEK-5% MWCNT
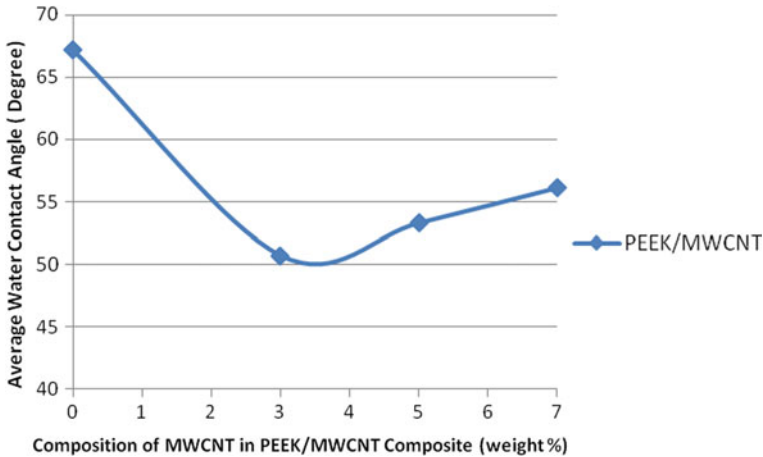
Fig. 8 Changes in average contact angle of PEEK/MWCNT samples with varying composition of MWCNT

2.2.2 Surface Characterization

Field Emission Scanning Electron Microscopy (FESEM) was performed on samples to observe the microstructure of composites. The samples were prepared by polishing with gold particles.

3 Result and Discussion

The water contact angle of pure PEEK is reported to be 67.18°. It is less than the reported water contact angle of PEEK in other works by small amount. It may be due to the micro porosity developed on surface due to entrapment of gases in small amount during compression molding of powder. However, design of die-heater setup was such that the chances of gas entrapment were very low. The step v/s angle graph in Fig. 9 shows that initial contact angle was 79.81° which decreases to 68.07° in next
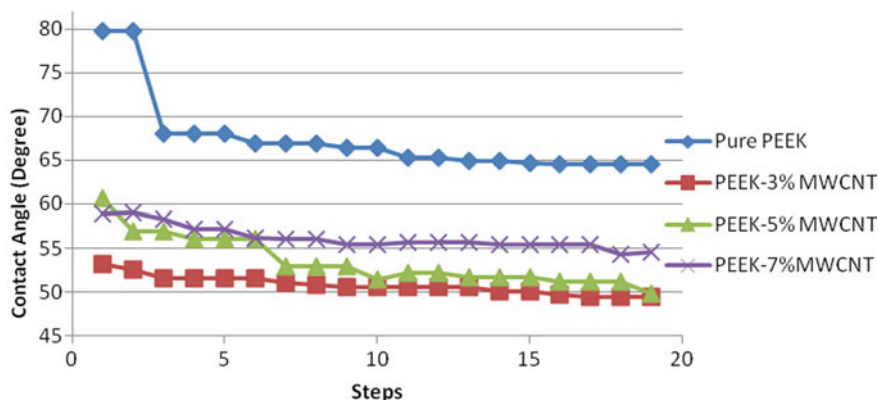
Fig. 9 Variations of water contact angle in different steps

step and remains almost constant afterward. On adding 3% of MWCNT, the water contact angle decreased to value of 50.71° as shown in Table 1 and Fig. 8. However after 3% MWCNT composition, it increased continues and reached to 56.09° at 7% MWCNT. This might have happened due to entanglement of MWCNT at higher composition as shown in FESEM image in Fig. 13(a). So the least value of water contact angle and further highest surface energy is obtained on surface of PEEK-3% MWCNT, which is 50.71°. This is 24.52% less than the contact angle obtained with pure PEEK. It is clear from Fig. 9 that the contact angle remains almost constant for all steps, shows that water did not sips into material with time. It is due to nonporous surface obtained by better blending and controlled compression molding process. Figure 10 shows the real time image of water contact angle on surface of PEEK-35%nHA nanocomposite.

The water contact angle of PEEK/nHA composite decreased continuously as shown in Table 2 and Fig. 11. This shows that surface energy and further bioactivity of PEEK/nHA samples increases with increasing composition of nHA. However, the decrement in contact angle is more noteworthy between 25 and 30% nHA than that of between 30 and 35% nHA. This may be due to more uniform distribution of nHA in PEEK at 30% composition. The FESEM image of PEEK/30% nHA in Fig. 13(b) shows the uniform distribution of nHA particles in PEEK. Figure 9 shows the real-time image of calculation of contact angle on surface of PEEK-35% nHA.

	Sr.No.	Sample	Contact angle
Table 1 Average water contact angle of PEEK/MWCNT composites	1.	Pure PEEK	67.18° (±4.54)
	2.	PEEK-3% MWCNT	50.71° (±1.03)
	3.	PEEK-5% MWCNT	53.28° (±2.79)
	4.	PEEK-7% MWCNT	56.09° (±1.42)
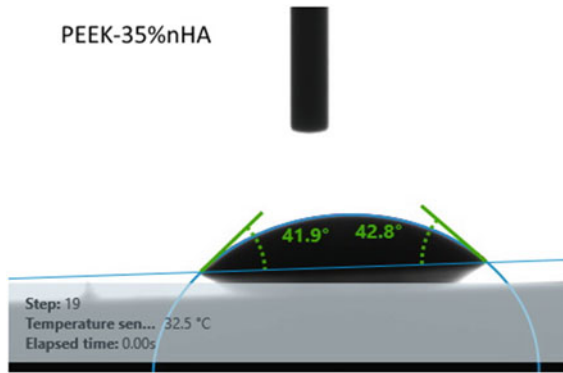
Fig. 10 Water contact angle of PEEK-35% nHA
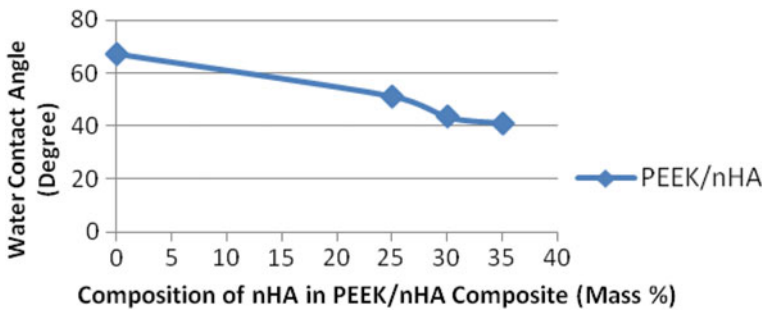
Fig. 11 Changes in average contact angle of PEEK/nHA surface with varying composition of nHA
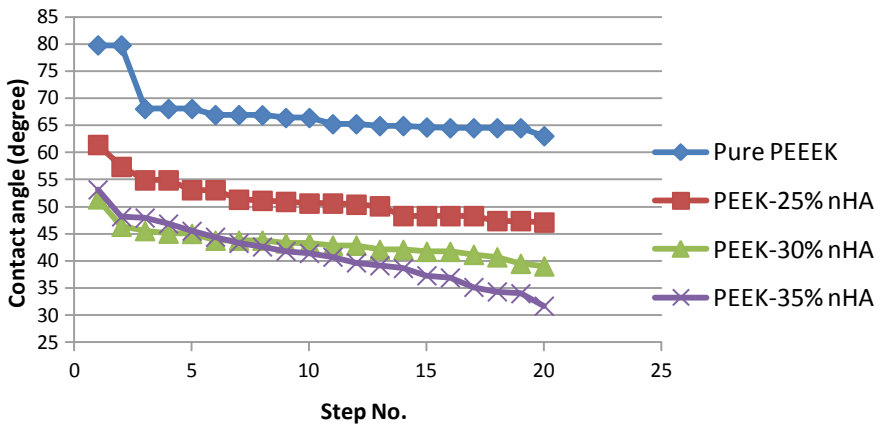
Fig. 12 Variation in contact angle in different steps
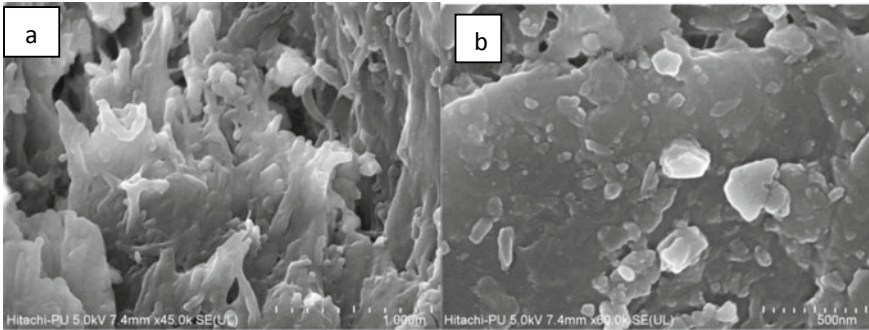
Fig. 13 FESEM images of **a** PEEK/7%–MWCNT and **b** PEEK/25% nHA samples

Table 2 Water contact angle of PEEK/nHA composite

Sr.No.	Sample	Contact angle
1.	Pure PEEK	67.18° (±4.54)
2.	PEEK-25% nHA	51.25° (±2.92)
3.	PEEK-30% nHA	43.35° (±3.12)
4.	PEEK-35% nHA	41.13° (±1.99)

The angle decreases gently with steps as shown in Fig. 12. This shows that the composite become more hydrophilic with time as water sip into the surface.

4 Conclusion

Bioactivity of biomaterial that intended to be used in bioimplants is depends upon surface energy or water contact angle. PEEK has poor bioactivity and need to be improved for more universal use of it in bio implants. Reinforcing with hydrophilic nanomaterial is one of the solutions to improve the bioactivity of PEEK. The powder mixing and compression molding method is best suited fabrication method for nanocomposites of PEEK, because it results in higher dense and stronger products. PEEK/MWCNT composite's water contact angle decreased up to 3% composition of MWCNT by weight to 50.71°, which is 16.47° less than that of pristine PEEK. It indicates that the wettability of PEEK/MWCNT enhances at lower dose of MWCNT. However at higher dose of MWCNT than 3% by weight, the water contact angle started increasing. The PEEK/nHA composite showed continues decrement in contact angle with increasing nHA % composition by weight. The PEEK-35%nHA sample showed 41.13° water contact angle, which is 38.77% less than the water contact angle of pristine PEEK. This implies that by reinforcing the PEEK with MWCNT and n-HA, the wettability and further the bioactivity of PEEK can be enhanced.

References

1. Williams, D.: Polyetheretherketone for long-term implantable devices. Med. Device Technol. **19**(1), 8–10 (2008)
2. Kurtz, S.M., Devine, J.N.: PEEK biomaterials in trauma, orthopedic, and spinal implants. Biomaterials **28**(32), 4845–4869 (2007)
3. He, M., Chen, X., Guo, Z., Qiu, X., Yang, Y., Su, C., et al.: Super tough graphene oxide reinforced polyetheretherketone for potential hard tissue repair applications. Compos. Sci. Technol. **174**, 194–201 (2019)
4. Wang, H., Xu, M., Zhang, W., Kwok, D.T.K., Jiang, J., Wu, Z., et al.: Mechanical and biological characteristics of diamond-like carbon coated poly aryl-ether-ether-ketone. Biomaterials **31**(32), 8181–8187 (2010)
5. Kurtz, S.M., Lanman, T.: Dynamic stabilization and semirigid PEEK rods for spinal fusion. In: PEEK Biomaterials Handbook. Elsevier, pp. 281–289 (2019)
6. Mishra, S., Chowdhary, R.: PEEK materials as an alternative to titanium in dental implants: a systematic review. Clin. Implant. Dent. Relat. Res. **21**(1), 208–222 (2019)
7. Murugan, R., Ramakrishna, S.: Development of nanocomposites for bone grafting. Compos Sci Technol. **65**(15–16), 2385–2406 (2005)
8. Ramakrishna, S., Mayer, J., Wintermantel, E., Leong, K.W.: Biomedical applications of polymer-composite materials: a review. Compos. Sci. Technol. **61**(9), 1189–1224 (2001)
9. Bahmani, A., Comeau, P.A., Montesano, J., Willett, T.L.: Extrudable hydroxyapatite/plant oil-based biopolymer nanocomposites for biomedical applications: Mechanical testing and modeling. Mater. Des. **174**, 107790 (2019)
10. Li, K., Yeung, C.Y., Yeung, K.W.K., Tjong, S.C.: Sintered hydroxyapatite/polyetheretherketone nanocomposites: mechanical behavior and biocompatibility. Adv. Eng. Mater. **14**(4), B155–B165 (2012)
11. Bansal, S.A., Singh, A.P., Kumar, S.: Synergistic effect of graphene and carbon nanotubes on mechanical and thermal performance of polystyrene. Mater. Res. Express. **5**(7), 75602 (2018)
12. Bai, Y., Shen, B., Zhang, S., Zhu, Z., Sun, S., Gao, J., et al.: Mechanical energy: storage of mechanical energy based on carbon nanotubes with high energy density and power density (Adv. Mater. 9/2019). Adv. Mater. **31**(9), 1970064 (2019)
13. Balasundaram, G., Webster, T.J.: An overview of nano-polymers for orthopedic applications. Macromol. Biosci. **7**(5), 635–642 (2007)
14. von der Mark, K., Park, J.: Engineering biocompatible implant surfaces. Part II: Cellular recognition of biomaterial surfaces: Lessons from cell-matrix interactions. Prog. Mater. Sci. **58**, 327–381 (2012)
15. Durrieu, M.-C., Pallu, S., Guillemot, F., Bareille, R., Amédée, J., Baquey, C.H., et al.: Grafting RGD containing peptides onto hydroxyapatite to promote osteoblastic cells adhesion. J. Mater. Sci. Mater. Med. **15**(7), 779–786 (2004)
16. Thakral, GK., Thakral, R., Sharma, N., Seth, J., Vashisht, P.: Nanosurface–the future of implants. J. Clin. Diagnostic Res. JCDR. **8**(5), ZE07 (2014)
17. Webster, T.J., Ergun, C., Doremus, R.H., Siegel, R.W., Bizios, R.: Specific proteins mediate enhanced osteoblast adhesion on nanophase ceramics. J. Biomed. Mater. Res. An Off J Soc Biomater Japanese Soc Biomater Aust Soc Biomater Korean Soc Biomater. **51**(3), 475–483 (2000)
18. Kumar, M., Kumar, R., Kumar, S., Prakash, C.: Biomechanical properties of orthopedic and dental implants: a comprehensive review. In: Handbook of Research on Green Engineering Techniques for Modern Manufacturing. IGI Global, pp. 1–13 (2019)
19. Ma, R., Tang, T.: Current strategies to improve the bioactivity of PEEK. Int. J. Mol. Sci. **15**(4), 5426–5445 (2014)
20. Wang, L., He, S., Wu, X., Liang, S., Mu, Z., Wei, J., et al.: Polyetheretherketone/nano-fluorohydroxyapatite composite with antimicrobial activity and osseointegration properties. Biomaterials [Internet]. **35**(25), 6758–6775. Available from: http://dx.doi.org/10.1016/j.biomaterials.2014.04.085 (2014)

21. Majeed, S., Fierro, D., Buhr, K., Wind, J., Du, B., Boschetti-de-Fierro, A., et al.: Multi-walled carbon nanotubes (MWCNTs) mixed polyacrylonitrile (PAN) ultrafiltration membranes. J. Memb. Sci. **403**, 101–109 (2012)
22. Choi, J.-H., Jegal, J., Kim, W.-N.: Fabrication and characterization of multi-walled carbon nanotubes/polymer blend membranes. J. Memb. Sci. **284**(1–2), 406–415 (2006)
23. Xu, A., Liu, X., Gao, X., Deng, F., Deng, Y., Wei, S.: Enhancement of osteogenesis on micro/nano-topographical carbon fiber-reinforced polyetheretherketone-nanohydroxyapatite biocomposite. Mater. Sci. Eng. C. [Internet] **48**, 592–598. Available from: http://dx.doi.org/10.1016/j.msec.2014.12.061 (2015)

Developments in Metallic Biomaterials and Surface Coatings for Various Biomedical Applications

Gurmohan Singh and Abhineet Saini

1 Introduction to Metallic Biomaterials

The use of metallic biomaterials in medical treatments can be dated back to about early twentieth century [1, 2]. Metallic biomaterials are used as implant devices and attribute for 70–80% of all the implants used in human body [3–5]. Applications of metallic biomaterials include repair of bones, repair of hard tissues, repair of fractures, etc. [6, 7]. Metallic biomaterials are preferred choice to be used in implants because they exhibit mechanical properties such as durability, corrosion resistance, high strength and toughness [7–9], and thus are used for replacing and restructuring various structural parts of human body. Because of ever-increasing world population and increase in number of traumas, there is an extensive demand of metallic biomaterials to be used as knee joint prosthesis, shoulder prosthesis, dental implants and bone fixations [10–12], with desirable mechanical properties so as they match the requirement of the human body. The metallic biomaterials can be mainly subdivided into these broad categories: stainless steel (316L), titanium-based alloys and cobalt-based alloys [13, 14]. For being used as implants, the metallic alloys have to own similar characteristics as that of human bones [15]. Table 1 summarises the clinical application of broad categories of biomaterials [11].

Amongst the three main commercially used implant devices, namely, stainless steel, titanium alloy and Co–Cr alloys, titanium and its alloys are considered to have the best biocompatibility [16]. Titanium, having an atomic number 22, is a silvery-grey metallic element in its pure form. Titanium is extracted from ores of Ilmenite ($FeTiO_3$) and Rutile (TiO_2), using Kroll's process, and is used especially in alloys,

G. Singh (✉)

Chitkara University School of Engineering and Technology, Chitkara University, Baddi, Himachal Pradesh, India

e-mail: gurmohan.singh@chitkarauniversity.edu.in

A. Saini

Chitkara University Institute of Engineering and Technology, Chitkara University, Rajpura, Punjab, India

197

Table 1 Applications of various metallic biomaterials [11]

Metallic biocompatible implants	Primary utilizations	Reference
Stainless steel	Fasteners (screws, nails), plates and hip bone replacement	[19]
Co-based alloys	Hip bones and dentistry castings	[19]
Ti-based alloys	Knee and hip replacements, dentures, fasteners and pacemakers	[22]
Mg-based alloys	Biodegradable orthopaedic implants	[22, 23]
NiTi	Orthodontic dental arch wires, orthopaedic staples, vascular stents, filters and catheter guide wires	[24, 25]
Ta	Sutures for neurosurgery and plastic surgery, and radiographic marker	[25]

refractory materials, pigments and medical as well as dental devices. Although titanium is the fourth most abundantly available metal in Earth's crust after aluminium, iron and magnesium, it is rarely found in high concentrations and never found in a pure state, so the extraction as well as processing of titanium results in higher cost of production. Saini et al. (2016) presented an in-depth review of various challenges faced in machining of titanium alloy [17]. But, with ever-increasing demand of implants and also due to its other applications in number of markets such as aerospace, sports and other industries, the prices of titanium alloys are coming down [18].

The major reason for this preference of titanium alloys is its lower Young's modulus, excellent anti-corrosive properties and lower density as compared to stainless steels and Co–Cr alloys. Young's modulus of titanium alloys closely matches with Young's moduli of the material of human bone which results in good remodelling as the load is transferred through both the implant and the bone [19]. Titanium alloys show excellent resistance for crevice as well as in vivo corrosion, hence increasing the life span of implants [20]. Furthermore, density of titanium alloys at 4.5 g/cm^3, which is almost half of the density of stainless steel alloys, is shown in Table 2 [21].

Table 2 Selected physical properties of titanium, compared to other metals

Property	Ti	Al	Fe	Ni
Density [g/cm^3]	4.5	2.7	7.9	8.9
Melting point [°C]	1670	660	1538	1455
Thermal conductivity [W/mK]	15–22	221–247	68–80	72–92
Elastic modulus [GPa]	115	72	215	200
Reactivity with oxygen	High+	High	Low	Low
Corrosion resistance	High+	High	Low	Medium

Table 3 Various titanium-based alloys used for biomedical applications [26]

S.No.	Application	Titanium alloy type
1	Biomedical applications	Ti–Mo, Ti–Mn, Ti–6Al–4 V, Ti–Nb–Zr, Ti–Nb–Si, Ti–Mo–Nb, Ti–Ta–Nb, Ti–Zr–Cr–Al, Ti–Mo–Zr–Cr, Ti–Zr–Cr–Sn, Ti–Nb–Mo–Sn
2	Dental applications	Ti–V, Ti–Si, Ti–Nb–Sn, Ti–Ag–Cu, Ti–Cr–Cu
3	Orthopaedic applications	Ti–Nb–Fe, Ti–Mo–Zr–Fe, Ti–Nb–Ta–Zr, Ti–Mo–Nb–Zr
4	Biomedical shape memory alloys	Ti–Nb, Ti–Nb–Zr–Sn
5	Shape memory and superelastic alloys	Ti–Fe–Sn, Ti–Ta–Zr, Ti–Ta–Sn
6	Implant materials	Ti–Zr, Ti–Nb–Sn, Ti–Mo–Zr–Fe, Ti–Nb–Ta–Zr, Ti–Nb–Ta–Sn, Ti–Nb–Ta–Mo, Ti–Ta–Nb–Zr, Ti–Zr–Hf–Fe
7	Prosthesis applications	Ti–Al–Nb, Ti–Al–Fe, Ti–Cr–Cu, Ti–Ta–Hf–Zr, Ti–Zr–Cr–Mo

1.1 Applications of Titanium and Its Alloys in Various Biomedical Fields

As discussed in earlier paragraphs, because of its desirable mechanical properties titanium and its alloys are quickly becoming the first choice for commercial development of implants and other biomedical fields. In Table 3, various applications and fields are described, where different titanium alloys are being used.

However, one problem with most commonly used titanium alloy for implants, i.e. Ti–6Al–4 V, is that the alloying elements Al and V can cause various health-related issues over the period of time such as allergic reaction, neurological disorders, cytotoxic reactions, decrease in cell growth and mutagenic reactions [27–30]. Bio-functionality of the metallic biomaterials is another concern, because bio-functions cannot be added during the process of manufacturing [31, 32]. As all the metal implants are artificial bio-inert materials, to make them bioactive, we need to apply some coatings over artificial surface of the implant, so that we get desirable properties which match the human body requirements.

2 Surface Coatings of Metallic Biomaterials

Hydroxyapatite (HAp) having chemical formula $Ca_{10}(PO_4)_6(OH)_2$ is the main inorganic component of bones and is majorly used as a coating onto the metallic implants. The major aim of using HAp coatings is to improve mechanical properties of the metallic implants [33] and to make the implant bioactive. Many researchers have

proven that controlled osseointegration can be done more rapidly with HAp adhesion [34].There are various coating techniques, which can be used to deposit hydroxyapatite coating on the metallic implants such as plasma sprayed coating technique, hot isostatic pressing technique, thermal spray coating technique, dip coating technique and sol–gel technique, etc. Table 4 summarises the various coating techniques used to deposit HAp coating and key points [41].

Cohesion and adhesion are two properties on which the durability and performance of coating depend. Combination of cohesion strength and adhesion strength is known as bonding effectiveness. Cohesion is the internal binding of particles within the adhesive or a coating while adhesion is ability of the adhesive to bind with different types of substrates/layers [46, 47]. Mechanical adhesion, specific adhesion and effective adhesion are three basic types of adhesion which are considered [48, 49]. Molecular attraction within contacting surface is referred to as specific adhesion and adhesion between surface to be bonded and the adhesive is called as mechanical adhesion. So, for a good bonding effectiveness, combination of both mechanical and

Table 4 Various techniques to deposit HAp

Name of technique	Key points	Reference
Plasma sprayed technique	Easy to use and ability to bond with the bone	[35, 36]
Hot isostatic pressing technique	Improved adhesion strength and improved porosity	[37]
Thermal spray coating technique	High deposition rate at low cost, poor adhesion amongst coating and substrate, and non-uniformity in crystal structure resulting in reduced lifetime of implants	[38–40]
Dip coating technique	Surface uniformity, short processing time even for complex shapes, least reaction as well as decomposition with the metal substrate	[41]
Pulsed laser deposited coating technique	For controlled micro-structure generation, helpful in improving bio-functionality of materials with modified surface textures, with limitation of deposition due to splashing of particulates onto the film	[42]
Electrophoretic deposition coating technique	Uniformity of coating and good sinter ability of the deposits, possibility of composite material deposition and deposition onto porous substrates as well	[43].
Sol–gel method	Low-temperature nature and ease of processing used for composite coating at nano levels	[44, 45]
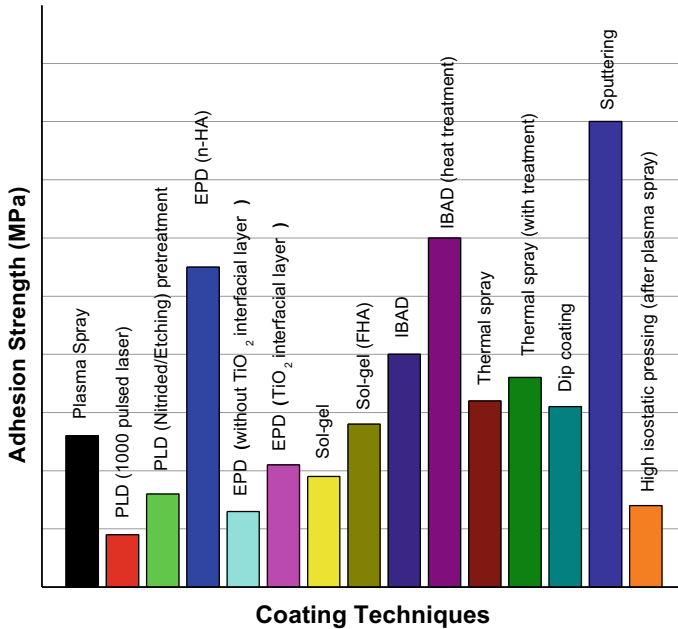
Fig. 1 Comparison of adhesion strength values for hydroxyapatite deposited by various techniques onto Ti–6Al–4 V alloy [41]

specific adhesion is vital. Figure 1 depicts the comparison of adhesion strength values for hydroxyapatite deposited by various techniques onto Ti–6Al–4 V alloy [41, 47, 50].

3 Current Issues of Coating for Metallic Biomaterials

The current coating techniques have resulted in certain limitations of HAp-based coatings onto metallic substrates. Some are related to coating and substrate bonding characteristics and some present limitations in terms of coating material and the methodologies followed for deposition. Here, certain significant reasons for this behaviour have been discussed.

Poor adhesion bonding and uniformity of coating: Since many years, hydroxyapatite is used as the major coating materials to improve bioactivity of titanium implants. Most of the research in this regard is carried out on Ti–6Al–4 V alloy [41, 47, 50]. Various techniques used for depositing the HAp coating were discussed in previous section and summarised in Table 4 [41]. The major issue with most of the techniques discussed is related to their poor adhesion bonding and the uniformity of coating on the metallic surface. Whenever the coating separation takes place either due to adhesion breaking apart or due to splitting of adhesion from substrate the

adhesion bonding is considered failed and due to which the implant as well as the surrounding human tissues will be exposed leading to a clinical consequence.

Poor antimicrobial property: Very common problems that are encountered whenever a metallic implant is transplanted into the human body are itching in the area near metallic implant, formation of puss cells, loosening of implants and the patient has to be re-operated for the same. All these problems that are stated above are bacteria-associated disease and are because of poor antimicrobial properties of pure HAp coating. If during the time of implant surgery even a small population of bacteria is present, it will keep growing over the HAp surface and can cause all these problems. These diseases carry a serious hazard for patient health as well as cause economical burden at same time [51].

Other than these two major issues with HAp coating, there are some other limitations such as low tensile strength and fracture toughness. To address these issues, various researchers have come forward with newer coatings and materials as discussed in detail in forthcoming paragraphs.

4 Newer Techniques of Functional Improvements of Metallic Biomaterials

The newer techniques to enhance the properties of biomaterials to mimic human body biological behaviour include certain promising techniques discussed further.

Peptide Coatings: Peptides, more commonly known as proteins, contains amino acid chained together. When the chain is of two peptides, it is called as di-peptide and if the chain consists of large number of amino acids, then it is known as polypeptide. Polypeptides can be used to increase cell adhesion on metallic surfaces because when we keep on adding amino acids in the polypeptide, the interactions between cells and the material surfaces can be increased which results in improved adhesion strength when polypeptide scaffolds are immobilised on to the surface of metallic implants [52]. Kelly et al. (2015) presented the technique to bind peptides on both hydroxyapatite and titanium through electrostatic interactions, and concluded that peptides can work as a unique linking molecule that will help in better binding of hydroxyapatite with titanium implants and it is simpler and economical than other commercial methods. Furthermore, it is concluded from tests that this process gave faster deposition of HAp on titanium surface [53].

Bioactive Glass coatings: Bioactive glasses are considered to be the benchmark materials in the field of biomaterials and were invented in late 1960s. As the name suggests these materials help in regeneration and self-repair of tissue cells as they are known to show good bonding with both hard and soft living tissues. Bioactive glasses find their applications as coatings where it is required to combine the already existing good mechanical properties of implant with high bioactivity. Bioactive glass coating is also used to add functions such as antimicrobial properties, etc. In recent years, apart from traditional application as discussed, the bioactive glass coatings

have also found their applications in variety of other areas as well, and some of these applications are polymeric meshes, ocular implants, 3-D porous scaffolds, etc. [54, 55].

Composite HAp Coatings: To improve the mechanical properties of HAp, some researchers have added other elements with HAp [56–58]. One of the most commonly researched examples of composite HAp coatings are hydroxyapatite/chitosan (HAp/CS) films, which primarily improves the adhesion strength of HAp coating and is prepared by chemical electro-deposition method [59, 60]. The composite coating made from mixing calcium silicate ($CaSiO_3$) with HAp is another example of composite coating and it shows better biocompatibility than the HAp coating mainly because of its porous structure [59, 61]. Oxides of some metals are also used as additives to improve properties of HAp coatings, and many recent studies have studied the effect of addition of oxides of titanium, zirconia, aluminium, etc. in the HAp coatings. Kiran et al. (2018) developed a composite coating based on titanium dioxide and electro spun poly(ε-caprolactone) on pure titanium substrates and concluded that the composite coating developed can be used to change the surface of cp-Ti implants to improve its antibacterial as well as biological properties [51]. Roxana et al. (2012) combined the alumina, Al_2O_3 and zirconia, ZrO_2 to form a composite HAp coating. The major advantage of zirconia is its high strength and fracture toughness, so it provides excellent mechanical properties to the composite coating; at the same time, the other constituent of the composite coating that is alumina is a bio-inert metal and provides chemical inertness to the composite coating [62, 63].

5   Conclusion

With ageing population all around the world and ever-increasing health complications, the demand for metallic implants is always going to be extensive. During last few decades lots of researches have been done to design metallic implants with desirable mechanical properties that can match the properties of human bones and tissues. For this purpose, various types of metals are researched but titanium and its alloys have been the most widely used in manufacturing of biometallic implants because of their desirable mechanical properties, coupled with hydroxyapatite coatings as the HAp coatings provide the required bioactive environment for the tissue cells growth on the implant. Over the period of time, certain issues have cropped up related to poor adhesion strength and non-uniformity of coating, poor antimicrobial properties, low tensile strength and ductility of HAp coatings. To overcome these limitations, researchers across the globe have come up with novel ideas, such as introduction of proteins, glass coatings and composite HAP coatings. But, because of the ever-evolving nature of medical sciences and need to improve the mechanical as well as biological properties of the implant, there is still a huge potential of research in the area of biometallic implants.

References

1. Saini, M., Singh, Y., Arora, P., Arora, V., Jain, K.: Implant biomaterials: a comprehensive review. World J. Clin Case. WJCC **3**(1), 52–57 (2015)
2. Hanawa, T.: In vivo metallic biomaterials and surface modification. Mater. Sci. Eng. A. **267**(2), 260–266 (1999)
3. Breme, H., Biehl, V., Reger, N., Gawalt, E.: A metallic biomaterials: Introduction. In Handbook of Biomaterial Properties, pp. 151–158. Springer, New York, NY (2016)
4. Navarro, M., Michiardi, A., Castano, O., Planell, J.A.: Biomaterials in orthopaedics. J. R. Soc. Interface **5**(27), 1137–1158 (2008)
5. Baino, F., Potestio, I.: Orbital implants: state-of-the-art review with emphasis on biomaterials and recent advances. Mater. Sci. Eng. C **69**, 1410–1428 (2016)
6. Niinomi, M.: Mechanical properties of biomedical titanium alloys. Mater. Sci. Eng. A **243**(1–2), 231–236 (1998)
7. Manam, N.S., Harun, W.S.W., Shri, D.N.A., Ghani, S.A.C., Kurniawan, T., Ismail, M.H., Ibrahim, M.H.I.: Study of corrosion in biocompatible metals for implants: a review. J. Alloy. Compd. **701**, 698–715 (2017)
8. Kuroda, P.A.B., Buzalaf, M.A.R., Grandini, C.R.: Effect of molybdenum on structure, microstructure and mechanical properties of biomedical Ti-20Zr-Mo alloys. Mater. Sci. Eng. C. **67**, 511–515 (2016)
9. Michael, F.M., Khalid, M., Walvekar, R., Ratnam, C.T., Ramarad, S., Siddiqui, H., Hoque, M.E.: Effect of nanofillers on the physico-mechanical properties of load bearing bone implants. Mater. Sci. Eng. C. **67**, 792–806 (2016)
10. Manivasagam, G., Dhinasekaran, D., Rajamanickam, A.: Biomedical implants: corrosion and its prevention-a review. Recent Pat. Corro. Sci. **2**, 40–54 (2010)
11. Chen, Q., Thouas, G.A.: Metallic implant biomaterials. Mater. Sci. Eng. R. Rep. **87**, 1–57 (2015)
12. Tang, T.T., Qin, L.: Translational study of orthopaedic biomaterials and devices. J. Orthop. Trans. **5**, 69–71 (2016)
13. Wang, K.K., Wang, A., Gustavson, LJ.: Metal-on-metal wear testing of Co-Cr alloys. In Cobalt-base alloys for biomedical applications. ASTM International, 135–144 (1999)
14. Niinomi, M.: Recent metallic materials for biomedical applications. Metall. Mater. Trans. A. **33**(3), 477–486 (2002)
15. Harun, W.S.W., Asri, R.I.M., Alias, J., Zulkifli, F.H., Kadirgama, K., Ghani, S.A.C., Shariffuddin, J.H.M.: A comprehensive review of hydroxyapatite-based coatings adhesion on metallic biomaterials. Ceram. Int. **44**(2), 1250–1268 (2018)
16. Yamamuro, T.: Patterns of osteogenesis in relation to various biomaterials. J. Jpn. Soc. Biomater. **7**, 19–23 (1989)
17. Saini, A., Pabla, B.S., Dhami, S.S.: Developments in cutting tool technology in improving machinability of Ti6Al4V alloy: a review. Proc. Inst. Mech. Eng. Part B: J. Eng. Manuf. **230**(11), 1977–1989 (2016)
18. Froes, F.H.: How to market titanium: lower the cost. JOM **56**(2), 39 (2004)
19. Niinomi, M., Nakai, M., Hieda, J.: Development of new metallic alloys for biomedical applications. Actabiomaterialia **8**(11), 3888–3903 (2012)
20. Niinomi, M., Boehlert, C.J.: Titanium alloys for biomedical applications. In Advances in Metallic Biomaterials, pp. 179–213. Springer, Berlin, Heidelberg (2015)
21. Veiga, C., Davim, J.P., Loureiro, A.J.R.: Properties and applications of titanium alloys: a brief review. Rev. Adv. Mater. Sci. **32**(2), 133–148 (2012)
22. Olding, T., Sayer, M., Barrow, D.: Ceramic sol–gel composite coatings for electrical insulation. Thin Solid Films **398**, 581–586 (2001)
23. Dorozhkin, S.V.: Calcium orthophosphate coatings on magnesium and its biodegradable alloys. Actabiomaterialia **10**(7), 2919–2934 (2014)
24. Liu, J.X., Yang, D.Z., Shi, F., Cai, Y.J.: Sol–gel deposited TiO2 film on NiTi surgical alloy for biocompatibility improvement. Thin Solid Films **429**(1–2), 225–230 (2003)

25. Kohn, D.H.: Metals in medical applications. Curr. Opin. Solid State Mater. Sci. **3**(3), 309–316 (1998)
26. Dinu, M., Franchi, S., Pruna, V., Cotrut, C.M., Secchi, V., Santi, M., Vladescu, A.: Ti-Nb-Zr system and its surface biofunctionalization for biomedical applications. In Titanium in Medical and Dental Applications, pp. 175–200. Woodhead Publishing (2018)
27. Niinomi, M.: Titanium alloys with high biological and mechanical biocompatibility. In Biomaterials in Asia: In Commemoration of the 1st Asian Biomaterials Congress, Tsukuba, Japan, pp. 269–290. World Scientific (2008)
28. Zhao, X., Niinomi, M., Nakai, M., Ishimoto, T., Nakano, T.: Development of high Zr-containing Ti-based alloys with low Young's modulus for use in removable implants. Mater. Sci. Eng. C. **31**(7), 1436–1444 (2011)
29. Rao, S., Ushida, T., Tateishi, T., Okazaki, Y., Asao, S.: Effect of Ti, Al, and V ions on the relative growth rate of fibroblasts (L929) and osteoblasts (MC3T3-E1) cells. Bio-Med. Mater. Eng. **6**(2), 79–86 (1996)
30. Perl, D.P., Moalem, S.: Aluminum and Alzheimer's disease, a personal perspective after 25 years. J. Alzheimers Dis. **9**(s3), 291–300 (2006)
31. Kannan, M.B.: Hydroxyapatite coating on biodegradable magnesium and magnesium-based allcccdoys. In Hydroxyapatite (HAp) for Biomedical Applications (pp. 289–306). Woodhead Publishing (2015)
32. Xiao, M., Chen, Y.M., Biao, M.N., Zhang, X.D., Yang, B.C.: Bio-functionalization of biomedical metals. Mater. Sci. Eng. C. **70**, 1057–1070 (2017)
33. Hadidi, M., Bigham, A., Saebnoori, E., Hassanzadeh-Tabrizi, S.A., Rahmati, S., Alizadeh, Z.M., Rafienia, M.: Electrophoretic-deposited hydroxyapatite-copper nanocomposite as an antibacterial coating for biomedical applications. Surf. Coat. Technol. **321**, 171–179 (2017)
34. Harun, W.S.W., Asri, R.I.M., Sulong, A.B., Ghani, S.A.C., Ghazalli, Z.: Hydroxyapatite-based coating on biomedical implant. Hydroxyapatite: Advances in Composite Nanomaterials, Biomedical Applications and its Technological Facets, pp. 69–88 (2018)
35. Groot, K.D., Geesink, R., Klein, C.P.A.T., Serekian, P.: Plasma sprayed coatings of hydroxyapatite. J. Biomed. Mater. Res. **21**(12), 1375–1381 (1987)
36. Sun, L., Berndt, C.C., Gross, K.A., Kucuk, A.: Material fundamentals and clinical performance of plasma-sprayed hydroxyapatite coatings: a review. J. Biome. Mater. Res. Off. J. Soc. Biomater. Jpn. Soc. Biomater. Aust. Soc. Biomater. Korean Soc. Biomater. **58**(5), 570–592 (2001)
37. Khor, K.A., Yip, C.S., Cheang, P.: Post-spray hot isostatic pressing of plasma sprayed Ti-6Al-4 V/hydroxyapatite composite coatings. J. Mater. Process. Technol. **71**(2), 280–287 (1997)
38. Yang, Y., Dennison, D., Ong, J.L.: Protein adsorption and osteoblast precursor cell attachment to hydroxyapatite of different crystallinities. Int. J. Oral Maxillofacial Implants, **20**(2) (2005)
39. Cheang, P., Khor, K.A.: Addressing processing problems associated with plasma spraying of hydroxyapatite coatings. Biomaterials **17**(5), 537–544 (1996)
40. Hanyaloglu, C., Aksakal, B., Bolton, J.D.: Production and indentation analysis of WC/Fe–Mn as an alternative to cobalt-bonded hardmetals. Mater. Charact. **47**(3–4), 315–322 (2001)
41. Mohseni, E., Zalnezhad, E., Bushroa, A.R.: Comparative investigation on the adhesion of hydroxyapatite coating on Ti–6Al–4 V implant: a review paper. Int. J. Adhes. Adhes. **48**, 238–257 (2014)
42. Cheung, J.T.: History and fundamentals of pulsed laser deposition Pulsed Laser Deposition of Thin Films ed DB Chrisey and G Hubler (1994)
43. Zhitomirsky, I., Gal-Or, L.: Electrophoretic deposition of hydroxyapatite. J. Mater. Sci. Mater. Med. **8**(4), 213–219 (1997)
44. Liu, D.M., Yang, Q., Troczynski, T.: Sol–gel hydroxyapatite coatings on stainless steel substrates. Biomaterials **23**(3), 691–698 (2002)
45. Piveteau, L.D., Gasser, B., Schlapbach, L.: Evaluating mechanical adhesion of sol–gel titanium dioxide coatings containing calcium phosphate for metal implant application. Biomaterials **21**(21), 2193–2201 (2000)

46. Packham, D.E.: The mechanical theory of adhesion. Handbook of Adhesive Technology, 69–93 (2003)
47. Surmenev, R.A.: A review of plasma-assisted methods for calcium phosphate-based coatings fabrication. Surf. Coat. Technol. **206**(8–9), 2035–2056 (2012)
48. Artzi, N., Zeiger, A., Boehning, F., bon Ramos, A., Van Vliet, K., Edelman, E.R.: Tuning adhesion failure strength for tissue-specific applications. Actabiomaterialia, **7**(1), 67–74 (2011)
49. Packham, D.E.: Surface energy, surface topography and adhesion. Int. J. Adhes. Adhes. **23**(6), 437–448 (2003)
50. Surmenev, R.A., Surmeneva, M.A., Ivanova, A.A.: Significance of calcium phosphate coatings for the enhancement of new bone osteogenesis–a review. Actabiomaterialia **10**(2), 557–579 (2014)
51. Kiran, A., Kumar, T.S., Sanghavi, R., Doble, M., Ramakrishna, S.: Antibacterial and bioactive surface modifications of titanium implants by PCL/TiO2 nanocomposite coatings. Nanomaterials **8**(10), 860 (2018)
52. Wronska, M.A., O'Connor, I.B., Tilbury, M.A., Srivastava, A., Wall, J.G.: Adding functions to biomaterial surfaces through protein incorporation. Adv. Mater. **28**(27), 5485–5508 (2016)
53. Kelly, M., Williams, R., Aojula, A., O'Neill, J., Trzińscka, Z., Grover, L., de Cogan, F.: Peptide aptamers: Novel coatings for orthopaedic implants. Mater. Sci. Eng. C. **54**, 84–93 (2015)
54. Baino, F., Verné, E.: Glass-based coatings on biomedical implants: A state-of-the-art review. Biomed. Glass. **3**(1), 1–17 (2017)
55. Bilsel, Y., Abci, I.: The search for ideal hernia repairs; mesh materials and types. Int. J. Surg. **10**(6), 317–321 (2012)
56. Barabás, R., Katona, G., Bogya, E.S., Diudea, M.V., Szentes, A., Zsirka, B., Czikó, M.: Preparation and characterization of carboxyl functionalized multiwall carbon nanotubes–hydroxyapatite composites. Ceram. Int. **41**(10), 12717–12727 (2015)
57. Kanhed, S., Awasthi, S., Goel, S., Pandey, A., Sharma, R., Upadhyaya, A., Balani, K.: Porosity distribution affecting mechanical and biological behaviour of hydroxyapatite bioceramic composites. Ceram. Int. **43**(13), 10442–10449 (2017)
58. Mukherjee, S., Kundu, B., Chanda, A., Sen, S.: Effect of functionalisation of CNT in the preparation of HAp–CNT biocomposites. Ceram. Int. **41**(3), 3766–3774 (2015)
59. Huang, Y., Han, S., Pang, X., Ding, Q., Yan, Y.: Electro deposition of porous hydroxyapatite/calcium silicate composite coating on titanium for biomedical applications. Appl. Surf. Sci. **271**, 299–302 (2013)
60. Czechowska, J., Zima, A., Siek, D., Ślósarczyk, A.: The importance of chitosan and nano-TiHA in cement-type composites on the basis of calcium sulfate. Ceram. Int. **42**(14), 15559–15567 (2016)
61. Kezhi, L., Qian, G., Leilei, Z., Yulei, Z., Shoujie, L., Kebing, G., Shaoxian, L.: Synthesis and characterization of Si-substituted hydroxyapatite bioactive coating for SiC-coated carbon/carbon composites. Ceram. Int. **43**(1), 1410–1414 (2017)
62. Family, R., Solati-Hashjin, M., Nik, S.N., Nemati, A.: Surface modification for titanium implants by hydroxyapatite nanocomposite. Caspian J. Intern. Med. **3**(3), 460 (2012)
63. Mobasherpour, I., Hashjin, M.S., Toosi, S.R., Kamachali, R.D.: Effect of the addition ZrO2–Al2O3 on nanocrystalline hydroxyapatite bending strength and fracture toughness. Ceram. Int. **35**(4), 1569–1574 (2009)

Effects of Shielded Metal Arc Welding Process Parameters on Dilution in Hardfacing of Mild Steel Using Factorial Design

Mandeep Singh, Loveleen Kumar Bhagi, and Hitesh Arora

1 Introduction

The components exposed to mechanical wear, abrasion, impact, fretting, erosion, and cavitations are generally deposited with thick coating of wear- and corrosion-resistant material through the technique called hardfacing [1]. Hardfacing is carried out by welding or spraying the hard metal over the base metal. SMAW is highly recommended for hardfacing, as of its low cost, versatility, and the availability of a wide range of sizes and type of hardfacing electrodes [2–5]. Welding can be done on any size and shape of job, in any position and at any location. Further, heat input rate controls the percentage dilution of the electrode material by base metal and can easily cover irregular areas [6]. Leitner et al. [7] in order to increase the service life and wear resistance of structural component investigated the effect of hardfacing done by arc welding of mild steel S355 with metal-cored and solid wire. Various researchers working in this field have observed that dilution has significant impact over wear resistance and numerous attempts have been made to find the association between welding parameters and dilution [8]. In arc welding, voltage, current, polarity, and travel speed have a significant effect on the dilution, whereas electrode stick out, electrode diameter, and preheat are found to have relatively little effect [9]. Banovic et al. discerned that there has been substantial correlation between arc current and dilution. Further, the author inferred high current intensities cause deeper penetration, consequently contributed toward higher level of dilution [10]. Srikarun et al. found that wear resistance and dilution depend upon the hardfacing alloy composition and welding process parameters [11]. Whereas Jorge et al. in [12] found that a uniform inter-pass temperature between hardfacing layers helps to maintain desired properties throughout the weld deposits. Investigation was done on

M. Singh · L. K. Bhagi (✉) · H. Arora
School of Mechanical Engineering, Lovely Professional University,
Phagwara 144411, India
e-mail: bhagiloveleen14@rediffmail.com

Table 1 Parameters with their levels and units

Parameters	Unit	Upper limit	Lower limit	Symbol
Current	Ampere	170	150	C
Hardfacing layer	–	3	1	H.L
Buffer layer	–	1	0	B.L

the effect of post-weld thermal aging techniques on the behavior of corrosion and the micro-hardness of the stainless steel 304 welded joints [13–16].

In the present study, dilution has been analyzed with the help of factorial design and the effects of SMAW process parameters on the dilution and wear rate were analyzed. None of the researchers has found the effect of the dilution on the hardness using SMAW and authors try to bridge this gap.

2 Design for Experiment

A two-level factorial design (23) of eight runs has been selected for investigating the effect of three independent process parameters. Currently, hardfacing layers and buffer layers have been identified as critical variables for carrying out the experimental work with their two levels as shown in Table 1.

2.1 Selection of Mathematical Model

Assuming a linear relationship in the first instance and taking into account all the possible two factor interaction and confounded interaction, the mathematical model could be written as (the physical meaning of the below terms is given in Table 2)

$$Y = b_0 + b_1 \times C + b_2 \times H.L + b_3 \times B.L + b_{12}C \times H.L + b_{13}C \times B.L + b_{23}H.L \times B.L \quad (1)$$

Table 2 Coefficients of model

Coefficients	Due to
b_0	Combined effect of all parameters
b_1	Current (C)
b_2	Hardfacing layer (H.L)
b_3	Buffer layer (B.L)
b_{12}	Interaction of C and H.L
b_{13}	Interaction of C and B.L
b_{23}	Interaction of H.L and B.L

Table 3 Chemical composition in percentage of weight

Description	Elements in percentage weight								
	C	Si	Mn	P	S	Cr	Mo	V	Fe
Base metal	0.26	0.17	0.40	0.095	0.033	–	–	–	Rest
Hardfacing electrode	0.65	1.0	0.7	–	–	7.8	1.1	0.8	Rest
Buffer electrode	0.1	0.65	1.50	0.03	0.03	–	–	–	Rest

3 Experimentation for Dilution

Weld beads on low carbon mild steel plates have been deposited using Fe-based hardfacing alloy by shielded metal arc welding process. The complete set of eight experimental runs has been prepared as per the design matrix and further experimentation was conducted as per the orthogonal array generated by Design Expert software. Table 3 shows compositions for metals which were used for the conduct of the experiments. In case of triple layer, inter-pass temperature of 250 °C is maintained between the subsequent passes.

3.1 Dilution Measurement

After hardfacing, the welded specimens were cut in transverse direction to measure the dilution. Specimens for microscopy were polished using standard metallographic techniques and have been etched with 3% Nital solution for 10 s, followed by measurement of area of reinforcement and the area of penetration with the help of image analyzer to calculate dilution. The macrostructure for all eight specimens is presented in Fig. 1 and calculated dilution is given in Table 4.

4 Development of Mathematical Model

Factorial design has been used to elucidate the correlation between the response, i.e., dilution and the process parameters. Adequacy of the mathematical model has been further determined by the ANalysis Of VAriance technique (ANOVA). The results obtained are recapitulated in Table 5. It has been seen from the ANOVA table (Table 5) that the fitted model has been significant with F-value of 4872.85 and the P-value less than 0.05 at 97.5% confidence level. For less than 0.05, the values of "Prob > F" have been observed for the main effects of process parameters current, hardfacing layer, and buffer layer. Significant contribution of the interactions in the model has also been noted.

It is apparent from the ANOVA shown in Table 5 that the effect of hardfacing layer, buffer layer, and current on dilution becomes significant at both 97.5 and 95%
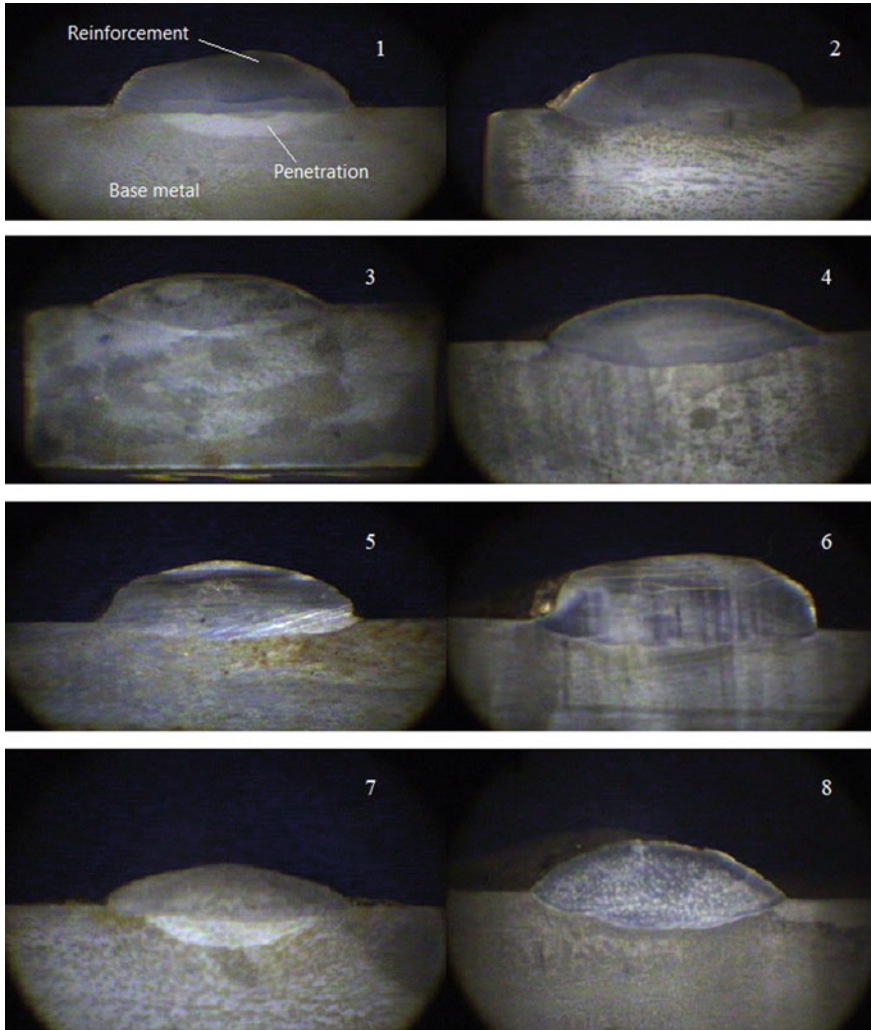
Fig. 1 Macrostructure of all samples (10 ×)

confidence levels (Table 6) and the P-values less than 0.05. The effect of hardfacing layer on dilution is found to be highly significant at 99% confidence level (Table 6) and P-value comes out to be less than 0.01, so from here it is concluded that the hardfacing layer is the most significant effect on the dilution at 99% confidence level.

From Tables 5 and 6, it has been observed that there is a significant interaction between hardfacing layer, buffer layer, and current at 90% confidence level. Table 7 shows the model summary statistics for dilution. The "predicted R^2" of 1.0000 is in good agreement with the "adjusted R^2" of 0.9998. The low value of coefficient of

Table 4 Design matrix with response dilution

Run	C	H.L	B.L	Percentage dilution
1	150	1	0	35
2	170	3	1	22.7
3	170	3	0	26.4
4	170	1	0	38
5	150	1	1	32
6	150	3	1	19.8
7	150	3	0	24.3
8	170	1	1	36.1

Table 5 ANOVA results for dilution

Source	Sum of square	DoF	Mean square	F-value	P-value (Prob > F)
Model	328.92	6	54.82	4872.85	0.0110
C	18.30	1	18.30	1626.78	0.0158
H.L	286.80	1	286.80	25493.44	0.0040
B.L	21.45	1	21.45	1906.78	0.0146
C*H.L	0.55	1	0.55	49	0.0903
C*B.L	0.45	1	0.45	40.11	0.0997
H.L*B.L	1.36	1	1.36	121	0.0577
Residual error	0.011	1	0.011		
Cor. total	328.93	7			

Table 6 Percentage points of the tabulated F-distribution (From standard F table)

$F_{0.10,1,1}$	$F_{0.05,1,1}$	$F_{0.25,1,1}$	$F_{0.01,1,1}$
39.86	161.4	647.8	4052

Table 7 Model summary statistics for dilution

Std. Dev.	0.11	(R^2)	0.9999
Mean	29.29	Adjusted (R^2)	0.9998
CV%	0.36	Predicted (R^2)	0.9978
PRESS	0.72	Adequate precision (AP)	184.195

variation (CV) obtained for the model indicates improved precision and reliability of the experiments performed. The ratio of 184.195 for adequate precision indicates adequate signal.

5   Wear Resistance Testing

Pin on disk machine was used for wear resistance and wear rate calculations of the hardfaced samples. For that purpose, the pins with dimensions of 6 mm dia. × 25 mm length had been prepared. Wear test is conducted with disk rotating at of 250 RPM having diameter of 80 mm with 3 kg load for the sliding distance of 1500 m in four intervals.

The sliding distance is divided into four parts and at every 375 meters of sliding distance, and the weight loss is calculated after every interval of 375 meters, which is further used for wear rate calculations as per the given equations:

$$Wear volume loss \left(mm^3\right) = \frac{weight loss}{10 \times Density} \tag{2}$$

$$Wear\ rate\ in\ mm^3 / Nm = \frac{weight \times 10000}{Sliding\ distance \times Density \times Time} \tag{3}$$

6   Result and Discussion

6.1   Effect of Current on Dilution

Figure 2 shows the effect of welding current on dilution. It is observed that dilution increased from 27.7 to 30.8% with an increase in welding current from 150 to 170 amp. It is evident that with increase in welding current the current density increases which means higher melting of the electrode.

6.2   Effect of Hardfacing Layers on Dilution

Figure 3 shows there is decrease in dilution from 34.9 to 23.5% as the hardfacing layers are increased from 1 to 3. This can be attributed as there is an increase in area of reinforcement as the number of hardfacing layers is increased.
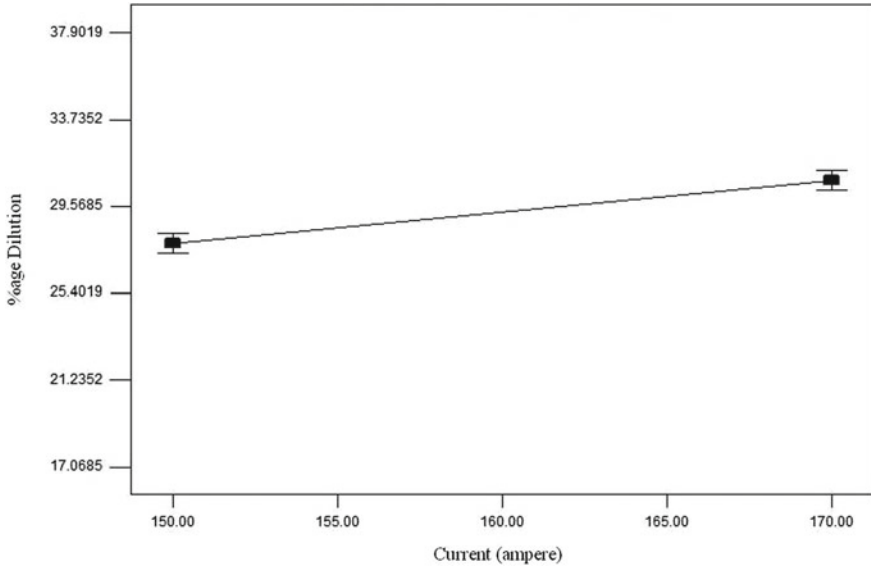
Fig. 2 Effect of welding current on dilution
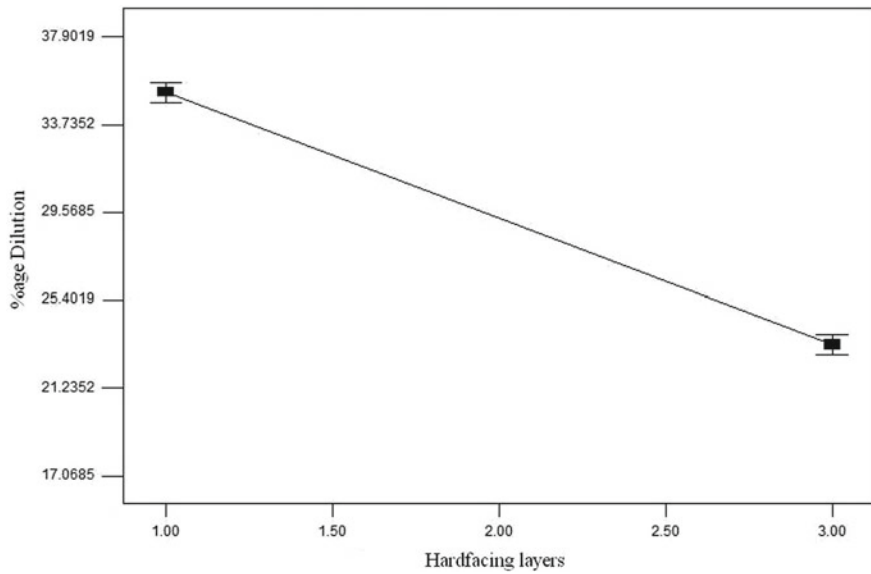
Fig. 3 Effect of hardfacing layers on dilution
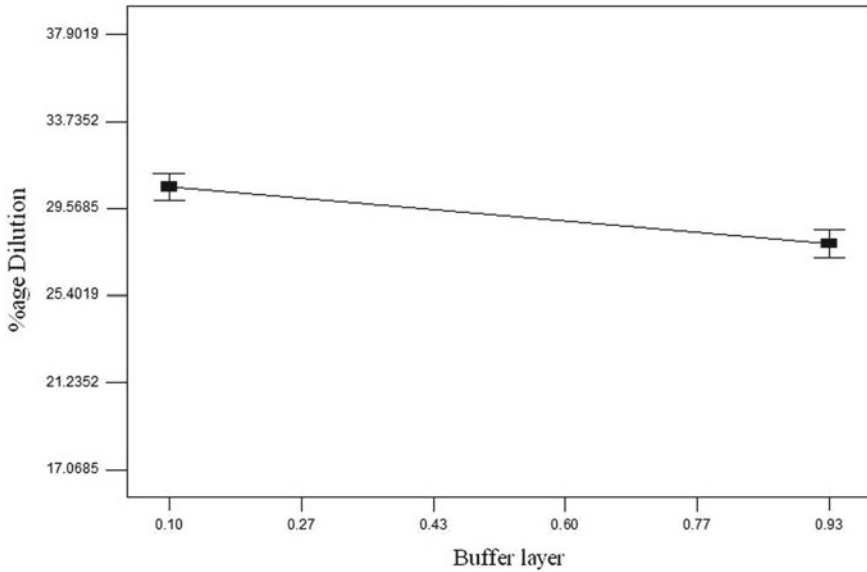
Fig. 4 Effect of buffer layer on dilution

6.3 Effect of Buffer Layer on Dilution

Figure 4 shows dilution decreases from 31 to 27.7% as the buffer layer is deposited prior to hardfacing. This is due to the fact that buffer layer reduces the mixing of hardfacing alloy with base metal as buffer layer has the chemical composition intermediate of both the mating phases.

6.4 Effect of Interaction of Current and Hardfacing Layers on Dilution

Figure 5 shows the interactive plot for combined effect of current and hardfacing layers. There is an increase in dilution from 22 to 24.5% as the current increases from 150 to 170 amp for three layers of hardfacing. Dilution increases from 32.5 to 37% as the current increases from 150 to 170 amp for the single layer hardfacing. Increase in dilution is higher in single layer of hardfacing as compared triple layer hardfacing for an increase of current from 150 to 170 amp, because in triple layer, increase in penetration is small as compared to single layer. Figure 6 shows the response surface for the interaction of current and hardfacing layers, respectively.
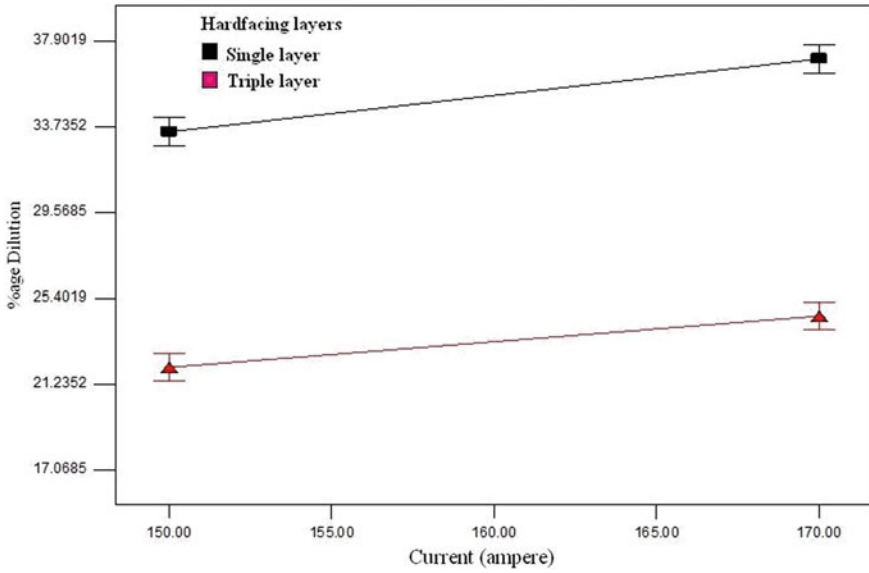
Fig. 5 Interactive effect of current and hardfacing layers on dilution
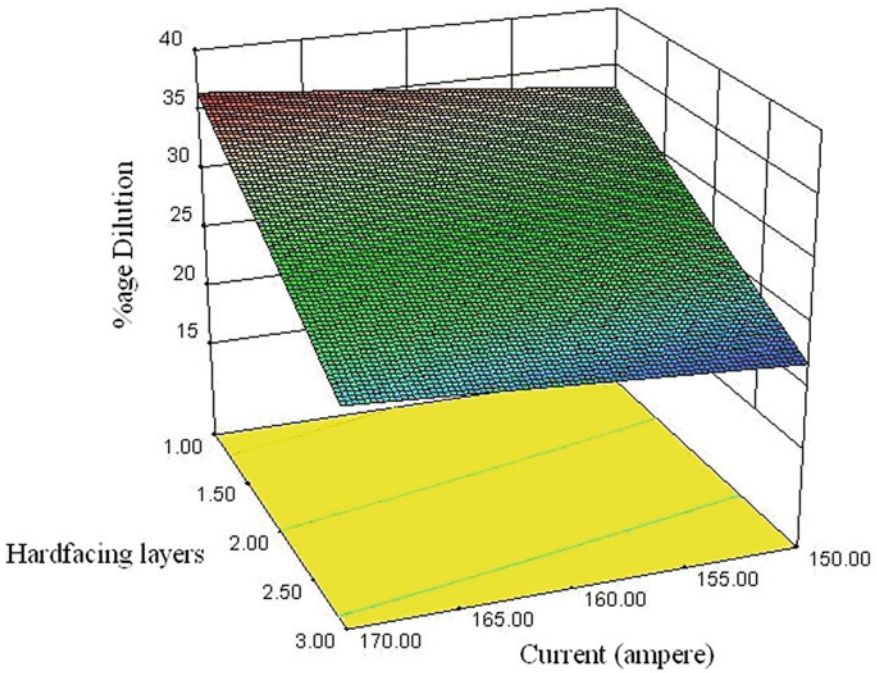
Fig. 6 Response surface plot due to interaction of hardfacing layers and current on dilution
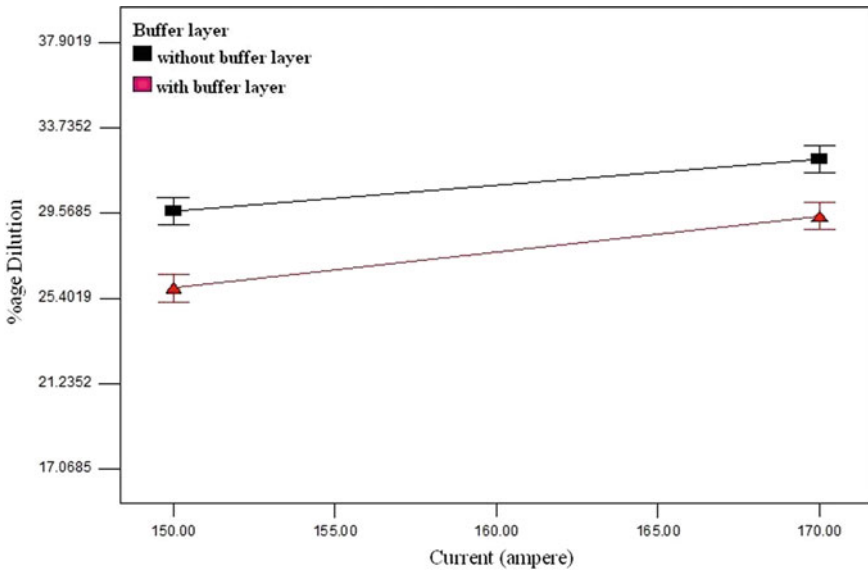
Fig. 7 Interaction effect of current and buffer layer on dilution

6.5 Effect of Interaction of Current and Buffer Layer on Dilution

Figure 7 shows effect of interaction of current and buffer layer upon dilution. When using buffer layer, the dilution increases from 26 to 29.3% as the current increases from 150 to 170 amp. When not using buffer layer, there is an increases in dilution from 29.1 to 32.8% as the current increases from 150 to 170 amp. It has been observed there is small increase in dilution as the buffer layer is not used, which reduces the intermixing of base metal to the hardfacing layers, which results in decreased area of penetration. Figure 8 shows the response surface for the interaction of current and buffer layer, respectively.

6.6 Effect of Interaction of Hardfacing Layers and Buffer Layer on Dilution

Figure 9 shows there is decrease in dilution from 36.5 to 25.5% as hardfacing layers are increased from 1 to 3, when not using buffer layer. Dilution is reduced from 33.6 to 21.9% as number of hardfacing layers are increased from 1 to 3 with buffer layer. At single layer, dilution reduces from 36.5 to 33.6% with buffer layer, whereas in triple layer reduction is from 25.5 to 21.9%. The response surface plot for the interaction of hardfacing layers and buffer layers is shown in Fig. 10.
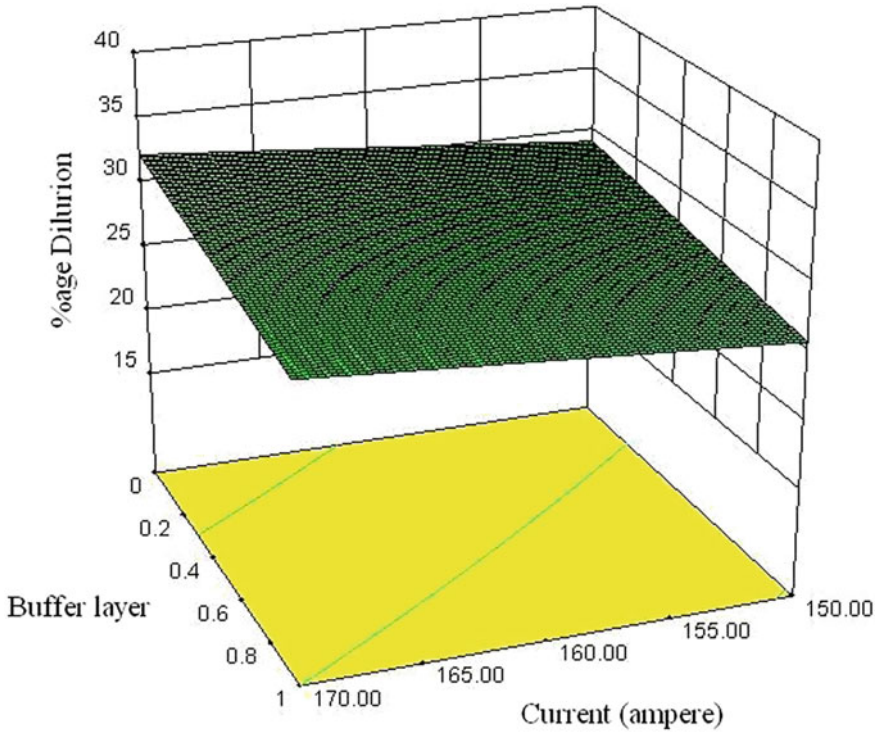
Fig. 8 Response surface due to interaction of current and buffer layer
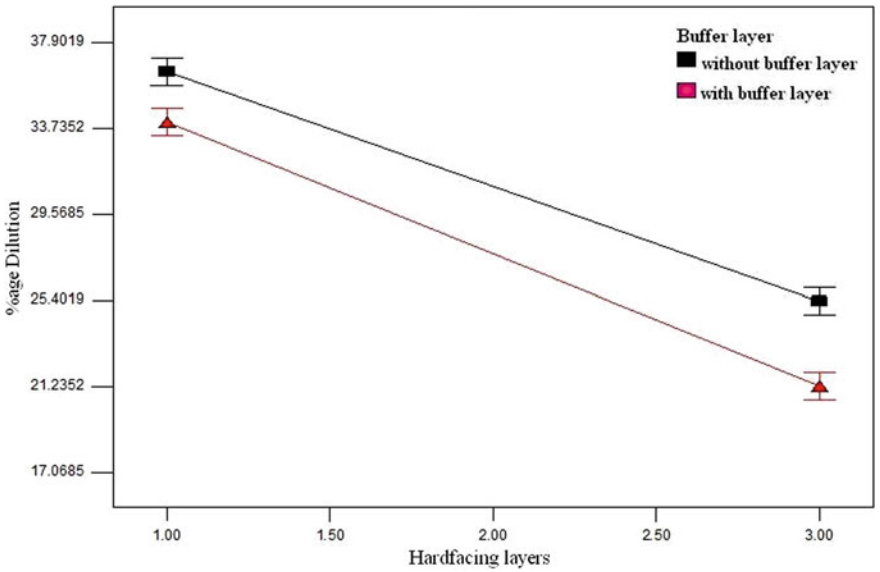
Fig. 9 Interaction effect of hardfacing layers and buffer layer on dilution
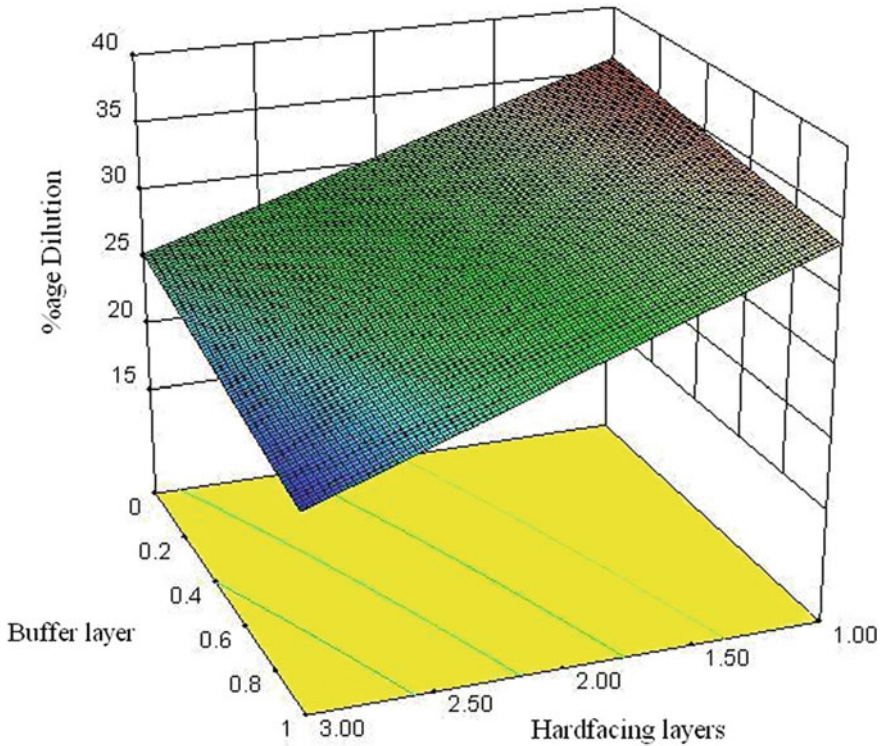
Fig. 10 Response surface due to interaction of hardfacing layer and buffer layer

6.7 Effect of Dilution on Wear Rate

Further study was done to predict effect of dilution on wear rate of hardfaced samples. Wear rate was calculated as per discussions under Sect. 6 and presented in Table 8. It had been observed that the sample 6, hardfaced with three hardfacing layers along with buffer layer at 150 amp shows minimum wear rate of 0.014245, which can be contributed to minimum dilution results in better hardfacing properties. Similar trend is observed in sample 2, hardfaced at 170 amp with wear rate of 0.014245.

Wear rate is maximum in sample 8 (0.081909) hardfaced with one hardfacing layer and a buffer layer at 170 amp which again justify that increased dilution will result in increased wear rate. Similar wear rates are also observed in sample 4 and 1 due to high dilution.

Table 8 Wear rate versus dilution

Sample	Sliding distance in meters				Dilution percentage
	375	750	1125	1500	
1	0.34188	0.156695	0.094967	0.067664	35
2	0.099715	0.049858	0.023742	0.014245	22.7
3	0.185185	0.064103	0.033238	0.021368	26.4
4	0.31339	0.178063	0.137702	0.071225	38
5	0.31339	0.163818	0.109212	0.078348	32
6	0.08547	0.035613	0.018993	0.014245	19.8
7	0.14245	0.049858	0.02849	0.017806	24.3
8	0.327635	0.163818	0.118708	0.081909	36.1

7 Conclusions

Following conclusions have been drawn from this work:

1. Dilution increases linearly with current. With an increase of 13.33% in current, dilution increases by 11.19%.
2. Dilution decreases as the hardfacing layers are increased. Dilution decreases by 32.6%, when the hardfacing layers are increased from 1 to 3.
3. Buffer layer decreases the dilution. Dilution is decreased by 10.6%, when the buffer layer is used before hardfacing.
4. Minimum wear rate of 0.014245 is observed at 19.8% dilution and maximum wear rate of 0.081909 is observed at 36.1% dilution.

References

1. Pawar, S., Jha, A.K., Mukhopadhyay, G.: Effect of different carbides on the wear resistance of Fe-based hardfacing alloys. Int. J. Refract. Met. Hard Mater. **78**, 288–295 (2019)
2. Ayoola, W.A., Suder, W.J., Williams, S.W.: Parameters controlling weld bead profile in conduction laser welding. J. Mater. Proc. Tech. **249**, 522–530 (2017)
3. Choteborsky, R., Hrabe, P., Muller, M., Savkova, J., Jirka, M.: Abrasive wear of high chromium Fe-Cr-C hardfacing alloys. Res. Agric. Eng. **54**(4), 192–198 (2008)
4. Choteborsky, R., Hrabe, P., Muller, M., Savkova, J., Jirka, M., Navratilova, M.: Effect of abrasive particles size on abrasive wear of hardfacing alloys. Res. Agric. Eng. **55**(3), 101–113 (2009)
5. Revesova, S., Pavel, B.: Selection of materials and technology for forming the layers resistant to abrasive wear. Res. Pap. Faculty Mater. Sci. Technol. Slovak Univ. Technol. **18**(28), 59–68 (2010)
6. Kirchgabner, M., Badisch, E., Franek, F.: Behaviour of iron-based hardfacing alloys under abrasion and impact. Wear **265**(5–6), 772–779 (2008)
7. Leitner, M., Pichler, P., Steinwender, F., Guster, C.: Wear and fatigue resistance of mild steel components reinforced by arc welded hard layers. Surf. Coat. Technol. **330**, 140–148 (2017)

8. Khanna, O.P.: A textbook of welding technology, 2015 (Dhanpat Rai Publication Pvt. Ltd., New Delhi)
9. Siva, K., Murugan, N., Raghupathy, V.P.: Modeling, analysis and optimization of weld bead parameters of ni-based overlay deposited by PTA surfacing. Comput. Mater. Sci. Surf. Eng. **1**(3), 174–182 (2009)
10. Banovic, SW., Dupont, I.N., Marder, A.R.: Dilution control in gas-tungsten-arc welds involving superaustenitic stainless steels and nickel-based alloys. Metall. Mater. Trans. **B32**(6), 1171–1176 (2001)
11. Srikarun, B., Zaw-Oo, H., Petchsang, S., Muangjunburee, P.: The effects of dilution and choice of added powder on hardfacing deposited by submerged arc welding. Wear **424–425**, 246–254 (2019)
12. Jorge, J.C.F., Monteiro, J.L.D., Gomes, A.J.C., Bott, I.S., Souza, L.F.G., Mendes, M.C., et al.: Influence of welding procedure and PWHT on HSLA steel weld metals. J. Mater. Res. Technol. **8**(1), 561–571 (2019)
13. Singh, R., Kumar, R., Feo, L., Fraternali, F.: Friction welding of dissimilar plastic/polymer materials with metal powder reinforcement for engineering applications. Compos. Part B: Eng. **101**, 77–86 (2016)
14. Kumar, R., Singh, R., Ahuja, I.P.: Friction stir welding of ABS-15Al sheets by introducing compatible semi-consumable shoulder-less pin of PA6-50Al. Measurement **1**(131), 461–472 (2019)
15. Babbar, A., Kumar, A., Jain, V., Gupta, D.: Enhancement of Activated Tungsten Inert Gas (A-TIG) Welding using multi-component TiO2-SiO2-Al2O3 hybrid flux. Measurement, 106912 (2019)
16. Kumar, M., Babbar, A., Sharma A., Shahi, A.S.: Effect of post weld thermal aging (PWTA) sensitization on micro-hardness and corrosion behavior of AISI 304 weld joints. J. Phy. Conf. Ser. **1240**(1), 012078 (IOP Publishing) (2019)

Some Investigations on the Tensile Strength of Additively Manufactured Polylactic Acid Components

Kamalpreet Sandhu, Jatinder Pal Singh, and Sunpreet Singh

1 Introduction

In a present scenario, AM is being growing day by day as of its cost-effectiveness, mass customization, and negligible human interventions [1]. Therefore, more industries are choosing AM instead of using conventional manufacturing [2]. The AM technologies are able to process different types of materials irrespective to their physical states [3]. Further, these are the one of the most preferable areas in the field of manufacturing of the products [4–9]. Furthermore, these enable to manufacture large range of prototype, functional components with complex geometries [10, 11]. Being a broader term, AM consists of numerous different technologies such as fused filament fabrication (FFF), stereo-lithography (SLA), laminated object manufacturing (LOM), selective laser sintering (SLS), ballistic particles (BP), etc. Among all, FFF is more popular due to its association with the desktop 3D printers [12, 13]. Further, FFF is able to print myriads of pure, reinforced, and blended thermoplastic and thermoset materials which can cover the overall manufacturing applications.

However, FFF is a complex process and often suffers from poor product quality and mechanical properties [5, 14]. Indeed, the various process parameters of FFF technology, including build orientation, raster angle, layer thickness, and head scan speed, infill density, infill patterns, feed rate, air gap, etc. affect the final quality and strength of the parts. [4, 5, 15–18]. The curious point is mechanical properties of

K. Sandhu (✉)
School of Design-II, Product and Industrial Design, Lovely Professional University, Phagwara, Punjab, India
e-mail: pr33t.sandhu1994@gmail.com

J. P. Singh
School of Mechanical Engineering, Lovely Professional University, Phagwara, Punjab, India

S. Singh
Center for Nano fibers and Nanotechnology, NUS, Singapore, Singapore

the functional parts and, absolutely, is the core of research interests of the community working with FFF technology [19–21]. Therefore, about 80% of the research activities cover the various innovations and methodologies which can enhance the mechanical performance of the resulting parts. Tymrak et al. [4] investigated mechanical properties (tensile strength and elastics modulus) in different open-source 3D printers. In their work, acrylonitrile butadiene styrene (ABS) and polylactic acid (PLA) have been used for making the test specimens as per ASTM-D638 standard. Ebel et al. [22] compared mechanical property of FFF parts under the influence of infill pattern and infill percentage. Wittbrodt et al. [23] verified the effect of coloring on mechanical properties. Lanzotti et al. [24] and Torres et al. [25] investigated the tensile strength and elastic modulus of PLA products by considering process parameter layer thickness, print orientation, and infill percentage. Li et al. extended the work reported by [24, 25] by considering deposition velocity [26] and deposition style [27] as new input parameters. However, Chacon et al. [23] investigated mechanical properties of PLA samples at different feed rates of the material.

From the literature review, it has been observed that massive research effort was made, till date, on the FFF printed parts; however, very few have studied the influence of head speed, layer thickness, and build orientation on the tensile strength of the PLA components. Therefore, in this work, an effort has been made to first print the PLA material in accordance with the selected parametric style and then to study the responses, statistically.

2 Materials and Method

In the present research work, samples having recommended geometry have been first designed by using licensed version of CREO-4.0 design software package. The computer-aided design (CAD) files were converted into standard tessellation language (.STL) format with ASCII conversation style. Chord height and angle conversation format for each test model were maintained to a precision of 0.0593 and 0°, respectively. The PLA feedstock filament of 1.75 mm diameter (supplier: Divide by Zero Technologies, India) has been used for the fabrication of samples on extrusion-based FFF system (Ultimaker 3 extended v1.8.indd, ultimaker, Singapore). The bed size of the selected FFF printer is 215 × 215 × 300 mm (XYZ), nozzle size is 20–200 micron, Printer able to run two filaments simultaneously and controlled the temperature of the build area. The working procedure of FFF is normally defined as a thermally controlled process wherein a thermoplastic filament melts in the moving head (along x- and y-axes) and thereafter pushed by a mechanical mechanism onto a fixtureless platform (along z-axis) to settle down [24–26]. The specifications of printer samples were shown in Fig. 1.

Table 1 shows the list of selected process parameters and their levels. Further, Table 2 shows the control log of experimentation as per design of experimentation. All the samples were tested for their tensile strength by using a computer-controlled
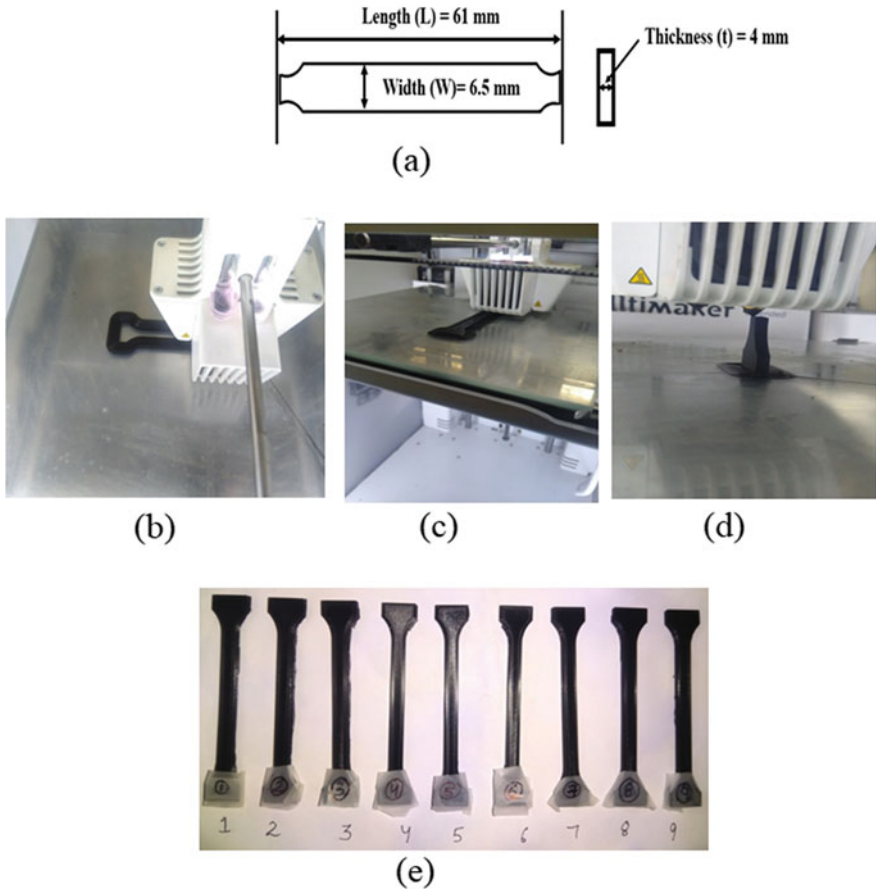
Fig. 1 **a** Specification of specimen, **b** 180° along table (x-axis), **c** 180′° along table (y-axis), **d** 90° built orientation, **e** printed specimens

Table 1 Printer process parameters with selected levels

Factors	Units	Levels		
		1	2	3
Orientation angle	Degree (°)	180	90	180′
Layer thickness	mm	0.18	0.20	0.22
Head scan speed	mm/s	30	35	40

Table 2 Log of experimentation

S. no.	Orientation angle (°)	Head scan speed (mm/s)	Layer thickness (mm)
1	180′	30	0.18
2	180′	35	0.20
3	180′	40	0.22
4	90	30	0.20
5	90	35	0.22
6	90	40	0.18
7	180	30	0.22
8	180	35	0.18
9	180	40	0.20

Universal Testing Machine (UTM, refer Fig. 2) of International Equipments, Mumbai, India having load capacity up to 5000 kg, load cells—2, cross travel—1000 mm, horizontal day light—450 mm, and speed—0.5 to 800 mm/min. Figure 3 shows the pictorial view of the fractured specimens.

(a)   (b)   (c)
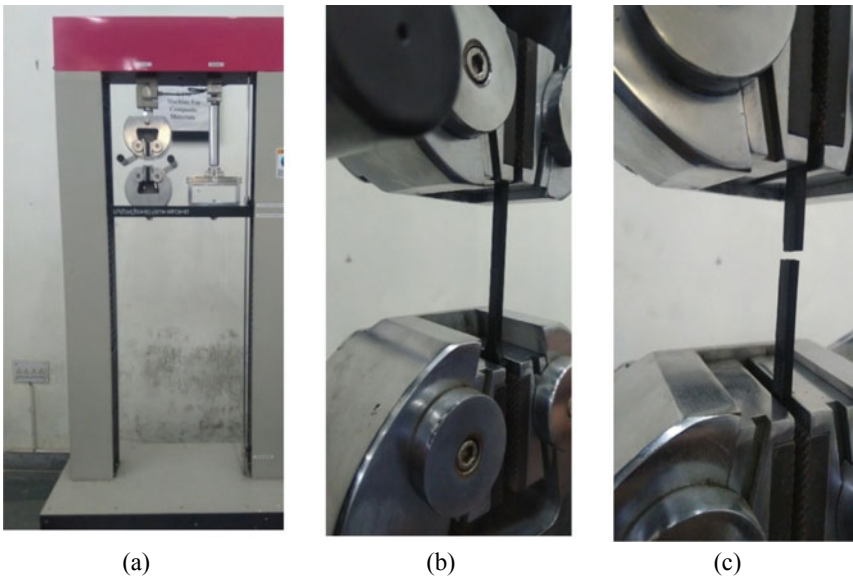
Fig. 2 Universal testing machine (**a**), sample during test (**b**) and after test (**c**) (Courtesy: Lovely Professional University, Phagwara, Punjab)
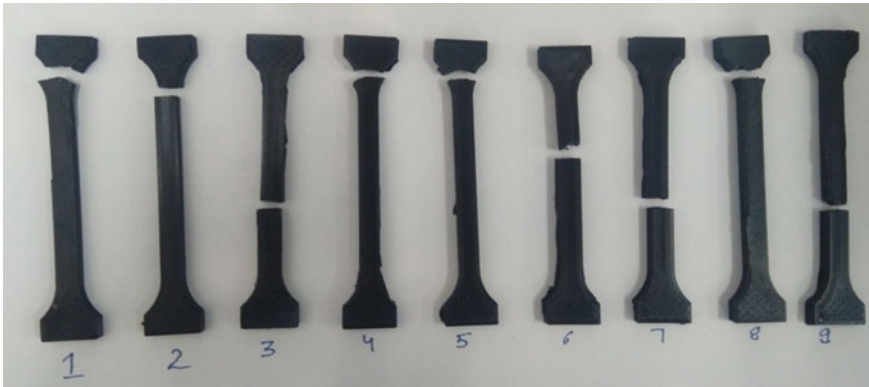
Fig. 3 Fractured tensile specimens

3 Result and Discussion

In present study, the tensile strength (TS) of the PLA has been investigated and the obtained raw data and signal/noise (S/N) ratio after the testing and analysis, respectively, are given in Table 3. The effect of the input process parameters on TS has been examined, statistically, by using MINITAB-17 statistical software package. Further, analysis of variance (ANOVA) approach has been used to find out the significance of the input parameters in response to TS. Regressing equation has also been obtained from ANOVA. Figures 4 and 5 show the S/N ratio plot for the TS and load displacement plots for PLA samples, respectively. It has been observed from the Fig. 4 that the TSs of the PLA are mainly a function of build orientation owing the steepness of the curve for this particular parameter.

It has been found that when the build orientation is changed from 180°′ (y-axis) to 90° and then further from 90° to 180° (x-axis), the TS of the PLA parts deteriorated.

Table 3 Results for raw data and S/N ratio

S. no.	TS (N/mm^2)	S/N ratio (dB)
1	39.82	32.00
2	40.71	32.19
3	41.76	32.41
4	32.18	30.15
5	30.23	29.50
6	29.35	29.35
7	26.90	28.59
8	27.34	28.73
9	24.41	27.75
Average S/N ratio, x = 30.08 dB		
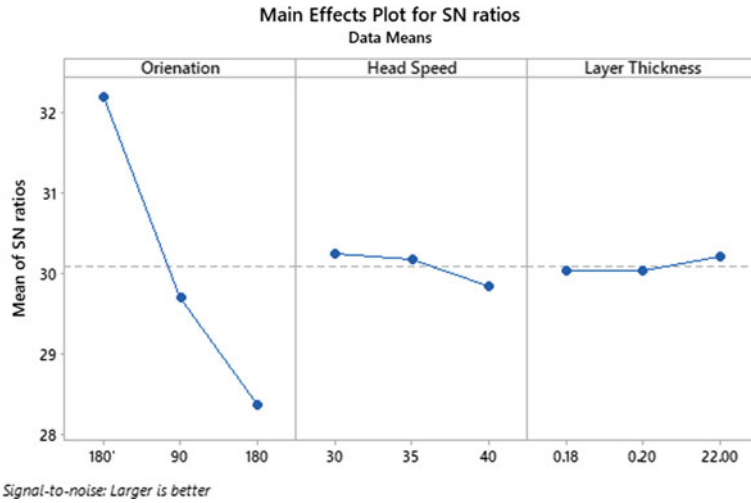
Fig. 4 S/N plot for the TS
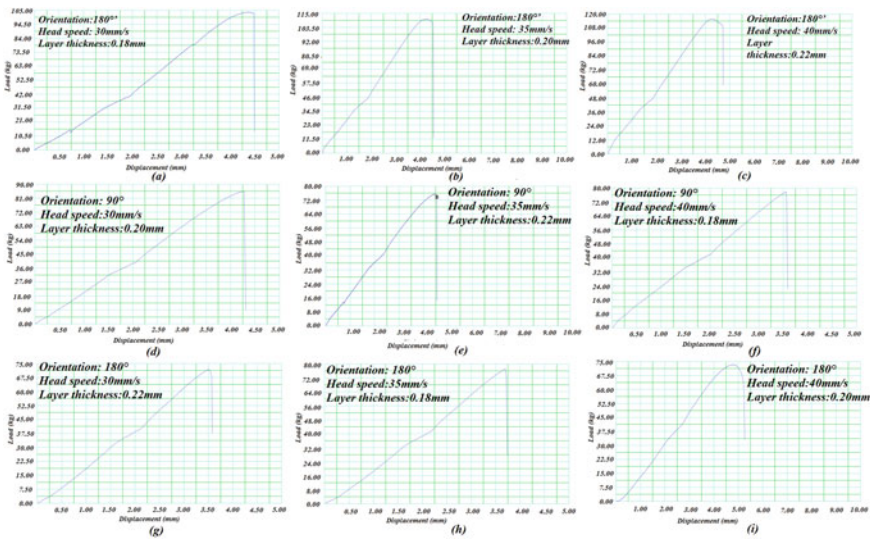
Fig. 5 Load displacement plots of PLA-based printed samples

It shows that at 180°′ (y-axis), the obtainable TS would be highest. This might be due to the fact that at 180°′ printing position, the heat transfer from the printing specimen was more stable which resulted into comparatively better inter-layer diffusion of the PLA beads, and thus enhanced the TS. However, in case of 90° orientation, the load is applied perpendicular to the direction of layer deposition, and the printed parts offered limited strength characteristics [7, 9, 28].

The variation in tensile strength with effect of head speed and layer thickness for 180°′ orientated sample is represented in Fig. 5a–c. It is observed from results that with the increase in head speed and layer thickness the tensile strength of the material is increased. Also, the drop in the displacement is also observed. This indicates that the material becomes more brittle, though its strength is increased. The PLA samples prepared at orientation of 180°′ result in the formation of high-strength material irrespective of other parameters. The tensile strength of the sample prepared in 180°′ orientation lies in the range of 38.82–41.76 N/mm². However, for 90° oriented samples, the tensile strength of the PLA lies within the range of 28.33–32.12 N/mm². Whereas the tensile strength of FDM produced sample oriented at 180° lies in the range of 24.41–29.09 N/mm². It has been seen in case of head speed that although this parameter did not contribute much in terms of the TS, however, lower levels of the head speed have been observed as more favorable. The increase in the feed rate results in decrease in tensile strength of the material. Though the increase in feed rate results in higher production rate and also the machining time is decreased [29, 30]. Similarly, in case of layer thickness, broader diameter of the fused layers is more helpful in obtaining the better TS. Further, as observed from ANOVA, only build orientation has been found as statistically significant at 95% confidence level (error 5%). It is observed from Fig. 5a–c that layer thickness and head speed play a significant role for the specimen printed in orientation of 180°′. It is seen from the results that increase in the head speed and layer thickness results in increase in the strength of the material. However, the displacement also increases. This means the ductility of the material was increased. Whereas the results for 90° orientations are plotted in Fig. 5d–f. It was seen that the trend between load and displacement is different from 180°′ orientation. The increase in the head speed and layer thickness results in decrease in load-carrying capacity of the material and the displacement was also decreased. Hence, the material becomes more brittle. Figure 5g–i shows the variation in load and displacement from 180° orientation. The results were found similar to 180°′ orientation. Increase in the head speed and layer thickness results in increase in strength of the material. However, the load-carrying capacity in 180°′ orientation was more than 180° orientation.

Singh et al. [31] reported a set of equations which can be used for the prediction of optimized S/N ratio through the use of optimum levels of input parameters. The theoretical value of S/N ratio "η" calculated can be denoted by "η_{opt}" as

$$\eta_{opt} = x + (x_{build\ orienataion} - x) + (x_{head\ scan\ speed} - x) + (x_{layer\ thickness} - x) \quad (1)$$

$$\eta_{opt} = 30.08 + (32.20 - 30.08) + (30.25 - 30.08) + (30.21 - 30.08)$$

$$\eta_{opt} = 32.5\ dB$$

The corresponding value TS is given by

$$y_{opt}^2 = 10^{\eta_{opt}/10} \quad (2)$$

$$\text{And } y_{\text{opt}} = 42.16 \, \text{N/mm}^2$$

In order to confirm the prediction accuracy of Taguchi approach, a confirmatory experimentation has been performed at the suggested optimized setting and obtained TS comes out as 41.76 N/mm^2. The experimental result is very close to the predicted value, highlighting the accuracy of the prediction and reliability of the optimal settings.

4 Conclusions

In the present work, PLA samples have been successfully developed using a FFF technology in response to the different levels of input process parameters. On the basis of observed S/N ratio and ANOVA, following conclusions may be drawn:

- It has been found that the build orientation is the most influential process parameters which affected the TS of the PLA specimens. The reason behind this may be credited to the uniform distribution of the heat into the PLA sample that enhanced the inter-layer diffusion of the deposited PLA beads. Further, as per ANOVA, the results are significant at 95% confidence levels.
- The optimal setting suggested by Taguchi L9 array is build orientation—180°′, head speed—30 mm/min, and layer thickness—0.22 mm.
- Further investigations may study the fracture mechanisms of the specimens with the help of optical micrographic approaches.

References

1. Dick, J., Hull, E., Jackson, K.: Requirements Engineering. Springer (2017)
2. Despeisse, M., Baumers, M., Brown, P., Charnley, F., Ford, S.J., Garmulewicz, A., Knowles, S., Minshall, T.H.W., Mortara, L., Reed-Tsochas, F.P., Rowley, J.: Unlocking value for a circular economy through 3D printing: a research agenda. Technol. Forecast. Soc. Change **115**, 75–84 (2017)
3. Singh, S., Ramakrishna, S., Singh, R.: Material issues in additive manufacturing: a review. J. Manuf. Process. **25**, 185–200 (2017)
4. Tymrak, B.M., Kreiger, M., Pearce, J.M.: Mechanical properties of components fabricated with open-source 3-D printers under realistic environmental conditions. Mater. Des. **58**, 242–246 (2014)
5. Sugavaneswaran, M., Arumaikkannu, G.: Analytical and experimental investigation on elastic modulus of reinforced additive manufactured structure. Mater. Des. (1980–2015) **66**, 29–36 (2015)
6. Melenka, G.W., Cheung, B.K., Schofield, J.S., Dawson, M.R., Carey, J.P.: Evaluation and prediction of the tensile properties of continuous fiber-reinforced 3D printed structures. Compos. Struct. **153**, 866–875 (2016)

7. Domingo-Espin, M., Puigoriol-Forcada, J.M., Garcia-Granada, A.A., Llumà, J., Borros, S., Reyes, G.: Mechanical property characterization and simulation of fused deposition modeling Polycarbonate parts. Mater. Des. **83**, 670–677 (2015)

8. Casavola, C., Cazzato, A., Moramarco, V., Pappalettere, C.: Orthotropic mechanical properties of fused deposition modelling parts described by classical laminate theory. Mater. Des. **90**, 453–458 (2016)

9. Rankouhi, B., Javadpour, S., Delfanian, F., Letcher, T.: Failure analysis and mechanical characterization of 3D printed ABS with respect to layer thickness and orientation. J. Fail. Anal. Prev. **16**(3), 467–481 (2016)

10. Chacón, J.M., Bellido, J.C., Donoso, A.: Integration of topology optimized designs into CAD/CAM via an IGES translator. Struct. Multidiscip. Optim. **50**(6), 1115–1125 (2014)

11. Donoso, A., Bellido, J.C., Chacón, J.M.: Numerical and analytical method for the design of piezoelectric modal sensors/actuators for shell-type structures. Int. J. Numer. Methods Eng. **81**(13), 1700–1712 (2010)

12. Matsuzaki, R., Ueda, M., Namiki, M., Jeong, T.K., Asahara, H., Horiguchi, K., Nakamura, T., Todoroki, A., Hirano, Y.: Three-dimensional printing of continuous-fiber composites by in-nozzle impregnation. Sci. Rep. **6**, 23058 (2016)

13. Van Der Klift, F., Koga, Y., Todoroki, A., Ueda, M., Hirano, Y., Matsuzaki, R.: 3D printing of continuous carbon fibre reinforced thermo-plastic (CFRTP) tensile test specimens. Open J. Compos. Mater **6**(1), 18–27 (2016)

14. Mohamed, O.A., Masood, S.H., Bhowmik, J.L.: Optimization of fused deposition modeling process parameters: a review of current research and future prospects. Adv. Manuf. **3**(1), 42–53 (2015)

15. Wu, W., Geng, P., Li, G., Zhao, D., Zhang, H., Zhao, J.: Influence of layer thickness and raster angle on the mechanical properties of 3D-printed PEEK and a comparative mechanical study between PEEK and ABS. Materials **8**(9), 5834–5846 (2015)

16. Sood, A.K., Ohdar, R.K., Mahapatra, S.S.: Parametric appraisal of mechanical property of fused deposition modelling processed parts. Mater. Des. **31**(1), 287–295 (2010)

17. Ning, F., Cong, W., Jia, Z., Wang, F., Zhang, M.: Additive manufacturing of CFRP composites using fused deposition modeling: effects of process parameters. In: ASME 2016 11th International Manufacturing Science and Engineering Conference, pp. V003T08A001–V003T08A001. American Society of Mechanical Engineers, June 2016

18. Vaezi, M., Chua, C.K.: Effects of layer thickness and binder saturation level parameters on 3D printing process. Int. J. Adv. Manuf. Technol. **53**(1–4), 275–284 (2011)

19. Anitha, R., Arunachalam, S., Radhakrishnan, P.: Critical parameters influencing the quality of prototypes in fused deposition modelling. J. Mater. Process. Technol. **118**(1–3), 385–388 (2001)

20. Rodriguez Matas, J.F., Thomas, J.P., Renaud, J.E.: Design of fused-deposition ABS components for stiffness and strength (2003)

21. Lee, B.H., Abdullah, J., Khan, Z.A.: Optimization of rapid prototyping parameters for production of flexible ABS object. J. Mater. Process. Technol. **169**(1), 54–61 (2005)

22. Ebel, E., Sinnemann, T.: 2014. Fabrication of FDM 3D objects with ABS and PLA and determination of their mechanical properties. RTejournal **2014**(1) (2014)

23. Chacón, J.M., Caminero, M.A., García-Plaza, E., Núñez, P.J.: Additive manufacturing of PLA structures using fused deposition modelling: effect of process parameters on mechanical properties and their optimal selection. Mater. Des. **124**, 143–157 (2017)

24. Wittbrodt, B., Pearce, J.M.: The effects of PLA color on material properties of 3-D printed components. Addit. Manuf. **8**, 110–116 (2015)

25. Pei, E., Lanzotti, A., Grasso, M., Staiano, G., Martorelli, M.: The impact of process parameters on mechanical properties of parts fabricated in PLA with an open-source 3-D printer. Rapid Prototyp. J. (2015)

26. Torres, J., Cotelo, J., Karl, J., Gordon, A.P.: Mechanical property optimization of FDM PLA in shear with multiple objectives. JOM **67**(5), 1183–1193 (2015)

27. Li, H., Wang, T., Sun, J., Yu, Z.: The effect of process parameters in fused deposition modelling on bonding degree and mechanical properties. Rapid Prototyp. J. **24**(1), 80–92 (2018)
28. Ahn, S.H., Montero, M., Odell, D., Roundy, S., Wright, P.K.: Anisotropic material properties of fused deposition modeling ABS. Rapid Prototyp. J. **8**(4), 248–257 (2002)
29. Ning, F., Cong, W., Jia, Z., Wang, F., Zhang, M.: Additive manufacturing of CFRP composites using fused deposition modeling: effects of process parameters. In: ASME 2016 11th International Manufacturing Science and Engineering Conference, pp. V003T08A001–V003T08A001. American Society of Mechanical Engineers, June 2016
30. Christiyan, K.J., Chandrasekhar, U., Venkateswarlu, K.: A study on the influence of process parameters on the mechanical properties of 3D printed ABS composite. In: IOP Conference Series: Materials Science and Engineering, vol. 114, no. 1, p. 012109. IOP Publishing, Feb 2016
31. Singh, S., Singh, R.: Effect of process parameters on micro hardness of Al–Al$_2$O$_3$ composite prepared using an alternative reinforced pattern in fused deposition modelling assisted investment casting. Robot. Comput. Integr. Manuf. **37**, 162–169 (2016)

Experimental Investigation and Parametric Optimization of Wire Electrical Discharge Machining for Ti–6Al–4V Alloy Using Response Surface Methodology

Sandeep Malik and Vineet Singla

1 Introduction

Due to its strong machinability and excellent physical and mechanical properties, Ti–6Al–4V super-alloy has a broad spectrum of use in a variety of fields. TI–6Al–4V alloy α-β titanium is considered to be the most common type of titanium alloy used in the aerospace industry with over 50% of global production [1]. These versatile qualities of titanium alloy have attracted the attention of researchers and industry staff worldwide. In contrast, the Ti–6Al–4V has become a priority of industrial research and engineering in the manufacturing industry because of its large variety of applications in different areas of engineering micromachining. The Ti–6Al–4V process requires a thorough knowledge of the system, however, because it contains specific process variables that affect machining parameters [2]. The recent research trend for specific production in the world of titanium superalloy micromachining is due to its traditional properties such as highly corrosive, high-temperature tolerant, high strength-to-weight ratio, and the wide range of applications in different engineering fields, from aerospace to vehicles and biomedical [3–5]. The poor thermal conductivity, weak elasticity, and high chemistral affinity of the alloy make it extremely difficult to process, as the small chips quickly reposition themselves in the cutting device due to their extremely high local temperature, stress and chemical affinity [6]. According to their above features, the methods of production suitable to the workpiece and the cutting instrument must be carefully selected and properly understood, as these processes deteriorate. For example, during the process of machining titanium chattering contributes significantly to the wear of tools [7]. In addition, titanium super-alloy is considered a highly difficult material to cut, and endures poor processing in most material removal processes, in particular microholes by conventional methods of machinery [8]. So Ti–6Al–4V was considered ideal for machining using

S. Malik (✉) · V. Singla
Department of Mechanical Engineering, UIET, Maharshi Dayanand University, Rohtak, Haryana, India
e-mail: sandymalik0077@gmail.com

unorthodox methods like electro discharge machining (EDM), as no direct contact occurs between the device and the workpiece [9].

The experiments with Ti–6Al–4V were carried out by Kuriakose and Shunmugam [10], and a optimization approach was used to evaluate the effect of different wire-EDM (WEDM) system input parameters on cutting rate and surface rugging. The WEDM framework was reformulated to define key decision parameters as a classification issue. EDM is essentially an electrothermal process that produces a large number of electric sparks within a fraction of a second, resulting in a high degree of heat energy that is sufficient to remove the product from operation [11]. In addition, EDM could, regardless of its hardness and strength, be used for electrically conducting materials. In the case of β-TiAl alloy cutting of electrically discharge wire, Sarkar et al. [12] conducted an analysis. The process had been modeled successfully using RSM and adequacy control of the model was also conducted. The main problem with EDM is that there are a large number of input system parameters and therefore difficulties in understanding the importance of input parameters on the component generated. Therefore, a number of approaches have helped numerous researchers refine the input parameters.

In WEDM procedures, Tosun et al. [13] studied the results and optimization of kerf machining parameters and MRRs. The very effective parameters of the kerf and MRR, both as open-circuit voltage and pulse duration, have been found based on ANOVA method. For the analysis of the specific discharge energy (SDE) theory in WEDM, Liao and Yu [14] used experimental approach model (DOE). Experimental results showed that, while all materials are machined at the same work conditions, the relative relation between different materials of SD is invariant. A quantitative relation between the machining parameters and width of the distance in WEDM was obtained through dimensional analysis of SDE. To optimize the WEDM process, Kuriakose and Shunmugam [15] have used several regression models to represent the relation between input and output variables and a multifaceted optimization approach based on a non-dominated genetic sorting algorithm (NSGA). In the parametric Taguchi methodology model, Ramakrishnan and Karunamoorthy [16] identified the multi-target optimization of the WEDM process. Sarkar et al. [17] conducted research with γ-titanium aluminide alloy as working material to estimate the frequency of cutting and devised mathematical models. In Literature, number of research work reported the application of EDM/PM-EDM/W-EDM for machining/surface modification of metallic biomaterials for biomedical applications [18–26]. Moreover, several optimization techniques were adopted to optimize the process of EDM/PM-EDM/W-EDM parameters to obtain the desired surface characteristic and properties [27–30].

Overall, three key points were determined from the literature review: (i) the machining of the super-alloys based on the Ti is extremely difficult, in particular in the sense of traditional methods, and (ii) the EDM technique is ideal for the machining and manufacture of Ti-based super-alloys in different contours. Therefore, an attempt has been made to refine the primarily selected feedback for the present work based on points accrued. On the basis of the obtained results, an attempt has been made at this research work, by using the response surface technique to refine

the primary selected WEDM input system parameters. Therefore, the value of the parameters input for the extraction level of material and surface roughness could be visualized on the basis of response plots and evaluation of variance.

2 Materials and Method

As a rectangular plate with lengths as 15–10–50 mm, the workpiece component is Ti–6Al–4V alloy. Experiments with an Electronoca WEDM as shown in Fig. 1 are conducted. Distilled liquid in this experiment was used as the dielectric fluid. The material extraction rate (MRR), as suggested by the design of the experiment, for all the included experimental runs was calculated by observing the average material quantity taken in relation to the time of cutting. In addition, the Surface Roughness

Fig. 1 Schematic representation of WEDM machine

Table 1 Process parameters and their levels

Process parameters	Units	Parameter designation	Levels		
			L-1	L-2	L-3
Peak current	A	I_p	80	120	160
Pulse duration	μs	T_{on}	100	150	200
Pulse interval	μs	T_{off}	50	100	150
Wire feed	mm/s	Wf	6	8	10

Tester (Talysurf: Mitutoyo) was used for measuring the machined samples' surface roughness (SR). The parameters and levels of the selected input processes can be found in Table 1. Throughout machining, flushing of the fluid was fixed to 1 kg/cm^3.

Experimentation has been performed as per the settings given in Table 1. The Table 2 also highlighted the observations made for MRR and SR. The obtained raw data has been optimized and further studied for its statistical significance through response surface methodology (RSM). For these activities, Design Expert-14, a statistical software package, has been used. The main objective of RSM employment is to get the best possible results with minimum variation, to generate response plots and to perform ANOVA.

3 Results and Discussion

3.1 Response Analysis

Figure 2a shows the three-dimensional (3D) surface plot for MRR in response of peak current (I_p) and pulse duration (T_{on}). It can be seen from the plot that when peak current increased from 80 to 120 A, the MRR has been increased. However, further increase in the peak current from 120 to 160 A reduced the MRR. As observed, the maximum MRR of the Ti–6Al–4V has been seen at 120 A of peak current. This means that, after 120 A of peak current, the formation of debris was quite rapid and was concentrated around the electrode. Due the accumulation of the debris between electrode and workpiece subsequent short-circuiting was reduced, which affected the MRR. Further, Fig. 2a also indicates that the pulse duration has marginal effect on the MRR and was found to be optimum at 150 μs. Similarly, in case of Fig. 2b, it can be seen that with an increase in the pulse off duration (T_{off}) the MRR of the Ti alloy has increased. This may be contributed toward the fact that an increase in this parameter's level allowed the spark active for the longer duration which later accumulated more heat on the work surface. However, in case of wire feed (F_d), it has been found that parametric levels beyond #7 have increased the MRR. This is an interesting observation, as the literature highlighted the opposite results.

Table 2 Process parameters and their levels

S. no.	Exp. no.	I_p	T_{on}	T_{off}	F_d	MRR	SR
1	9	80	100	50	6	0.9735	1.191
2	17	160	100	50	6	1.2855	1.943
3	26	80	200	50	6	1.122	1.0345
4	20	160	200	50	6	1.4475	1.711
5	7	80	100	150	6	1.1745	1.171
6	30	160	100	150	6	1.4865	1.824
7	23	80	200	150	6	1.3425	0.996
8	1	160	200	150	6	1.653	1.6425
9	6	80	100	50	10	1.0875	0.7455
10	22	160	100	50	10	1.638	1.441
11	8	80	200	50	10	1.2975	0.631
12	21	160	200	50	10	1.839	1.42
13	12	80	100	150	10	1.014	0.745
14	27	160	100	150	10	1.4625	1.423
15	15	80	200	150	10	1.3215	0.7295
16	24	160	200	150	10	1.782	1.3475
17	10	40	150	100	8	0.84	0.825
18	29	200	150	100	8	1.7355	1.6255
19	13	120	50	100	8	1.044	1.3255
20	16	120	250	100	8	1.3545	0.9675
21	3	120	150	50	8	1.0605	1.296
22	25	120	150	200	8	1.2675	1.005
23	5	120	150	100	4	1.701	1.935
24	11	120	150	100	12	1.791	1.0105
25	28	120	150	100	8	1.185	1.2425
26	2	120	150	100	8	1.158	1.1815
27	4	120	150	100	8	1.0965	1.276
28	14	120	150	100	8	1.188	1.241
29	19	120	150	100	8	1.134	1.1815
30	18	120	150	100	8	1.113	1.226

In case of SR, it has been indicated by Fig. 3a that the SR of the Ti-based super-alloy has been first increased with an increase in the pulse on duration up to 137.5 µs and then decreased slightly till 150 µs. Indeed, the larger pulse on duration will be responsible for the more heat development and, therefore, higher MRR will produce more SR. However, in the present case, the fall in the SR beyond 137.5 µs might be due to the distribution of the produced debris away from the workpiece-electrode zone, thus, interrupted the spark propagation. In case of peak current, the values of

Fig. 2 Surface plots of
MRR in response of input
parameters
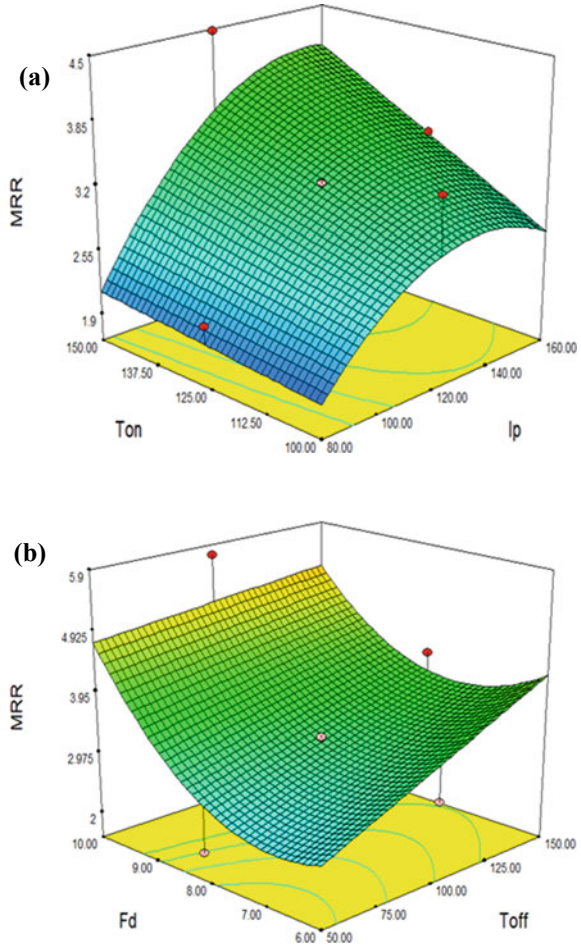
SR increased with an increase in the peak current. This is due to the same reason as
discussed above. In case of Fig. 3b, it has been found that the surface roughness of
the Ti alloy was first reduced by increasing the wire feed to 8, however, it further
increased when wire feed duration increased to 10. As seen, 8 has been observed as
the best parametric level of wire feed for SR. Further, in case of pulse off duration,
there is no noticeable change in SR.

From ANOVA results, refer Table 3, it has been found that in case of MRR,
the regression model as well as other process parameters are significant at 95%
confidence level. As required, the lack of fit is non-significant indicating the accuracy
of the analysis. Further R^2 and R^2 (adj) values are 0.889 and 0.847, respectively,
indicating that the model equation is able to predict the output responses, closely.

Fig. 3 Surface plots of SR in response of input parameters
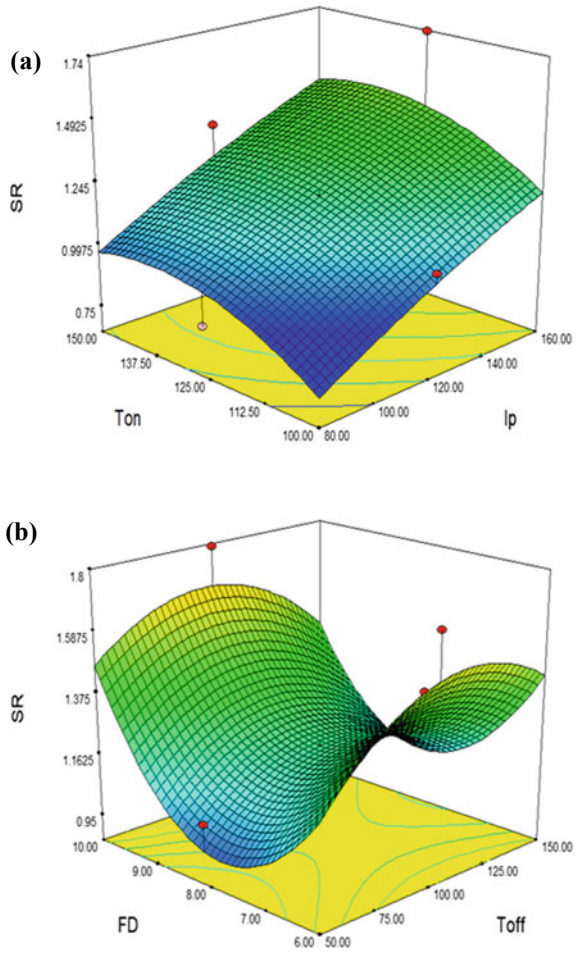
In case of SR also, as presented in Table 4, all the input process parameters, except T_{off}, are significant at 95% confidence level. In this case too, lack of fit is non-significant. The values of R^2 and R^2 (adj) are 0.85 and 0.80, respectively, indicating that the model equation is able to predict the output responses, closely.

4 Conclusions

From the present research work, the following observations have been made:

- The input process parameters of WEDM process have been successfully studied and optimized for their effects on the MRR and SR of Ti–6Al–4V alloy.

Table 3 ANOVA for MRR

Source	Sum of squares	DOF	Mean square	F-value	Prob. > F (p-value)	Remarks
Model	32.828	10	4.104	21.215	<0.0001	Significant
I_P	8.583	1	8.583	44.371	<0.0001	Significant
T_{on}	2.571	1	2.571	13.293	<0.0015	Significant
T_{off}	4.944	1	4.944	25.557	<0.0001	Significant
Fd	10.984	1	10.984	56.783	<0.0001	Significant
$I_P \times T_{on}$	1.285	1	1.285	6.644	<0.0176	Significant
$T_{off} \times F_d$	1.646	1	1.646	8.510	<0.0082	Significant
I_P^2	1.068	1	1.068	5.521	<0.0286	Significant
F_d^2	2.758	1	2.758	14.261	<0.0011	Significant
Residual	4.062	19	0.193			
Lack of fit	3.938	14	0.246	9.889	0.0095	Not significant
Pure error	0.124	5	0.025			
Cor. total	36.890	29				
Standard deviation = 0.43				$R^2 = 0.889$		
Mean = 3.49				Adjusted $R^2 = 0.847$		
Coefficient of variation = 12.60				Predicted $R^2 = 0.78$		
PRESS = 8.02				Adequate precision = 19.70		

- It has been found that MRR observations have strongly influenced by peak current, wire feed, of pulse off duration, however, pulse on duration remained non-influential.
- Similarly, in case of SR, wire feed and peak current showed strong influence.
- Further, from ANOVA, it has been found that all the input parameters for MRR are statistically significant, whereas, in case of SR, Toff has been found as insignificant parameter.

Table 4 ANOVA for SR

Source	Sum of squares	DOF	Mean square	F-value	Prob. > F (p-value)	Remarks
Model	1.877	7.000	0.268	18.462	<0.0001	1.877
I_P	0.960	1.000	0.960	66.092	<0.0001	0.960
T_{on}	0.221	1.000	0.221	15.203	<0.00085	0.221
T_{off}	0.032	1.000	0.032	2.169	0.1558	0.032
Fd	0.061	1.000	0.061	4.194	<0.0489	0.061
$T_{off} \times F_d$	0.077	1.000	0.077	5.303	0.0311	0.077
T_{off}^2	0.143	1.000	0.143	9.864	<0.0048	0.143
F_d^2	0.492	1.000	0.492	33.903	<0.0011	0.492
Residual	0.319	22.000	0.015			0.319
Lack of fit	0.312	17.000	0.018	12.919	0.0051	0.312
Pure error	0.124	5	0.025			
Cor. total	36.890	29				
Standard deviation = 0.12				$R^2 = 0.85$		
Mean = 1.30				Adjusted $R^2 = 0.80$		
Coefficient of variation = 9.13				Predicted $R^2 = 0.72$		
PRESS = 0.60				Adequate precision = 15.08		

References

1. Lütjering, G., Williams, J.C.: Titanium, 2nd edn. Springer, New York (2007)
2. Tiwary, A.P., Pradhan, B.B., Bhattacharyya, B.: Study on the influence of micro-EDM process parameters during machining of Ti–6Al–4V superalloy. Int. J. Adv. Manuf. Technol. **76**(1–4), 151–160 (2015)
3. Boyer, R.R.: An overview on the use of titanium in the aerospace industry. Mater. Sci. Eng. A **213**(103–114), 2 (1996)
4. Schauerte, O.: Titanium in automotive production. Adv. Eng. Mater. **5**(411–418), 3 (2003)
5. Yoshinari, M., Matsuzaka, K., Inoue, T., Oda, Y., Shimono, M.: Biofunctionalization of titanium surfaces for dental implants. Mater. Trans. **43**, 2494–2501 (2002)
6. Setti, D., Sinha, M.K., Ghosh, S., Rao, P.V.: Performance evaluation of Ti–6Al–4V grinding using chip formation and coefficient of friction under the influence of nanofluids. Int. J. Mach. Tools Manuf. **88**, 237–248 (2015)
7. Sun, S., Brandt, M., Dargusch, M.S.: Effect of tool wear on chip formation during dry machining of Ti–6Al–4V alloy, part 1: effect of gradual tool wear evolution. Proc. Inst. Mech. Eng. Part B: J. Eng. Manuf. **231**(9), 1559–1574 (2017)
8. Ezugwu, E.O., Wang, Z.M.: Titanium alloys and their machinability—a review. J. Mater. Process. Technol. **68**(3), 262–274 (1997)
9. Lin, Y.C., Yan, B.H., Chang, Y.S.: Machining characteristics of titanium alloy (Ti–6Al–4V) using a combination process of EDM with USM. J. Mater. Process. Technol. **104**, 171–177 (2000)
10. Kuriakose, S., Shunmugam, M.S.: Characteristics of wire-electro discharge machined Ti6Al4V surface. Mater. Lett. **58**, 2231–2237 (2004)

11. Altpeter, F., Roberto, P.: Relevant topics in wire electrical discharge machining control. J. Mater. Process. Technol. **149**, 147–151 (2004)

12. Sarkar, S., Sekh, M., Mitra, S., Bhattacharyya, B.: Modeling and optimization of wire electrical discharge machining of γ-TiAl in trim cutting operation. J. Mater. Process. Technol. **205**, 376–387 (2007)

13. Tosun, N., Cogun, C., Tosun, G.: A study on kerf and material removal rate in wire electrical discharge machining based on Taguchi method. J. Mater. Process. Technol. **152**, 316–322 (2004)

14. Liao, Y.S., Yu, Y.P.: The energy aspect of material property in WEDM and its application. J. Mater. Process. Technol. **149**, 77–82 (2004)

15. Kuriakose, S., Shunmugam, M.S.: Multi-objective optimization of wire-electro discharge machining process by non-dominated sorting genetic algorithm. J. Mater. Process. Technol. **170**, 133–141 (2005)

16. Ramakrishnan, R., Karunamoorthy, L.: Multi response optimization of wire EDM operations using robust design of experiments. Int. J. Adv. Manuf. Technol. **29**, 105–112 (2006)

17. Sarkar, S., Mitra, S., Bhattacharyya, B.: Parametric analysis and optimization of wire electrical discharge machining of γ-titanium aluminide alloy. J. Mater. Process. Technol. **159**, 286–294 (2005)

18. Prakash, C., Kansal, H. K., Pabla, B. S., Puri, S.: Experimental investigations in powder mixed electric discharge machining of Ti–35Nb–7Ta–5Zrβ-titanium alloy. Mater. Manuf. Process. **32**, 274–285 (2017)

19. Prakash, C., Kansal, H. K., Pabla, B. S., Puri, S., & Aggarwal, A.: Electric discharge machining–a potential choice for surface modification of metallic implants for orthopedic applications: a review. Proc. Inst. Mech. Eng B-J. Eng. **230**, 331–353 (2016)

20. Prakash, C., Kansal, H. K., Pabla, B. S., Puri, S.: Processing and characterization of novel biomimetic nanoporous bioceramic surface on β-Ti implant by powder mixed electric discharge machining. J. Mater. Eng. Perform. **24**, 3622–3633 (2015)

21. Prakash, C., Uddin, M. S.: Surface modification of β-phase Ti implant by hydroaxyapatite mixed electric discharge machining to enhance the corrosion resistance and in-vitro bioactivity. Surf. Coat. Technol. **326**, 134–145 (2017)

22. Prakash, C., Kansal, H. K., Pabla, B. S., Puri, S.: Powder mixed electric discharge machining: an innovative surface modification technique to enhance fatigue performance and bioactivity of β-Ti implant for orthopedics application. J. Comp. Inform. Sci. Eng. **16**, 1–9 (2016)

23. Prakash, C., Singh, S., Pabla, B. S., Uddin, M. S.: Synthesis, characterization, corrosion and bioactivity investigation of nano-HA coating deposited on biodegradable Mg-Zn-Mn alloy. Surf. Coat. Technol. **346**, 9–18 (2018)

24. Aliyu, A. A. A., Abdul-Rani, A. M., Ginta, T. L., Prakash, C., Axinte, E., Razak, M. A., Ali, S.: A review of additive mixed-electric discharge machining: current status and future perspectives for surface modification of biomedical implants. Adv. Mater. Sci. Eng. (2017)

25. Prakash, C., Singh, S., Pruncu, C. I., Mishra, V., Królczyk, G., Pimenov, D. Y., Pramanik, A.: Surface modification of Ti-6Al-4V alloy by electrical discharge coating process using partially sintered Ti-Nb electrode. Materials **12**, 1006 (2019)

26. Prakash, C., Kansal, H. K., Pabla, B. S., Puri, S.: Effect of surface nano-porosities fabricated by powder mixed electric discharge machining on bone-implant interface: an experimental and finite element study. Nanosci. Nanotechnol. Let. **8**, 815–826 (2016)

27. Prakash, C., Singh, S., Singh, M., Verma, K., Chaudhary, B., Singh, S.: Multi-objective particle swarm optimization of EDM parameters to deposit HA-coating on biodegradable Mg-alloy. Vacuum **158**, 180–190 (2018)

28. Prakash, C., Kansal, H. K., Pabla, B. S., Puri, S.: Multi-objective optimization of powder mixed electric discharge machining parameters for fabrication of biocompatible layer on β-Ti alloy using NSGA-II coupled with taguchi based response surface methodology. J. Mech. Sci. Technol. **30**, 4195–4204 (2016)

29. Prakash, C., Kansal, H. K., Pabla, B. S., Puri, S.: To optimize the surface roughness and micro-hardness of β-Ti alloy in PMEDM process using Non-dominated Sorting Genetic Algorithm-II. 2nd International Conference on Recent Advances in Engineering & Computational Sciences (RAECS), pp. 1–6 (2015)
30. Prakash, C., Singh, S., Singh, M., Antil, P., Aliyu, A. A. A., Abdul-Rani, A. M., Sidhu, S. S.: Multi-objective optimization of MWCNT mixed electric discharge machining of Al–30SiCp MMC using particle swarm optimization. Futuristic Composites, pp. 145–164 (2018)

Effect of Process Parameters on Volume and Geometrical Features of Electric Discharge Machined Channels on a Cast AA6061-B$_4$C Composite

Suresh Gudipudi ⓘ**, Selvaraj Nagamuthu, Taraka Sarath Chandra Dongari, Kanmani Subbu Subbian, and Surya Prakasa Rao Chilakalapalli**

1 Introduction

Machining of mini channels on a different type of work material is being gained a lot of attention due to higher heat dissipation capability by allowing the fluids or gases to flow through them [1, 2]. Various machining methods are being practiced to make these channels and were reported in the literature. Abrasive water-jet micro-milling, laser beam micro-milling, Micro Electric Discharge milling, Electrochemical micro-micromachining, friction stir process, and sinker EDM were reported [3–9]. For better heat dissipation rate with low coefficients of thermal expansion, the composites were reported to be advantageous than pure metal or alloys [10–12]. AA6061-B$_4$C is the one such composite and found application in various high technology industries [13]. These composites are also proved to be a potential material in the defense and space sectors [14, 15]. An EDM is being widely used while machining the composite materials [16–20]. The non-contacting type with lower material removal rate characteristics of the EDM process has succeeded to attain the high surface finish and good dimensional accuracy [21–41]. Therefore, in the present work, the stir casting method was used to fabricate the AA6061-B$_4$C composites and the sinker EDM to make the channels. However, the cooling and fluid characteristics of the given fluid and flow type depends on both the physical and geometric profile characteristics of a produced channel. But these characteristics of the produced channel would

S. Gudipudi (✉) · S. Nagamuthu · T. S. C. Dongari · S. P. R. Chilakalapalli
Department of Mechanical Engineering, National Institute of Technology Warangal, Warangal 506004, Telangana, India
e-mail: gudipudi.suresh@gmail.com

K. S. Subbian
Discipline of Mechanical Engineering, Indian Institute of Technology Palakkad, Palakkad 678557, Kerala, India

S. P. R. Chilakalapalli
National Institute of Technology Andhra Pradesh, Tadepalligudem 534102, Andhra Pradesh, India

greatly be affected by the chosen manufacturing method and conditions. Therefore, the present work was focused to study the effect of EDM conditions on volume and geometrical profile aspects like volume, taper, and overcut of the produced channel. Therefore, a proper way of experimentation is needed which can overcome the cost and time limitations with a minimum number of experimental runs to get a better understanding of the relation between input parameters and output responses. Moreover, it will be highly appreciated when experimenting with novel materials. Taguchi's design of experiments is one such experimental design which can give a better combination of input parameter levels with a minimum number of experiments to get the desired level of output response. Therefore, the present study was conducted based on the L9 orthogonal array for EDM experimentation.

2 Materials and Methods

2.1 Development of AA6061-4Wt%B$_4$C Work Specimen

The stir-cast process was used to develop the composite work specimens. The AA6061 pieces were heated at 750 °C. Preheated (at 280 °C) 4wt% B$_4$C reinforcement particles and 10wt% F$_6$K$_2$Ti flux were added through the vortex formed due to mechanical stirring. The stirring was done at two stages by allowing the composite mix to semi-solidified state and reheating again. The ultrasonic sound waves at 18 kHz were also introduced for a time of 20 min in the molten matrix to induce a cavitation effect with the help of titanium made an ultrasonic probe. The two-stage heating and ultra-sonication of the composite mix would promote the better dispersion of B$_4$C particles in the AA6061 matrix material and particle wetting with the matrix. The solidified cast composites were heat-treated (T6 condition). The density of the composite was calculated as 2.612 g/cm^3. The individual distribution of B$_4$C particles in the AA6061 matrix was noticed from optical and scanning electron micrographs.

2.2 EDM Experimental Design of Composite

The tool made of copper having 1 mm thickness and composite work material of 2 mm thickness were machined as shown in Fig. 1. The diesinker EDM setup of straight polarity was used to make the channels (rectangular type) in the developed composite. The copper tool electrode was positioned at the discharge gap of 0.25 mm. Electric potential (85 ± 15) was applied to initiate the plasma at the discharge gap by breakdown of the dielectric strength. The voltage of 55 ± 10 V was maintained until the machining time of 5 min. Therefore, the melting and vaporization of the composite occurred because of the intensive heat of the generated plasma. Thus, the
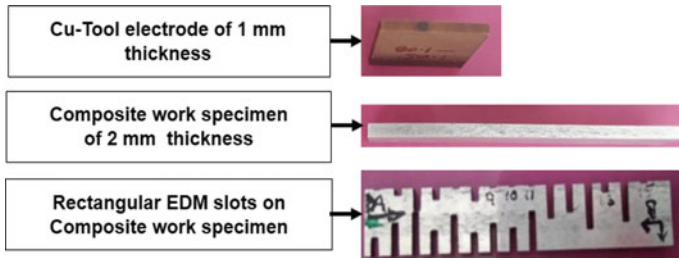
Fig. 1 The photographs of tool and AA6061-B$_4$C composite work specimens

Table 1 The EDM experimental input parameter levels and output responses

Input parameters			
Parameter	Level 1	Level 2	Level 3
Current, I (A)	4	6	8
Pulse-on time, T-on (μs)	25	45	65
Pulse-off time, T-off (μs)	24	36	48
Output responses			
Response 1	*Volume of the channel, V* (mm^3)		
Response 2	*Taper, θ* (°)		
Response 3	*Overcut, OC* (mm)		
Response 4	*The difference in depth, Δd* (mm)		

crater was created in the composite specimen which is the replica of the shape of the tool. The EDM input parameter levels and output characteristics for L-9 orthogonal array experimental design were tabulated in Table 1.

2.3 Model Calculation of Volume, V *(mm³)*

The data points which are obtained for both the entrance and the exit of each rectangular channel from the optical profile projector were used to generate entrance and exit profiles as shown in Fig. 2. These profiles were used to develop a CAD-based 3-dimensional geometric model to estimate the *volume, V* (mm^3) of the channel produced for EDM time of 5 min as indicated in Fig. 3. The various geometrical features (*taper, overcut, the difference in depth*) of each channel at both the entrance and exit cross-sections were calculated by using Eqs. 1, 2, and 3.

$$\text{Taper, } \theta = \tan^{-1}\left(\frac{W_{\text{top}} - W_{\text{bot}}}{2d}\right) \tag{1}$$
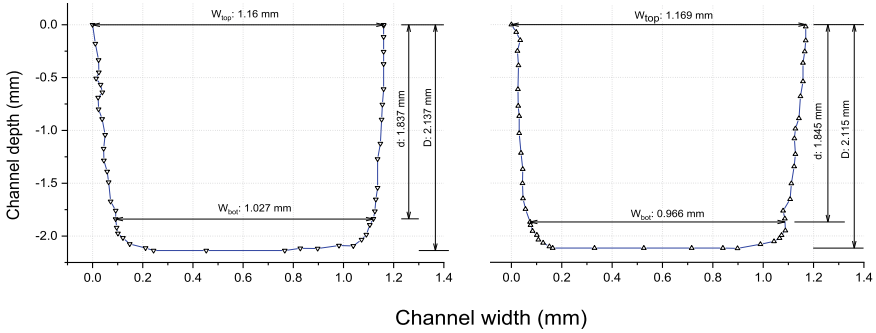
Fig. 2 Entrance and exit cross sectional profiles

Fig. 3 Geometric model (not to scale) to estimate the volume of the channel
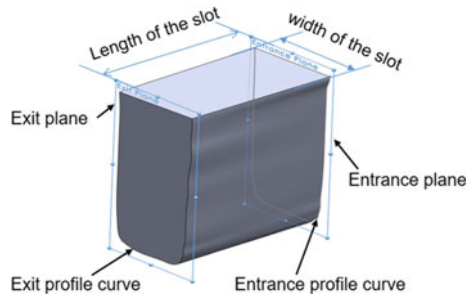
$$\text{Overcut, } OC = \frac{T_t - W_{\text{top}}}{2} \tag{2}$$

$$\text{Difference in depth, } \Delta d = D - d \tag{3}$$

The various terms involved in the above equations were obtained from the entrance and exit profile of the corresponding channel (Fig. 2). The geometric model was developed at each experimental run as shown in Fig. 3.

3 Results and Discussion

The Taguchi L-9 experimental design and results were represented in Table 2.

Table 2 Representation of Taguchi L9 experimental design and results

Trail no	I (A)	T-on (µs)	T-off (µs)	V (mm³)	θ (°)		OC (mm)		Δd (mm)	
					Entrance	Exit	Entrance	Exit	Entrance	Exit
1	4	25	24	0.4683	7.01	16.01	0.011	0.032	0.102	0.078
2	4	45	36	0.3077	21.60	20.46	0.005	0.005	0.069	0.026
3	4	65	48	0.2812	22.88	20.20	0.003	0.030	0.054	0.063
4	6	25	36	3.2491	2.69	3.09	0.057	0.074	0.364	0.355
5	6	45	48	1.5237	4.12	6.05	0.052	0.049	0.207	0.224
6	6	65	24	1.0337	9.37	4.40	0.057	0.028	0.151	0.16
7	8	25	48	10.20	1.83	1.66	0.101	0.094	0.572	0.566
8	8	45	24	3.8742	3.49	3.66	0.079	0.095	0.402	0.384
9	8	65	36	2.6199	3.78	4.69	0.063	0.069	0.315	0.28

3.1 Effect of EDM Conditions on the Volume of the Machined Channel

The results of the regression analysis for the *volume* of the channel was shown in Table 3. The main effect plots and residuals of the EDM parameters for volume were shown in Fig. 4. The developed linear model (regression) was represented with the Eq. 4. The higher value of *volume* was observed at higher '*I*' (8A) and lower *T-on* (25 μs) values. The reason is at higher '*I*' value, the amount of available heat energy would increase due to generated plasma. Hence, the more amount of work material gets melted and evaporated. At the lower *pulse-on time* the growth of the plasma was confined to small radius values. Hence the area which exposed to this plasma subjected to high intensive heating. Moreover, the short duration of pulse results in creating some forces of impulsive in nature and the more amount of

Table 3 The experimental (L-9) results for *volume*

Model		
S	R^2	R^2 (adjusted)
1.7360	99.35%	97.39%

SNR (signal to noise ratio) response table (larger is better)			
Level	*I*	*T-On*	*T-Off*
1	−9.2822	7.9392	1.8207
2	4.7270	1.7281	2.7878
3	13.4338	−0.7887	4.2701
Delta	22.7160	8.7280	2.4494
Rank	1	2	3

Analysis of variance (ANOVA)						
Source	DF	Seq SS	Adj SS	Adj MS	F	P
I	2	788.083	788.083	394.042	130.75	**0.008**
T-on	2	121.090	121.090	60.545	20.09	**0.047**
T-off	2	9.132	9.132	4.566	1.52	0.398
Residual Error	2	6.028	6.028	3.014		
Total	8	924.333				

Fig. 4 Main effect plots of SN ratios, means, and residual plots for *volume*

heat was concentrated on less area. Thus, the material gets removed quickly during successive pulses. The ANOVA results showed that both the '*I*' and *pulse-on time* are the significant parameters for *volume* of the channel with p-values 0.008 and 0.047, respectively. Hence, the experiment trail number 7 (*current:* 8 A; *T-on:* 25 µs; *T-off:* 48 µs) was obtained higher volume as 10.2 mm^3.
Regression equation

$$\text{Volume} = -4.77 + 1.303\,A - 0.0832\,B + 0.0921\,B \tag{4}$$

3.2 Effect of EDM Conditions on the Taper at the Entrance

The results of the regression analysis for the taper at the entrance cross-section profile of channels were tabulated (Table 4). The main effect and residual plots of the EDM parameters for the taper were shown in Fig. 5. The developed linear model (regression) was represented with Eq. 5. From the results, it was observed that the taper was less at higher *current*, lower *T-on*, and lower *T-off*. The reason is at the higher current the composite work material gets sufficient heat to reach completely molten state, at lower *pulse-on time* the high energy-intensive pulses could eject the debris and re-solidified matrix metal from the machining area.

Table 4 The L-9 Taguchi experimental results for *taper* at the entrance

Model					
S	R^2	R^2 (adjusted)			
3.0690	96.07%	84.28%			
SNR response table (smaller is better)					
Level	*Current*	*T-on*	*T-off*		
1	−23.598	−10.253	−15.735		
2	−13.443	−16.615	−15.611		
3	−9.218	−19.391	−14.912		
Delta	14.379	9.138	0.823		
Rank	1	2	3		
ANOVA					
Source	DF	Seq SS	Adj SS	Adj MS	F	P
I	2	327.723	327.723	163.862	17.40	**0.054**
T-on	2	131.693	131.693	65.846	6.99	0.125
T-off	2	1.182	1.182	0.591	0.06	0.941
Residual Error	2	18.838	18.838	9.419		
Total	8	479.436				
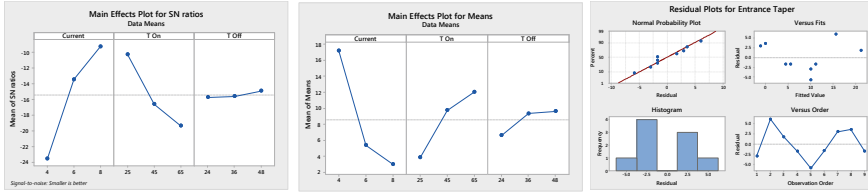
Fig. 5 Main effect plots of SN ratios, means, and residual plots for *taper* at the entrance

Regression equation

$$\text{Taper at the entrance} = 16.06 - 3.533\,A + 0.2042\,B + 0.124\,C \qquad (5)$$

3.3 Effect of EDM Conditions on Overcut at the Entrance

The results of the regression analysis for the *overcut* along the width of the channel at the entrance cross-section profile of channels were shown in Table 5. The main effect and residual plots of the EDM parameters for the *overcut* were shown in Fig. 6. The developed linear model (regression) was represented with Eq. 6. It was observed

Table 5 The L-9 Taguchi experimental results for *overcut* at the entrance

Model					
S	R^2	R^2 (adjusted)			
2.5778	98.70%	94.82%			
SNR response table (smaller is better)					
Level	*Current*	*T-on*	*T-off*		
1	45.22	27.99	28.70		
2	25.15	31.25	31.64		
3	21.99	33.12	32.02		
Delta	23.23	5.13	3.32		
Rank	1	2	3		
ANOVA					
Source	DF	Seq SS	Adj SS	Adj MS	F	P
I	2	952.13	952.13	476.063	71.64	**0.014**
T-on	2	40.42	40.42	20.209	3.04	0.247
T-off	2	19.77	19.77	9.887	1.49	0.402
Residual Error	2	13.29	13.29	6.645		
Total	8	479.436				
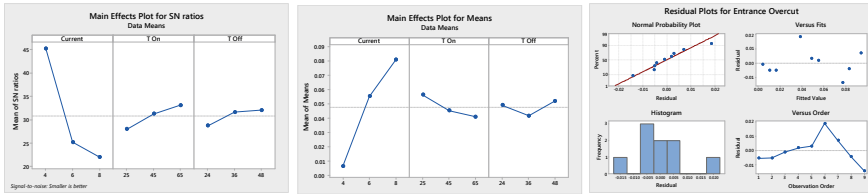
Fig. 6 Main effect plots of SN ratios, means, and residual plots for *overcut* at the entrance

that the lower '*I*' (4A) and longer '*T-on*' (45 and 65 µs). It is because of the low tool wear around the edges, lower heat energy, and current density could melt the vicinity of the machining zone only.

Regression equation

$$\text{Overcut} = -0.0517 + 0.01867\,A - 0.000383\,B + 0.000125\,C \qquad (6)$$

3.4 *Effect of EDM Conditions on* the Difference in Depth at the Entrance

The results of the regression analysis for *the difference in depth* of the channel at the entrance cross-section profile were shown in Table 6. The main effect and residual plots of the EDM parameters for *the difference in depth* were shown in Fig. 7. The developed linear model (regression) was represented with Eq. 7. Results showed that *the difference in depth* value is minimum at lower '*I*' and '*T-on*'. The lower heat energy and power density are the reasons which could not penetrate the work material through the depth below the tapered portion. Hence, the experiment trail numbers 4 and 5 were yielded a minimum value in *the difference in depth* of the channel.

Regression equation

$$\text{Difference in depth} = -0.1783 + 0.08867\,A - 0.004317\,B + 0.00247\,C \qquad (7)$$

4 Conclusions

The AA6061-4wt% B$_4$C composites work specimens were developed by stir casting method. The sinker EDM at varied input process parameters was used to create the channels using Taguchi L9 experimental design. The output responses such as *volume* and geometrical features such as *Taper, Overcut*, and *The difference in depth* of the

Table 6 The L-9 Taguchi experimental results for *the difference in depth* at the entrance

Model		
S	R^2	R^2 (adjusted)
0.7130	99.76%	99.02%
SNR response table (smaller is better)			
Level	*Current*	*T-on*	*T-off*
1	22.801	11.153	14.721
2	12.960	14.940	14.012
3	7.600	17.269	14.628
Delta	15.201	6.116	0.710
Rank	1	2	3
ANOVA						
Source	DF	Seq SS	Adj SS	Adj MS	F	P
I	2	356.632	356.632	178.316	350.73	**0.003**
T-on	2	57.173	57.173	28.586	56.23	**0.017**
T-off	2	0.893	0.893	0.446	0.88	0.533
Residual Error	2	1.017	1.017	0.508		
Total	8	415.714				
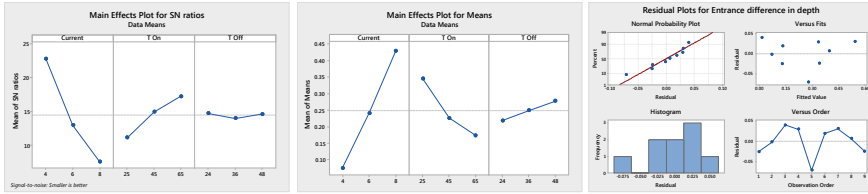
Fig. 7 Main effect plots of SN ratios, means, and residual plots for *the difference in depth*

channel were obtained by developing the geometric model. The linear regression model was developed to relate the EDM input parameters and output responses (channel *volume* and its features). The developed models for all outputs responses could explain the variation in the process to the extent of 99.35% (R^2 of *volume*), 96.07% (R^2 of *taper*), 98.70% (R^2 of *overcut*), and 99.76% (R^2 of *the difference in depth*). ANOVA was performed to identify the significant input parameters which affect the output response. ANOVA showed that the both '*I*' and '*T-on*' are significant parameters affecting the *volume* (p-value 0.008 for *current* and p-value 0.047 for *T-On*) and *the difference in depth* (p-value 0.003 for *current* and p-value 0.017 for *T-On*), whereas the *current* for a *taper* (p-value 0.05) and *overcut* (p-value 0.014). The arrived major conclusions from the present study are as follows.

- The higher *current* and lower *T-on* values are preferred to get high *volume*.
- The higher *current* and higher *T-on* values are suggested to reduce the *taper*.

- The Lower *current* and higher *T-on* are helping in reducing the *overcut.*
- The Lower *current* and higher *T-on* are helping in decreasing *the difference in depth.*

References

1. Smakulski, P., Pietrowicz, S.: A review of the capabilities of high heat flux removal by porous materials, microchannels and spray cooling techniques. Appl. Therm. Eng. **104**, 636–646 (2016)
2. Naqiuddin, N.H., Saw, L.H., Yew, M.C., Yusof, F.: Overview of micro-channel design for high heat flux application. Renew. Sustain. Energy Rev. **82**, 901–914 (2018)
3. Naser, H., Jan, K.S., Marcello, P.: Abrasive waterjet micro- machining of channels in metals: comparison between machining in air and submerged in water. Int. J. Mach. Tools Manuf. **88**, 108–117 (2015)
4. Darwish, S., Ahmed, N., Alahmari, A.M.: A study of micro-channel size and spatter dispersion for laser beam micro-milling. Mater. Manuf. Process. **32**(2), 171–184 (2017)
5. Karthikeyan, G., Garg, A.K., Ramkumar, J., Dhamodaran, S.: A microscopic investigation of machining behavior in μED-milling process. J. Manuf. Process. **14**(3), 297–306 (2012)
6. Ghoshal, B., Bhattacharyya, B.: Investigation on profile of microchannel generated by electrochemical micromachining. J. Mater. Process. Technol. **222**, 410–421 (2015)
7. Salimi, S., Haghpanahi, M., Bahemmat, P.: Fabrication of cooling channels employing worm voids caused by friction stir based process: considering cooling and fluid parameters. J. Manuf. Process. **35**, 61–70 (2018)
8. Suresh, G., Selvaraj, N., Kanmani, S.S., Rao, C.S.P.: Experimental investigation and mathematical modelling for material removal and tool wear in making of rectangular channels by Electric Discharge Machining (EDM) on Aluminium-Boron carbide composite sintered preforms. In: International Conference on Applied Mechanical Engineering Research, Warangal, India, paper no. ICP-080, 2–4 May 2019
9. Suresh, G., Selvaraj, N., Kanmani, S.S., Rao, C.S.P.: Fabrication and experimental study to optimize the recast layer and the material removal in electric discharge machining (EDM) of AA6061-B$_4$C composite. Mater. Today: Proc. **19P2**, 448–454(2019)
10. Okumus, S.C., Aslan, S., Karslioglu, R., Gultekin, D., Akbulut, H.: Thermal expansion and thermal conductivity behaviors of Al-Si/SiC/graphite hybrid Metal Matrix Composites (MMCs). Mater. Sci. **18**(4), 341–346 (2012)
11. Arslan, G., Kalemtas, A.: Processing of silicon carbide–boron carbide–aluminium composites. J. Eur. Ceram. Soc. **29**, 473–480 (2009)
12. Pozdniakov, A.V., Lotfy, A., Qadir, A., Shalaby, E., Khomutov, M.G., Churyumov, A.Y.: Development of Al-5Cu/B$_4$C composites with low coefficient of thermal expansion for automotive application. Mater. Sci. Eng. A **688**, 1–8 (2017)
13. Miracle, D.B.: Science and metal matrix composites—from science to technological significance. Compos. Sci. Technol. **65**, 2526–2540 (2005)
14. NMLINDIA Homepage: http://eprints.nmlindia.org/2642/1/103-115.PDF. Accessed 10 Dec 2018
15. Park, S., Jo, I., Lee, S.: Analysis of metal matrix composite (MMC) applied armor system. Procedia Eng. **204**, 100–107 (2017)
16. Lorelei, G., Andrew, G., Otto, B., Svetan, R.: Manufacturing technology: micro-machining. In: Fassi, I., David, S. (eds.) Micro-Manufacturing Technologies and Their Applications. Springer Tracts in Mechanical Engineering. Switzerland, pp. 97–128 (2017)
17. Liu, J., Li, J., Xu, C.: Interaction of the cutting tools and the ceramic-reinforced metal matrix composites during micro-machining: a review. CIRP J. Manuf. Sci. Technol. **7**(2), 55–70 (2014)

18. Devor, R.E., Kapoor, S.G.: The mechanics of machining at the microscale: assessment of the current state of the science. J. Manuf. Sci. Eng. **126**, 66678 (2004)
19. Taya, M., Ramulu, M.: EDM machinability of SiCw/AI composites. J. Mater. Sci. **24**, 1103–1108 (1989)
20. Rozenek, M., Kozak, J., Da, L.: Electrical discharge machining characteristics of metal matrix composites. J. Mater. Process. Technol. **109**, 367–370 (2001)
21. Garg, R.K., Singh, K.K., Sachdeva, A., Sharma, V.S., Ojha, K., Singh, S.: Review of research work in sinking EDM and WEDM on metal matrix composite materials. Int. J. Mach. Tools Manuf. **50**(5–8), 611–624 (2010)
22. Hocheng, H., Lei, W.T., Hsu, A.S.: Preliminary study of material removal in electrical-discharge machining of SiC/Al. J. Mater. Process. Technol. **63**, 813–818 (1997)
23. Kumar, S.S., Uthayakumar, M., Kumaran, S.T., Varol, T.: Investigating the surface integrity of aluminium based composites machined by EDM. Def. Technol. **15**, 338–343 (2019)
24. Rajurkar, K.P., Sundaram, M.M., Malshe, A.P.: Review of electrochemical and electrodischarge machining. Procedia CIRP **6**, 13–26 (2013)
25. Pachaury, Y., Tandon, P.: An overview of electric discharge machining of ceramics and ceramic based composites. J. Manuf. Process. **25**, 369–390 (2017)
26. Antil, P., Singh, S., Manna, A., Prakash, C.: Electrochemical discharge drilling of polymer matrix composites. In: Futuristic Composites, Materials Horizons: From Nature to Nano-materials. Springer Nature Singapore Pte Ltd. (2018). https://doi.org/10.1007/978-981-13-2417-8_11
27. Prakash, C., Singh, S., Singh, M., Antil, P., Aliyu, A.A.A., Abdul-Rani, A.M., Sidhu, S.S.: Multi-objective optimization of MWCNT mixed electric discharge machining of Al–30SiCp MMC using particle swarm optimization. In: Futuristic Composites, Materials Horizons: From Nature to Nano-materials. Springer Nature Singapore Pte Ltd. (2018). https://doi.org/10.1007/978-981-13-2417-8_7
28. Pramanik, A., Islam, M.N., Basak, A.K., Dong, Y., Littlefair, G., Prakash, C.: Optimizing dimensional accuracy of titanium alloy features produced by wire electrical discharge machining. Mater. Manuf. Process. **34**(10), 1083–1090 (2019)
29. Prakash, C., Singh, S., Pruncu, C.I., Mishra, V., Królczyk, G., Pimenov, D.Y., Pramanik, A.: Surface modification of Ti-6Al-4V alloy by electrical discharge coating process using partially sintered Ti-Nb electrode. Materials **12**(7), 1006 (2019)
30. Basak, A., Pramanik, A., Prakash, C.: Surface, kerf width and material removal rate of Ti6Al4V titanium alloy generated by wire electrical discharge machining. Heliyon **5**(4), 01473 (2019)
31. Prakash, C., Singh, S., Pabla, B.S.: Multi-objective optimization of EDM parameters to deposit HA-containing coating on Mg-Zn-Mn alloy using particle swarm optimization. Vacuum **158**, 180–190 (2018)
32. Prakash, C., Singh, S., Pabla, B.S., Uddin, M.S.: Synthesis, characterization, corrosion and bioactivity investigation of nano-HA coating deposited on biodegradable Mg-Zn-Mn alloy. Surf. Coat. Technol. **346**, 9–18 (2018)
33. Prakash, C., Uddin, M.S.: Surface modification of β-phase Ti implant by hydroxyapatite mixed electric discharge machining to enhance the corrosion resistance and in-vitro bioactivity. Surf. Coat. Technol. **236**(Part A), 134–145 (2017)
34. Aliyu, A.A., Abdul-Rani, A.M., Ginta, T.L., Prakash, C., Axinte, E., Razak, M.A., Ali, S.: A review of Additive-Mixed Electric Discharge Machining: Current status and future perspectives for surface modification of biomedical implants. Adv. Mater. Sci. Eng. **28** (2017) (accepted)
35. Prakash, C., Kansal, H.K., Pabla, B.S., Puri, S., Aggarwal, A.: Electric discharge machining—a potential choice for surface modification of metallic implants for orthopedic applications: a review. Proc. Inst. Mech. Eng. Part B: J. Eng. Manuf. **230**(2), 231–253 (2016)
36. Prakash, C., Kansal, H.K., Pabla, B.S., Puri, S.: Processing and characterization of novel biomimetic nanoporous bioceramic surface on β-Ti implant by powder mixed electric discharge machining. J. Mater. Eng. Perform. **24**, 3622–3633 (2015)
37. Prakash, C., Kansal, H.K., Pabla, B.S., Puri, S.: Experimental investigations in powder mixed electrical discharge machining of Ti-35Nb-7Ta-5Zr β-Ti alloy. Mater. Manuf. Process. **32**(3), 274–285 (2017)

38. Prakash, C., Kansal, H.K., Pabla, B.S., Puri, S.: Effect of surface nano-porosities fabricated by powder mixed electric discharge machining on bone-implant interface: an experimental and finite element study. Nanosci. Nanotechnol. Lett. **8**(10), 815–826 (2016)
39. Prakash, C., Kansal, H.K., Pabla, B.S., Puri, S.: Multi-objective optimization of powder mixed electric discharge machining parameters for fabrication of biocompatible layer on β-Ti alloy using NSGA-II coupled with Taguchi based response surface methodology. J. Mech. Sci. Technol. **30**(9), 4195–4204 (2016)
40. Prakash, C., Kansal, H.K., Pabla, B.S., Puri, S.: Powder mixed electric discharge machining an innovative surface modification technique to enhance fatigue performance and bioactivity of β-Ti implant for orthopaedics application. J. Comput. Inf. Sci. Eng. **14**(4), 1–9 (2016)
41. Prakash, C., Kansal, H.K., Pabla, B.S., Puri, S.: Potential of powder mixed electric discharge machining to enhance the wear and tribological performance of β-Ti implant for orthopedic applications. J. Nanoeng. Nanomanuf. **5**(4), 261–269 (2015)

Characterization of Plasma Sprayed $87\%Al_2O_3$–$13\%TiO_2$ and $88\%WC$–$12\%Co$ Coatings on ASTM A36 Steel

Varun Panwar, Vikas Chawla, and Neel Kanth Grover

1 Introduction

In today's industrial era thermal spray coating has turn into a significant model as it offers diverse surface properties for variety of industrial applications as per customer requirement. The surface coatings act as a protective layer for many mechanical components and boiler parts like Induced draft fans, forced draft fans, and boiler tubes from erosion and corrosion [1, 2]. However, due to high demand in industry for enhancing the surface properties and working life of mechanical components from erosive wear and corrosion, the protection by thermal spray coating is the best approach. This theory has been used since ancient times in which some defensive layer is applied on substrate which act as a protective barrier to preserve the surface of material from environmental effect [3]. Out of all the thermal spray coating techniques (HVOF, D-gun, Plasma spraying) the most adaptable technology is the plasma spraying which is being utilized by most of the industries for solving the problem of wear and corrosion. Plasma spray coating is the greatest adaptable thermally spraying process with respect to material to be sprayed [4]. High temperature permits the material to have good bond with the base material for the applications of engineering component which are exposed to high temperature abrasive wear and corrosion. The same process is also utilized in areas of electrical and medical science [5]. WC–Co is so-called hard metal which is characterized by an extraordinary hardness and wear resistance properties. Carbide diffusion coatings are typically for the protections of alloys against the abrasive wear [6, 7]. Al_2O_3–TiO_2 coating powder utilized for protection of mechanical components from abrasive wear, and corrosion at elevated

V. Panwar (✉)
Department of Mechanical Engineering, Lovely Professional University, Phagwara 144411, Punjab, India
e-mail: varun.17806@lpu.co.in

V. Chawla · N. K. Grover
IKG PTU, Kapurthala, Punjab, India

temperature. Due to low coefficient of friction it is being utilized for shafts of pumps to prevent from wear and corrosion. During the plasma spraying process the material like ceramics undergoes some changes due to fast cooling, modification in crystallographic structure [8]. However, metastable phase is created and leads to decrease in toughness of coating. Although some studies are performed on metallographic preparation and assessment of thermal spray materials only a few research have been done for examination of physical structure and chemistry of sprayed coating [9].

For low and elevated temperature applications, surface coating is extensively utilized. Elevated temperature applications are common to power plant boiler components and aerospace industry. To apply coatings and to have good bond strength on these high-temperature applications it's a big challenge for industry. The major function of these coatings is to offer superior defense of oxides scale layer performed using thermal spray coating process which are efficient enough to protect the substrate from abrasive wear and corrosive environment [10, 11]. Maintenance and replacement cost of eroded ID fans and turbines blades account for 54% of the total running cost of coal-based thermal power plants. So, to tackle this serious problem there is one way to apply the thin defensive layer of antiwear, anti-oxidation and with high-quality thermal conductivity characteristics. These thin films are of majorly iron based, nickel-chromium alloy based [12].

Higuera et al. study was based on plasma sprayed mechanical components and their oxidation behavior which breakdown while performing their application in power generation plants (coal-fired power plants) in order to decrease the cost of maintenance. Different coatings are utilized for protection of ID fans, boiler tubes, and turbine blade, etc., components from wear and corrosion. Extensively used coating technique is the plasma spraying because in this process a protective thin layer can be formed of any material and on any material, i.e., substrate [13–15]. From all the other thermal spraying techniques plasma is one of the best technique for modification of surface properties to protect from wear and corrosion, etc. In this current study characterization of plasma-sprayed tungsten carbide-cobalt and aluminium oxide- titanium oxide material coating with coating thickness of approximately 250–300 μm is deposited on surface of substrate, i.e., ASTM-A36 steel. The microstructure, phases formed, microhardness and porosity have been examined using metallurgical microscope, XRD, micro Vickers testing and SEM/EDAX techniques have been used on coated and uncoated samples.

2 Experimental Details

2.1 Development of Coatings

Substrate material. A low carbon steel material is used as a substrate (ASTM-A36 steel), which exhibits formability and superior strength. Selection of material is done by consulting the leading manufacturing company of Boilers. The actual and nominal

chemical composition of material used for ID fan is given in Table 1. The chemical (wt%) composition is examined with the help of spectrometer which is located at Central Institute of Hand Tool, Jalandhar (Punjab).

Preparation of test specimens. These samples were cut to form approximately 20 mm X 15 mm X 5 mm size specimens. These all specimens were polished on grit paper ranging from P220 (Macrogrit particle size 68 µm), P400 (35.0 µm), P600 (25.8 µm), P800 (21.8 µm), P1000 (super fine average particle size 18.3 µm) to P2000 (super fine average particle size 9.3 µm) grade for high surface finish. Before performing plasma spraying the samples are grit blasted for better bond strength between base material and coating power. Samples for characterization are shown in Fig. 1.

Feedstock material for coating. 88%WC–12%Co powder was used with the particle size 15–45 µm, product code 519.074 which was supplied by H. C. Starck, Germany. Al$_2$O$_3$–13%TiO$_2$. Al$_2$O$_3$–13%TiO$_2$ powder was used with the particle size 5–22 µm, product code 704.000 which was supplied by H. C. Starck, Germany. Morphology of coating powders was detected with SEM/EDAX as shown in Fig. 2.

Plasma spray coating powder. After a deep study of literature survey author has selected the two different types of cermet coating powders, specifically 87%Al$_2$O$_3$–13%TiO$_2$ and 88%WC–12%Co by plasma spraying technique on ASTM-A36 steel. SEM/EDAX and XRD patterns show the different element compositions, microstructure and morphologies of 88%WC–12%Co and 87%Al$_2$O$_3$–13%TiO$_2$, respectively.

Formulation of coating. Before plasma spray coating all the samples are grit blasted for better bond strength between base material and coating. A 80kw 9MBM plasma gun machine was utilized to deposit the surface coating thickness of 250–300 µm. The deposited coating on base material was dense and hard with average adhesion strength of 29.78 Mpa on 87%Al$_2$O$_3$–13%TiO$_2$ and 23.34 Mpa on 88%WC–12%Co coating. ASTM C633 standard at NABL accredited laboratory of Metallizing equipment Co. Pvt. Ltd. Jodhpur was utilized for examination of bond strength. The coating powder particle size of 87%Al$_2$O$_3$–13%TiO$_2$ and 88%WC–12%Co is 10–50 µm. Plasma spraying parameters are in Table 2.

3 Results

Measurement of coating thickness. The scanning electron microscope studies have been performed along the cross section of the coatings. Back scattered electron images of plasma sprayed 88%WC–12%Co and 87%Al$_2$O$_3$–13%TiO$_2$ coated samples are shown in Figs. 3a and 4a. Figures 3b and 4b shows the plasma sprayed coating thickness with differentiating layer of epoxy, coating, and substrate. Thickness of the coatings was measured with Back Scattered Electron Image micrograph. Bond strength of coatings is shown in Table 3. Adhesion test was performed on universal testing machine made of INSTRON according to ASTM C633 standards. It

Table 1 Shows the chemical composition of Substrate (IS2062) [16]

	% C	% Si	% Mn	% P	% S	%Al	% Cu	% Cr	% Mo	% Ni	% Pb	% Ti	% V	% W	% Fe
Nominal	0.16	0.17	0.46	0.026	0.019	0.007	0.048	0.084	0.018	0.039	0.039	0.007	0.003	<0.001	98.89
Actual	0.19	0.18	0.92	0.019	0.022	0.01	0.01	0.01	0.002	0.01	–	–	0.001	–	98.626
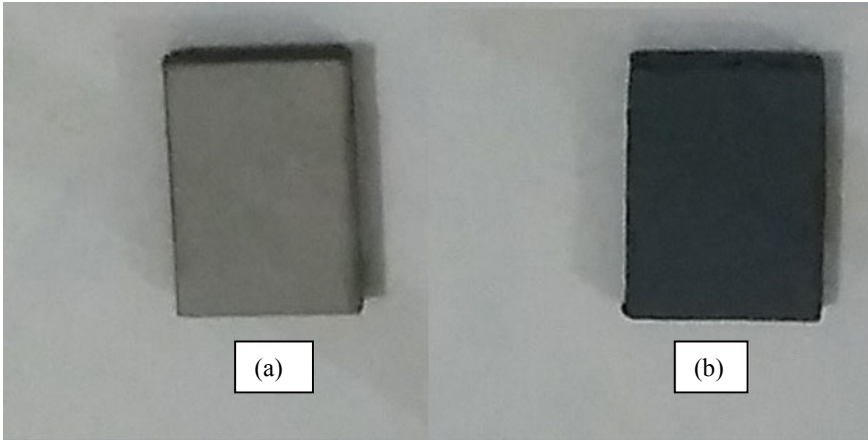
Fig. 1 Plasma sprayed coated samples, **a** 88%WC–12%Co, **b** 87%Al$_2$O$_3$–13%TiO$_2$

was observed that both the type of coating shows good bond strength and the coating failure was examined during the test.

Porosity analysis. Porosity measurement of plasma sprayed coated ASTM A36 according to standards ASTM- B276 with image analyser software of Dwinter material plus 1.01. The porosity for the sprayed coating of 88%WC–12%Co was found to be in a range of 0.23%. On the other hand porosity for 87%Al$_2$O$_3$–13%TiO$_2$ was found to be in a range of 0.82%. which was observed less than 1% in both the coatings.

Evaluation of microhardness of coatings. Investigation of microhardness profile by using Microvicker hardness Tester, Make Akashi, Model: MVK-H2, Japan and hardness values are measured along the cross section of the coated samples. Test method used IS6416-1988(RA 2012). Values of hardness and distance from the interface of substrate and coating are given in Figs. 5 and 6. Microhardness values were recorded using Vicker hardness tester across the cross section of sample, three readings were examined with the distance of 50 microns from interface of coating and substrate on both the sides, base material, and coating layers. Hardness of base material, 88%WC–12%Co, and 87%Al$_2$O$_3$–13%TiO$_2$ coating were in the range of 190–218 Hv, 997–1076 Hv, and 682–703 Hv, respectively.

Surface structure of coated specimens. Figure 7 shows the optical morphology of 88%WC–12%Co on ASTM A36 steel substrate. Optical micrograph of the sprayed coating and occurrence of small globules of irregular shaped crystals can be seen. Figure 8 shows the optical micrograph of 87%Al$_2$O$_3$–13%TiO$_2$ coating on ASTM A36 steel. A deposited layer is of massive structure and unmelted particles can be observed.

XRD analysis. X-ray diffraction of 88%WC–12%Co coated samples have the formation of WC, Co, and W$_2$C on the surface have been indicated in Fig. 9. XRD
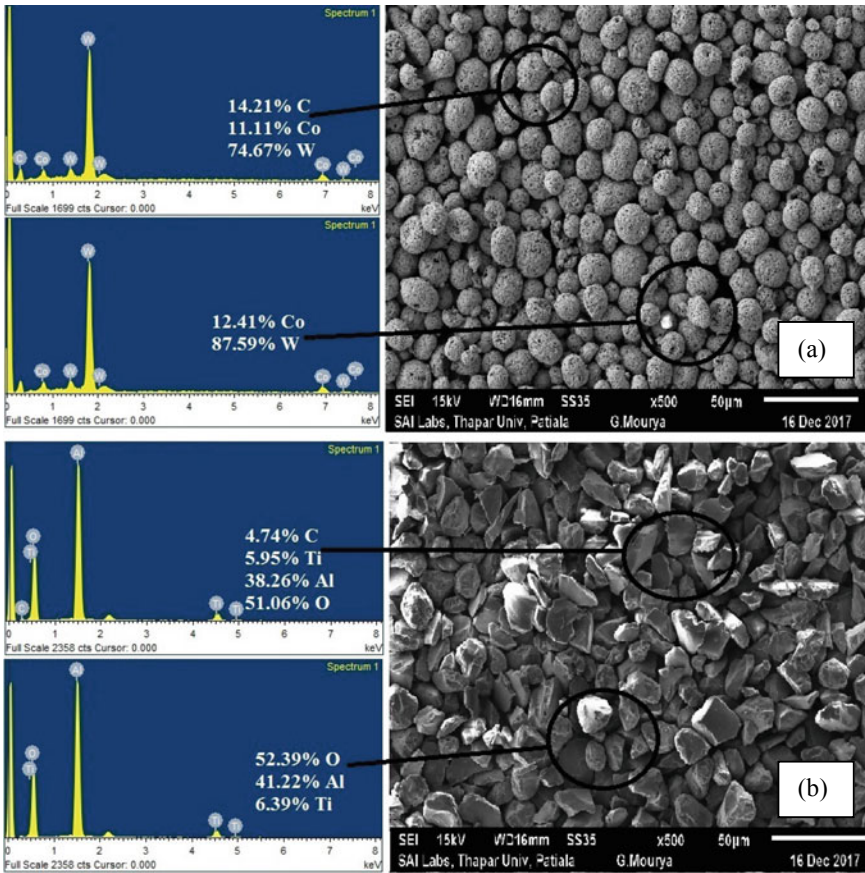
Fig. 2 SEM/EDAX patterns; **a** 88%WC–12%Co coating powder, and **b** Al_2O_3–13%TiO_2 coating powder

Table 2 Shows parameters of plasma spraying process

Parameters	Values
Power	32.1 KW
Current	506 Amps
Voltage (DC)	63.7 V
Spraying distance	70 mm
Hydrogen: secondary gas	7.7 L/min
Nitrogen: primary gas	40 L/min
Injector position	90°
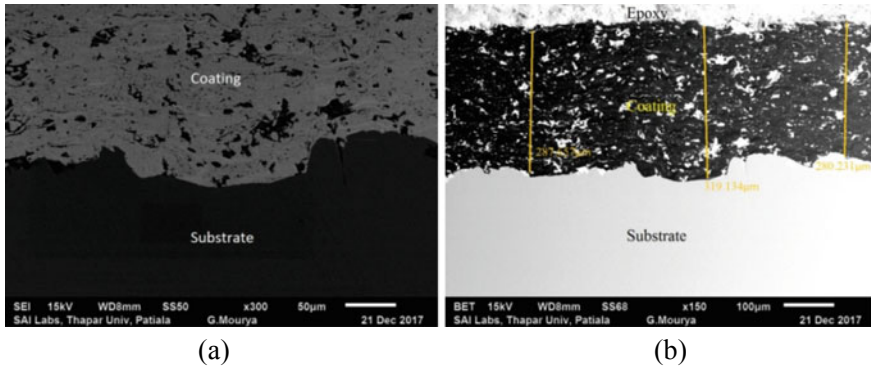
Fig. 3 Cross-section morphology of 88%WC–12%Co coating on base material **a** as coated and **b** coating thickness
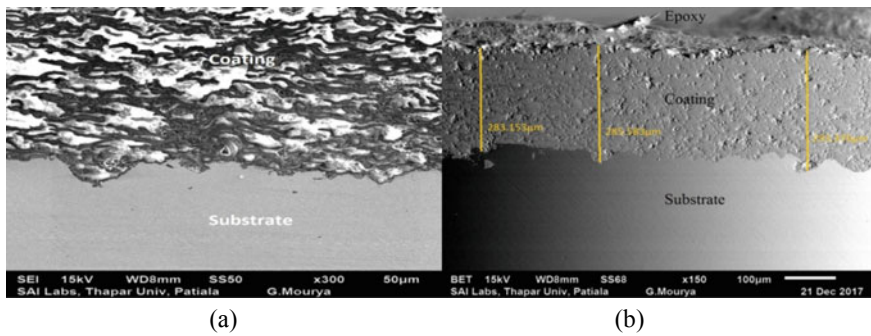
Fig. 4 Cross-section morphology of 87%Al$_2$O$_3$–13%TiO$_2$ coating on base material **a** as coated and **b** coating thickness

Table 3 Average coating thickness

Type of coating	Average coating thickness (μm)	Average adhesion strength (MPa)
88%WC–12%Co	295.674	23.34
87%Al$_2$O$_3$–13%TiO$_2$	287.370	29.78

analysis of 87%Al$_2$O$_3$–13%TiO$_2$ the formation of Al$_2$O$_3$, TiO$_2$ and O$_2$Ti can be seen on the surface and major phase of Al$_2$O$_3$ is represented in Fig. 10.

SEM/EDAX analysis. Figure 11 shows the phases of 88%WC–12%Co coating and it can be clearly inferred that the formation of matrix contains mainly WC, Co, and some amount of Fe. In this matrix the white-colored phase is mainly WC with 1.57% Fe which is randomly distributed. There are certain dark (black) areas which are W$_2$C and there is an indication of small globules particles. Figure 12 shows the
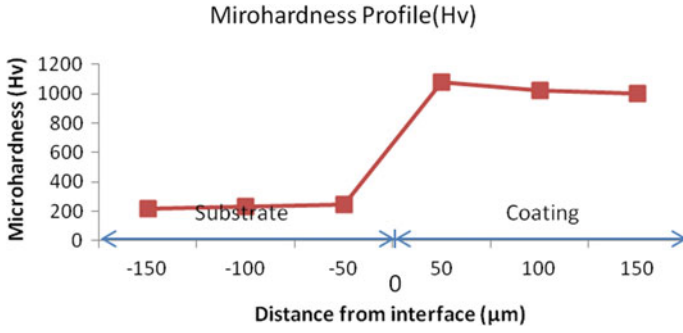
Fig. 5 Microhardness profile for 88%WC–12%Co coating
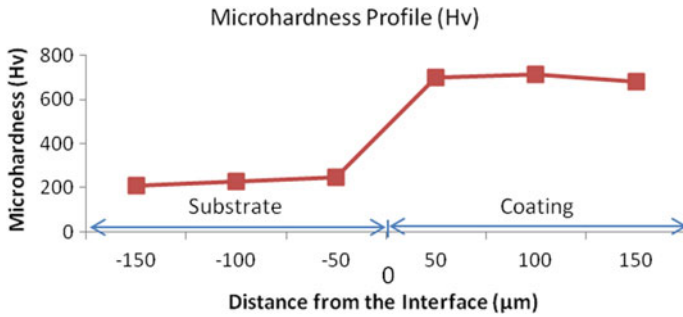
Fig. 6 Microhardness profile for 87%Al$_2$O$_3$–13%TiO$_2$ coating
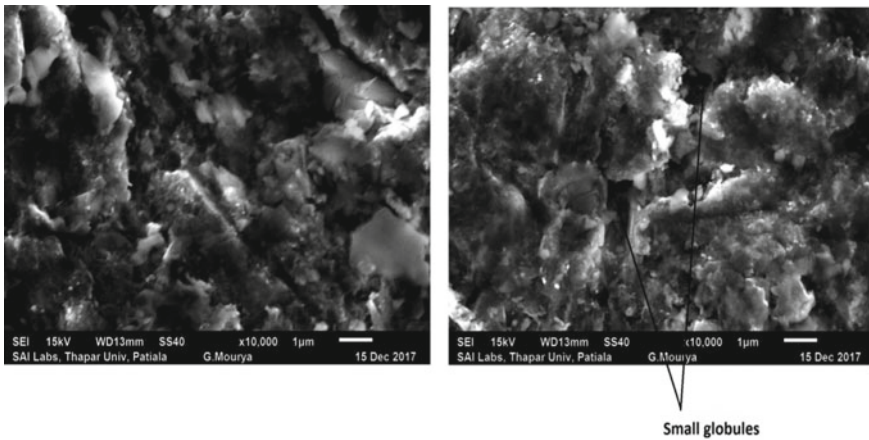
Fig. 7 Optical micrographs of 88%WC–12%Co coating plasma sprayed and small globules located
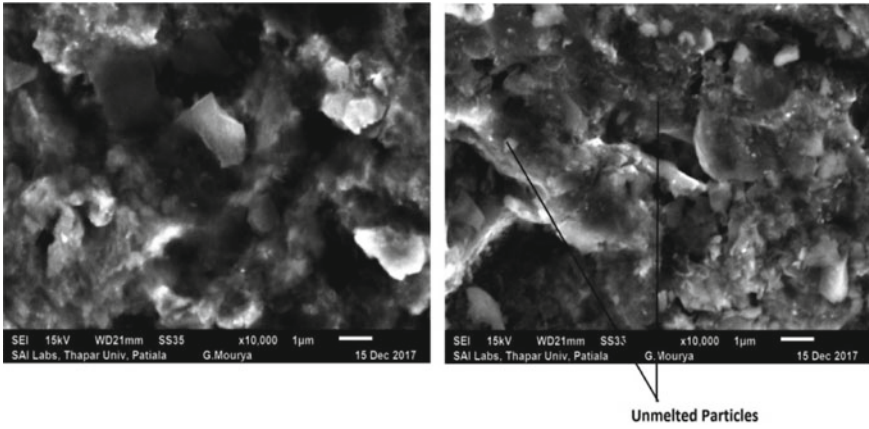
Fig. 8 Optical micrographs of 87%Al$_2$O$_3$–13%TiO$_2$ coating plasma sprayed and unmelted particles located
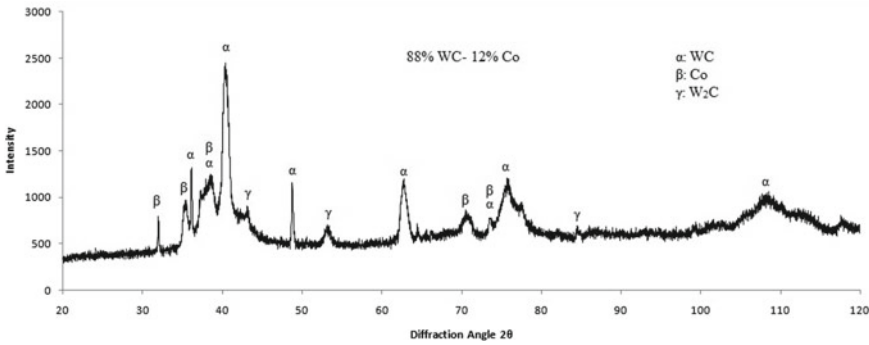
Fig. 9 X-ray diffraction profiles of 88%WC–12%Co coating
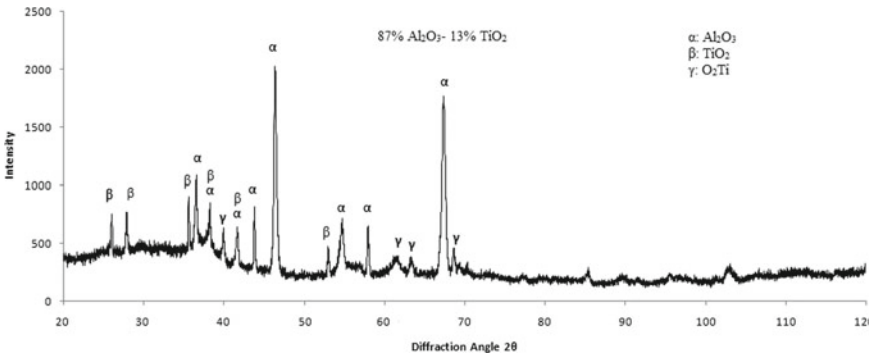
Fig. 10 X-ray diffraction of 87%Al$_2$O$_3$–13%TiO$_2$ coating
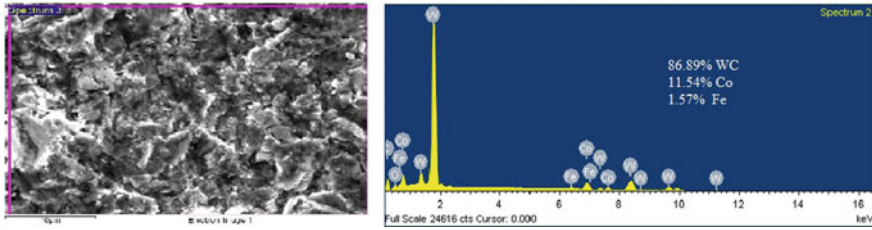
Fig. 11 SEM/EDAX analysis of 88%WC–12%Co coating showing elemental composition (wt%)
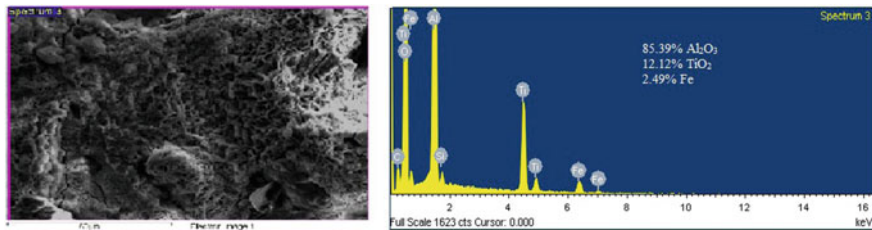
Fig. 12 SEM/EDAX analysis of 87%Al$_2$O$_3$–13%TiO$_2$ coating showing elemental composition (wt%)

matrix of Al$_2$O$_3$–TiO$_2$ and some elements of 2.49% Fe. On the other hand matrix of Aluminium oxide and titanium oxide is formed in a well manner.

4 Discussions

Coating thickness of approximately 250–300um of thermal sprayed coating performs the good bonding and solve the purpose by preventing the coated components from abrasive wear and corrosion. Many times while operation of plasma spray coating 9MBM torch gets chocked due to aluminium throughout the application of Al$_2$O$_3$–TiO$_2$ coating and phases of aluminium and titanium are revealed through XRD analysis (see Fig. 10). Phases of WC and Co can be observed from XRD analysis (see Fig. 9). Decline in the deepness of coating thickness is due to the metal evaporation from the surface at the time of melting process during coating. Yilmaz et al. [9], Vargas et al. [17], Hidalgo et al. [13–15] finding of porosity values are almost in the conformity of measured values. Values of microhardness are almost in the conformity of the results finding by Murthy et al. [18], Vuoristo et al. [19], and Westergard et al. [20] for 87%Al$_2$O$_3$–13%TiO$_2$ coating. Values of microhardness for 88%WC–12%Co coating are higher than values reported by Wang et al. [21]. Phases of tungsten carbide and cobalt are formed and XRD/EDAX analysis illustrates the diffusion of Fe and coating powder from the substrate which resembles the same as investigated by Wang et al. [21]. Phases of aluminium oxide and titanium oxides

are observed as investigated by song et al. [22]. Some of the Fe particles from the base material might have combined with the elements of the upper coating during the melting process to form the above stated intermetallics. This was clearly seen by XRD/EDAX analysis, and it can be further supported by the outcomes of EDS analysis as investigated by Goberman et al. [23]

5 Conclusions

The following conclusions are drawn from the above study:

1. Coating thickness for 88%WC–12%Co coating was 295.674 μm and 87%Al$_2$O$_3$–13%TiO$_2$ coating was 287.370 μm.
2. Bond strength of 88%WC–12%Co coating was observed 23.34 MPa and 87%Al$_2$O$_3$–13%TiO$_2$ coating was observed 29.78 MPa.
3. Porosity of coatings was 0.23 for 88%WC–12%Co coating and 0.82% in 87%Al$_2$O$_3$–13%TiO$_2$ coating, which was less than 1% in both the coatings.
4. Microhardness of 88%WC–12%Co coating was 997–1076Hv and for 87%Al$_2$O$_3$–13%TiO$_2$ coating was 682–703Hv.
5. Examination of microstructure shows small globules in 88%WC–12%Co coating and unmelted particles in 87%Al$_2$O$_3$–13%TiO$_2$ coating.
6. XRD analysis shows the main phases in coatings, like WC, Co, and W2C in 88%WC–12%Co coating and phases like Al$_2$O$_3$, TiO$_2$, and O$_2$Ti in 87%Al$_2$O$_3$–13%TiO$_2$ coating.

References

1. Bhushan, B., Gupta, B.K.: Handbook of Tribology: Materials, Coatings, and Surface Treatments (1991)
2. Archard, J.F.: In: Peterson, M.B., Winer, W.O. (eds.) Wear Control Handbook: Wear Theory and Mechanisms. ASME, New York, NY, USA (1980)
3. Budinski, K.G.: Surface Engineering for Wear Resistance (Retroactive Coverage). Prentice-Hall, Inc, Englewood Cliffs, New Jersey 07632, United States, 1988. 420 (1988)
4. Sidhu, B.S., Puri, D., Prakash, S.: Characterisations of plasma sprayed and laser remelted NiCrAlY bond coats and Ni$_3$Al coatings on boiler tube steels. Mater. Sci. Eng. A **368**(1–2), 149–158 (2004)
5. Pawlowski, L.: The Science and Engineering of Thermal Spray Coatings. Wiley (2008)
6. Rhys-Jones, T.N.: Thermally sprayed coating systems for surface protection and clearance control applications in aero engines. Surf. Coat. Technol. **43**, 402–415 (1990)
7. Xiong, Y., Smugeresky, J.E., Schoenung, J.M.: The influence of working distance on laser deposited WC–Co. J. Mater. Process. Technol. **209**(10), 4935–4941 (2009)
8. Singh, H., et al.: Sliding wear performance of high-velocity oxy-fuel spray Al$_2$O$_3$/TiO$_2$ and Cr$_2$O$_3$ coatings. Proc. Inst. Mech. Eng. Part J: J. Eng. Tribol. **222**(4), 601–610 (2008)
9. Yılmaz, R., et al.: Effects of TiO$_2$ on the mechanical properties of the Al$_2$O$_3$–TiO$_2$ plasma sprayed coating. J. Eur. Ceram. Soc. **27**(2–3), 1319–1323 (2007)

10. Hasan, S., Stokes, J.: Design of experiment analysis of the Sulzer Metco DJ high velocity oxy-fuel coating of hydroxyapatite for orthopedic applications. J. Therm. Spray Technol. **20**(1–2), 186–194 (2011)
11. Halling, J.: Introduction: Recent Development in Surface Coating and Modification Processes, pp. 1–2. MEP, London (1985)
12. Bunshah, R.F. (ed.): Handbook of Deposition Technologies for Films and Coatings: Science, Technology, and Applications. William Andrew (1994)
13. Hidalgo, V.H., Belzunce Varela, F.J., Fernández Rico, E.: Erosion wear and mechanical proper-ties of plasma-sprayed nickel-and iron-based coatings subjected to service conditions in boilers. Tribol. Int. **30**(9), 641–649 (1997)
14. Hidalgo, V.H., Varela, F.J.B., Menendez, A.C.: In: Proceedings of the 15th International Thermal Spray Conference, NICE, France, vol. 1, pp. 617–621 (1998)
15. Hidalgo, V.H., Varela, F.J.B., Martinez, S.P., Gijon/E: In: Lugscheider, E., Kammer, P.A. (eds.) Proceedings of the United Thermal Spray Conference. DVS-Verl., pp. 683–686 (1999)
16. Shibe, V., Chawla, V.: Combating wear of ASTM A36 steel by surface modification using thermally sprayed cermet coatings. In: Advances in Materials Science and Engineering 2016 (2016)
17. Vargas, F., et al.: Mechanical and tribological performance of Al_2O_3–TiO_2 coatings elaborated by flame and plasma spraying. Surf. Coat. Technol. **205**(4), 1132–1136 (2010)
18. Murthy, J.K.N., Rao, D.S., Venkataraman, B.: Effect of grinding on the erosion behaviour of a WC–Co–Cr coating deposited by HVOF and detonation gun spray processes. Wear **249**(7), 592–600 (2001)
19. Vuoristo, P., Niemi, K., Makela, A., Mantyla, T.: In: Proceedings of the 7th National Thermal Spray Conference, Boston, Massachusetts, pp. 121–126 (1994)
20. Westergård, R., et al.: The erosion and abrasion characteristics of alumina coatings plasma sprayed under different spraying conditions. Tribol. Int. **31**(5), 271–279 (1998)
21. Wang, D.S., Tian, Z.J., Shen, L.D., et al.: Preparation and characterization of nanostructured Al_2O_3-13wt.% TiO_2 ceramic coatings by plasma spraying. J. Rare Met. **28**(5), 465–470 (2009)
22. Song, E.P., et al.: Effects of critical plasma spray parameter and spray distance on wear resis-tance of Al_2O_3–8 wt.% TiO_2 coatings plasma-sprayed with nanopowders. Surf. Coat. Technol. **202**(15), 3625–3632 (2008)
23. Goberman, D., et al.: Microstructure development of Al_2O_3–13wt.% TiO_2 plasma sprayed coatings derived from nanocrystalline powders. Acta Mater. **50**(5), 1141–1152 (2002)

Influence of 3D Printing Technology on Biomedical Applications: A Study on Surgical Planning, Procedures, and Training

Vishal Francis, Piyush Ukey, Ankit Nayak, Mohammad Taufik, Prashant K. Jain, Sushil H. Mankar, and Sushant S. Srivastava

1 Introduction

The advancement in the field of 3D printing technology has greatly influenced the medical sector. It is now possible to manipulate the medical images to 3D print any complex anatomical features within a few hours [1]. This has aided the pre-operative surgical planning process by providing accurate 3D models of the region of interest [2]. Due to this, surgeons can now have a real model of the affected part and plan the surgeries accordingly. This can provide additional haptic information compared to the computer-aided design (CAD) model which gives only the virtual information [3]. These models can even be used to educate the patients about their situations which helps in better communication between the surgeon and the patient.

The 3D printed models of complex anatomical parts can be utilized to train the new surgeons in terms of dissection practices and mock surgeries. Moreover, the gap in medical training due to the limited availability of the cadaver bones can be fulfilled by 3D printed models of artificial bones [4]. It is possible to print multi-color

V. Francis
School of Mechanical Engineering, Lovely Professional University, Phagwara, India

P. Ukey
Nu Ossa Mediquip Pvt. Ltd, Nagpur, India

A. Nayak · P. K. Jain
CAD/CAM Lab, Mechanical Engineering Discipline, PDPM Indian Institute of Information Technology, Design and Manufacturing, Jabalpur, Jabalpur, India

M. Taufik (✉)
Mechanical Engineering Department, Maulana Azad National Institute of Technology, Bhopal, India
e-mail: mohammad.taufik@manit.ac.in

S. H. Mankar · S. S. Srivastava
Department of Orthopedics, NKP Salve Institute of Medical Sciences and Research Centre, Nagpur, India

parts which can distinguish one anatomical feature from another feature. Due to the extensive research in the area of materials for 3D printing, nowadays it is possible to print with novel materials which have properties very similar to the properties of the bone [5, 6]. Thus making it a viable alternative of cadaver bones. Moreover, the technology also finds tremendous applications in the field of dentistry. 3D printing is used by the dentists for root canal treatment of the calcified tooth [7, 8], in the fabrication of transparent braces, drill guides, and dental implants. It also provides assistance in oral and maxillofacial surgeries [9].

The entire process flow of converting the medical images into an effective physical model for treatment and training purposes requires a combined effort of medical practitioners and engineers. In this scenario, the adaptation of technology in developing countries like India requires initial endeavors to justify the usage of this technology. In this regard, an attempt has been made to demonstrate the utilization of 3D printing technology for biomedical applications.

In this article, the procedure of data preparation from medical images for 3D printing is discussed. Also, a decision-making methodology is presented for obtaining the better surface finish of crucial regions of the biomedical models. Moreover, case studies of pre-operative surgical planning of tibial plateau fracture, fabrication of temporal bone for training/educational purpose, and fabrication of drill guide using 3D printing are discussed.

2   Processing Medical Image Data for 3D Printing

With the advancement in medical image processing tools, it is possible to get the anatomical details of the patient's intended organ or parts. These details play a major role in diagnosis and treatment procedures. Most popular techniques for medical imaging are computed tomography (CT), magnetic resonance imaging (MRI), and x-ray, which are used to gather the anatomical details of the patient. Cone-beam computed tomography (CBCT) can also be used to capture the patient's details. After acquiring the data, these images are processed to prepare the geometric model of the region of interest for visualization or fabrication purposes. Biomedical imaging softwares such as materialise interactive medical image control system (MIMICS) and Slicer are widely used software to prepare the model directly from DICOM files. Figure 1 shows the procedure for converting the medical images to the geometric model which can be used for visualization purposes or 3D printing the model.

The process starts with the acquisition of patient's data using any medical imaging technique. Then the data in the form of DICOM files are processed in MIMICS software. The region of interest is first segmented from the remaining acquired data. The segmentation can be achieved either by using auto segmentation or manual segmentation or by combining both. Further, the segmented region is converted into a 3D model. The model can be converted into an STL format which further can be used for 3D printing the model. Figure 2 illustrates a voxel image of the segmented part and the source of images is M. Tech dissertation work [10].
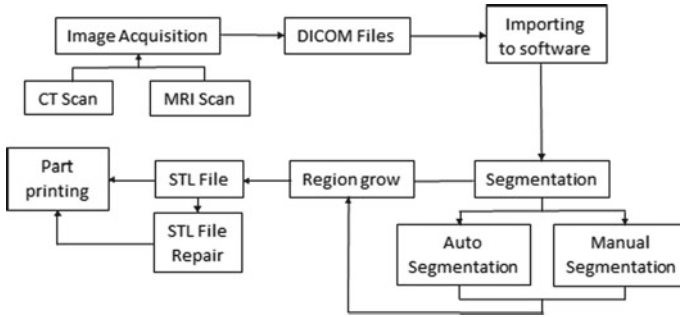
Fig. 1 Procedure of data conversion from medical image to STL file for 3D printing
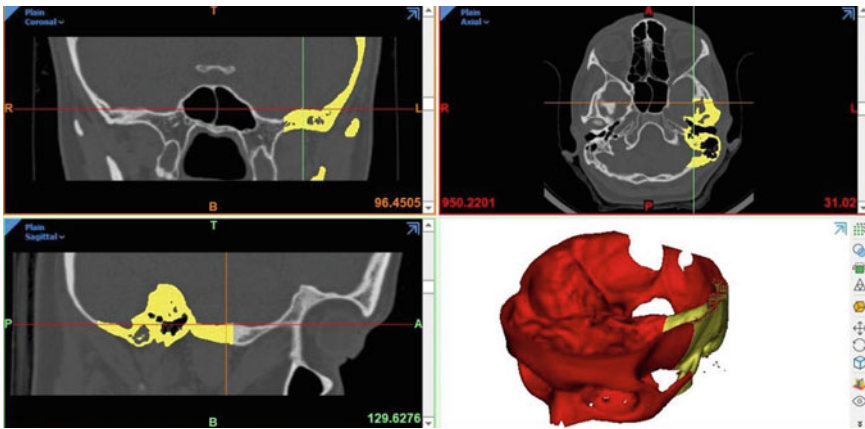
Fig. 2 Image matrix to 3D model conversion [10]

3 Simulation of Biomedical Models for Surface Characterization

Once the 3D model is prepared from medical images, it is utilized for preparing the data for 3D printing purpose. However, due to the layer by layer manufacturing nature of the technology the surface finish of the fabricated model is not as smooth as the virtual model. This poses a limitation on the technology in terms of achieved surface finish of the model or implant. Surface finish is one of the crucial parameters in any biomedical models, medical devices, implants, and surgical instruments. The surface roughness of 3D printed parts majorly depends upon the layer thickness and build orientation selected for the printing. By reducing the layer thickness, lower surface roughness can be achieved. However, for further manipulating the surface roughness of specific and critical surfaces, build orientation can be used. Therefore, in the case of complex geometrical shapes, build orientation would play an important role in

deciding the surface finish [11]. However, surface roughness can only be measured after the part is printed. For complex parts as in the case of anatomical and biomedical models, it would tremendously increase the time span and cost, if the model has to be re-printed due to the surface finish issue. On the other hand, if the surface of the model can be characterized and predicted based on the build orientation directly from the CAD model then the said issues can be reduced. For critical surgical cases, time is a very crucial factor, therefore, methodologies which can reduce the fabrication time are important. Taufik et al. [12] have suggested surface roughness-based visualization modelers for simulating the effect of layering fabrication on the surface of a CAD image. The methodology proposed by them predicts the surface roughness of the CAD model based on the orientation of the part. Utilizing this approach would help in deciding the orientation of the model based on the desired surface roughness that can be achieved. For the simulation of the surface characteristics of the biomedical model, first the angle between the vertical axis (Z), i.e., build direction and normal (Ŝ) to the surface axis is analyzed for each facet (Fig. 3). The methodology for calculation of the surface roughness based on the orientation can be seen elsewhere [11, 12].

Figure 4a and b shows a 3D printed biomedical model and surface characterized STL model based on the orientation of each facet, respectively. These color STL
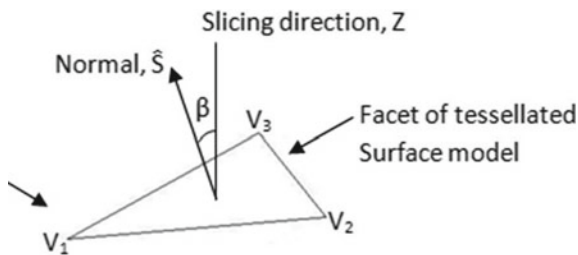
Fig. 3 Angle between build direction and facet normal of facet
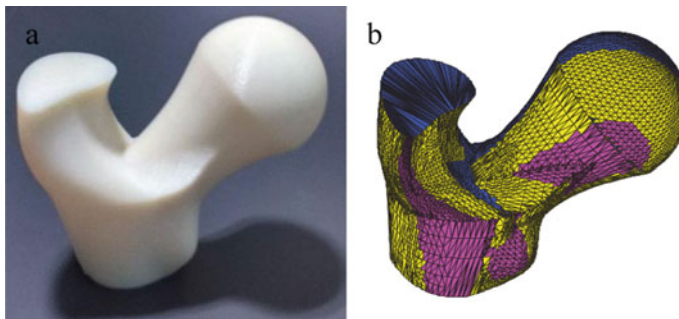
Fig. 4 Surface characterization simulation for 3D printed part. **a** 3D printed part. **b** Surface profile characterization on STL file of femur bone [12]

models can be utilized for decision making in the data preparation stage to orient the part based on the desired surface characteristics of the critical surfaces. Each color represents a certain orientation of those facets. The surface roughness can be calculated based on the orientation of the facets to analyze the surface roughness of the critical regions of the model [11, 12].

The color STL model can further be used to plan the post-processing approaches that could be adopted for improving the surface of the fabricated model [13]. Desired surface properties can be achieved by post-processing the fabricated 3D printed part by utilizing the above-mentioned approach.

4 Pre-operative Surgical Planning

Tibial Fracture: Precise evaluation of the medical images are crucial for planning the surgery. Pre-operative surgical planning is an essential step to ensure proper surgical treatment. Studies reveal that the utilization of a physical 3D model of the affected area aids in the improvement of surgical planning and treatment. Figure 5 shows a case of a 34 years old male patient who had an issue of left medial condyle fracture of the tibia. The patient had swelling and deformity in his left knee. The CT scan images of the patient were utilized to develop a virtual model using MIMICS software. Further, the STL file of the model was used to process the data for 3D printing the scaled-down tibia model of the affected knee was printed using a desktop
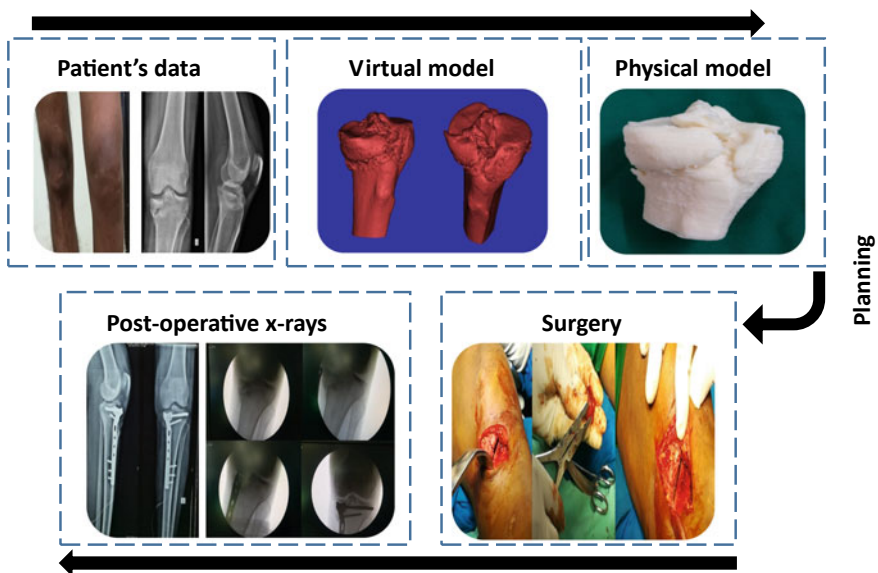
Fig. 5 A case of the 34 years old male patient

3D printer. The model was used for pre-operative surgical planning and the surgery was conducted at NKP Salve Institute of Medical Sciences and Research Centre, Nagpur. The procedure influenced the operative time and also the intra-operative blood loss.

5 Training and Education

For the dissection, mock surgery and study of complex irregular bones like vertebrae and facial, generally cadaver bones are used in medical institutions. This practice enhances the skill of students and surgeons. However, the availability of cadaver bones is an issue which restricts its usage for training purposes. In this regard, fabrication of artificial bones using 3D printing is a viable solution for the above-mentioned issue. Temporal bone has one of the most complicated structures in human anatomy. Fabrication of this bone with complete internal anatomical details is a challenging task. For mock surgery and training purpose, a temporal bone was printed at Nu Ossa Mediquip Pvt. Ltd, Nagpur, using a desktop printer as shown in Fig. 6. The external anatomical details were present as identified on the printed bone (Fig. 6). In order to clearly represent the nerves and arteries in the temporal bone, certain post-processing
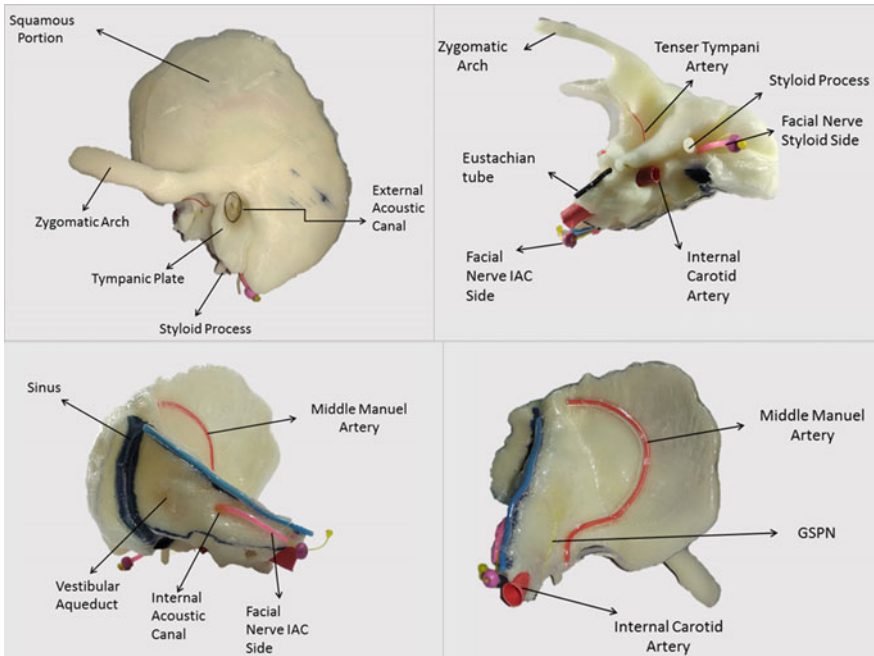
Fig. 6 3D printed temporal bone
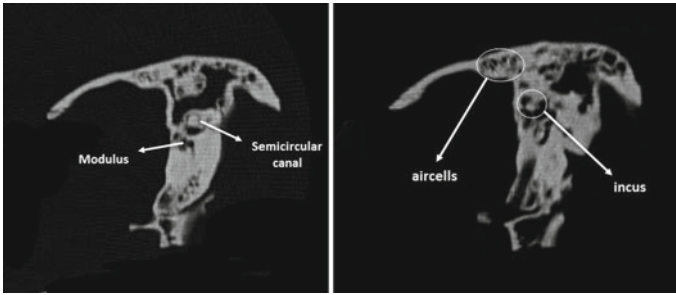
Fig. 7 CT scan of the artificial printed bone

was done. This will allows the students to better visualize, relate, and understand the surgical procedures.

CT scan of the printed bone was also taken to validate 3D printing of its internal anatomical details. Figure 7 shows a slice of the CT scan. Internal features like air cells, incus, semicircular canal, and modulus can be easily identified within the printed bone. The accurate printed model will allow to mimic a cadaver bone during mock surgeries and dissection for training and education purposes.

6 Dentistry

Dentistry is one of the medical sectors which has embraced technologies like CAD/CAM and 3D printing. Due to improper oral hygiene and feeding habits, teeth may get weak or infected. These teeth cause oral health issues like infection and mobility. In case of infection, the tooth is removed or disinfected by the root canal treatment. Root canal treatment starts with the clinical examination of the tooth using radiograph or CBCT scan [14]. Radiograph helps create the root canal access cavity. This cavity provides a path from the tooth crown to the pulp chamber of the tooth. After root canal access cavity (RCAC) preparation [15] the tooth deification is performed using endodontic files. Endodontic files remove the infected part of the tooth and then it is filled with the gutta-percha and endodontic sealers [16]. The entire procedure becomes complicated when the tooth has a calcified root canal. In that case, the endodontic guide has to be used to create the root canal access cavity. The endodontic guide is designed to create the liner root canal access cavity [8]. This cavity provides the shortest path to the endodontic files to reach up to the pulp chamber as shown in Fig. 8.

The CAD model of the endodontic guide is converted into the STL file and send for the 3D printing. The technology provides the livery to design the customized endodontic guide for each patient. For this purpose, the CBCT of the patient is examined in the computer program and the optimal path for the burr is obtained. Based on the coordinates of the optimum path the endodontic guides are designed.
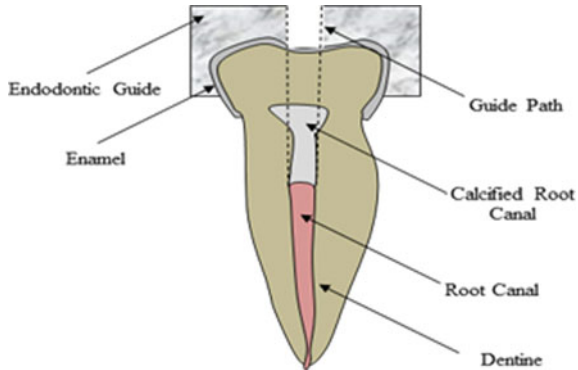
Fig. 8 Anatomy of the human tooth

Fig. 9 3D printed drill guide

Moreover, drill guides can be prepared for implant dentistry using scan data and 3D printing. This helps to accurately locate the point of drilling and helps in precision placement of implants. Figure 9 shows the 3D printed drill guide, designed using CT scan data of mandible/maxilla. The CAD model of the drill guide was prepared in SolidWorks software and fabricated on a desktop 3D printer at Indian Institute of Information Technology, Design and Manufacturing, Jabalpur.

3D printing helps to obtain accurate dimensions in the endodontic/orthodontic guides. Researchers are also working in the area of automatic designing of guides which can be easily printed on the 3D printing machine [17].

7 Conclusions

3D printing technology offers tremendous potential to be used in the healthcare sector. Any complex anatomical features can be printed in short span of time. However, the adaptation of the technology for biomedical applications is limited in Indian context. In this regard, an attempt has been made to demonstrate the usage of 3D printing in pre-operative surgical planning process, in development of artificial temporal bone

for training and education purpose and for the fabrication of drill guides for dentistry. A systematic approach is also presented to process the medical images for 3D printing of biomedical models with better surface properties. It can be concluded that 3D printing technology has the potential to greatly influence the surgical and training procedures.

Informed Consent   Informed consent was obtained from all individual participants included in the study.

References

1. Rengier, F., Mehndiratta, A., Tengg-Kobligk, H.V., Zechmann, C.M., Unterhinninghofen, R., Kauczor, H.U., Giesel, F.L.: 3D printing based on imaging data: review of medical applications. Int. J. CARS **5**, 335–341 (2010)
2. Ganguli, A., Pagan-Diaz, G.J., Grant, L., Cvetkovic, C., Bramlet, M., Vozenilek, J., Kesavadas, T., Bashir, R.: 3D printing for preoperative planning and surgical training: a review. Biomed. Microdevice **20**, 65 (2018)
3. Zheng, Y.X., Yu, D.F., Zhao, G.J., Wu, Y.L., Zheng, B.: 3D printout models vs. 3D-rendered images: which is better for preoperative planning?. J. Surg. Educ. **73**(3), 518–523 (2016)
4. Ukey, P.D., Nayak, A., Uddanwadiker, R.V., Jain, P.K.: Temporal bone fabrication using FDM technique: issues and opportunities. Int. J. Adv. Prod. Ind. Eng. **1**(2), 47–52 (2016)
5. Francis, V., Jain, P.K.: Advances in nanocomposite materials for additive manufacturing. Int. J. Rapid Manuf. **5**, 215–233 (2015)
6. Francis, V., Jain, P.K.: Experimental investigations on fused deposition modelling of polymer-layered silicate nanocomposite. Virtual Phys. Prototyp. **11**(2), 109–121 (2016)
7. Nayak, A., Jain, P.K., Kankar, P.K., Jain, N.: Computer-aided design–based guided endodontic: a novel approach for root canal access cavity preparation. Proc. Inst. Mech. Eng. Part H J. Eng. Med. **232**, 787–795 (2018)
8. Fonseca Tavares, W.L., Diniz Viana, A.C., de Carvalho Machado, V., Feitosa Henriques, L.C., Ribeiro Sobrinho, A.P.: Guided endodontic access of calcified anterior teeth. J. Endod. **44**, 1195–1199 (2018)
9. Dawood, A., Marti, B.M., Sauret-Jackson, V., Darwood, A.: 3D printing in dentistry. Br. Dent. J. **219**, 521–529 (2015)
10. Ukey, P., Jain, P.K., Uddanwadiker, R.V.: Fabrication of Artificial Temporal Bone From CT Scan Data Using FDM Technique For Dissection Training. Unpublished Dissertation, PDPM Indian Institute of Information Technology Design and Manufacturing Jabalpur, Madhya Pradesh, India (2016)
11. Taufik, M., Jain, P.K.: A study of build edge profile for prediction of surface roughness in fused deposition modeling. J. Manuf. Sci. Eng. **138**, 061002 (2016)
12. Taufik, M., Jain, P.K.: Characterization, modeling and simulation of fused deposition modeling fabricated part surfaces. Surf. Topogr.: Metrol. Prop. **5**, 045003 (2017)
13. Francis, V., Jain, P.K.: Investigation on the effect of surface modification of 3D printed parts by nanoclay and dimethyl ketone. Mater. Manuf. Process. **33**(10), 1080–1092 (2018)
14. Nayak, A., Jain, P.K., Kankar, P.K., Jain, N.: Image-Based Method for Analysis of Root Canal Geometry (2019)
15. Nayak, A., Kankar, P.K., Jain, N., Jain, P.K.: Force and vibration correlation analysis in the self-adjusting file during root canal shaping: an in-vitro study. J. Dent. Sci. (2018)

16. Ahn, S.-Y.Y., Kim, N.-H.H., Kim, S., Karabucak, B., Kim, E.: Computer-aided design/computer-aided manufacturing–guided endodontic surgery: guided osteotomy and apex localization in a mandibular molar with a thick buccal bone plate. J. Endod. **44**, 665–670 (2018)
17. Zehnder, M.S., Connert, T., Weiger, R., Krastl, G.: Guided endodontics: accuracy of a novel method for guided access cavity preparation and root canal location 1–7 (2015)

Validation and Multi-response Optimization of Topological and Geometrical Parameters of Stainless Steel Cantilever Beam with Finite Element Analysis Subjected to Point Load Using Taguchi L$_9$ Orthogonal Array Integrated with Utility Methodology

Shubham Sharma ⓘ**, Shalab Sharma, J. Singh** ⓘ**, Gursharan Singh, Abhinav Sharma, Vivek Agarwal, Munish Mehta, S. K. Mahla** ⓘ**, and Gurpreet Singh**

Abbreviations and Nomenclature Used

FEM	Finite element method
FEA	Finite element analysis
S/N	Signal-to-noise proportion
B$'$	Width/Breadth of cantilever strut

S. Sharma (✉) · J. Singh · G. Singh · A. Sharma · V. Agarwal
Department of Mechanical Engineering, I.K. Gujral Punjab Technical University, Kapurthala 144603, Punjab, India
e-mail: rs.shubhamsharma@ptu.ac.in

S. Sharma
Department of Mechanical Engineering, DAV University, Jalandhar, Punjab, India

M. Mehta
School of Mechanical Engineering, Lovely Professional University, Phagwara 144411, Punjab, India

S. K. Mahla
I.K. Gujral Punjab Technical University Campus, Hoshiarpur 146001, Punjab, India

G. Singh
Department of Mechanical Engineering, Chandigarh University, NH-95, State Hwy, Ludhiana, Chandigarh 140413, Punjab, India

D′	Depth/Height/Altitude of cantilever strut
L′	Span length of cantilever strut
P	Concentrated load applied on cantilever strut
η'_1	Internal resisting force/stress response value
η'_2	Buckling/deflection response value
$\eta'_{observations}$	Predicted observed multi-response value for Internal resisting force/stress and buckling/deflection
x'_i	Evaluation of adequacy of ith procedure response reaction attribute
n	Number of response reaction outcomes
$U'(X'_1, X'_2…X'_n)$	Generalized summed fitness or objective function of "n" process route retort reaction attributes
$U'_i(X'_i)$	Utility of ith riposte or reaction outcome characteristics
W'_i	Weight allocated to ith retort reaction characteristics
W'_1 and W'_2	Weights allocated to internal resisting force and twisting/swerving

1 Introduction

Best design feasible or advanced optimized approach can be delineated as the technique for expanding or diminishing a required utility or fitness function, target work with defined objective or while fulfilling the predominant limitations. Contingent upon the sort of achieving our utility or objective function for the draft outline factors might be categorized as size, shape and material layout topology entities performance. The utility or fitness function concept is usually the weight of structure during performance enhancement, especially for parametric size, and limitations contemplating breaking points on internal resisting force as well as displacement. Accomplishing objective function of cantilever strut is a standout amongst the most imperative models utilized in any building frameworks. The intention of this utility function is to decrease mass of strut or pillar. Hence, altering parameters of the strut like altitude, width and length fulfilling constriction induced internal deformation and buckling of pillar. Thus, Taguchi orthogonal array technique and fitness concept are utilized for achieving our prescribed objective or utility function. Utilization of such techniques to optimize cantilever bar is uncommon. Topological and design optimization of cantilever bars have been investigated or considered [1]. Machine intelligence with computational model and strings of algorithms is utilized to examine the outcomes generated from numeric simulation FEM approach. Researchers put emphasis on diminution of weight to reinforce structural member utilizing customary strategy, Johnson's technique for endurance strength of stuff [2]. Md. Israr Equbal et al. has successfully attained the objective function of topological and geometrical parameters specifically in the connecting rod of an engine by using FEM and Taguchi technique [3]. Optimal conduct contour profile in the view of an effect

of metallic stream contortion and distortion in metal-shaping/forming manufacturing process was used by investigators in their studies. The aim of re-enactment and achieving objective function is to limit the shaping or forging external resistance force and create sound forgings with no discontinuity/defect. Whereas [4] carried out the geometric as well as structure layout optimization of continuum architectural arrangements using utility model methodology in Swanson analysis tool system. Researchers investigated the mathematical programming of topological parameters of a rigid structural strut bar fastened at one end making an allowance for implementing to the stem of cereal grains (in crop farming), beneath distortion heaps [5]. Our goal was towards reaching the objective function in a cantilever bar having measurements of altitude (D′), breadth (B′) and span length (L′). Influence of internal resisting force contemplated like concentrated force (P) or heap stuff load. A stuff matter of cantilever bar was Stainless Steel having permissible internal resisting force of 78–85 Giga-pascal and buckling/distortion of 7.4 mm separately. All measurements assessed for the duration of investigation were in standard system international entities as shown in Fig. 1.
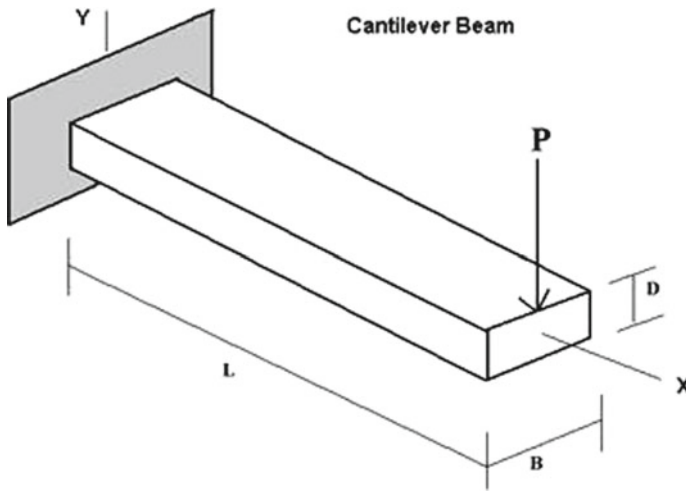
Fig. 1 Cantilever strut with loading configuration and co-ordinate system

Table 1 Stages of several controls on hegemonize factors

Control parameters	Stage 1	Stage 2	Stage 3
Width (B′)	B′0	B′1	B′2
Height (D′)	D′0	D′1	D′2
Length (L′)	L′0	L′1	L′2

Table 2 Taguchi L_9 orthogonal array with allocated values of control parameters

Experimental trial runs	Width (B′) (mm)	Height (D′) (mm)	Length (L′) (mm)
1	B′0	D′0	L′0
2	B′1	D′1	L′0
3	B′2	D′2	L′0
4	B′0	D′1	L′1
5	B′1	D′2	L′1
6	B′2	D′0	L′1
7	B′0	D′2	L′2
8	B′1	D′0	L′2
9	B′2	D′1	L′2

2 Experimentation

2.1 Design of Experiments Using Taguchi L_9 Orthogonal Array

The experimental layout trials configuration is carried out in view of the Taguchi Technique. G. Taguchi, Japanese "guy of skill and knowledge" surrounded and characterized a technique which relies on a symmetrical cluster of orthogonal array. This system has been broadly utilized in various sectors, such as building headed for streamline procedure factors. Affecting hegemonize factors evaluated for this research examination were altitude (D′), breadth (B′) and span length (L′). To carry out this design experimentation, 3 stages for both control or hegemonize aspects were utilized. In light of the amount of control/hegemonize factors and their respective stages, L_9 symmetrical cluster-based arrays were taken. Table 1 illustrates different stages of control of hegemonize factors and Table 2 shows research trial arrangement amid allotted estimations of control factors.

2.2 Taguchi Technique

Taguchi procedure utilizes a proportion of signal-to-noise power (*S/N*) as an execution measure to pick control levels. The signal–to-noise power proportion considers

both the average arithmetic mean and the manufacturing changeability. In this tentative research trial, an efficient multi–reaction-based response variables examination which relies on Taguchi symmetrical cluster-based orthogonal array strings technique and Utility idea are utilized for accomplishing the multi-responses reactions (Internal resisting force and Buckling). Taguchi projected various conceivable *S/N* proportions to acquire the amendment of ideal variable factors. Ostensible was a better decisive factor chosen for this present research investigation.

$$[\eta_1'] = \left(10 \times \text{Log}_{10} \frac{\text{Stress}^2}{S^2}\right) \tag{1}$$

$$[\eta_2'] = \left(10 \times \text{Log}_{10} \frac{\text{Deflection}^2}{S^2}\right) \tag{2}$$

2.3 Optimization of Multi-responses Using Fitness Approach

To enhance the realistic higher cognitive process, the assessments of several assorted aspects ought to be commonly shared to offer performance composite indices. Group of these composite indices is termed as utility or effectiveness of an item. It is hard to acquire the finest mix of process parameters during experimentation trials, when there are numerous reaction responses to be optimized in order to attain the criterion of the best objective function as an ideal approach for one particular response reaction as a consequence of non-ideal elucidation of an additional response. An implementation of loads or weights within a fitness model facilitates in these troublesome circumstances by distinguishing virtual comparative criticality of several diverse outcomes. On the off chance that x_i' illustrates evaluation of adequacy of ith procedure response reaction attribute and "*n*" signifies the number of response reaction outcomes, in that case, the generalized summed fitness or objective function can be composed as specified underneath in condition (3) [6]:

$$U'\left(X_1', X_2' \ldots X_n'\right) = f[U_1'\left(X_1'\right), U_2'\left(X_2'\right) \ldots U_n'\left(X_n'\right)] \tag{3}$$

where $U'(X'_1, X'_2 \ldots X'_n)$ was generalized summed fitness or objective function of "*n*" process route retort reaction attributes and $U'_i(X'_i)$ was utility of *i*th riposte or reaction outcome characteristics. Allotment of weights totally depends upon the necessities and preferences amid an assortment of diverse reaction outcomes. Thus, the specific weighted form of condition can be articulated as mentioned in eq. (4):

$$U'\left(X_1', X_2' \ldots X_n'\right) = \sum_{i=1}^{n} W_i' \times U_i'(X_i') \tag{4}$$

where

$$\sum_{i=1}^{n} W_i' = 1.0$$

where W_i' is the weight allocated to ith retort reaction characteristics, and

$$\eta_{\text{Observation}}' = (\eta_1' W_1' + \eta_2' W_2') \tag{5}$$

where W_1' and W_2' are weights allocated to internal resisting force and twisting/swerving correspondingly as mentioned in Eq. (5). Allotment of weights to the progress attributes and traits were depended upon background knowledge and practice of engineers.

3 Results and Discussions

Imitation or simulation model for particular key aspects was performed according to Taguchi's investigation plan in view of the tentative research design format delineated in Table 2, and individual estimations of internal resisting force, distortion and buckling for every simulation run are transformed over into their relevant S/N proportions according to condition (1) and condition (2) and are mentioned within Tables 3 and 4, respectively.

3.1 Single Objective Riposte Optimization

Ideal regulated arrangements and anticipated optimum entities for internal resisting force and buckling were resolved independently by utilizing Taguchi orthogonal

Table 3 Tentative investigational research trial outcomes for internal resisting force in conjunction with Signal-to-noise proportion curve

Stress 1 (GPa)	Stress 2 (GPa)	Stress 3 (GPa)	η_1'
78.7	35	105	6.219
67.81	30	92	6.129
58.85	26	78	6.289
70.64	32	98	6.097
61.2	30	84	6.668
72.65	33	101	6.097
63.75	30	90	6.179
75.56	35	106	6.139
65.2	31	92	6.238

Table 4 Tentative experimental research trial outcomes for deflection in conjunction with signal-to-noise proportion curve

Deflection 1 (mm)	Deflection 2 (mm)	Deflection 3 (mm)	η'_2
6.319	6.219	5.549	23.379
5.158	4.989	4.499	23.048
4.249	4.139	3.679	22.449
5.858	5.689	5.059	22.378
4.819	4.669	4.159	22.379
6.358	6.258	5.569	22.979
5.529	5.288	4.699	21.689
7.219	6.989	6.209	21.829
5.949	5.849	5.199	22.869

Table 5 Reaction response for internal resisting force

Levels	Width (B′) (mm)	Height (D′) (mm)	Length (L′) (mm)
1	6.189	6.169	6.238
2	6.309	6.151	6.280
3	6.211	6.380	6.191
Delta	0.119	0.219	0.101
Rank	2	1	3

Table 6 Reaction riposte for buckling force

Levels	Width (B′) (mm)	Height (D′) (mm)	Length (L′) (mm)
1	22.48	22.73	22.96
2	22.41	22.76	22.57
3	22.76	22.16	22.13
Delta	0.349	0.598	0.829
Rank	3	2	1

array methodology. At that point, the overall summed arithmetic average for *S/N* proportions internal resisting force and buckling are figured as mean of all cured response reactions for every stage as appeared in Tables 5 and 6. Figures 2 and 3 portrays the effect of three control factors on internal resisting force and buckling force correspondingly.
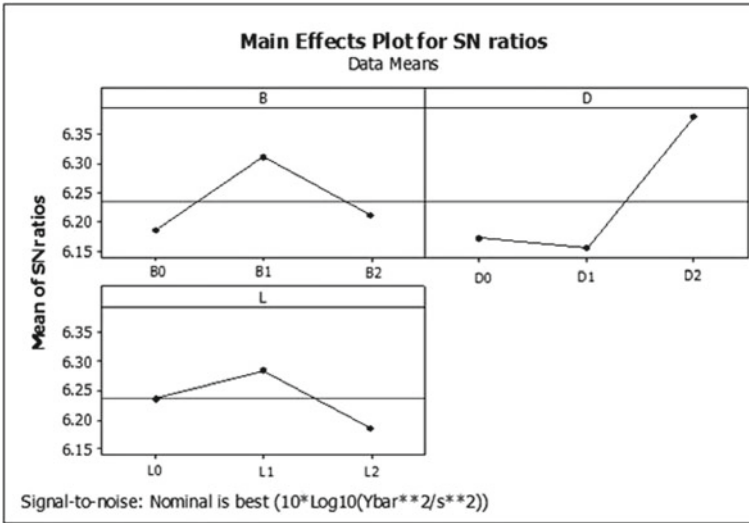
Fig. 2 Mean effect plot for internal resisting force
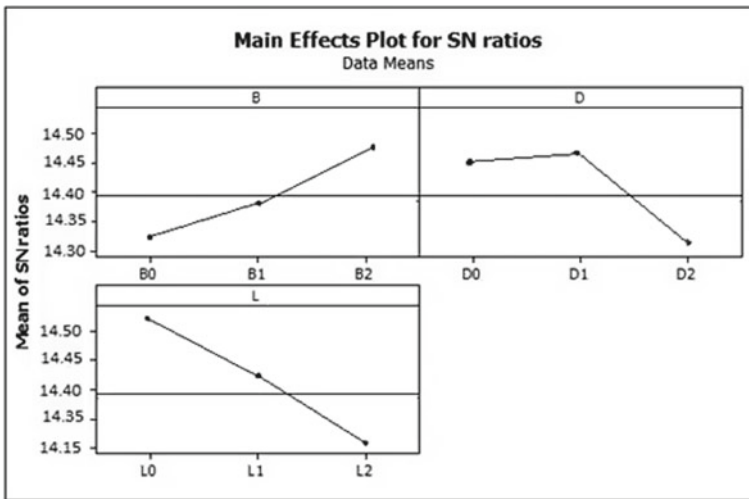
Fig. 3 Mean effect plot showing influence of three control factors on buckling force

Table 7 Taguchi orthogonal array amid multi-reaction response/Riposte S/N proportions

Experimental trial runs	η'_1	η'_2	$\eta'_{observations}$
1	6.219	23.379	14.799
2	6.129	23.048	14.588
3	6.289	22.449	14.369
4	6.097	22.378	14.2375
5	6.668	22.379	14.5235
6	6.097	22.979	14.538
7	6.179	21.689	13.934
8	6.139	21.829	13.984
9	6.238	22.869	14.5535

Table 8 Reaction response outcomes for achieving Multi-objective utility function

Levels	Width (B′) (mm)	Height (D′) (mm)	Length (L′) (mm)
1	14.329	14.448	14.603
2	14.358	14.459	14.432
3	14.489	14.271	14.164
Delta	0.149	0.188	0.441
Rank	3	2	1

3.2 Multi-objective Response Optimization

Ideal amalgamation of operation route factors for concurrent enhancement in achieving objective function of internal resisting force and buckling is acquired by the arithmetic average entities of multi-reaction retort signal-to-noise proportion of a generalized summed fitness approach. Table 7 demonstrates an estimation of signal-to-noise proportion for particular reaction riposte and Table 8 illustrates signal-to-noise proportion for generalized summed fitness function. The graphical portrayal of the impact and influence of three control factors is shown in Fig. 4. In this present research task, break even with significance is given for both internal resisting force and buckling. In this way, weights allocated to internal resisting force and twisting/swerving force were obtained, W'_1 and $W'_2 = 0.5$. The investigation is completed by utilizing the programmable coded software tool particularly used for outline framed design layout of trial relevance applications usually termed as MINITAB 15.0.
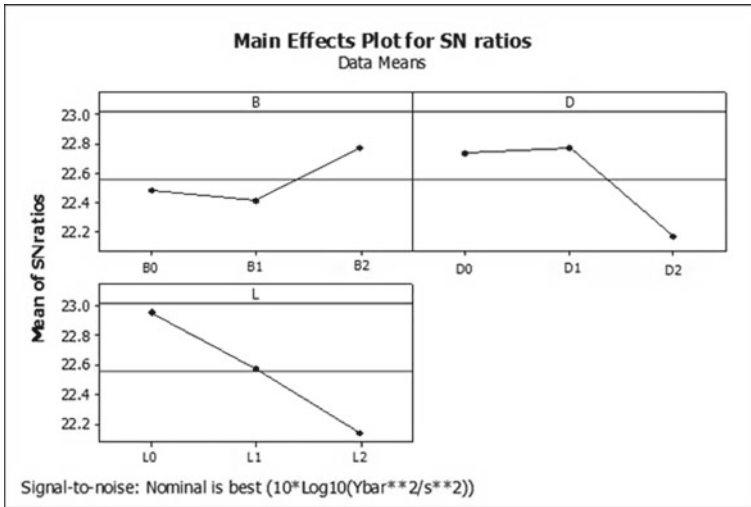
Fig. 4 Multi-objective optimization showing the combined effect of three control factors on internal resisting force and buckling force

4 Validation of Performed Tentative Research Trials Using Finite Element Analysis (FEA)

Outcomes generated are approved with the assistance of mercantile business FEA bundle ANSYS11 for imitation or building model for predefined key variables, demonstrating, creating grid nodes-based network and experimental investigation. The material utilized is Stainless Steel A36 with 204GPa as tensile or elastic modulus and dimensionless Poisson's proportion as 0.32. The component compose kind utilized is Solid Tet10node92. Grid nodes-based network generated is of fine quality mesh for an effective outcome. After deep examination, the internal resisting force and buckling detected are abridged by 11% than novel entities, which well thought out as safe and sound for cantilever strut.

5 Results and Discussions

From an arithmetic average of S/N proportions as appeared in Table 5 for internal deformed force, it is discovered that height/depth has the most astounding rank "1". In this way, altitude or depth has the most noteworthy impact on internal deformed force whereas length has the slightest impact. The ideal amalgamation of control factors for optimum internal deformed force is observed as (B′-2D′-3L′2) where characters B′, D′, L′ signifies hegemonize/control factors: breadth, height and span length, respectively, whereas statistics symbolizes their stages.

Table 9 Validation of performed tentative research trials using Finite element analysis (FEA)

Combinations	Stress (GPa)		Deflection (mm)		Volume
	Actual	Experimental	Actual	Experimental	
B′2D′3L′2	61.198	54–86	4.819	4.678	30880
B′3D′2L′1	65.149	55–87	4.959	4.912	29645
B′3D′2L′1	65.149	55–87	4.959	4.912	29645

Additionally, commencing an arithmetic average of signal-to-noise proportions as appeared in Table 6 for buckling/deflection force, result shows that span length has the most elevated rank "1" and in this way, it influences buckling essentially whilst the breadth/width have a minimum impact on buckling/deflection. Ideal amalgamation or combinations of hegemonize/control factors for optimum buckling was observed as (B′-3D′-2L′1) where characters B′, D′, L′ signify control/hegemonize parameters: breadth, height and span length, respectively, and statistics strings illustrate their individual levels as shown in Table 9.

From Table 7 ideal amalgamation or combination of control factors with accomplished objective function for instantaneous optimization to get an optimal internal resisting force and buckling is observed as (B′-3D′-2L′1). Where characters B′, D′, L′ signify control parameters or factors that were width/breadth, height and span length, respectively, and statistic values illustrate their particular relevant stage. Validation of research trials demonstrates that volume is abridged by 11% and subsequently the weight of structural member is likewise condensed by same without co-operating off internal resisting force and buckling entities.

6 Conclusions

Geometrical entities are imperative for any kind of structural member like length, height and width to thwart breakdown because of internal resisting force, i.e. stress, deflection or buckling, and so on when subjected to concentrated stack load. In this research task, investigation is carried out by taking cantilever bar. As clarified in this investigation, evaluation and assurance of geometrical entities prompt ideal amalgamation for the same. The result shows that altitude or depth has the most noteworthy impact on internal deformed force whereas length has the slightest impact. An ideal amalgamation of control factors for optimum internal deformed force is observed as (B′-2D′-3L′2). For buckling/deflection force, result shows that span length mostly influences the deflection whilst the breadth/width has a minimum impact on buckling/deflection. Ideal amalgamation or combinations of hegemonize/control factors for optimum buckling was observed as (B′-3D′-2L′1). Multi-objective response function for instantaneous optimization resulted in an ideal combination of control factors for both internal resisting force and buckling was observed as (B′-3D′-2L′1). The outcomes of this enhanced utility function are affirmed with imitated model

(for predefined key variables) consequences by FEA mercantile business programming bundle ANSYS11.00 tool. Hence, an endeavour is prepared to offer a summed up ideal or optimum solutions particularly for topological attributes of bar. In any case, one can go for shape as well as structural layout and orientation attributes for attaining objective function with quantitative examination with tentative trials based information for the same.

Ethical Approval This article does not contain any studies with human participants or animals performed by the author.

References

1. Yadav, S., Pathak, K., Shrivastav, R.: Shape optimization of cantilever beam using neural network. Appl. Math. Sci. **4**(32), 1563–1572 (2010)
2. Darshan, S., Varik, A., Katti, A.N., Singh, A.K., Kamath, R.R.: Size and topological optimization of cantilever beam. Int. J. Eng. Trends Technol. **4**(5), 2077–2082 (2013)
3. Equbal, M.I., Ohdar, R., Bhat, M.N., Lone, S.A.: Perform shape optimization of connecting rod using Finite element method and Taguchi method. Int. J. Modern Eng. Res. **2**(6), 4532–4539 (2012)
4. Gunwant, D., Misra, A.: Topology optimization of continuum structures using optimality criterion approach in ANSYS. Int. J. Adv. Eng. Technol. **5**(1), 470–485 (2012)
5. Sivanagendra, P., Anathasuresh, G.K.: Size optimization of cantilever beam under deformation-dependant loads with application to wheat stalks. Struct. Multidisc. Optim. **39**(3), 327–336 (2009)
6. Kaladhar, M., Subbaiah, K.V., Rao, C.S., Rao, K.N.: Application of Taguchi approach and utility concept in solving the multi-objective problem when turning AISI 202 Austenitic Stainless Steel. J. Eng. Sci. Technol. **4**(1), 55–61 (2011)
7. Polajnar, M., Drazumeric, R., Kosel, F.: Geometry optimization of a slender cantilever beam subjected to lateral buckling. Struct. Multidisc. Optim. **47**(6), 809–819 (2013)

Micro-Feature Fabrication on External Cylindrical Surface by Centreless Electric Discharge Grinding

M. S. Shekhawat, H. S. Mali, and A. P. S. Rathore

1 Introduction

Surface texturing is performed to produce surface with designed pattern of features and controlled surface roughness to fulfil specific requirements [1]. Texturing includes designed pattern, in addition to the surface irregularities generated due to machine–material interaction [2]. Electrical discharge texturing or electro-erosion texturing (EET) is emerging and the most popular EDM technique used for optimization of surface roughness along flat as well as curved surfaces. High degree of control of process influencing factors such as discharge current and pulse on time along with selective matching electrode; it is possible to achieve predetermined surface roughness of cold mill rolls within the range of 0.5 to 10 μm Ra [3]. Contactless electric discharge machining due to absence of vibration and chatter is most suitable for small size easily deformable components [4]. Honey-comb seals used in aircraft are being produced by turning on EDM [5]. Janardhan and Samuel reported about the significant increase of MRR with work speed during wire electrical discharge turning [6]. Gjeldum et al. studied the effect of workpiece dimension and machining parameters and reported that pulse current and discharge area length have significant effect, but spindle speed (up to 1000 rpm) has no observable effect on MRR. Also they developed mathematical model to predict maximum achievable MRR during cylindrical wire electrical discharge turning of X5Cr Ni 18-10 steel [7]. Song et al. developed conventional EDM-based strip electrode turning method to produce cusp free surface and reported that the new method is more efficient than wire electrical discharge turning [8]. Increase in MRR and improvement of surface finish achieved

M. S. Shekhawat
School of Manufacturing Skills, Bhartiya Skill Development University, Jaipur 302042, India

H. S. Mali (✉) · A. P. S. Rathore
Department of Mechanical Engineering, Malaviya National Institute of Technology, Jaipur 302017, India
e-mail: harlal.sngh@gmail.com

during EDG is due to improved flushing of the machining zone [9]. Evin observed surface defects like roll scorching, show-through surface, etc., during block texturing EDM of the rolling mills work rolls due to insufficient flushing of inter-electrode gap [10]. Gohil et al. during electric discharge turning of titanium alloy, noticed that discharge current, pulse on time and open gap voltage have significant effect on MRR and surface roughness [11].

Limitation of EDM for low productivity and surface defects could be overcome by the development of electrical discharge grinding (EDG) using rotating disc electrode instead of stationary electrode used in electric discharge turning [9, 12, 13]. Two variants electrical discharge grinding (EDG using metal disc electrode) and electrical discharge abrasive grinding (EDAG using metal bonded abrasive wheel electrode) were developed to widen the scope of EDM. In EDAG, frequent dressing of abrasive grinding wheel requires to restore efficiency of the process [9]. Abothula et al. stated that performance of EDG to great extent depends on the pressure and application of the dielectric [14]. At the same operating condition, responses (MRR, surface finish, TWR) of EDG output are better than EDM and extremely hard materials can be machined 2–3 times faster as compared to the conventional grinding due to improved flushing of inter-electrode gap [15–17]. Three developed variants of EDG, i.e. electro-discharge cut-off grinding, electro-discharge face grinding and electro-discharge surface grinding of process are in common use [16]. Electro-discharge cut-off grinding is used for producing grooves or parting off the workpiece. Kozak et al. concluded that EDAG can be applied in profiling and dressing of super hard metal bonded wheel due to its self-dressing mechanism [17]. Shahab Hamdavi et al. verified that load capacity and wear resistance characteristics of hydrodynamic type sliding journal bearing significantly improve by applying texturing along the mating surfaces [18].

To the best of our knowledge no research initiative was identified concerning to the development of EDG as fine texturing technique along curved surfaces using disc electrode. Effective and economic machining of advanced materials like Ni-alloy and Ti–alloy used in space craft engine still remain un addressed challenge [19].

Centreless grinding operation involves compression and shear forces which tend to deform components with low stiffness value and hence becomes unsuitable for texturing on fragile and brittle parts. On the other hand, EDM is contactless machining and encounters negligible forces but suffers poor productivity.

The current research was carried out on innovative EDM setup using newly developed centreless grinding attachment to make precise controlled grooving pattern on Inconel 600 tubular workpiece (OD 38, ID 36.80, length 40.00) using thin graphite disc wheels. The new process utilizes merits of both the processes for efficient and economic machining of challenging parts. In this research paper, authors have presented their experimental observations about the effects of current and voltage on MRR, surface roughness (Ra) and run out accuracies of the processed thin-walled parts by electric discharge centreless grinding.

2 Experimental Setup

This study is intended for the micro-feature fabrication along external surface of thin-walled Inconel 600 tube by a novel hybrid machining process, i.e. Centreless Electric Discharge Grinding (CEDG). The setup details are provided in Table 1. Amongst the various process variables affecting CEDG, peak current and open gap voltage are selected for present study to investigate their influence on MRR, surface roughness and run out accuracies. Values of other parameters are suitably adjusted for process stability.

Wheel flanges were designed and fabricated in house to adopt the thin graphite disc electrodes (Fig. 1a). A highly flexible and productive miniature work support and drive device "centreless grinding attachment" (CGA) was designed and fabricated in house. The process schematic for hybrid centreless electric discharge grinding is shown in Fig. 2. Application is filed for hybrid process patenting. The centreless grinding attachment with its independent drive is adopted on ENC-35 EDM. Cylindrical tubular trial components as detailed in Table 1 and Fig. 1b were prepared from Inconel 600 pipe. On preliminary trial with the specimen, it was observed that electric discharge centreless grinding process for the present setup stabilizes at wheel and work speed of 16 rpm and 58 rpm, respectively, with infeed rate of 0.035 mm/min. Other parameters with constant values are specified in the Table 2.

Table 1 Machine, workpiece and electrode details

Machine used	Die sinker EDM "Microtechnica® ENC-35"
Modification done for setup preparation	(i) Independently driven grinding wheel attachment mounted with thin graphite disc wheels in place of standard rod electrode holder
	(ii) Designed and developed independently driven table mounted centreless grinding attachment for workpiece support and its rotary motion
Workpiece details	Material: Inconel 60, qty.: 10 nos. (Fig. 1b) Composition: Cr-14.24%, Ni-76.35%. Fe-8.06% Melting point: 1260 °C Density: 7.94 grams/cubic centimetre Tensile strength: 620 MPa
Electrode details	Material: Thin graphite disc wheels (E25 grade) (Fig. 1a) Density:1.83 g/cubic centimetre Sublimation temperature 3652 °C
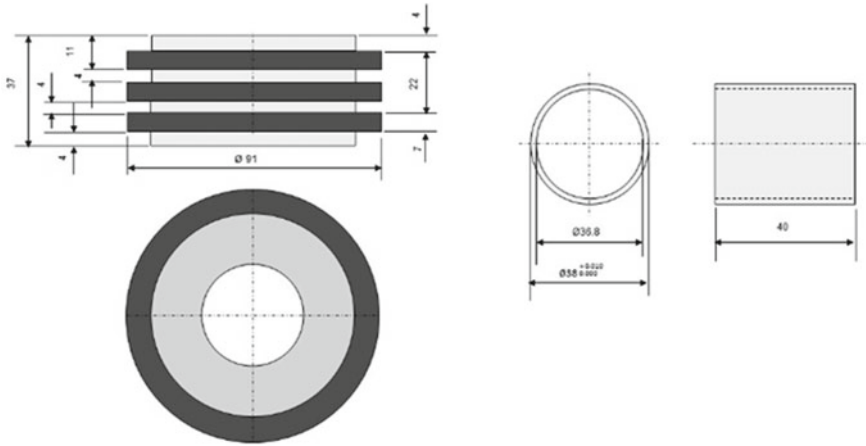
(a) Graphite wheel and flange   (b) Workpiece before grooving

Fig. 1 Disc electrode and initial workpiece dimension details
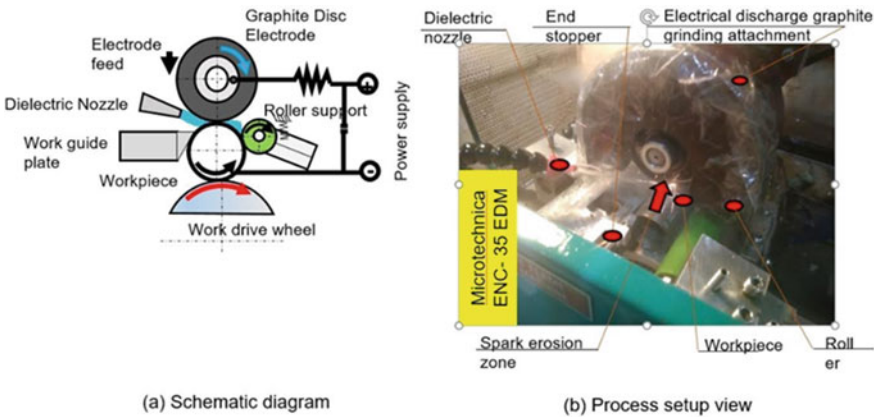
(a) Schematic diagram   (b) Process setup view

Fig. 2 Experimental setup for centreless electric discharge texturing

2.1 Centreless Electrical Discharge Texturing

Initial machine setting was performed for relative positioning of workpiece and grinding wheel. Adjustment in horizontal plane is affected through motorized table movements along X-/Y-direction. Adjustment in vertical plane is affected through servo-controlled vertical movement of tool slide carrying spinning graphite disc wheel. Process infeed is imparted to graphite disc wheel. Constant parameters, i.e. tool infeed rate, wheel speed, work speed and dielectric pressure were predetermined on the basis of trial run and values as mentioned in the table were incorporated into

Table 2 Processing data

Processing data	Description
Electrode polarity	+
Supply rating	415 ± 10%,3 phase,50 Hz
Wheel feed rate	0.035 (mm/min)
Disc electrode (graphite) speed	16 (rpm)
Sense of wheel rotation	Clockwise
Disc electrode (graphite) density	1.83 (g/cc)
Workpiece speed	58 (rpm)
Sense of component rotation	Counter clockwise
Dielectric	Dearomatized hydrocarbon fluid EDM100 (strength: 45, density: 0.784 kg/m^3)
Dielectric application	Through nozzle

the program. In this experiment, dielectric is applied through nozzles (Fig. 2) instead of submerged type EDG.

Total of 30 experiment trials were performed on 10 workpieces. Five workpieces were used for investigating the effect of peak current and other five were used to study the effect of gap voltage on MRR, surfaces roughness and run out accuracies. Each trial was conducted for 2 min with 3 times repetition at same machining variables to find average MRR, surface roughness and run out accuracy. Mass of each workpiece was measured before and after each trial on Wensar® PGB-301 (least count 0.001 g) to compute MRR. The surface roughness was measured at three positions a, b and c using Filmetrix ® Profilm 3D (20× magnification) to compute average roughness for each set of process variable. The results of experiments with their respective input parameters are presented in Table 3 and 4. Initial diameter 'd' of workpieces were measured by dial comparator (range 25–50 mm with least count 0.001 mm) set for 38.000 mm using slip gauge set. Subsequent diameter dimensions D_i and D_f were computed from material removal and verified by comparator. MRR was computed using Eq. 1.

$$\text{Material removal rate (mg/min)} = (W_s - W_e)/t \tag{1}$$

Here W_s and W_e are mass of workpiece at the start and end of each trial and t is time in min.

Table 3 Effect of current on MRR surface roughness and run out accuracies

Workpiece no.	Experiment no.	Peak current (Amps)	Gap voltage (V)	Diameter Ø d (mm)		MRR (mg/min)	Run out error (μm) (w.r.t. P, Q)	Average surface roughness (μm Ra)
				D_i	D_f			
I	1	3	50	38.005	38.002	32.00	7	2.67
	2	3	50	38.002	37.990	**37.97**	7	
	3	3	50	37.990	37.977	43.94	**8**	
II	4	6	50	38.007	37.998	88.00	6	3.26
	5	6	50	37.998	37.989	**92.00**	7	
	6	6	50	37.989	37.979	96.00	7	
III	7	9	50	38.006	37.993	127	7	4.37
	8	9	50	37.993	37.980	**131.40**	8	
	9	9	50	37.980	37.966	135.8	8	
IV	10	12	50	38.010	37.991	190	6	5.14
	11	12	50	37.991	37.971	**195.36**	6	
	12	12	50	37.971	37.951	200.72	**8**	
V	13	15	50	38.000	37.978	216	6	5.2
	14	15	50	37.978	37.956	**219**	7	
	15	15	50	37.956	37.934	222	**8**	

3 Result and Discussion

The experiment results showing the effect of current and gap voltage on process response are presented in Tables 2 and 3, respectively.

3.1 Effect of Current on MRR, Surface Roughness and Run Out Accuracies

The effect of peak current on process output is presented in Table 3 and Fig. 3. MRR and surface roughness increase with the increase of peak current whereas run out accuracy remains unaltered. Higher current electric discharge penetrates deeper into the material and forms large crater size. The surface roughness is related to crater depth that depends on the peak current (Fig. 4).

Table 4 Effect of gap voltage on MRR surface roughness and run out accuracies

Workpiece no.	Experiment no.	Peak current (Amps)	Gap voltage (V)	Diameter Ø d (mm)		MRR (mg/min)	Run out error (μm) (w.r.t. P, Q)	Average surface roughness (μm Ra)
				D_i	D_f			
I	1	20	30	38.003	37.970	325	6	9
	2	20	30	37.970	37.937	**332.39**	7	
	3	20	30	37.937	37.903	339.78	**7**	
II	4	20	35	38.005	37.979	260	6	7.87
	5	20	35	37.979	37.952	**266.31**	**8**	
	6	20	35	37.952	37.925	272.62	7	
III	7	20	40	38.004	37.981	227.2	7	7.76
	8	20	40	37.981	37.957	**233.6**	**6**	
	9	20	40	37.957	37.933	240	8	
IV	10	20	45	38.007	37.987	203	6	7.09
	11	20	45	37.987	37.966	**209.7**	7	
	12	20	45	37.966	37.944	216.4	**8**	
V	13	20	50	38.002	37.990	117.5	7	6.35
	14	20	50	37.990	37.978	**121.37**	**8**	
	15	20	50	37.978	37.965	125.24	8	
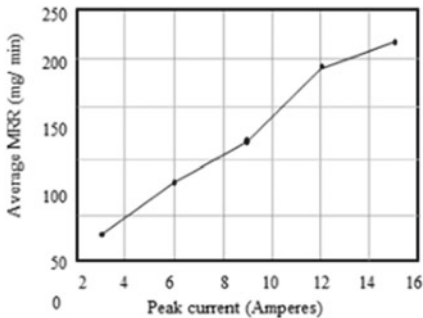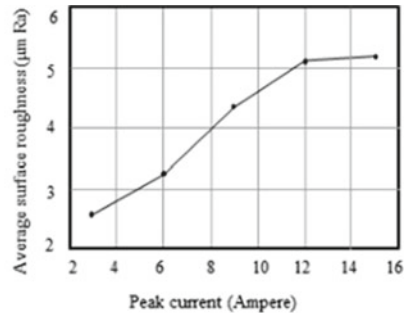
(a) Current v/s MRR **(b)** Current v/s Surface roughness

Fig. 3 Plot for effect of peak current

3.2 Effect of Gap Voltage on MRR, Surface Roughness and Run Out Accuracies

The effect of gap voltage on considered process output is presented in Table 4 and Fig. 5. MRR and surface roughness both decrease with the increase of gap voltage. The run out accuracies in this case also remains. Higher gap voltage increases the

(a)

(b)
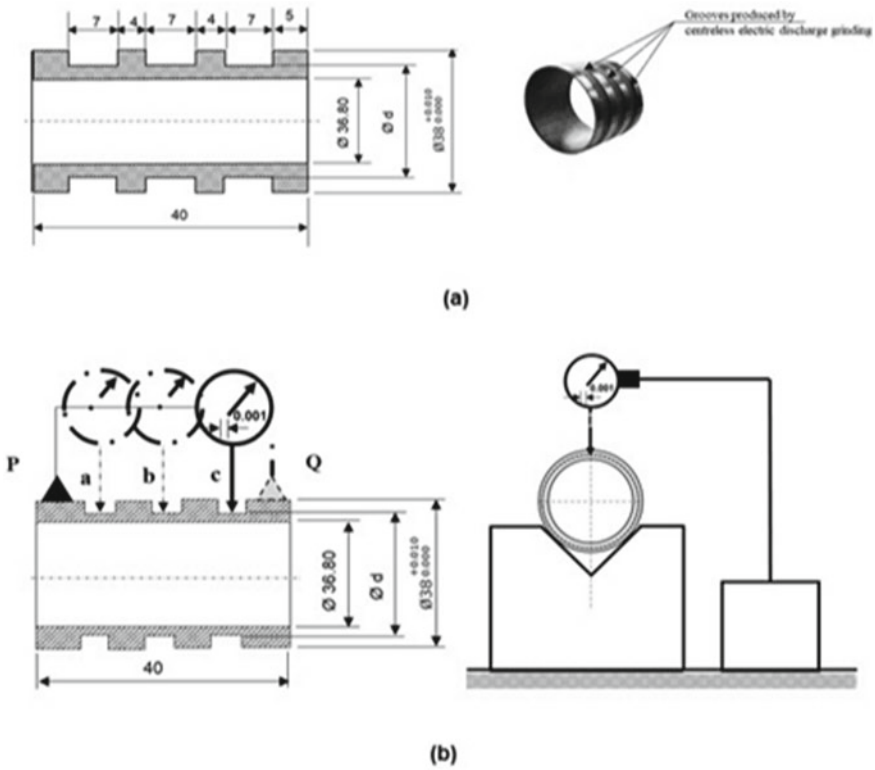
Fig. 4 Setup for run out check
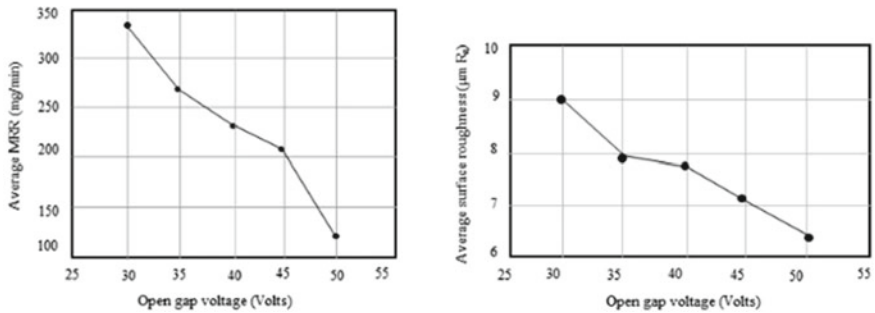
Fig. 5 Plot for effect of gap voltage

inter-electrode gap and discharge penetrates relatively less depth into the material and forms smaller crater size. The surface roughness is related to crater depth and reduces with the increase of gap voltage.

4 Conclusion

Newly developed hybrid centreless electric discharge grinding process found to be was a precise and efficient method for micro-feature fabrication on rotationally symmetric electrically conductive components. Groove of 7 mm width with controlled depth of cut 1.5 to 17 μm (to reduce diameter by 3–34 μm) could be produced and run out accuracy is maintained below 8 μm. For the above depth of cut, no variation for width dimension and squareness error along groove was observed. The increase of peak current significantly increases MRR and surface roughness whereas both the responses have inverse effect for increase of gap voltage. Hybrid centreless electric discharge texturing by grinding does not affect run out accuracies of the component. Run out accuracy of driving wheel which in this case is less than 8 μm, governs the accuracy of parts (6–8 μm) textured by centreless electric discharge grinding. Maximum average MRR of 332.96 mg/min could be achieved at peak current 20 amp and gap voltage 30 V with average surface roughness of 9 μm Ra. Minimum average surface roughness of 2.67 μm Ra could be achieved at peak current of 3 amp and gap voltage of 50 V. Maximum outer diameter to wall thickness ratio (D/W) for 38 mm OD, in the present case it is 66.9:1. Further research can be carried out to optimize the process parameters to process the parts with D/W ratio even greater than 66.9:1. The process is capable to produce micro-sized different types of profile grooving, i.e. vee, trapezoidal, curved, etc., with precisely controlled width and depth on thin-walled fragile cylindrical parts using suitably profiled wheel electrode.

References

1. Evan, C.J., Bryan, J.B.: "Structured", "textured" or "engineered" surfaces. CIRP Ann. Manuf. Technol. **48**, 541–555 (1999)
2. Off shore Power System Division Westinghouse and Avondale Shipyard Incorporation.: Surface texture (profile) measurement (1992)
3. Gohil, V., Puri, Y.M.: Turning by electric discharge machining: A review. J. Eng. Manuf. **23**(2), 195–208 (2015)
4. Mohammadi, A., Tehrani, A.F., Emanian, E., Karimi, D.: Statistical analysis of wire electrical discharge turning on material removal rate. J. Mater. Process. Technol. **205**(1), 283–289 (2008)
5. Gohil, V., Puri, Y.M.: Turning by electrical discharge machining: A review. Proc. Inst. Mech. Eng. B J. Eng. Manuf. **231**(2), 195–208 (2017)
6. Janardhan, V., Samuel, G.L.: Pulse train data analysis to investigate the effect of machining parameters on the performance of wire electro discharge turning (WEDT) process. Int. J. Mach. Tools Manuf **50**(9), 775–788 (2010)
7. Gjeldum, N., Bilic, B., Veza, I.: Investigation and modelling of process parameters and workpiece dimensions influence on material removal rate in CWEDT process. Int. J. Comput. Integr. Manuf. **28**(7), 715–728 (2015)
8. Song, K.Y., Park, M.S., Chu, C.N.: EDM turning using a strip electrode. J. Mater. Process. Technol. **213**, 1495–1500 (2013)
9. Hofy, H.E.: Advance machining processes: Non-traditional and hybrid machining processes. McGraw-Hill Companies, New Delhi, (2005)
10. Evin, I.E.: Electro-discharge texturing of tool steel surfaces for rolling of steel sheets. Transfer Inovaci (2015)

11. Gohil, V., Puri, Y.M.: Statistical analysis of material removal rate and surface roughness in electrical discharge turning of titanium alloy (Ti-6Al-4 V). In: Proceedings of the Institution of Mechanical Engineers, Part B: Journal of Engineering Manufacture (2016)
12. Shu, K.M., Tu, G.C.: Study of electrical discharge grinding using metal matrix composite electrodes. Int. J. Mach. Tool Manuf. **4**, 845–854 (2008)
13. Jain, V.K.: Advance machining processes, p. 2007. Allied Publisher, New Delhi (2007)
14. Abothula, B.C., Yadava, V., Singh, G.K.: Development and experimental study of electrical discharge face grinding. Mater. Manuf. Process. (2010)
15. Proceedings of the National Conference on Trends and Advances in Mechanical Engineering, pp. 19–20. YMCA University of Science and Technology, Faridabad, Haryamna (2012)
16. Shih, H.R., Shu, K.M.: A study of electrical discharge grinding using a rotary disc electrode. Int. J. Adv. Manuf. Technol. (2008)
17. Kojak, J., Rajurkar, K.P., Wei, B., Nooka, S.R.: Abrasive electro-discharge grinding of advanced materials. In: Proceedings of the 11th National Conference on Trends and Advances in Mechanical Engineering. YMCA University of Science and Technology
18. Hamdavi, S., Ya, H.H., Rao, T.V.V.L.N.: ARPN. J. Eng. Appl. Sci. **11**(2016), 172 (2016)
19. Gaur, S., Bharti, P.K.: Experimental study with rotating tool electrode of EDM for Ni-alloy. Int. J. Modern Eng. Res. **5** (2015)
20. Van Wezel, W., Jorna, W.J.: Paradoxes in planning. Eng. Appl. Artif. Intell. **14**(3), 269–286 (2001)

Feasibility Study on Machining of Niobium to Achieve Nanometric Surface Finish

Harsh Sanmotra, Vinod Mishra, Sukhdev Gangwar, Gagandeep Singh, Rajbir Singh, Harry Garg, and Vinod Karar

1 Introduction

Niobium is a versatile metal that holds good plasticity, high melting point, low evaporating point, better corrosion resistance, and good superconductivity. All these properties make niobium suitable for its direct application in areas related to cryogenics, medical diagnostics, atomic energy, and aerospace. Another major area in which niobium finds its use is in SRF (Superconducting Radio Frequency) cavities. Sophisticated systems such as electron lasers and ions colliders rely on these resonating cavities for efficiently accelerating the particle beams. SRF cavities are generally made of pure niobium with the layering of Nb3Sn, as at lower temperatures niobium acts as a superconductor. Unlike cavities made of other conductive metal, niobium cavities are eminent for its ability to store a greater amount of energy with less dissipation. It was discovered by researchers [1] that the residual surface resistance depends upon the quality of the cavity surface, hence achieving high surface finish, and material purity is the main challenge that decides the effectiveness of these cavities. Finishing operations by chemical and mechanical polishing methods fall under the final step of the production of these cavities. The buffered chemical polishing and electro-polishing of niobium are studied by researchers. However, the use of strong acids makes these processes environmentally unfriendly [2, 3]. Laser

H. Sanmotra · R. Singh
Punjabi University, Patiala, India

V. Mishra (✉) · H. Garg · V. Karar
Optical Devices & Systems, Central Scientific Instruments Organisation, Sector 30C, Chandigarh 160030, India
e-mail: vnd.mshr@csio.res.in

S. Gangwar
National Institute of Technical Teachers Training and Research, Sector 26, Chandigarh, India

G. Singh
Doaba Institute of Engineering and Technology (DIET) College, Ghataur, Mohali, Punjab, India

ablation-based polishing is also explored as a potential process to polish the niobium surface along with added advantage to avoid the use of harmful chemicals [4]. However, non-deterministic material removal mechanism of polishing methods is limiting the uniform surface quality throughout the cavity. Precision machining is another aspect to achieve the desired profile and finish. Extensive work is reported to understand the machining of the niobium. The study is reported on machining of niobium by cemented carbide tool with the limited surface roughness of 0.8 μm [5]. While machining the niobium it was reported that cutting force and feed force are strongly affected by the depth of material removal. The cutting speed is reported relatively less significant [6, 7], Ultra-precision machining by utilizing a diamond tool is another approach to achieve the controlled form accuracy and nanometric surface finish. Various factors of ultra-precision machining are explored by researchers to cut a variety of materials, e.g., polymers, metals, crystals, alloys of materials to achieve superior surface quality [8–12]. However, due to the chemical wear of costly diamond tool, this process is not economical and not explored much.

In the current study, we explored machining of niobium by CBN cutting tool. Different machining parameters are explored to verify their effects on surface quality. The surface topology of the machined surface is studied in detail. The relationship between surface quality and input parameters is developed and optimum combination to achieve a good surface finish is found. The study is helpful to understand the various issues of precision machining of niobium material for various industrial applications.

2   Methods and Materials

In order to perform this experiment, Precitech Nanoform-200 ultra-precision lathe is used as shown in Fig. 1. The Nanoform-200 machine is having T-configuration on which the workpiece is mounted on *X*-axis and the tool is mounted on tool post at *Z*-axis. The additional *C*-axis is also provided, which is required for machining of complicated shapes by utilizing the simultaneous motion of all three (*CXZ*)-axis [13]. As CBN tool inserts are known for their excellent fracture and wear resistance, they are mostly used for dry machining of hard materials. In this work, the kyocera make CBN tool of 0.75 mm tool nose radius, rake angle 0°, included angle of 30° is utilized for experiments. The tool is mounted on the tool post and the tool tip is aligned with the rotation axis of the machine by using available video tool setter with the machine. The niobium material with Body Centered Cubic (BCC) structure is used for machining trials. The hardness of the niobium workpiece is 50HRC. The disks of diameter 13.5 mm and thickness 2.44 mm are prepared by wire-cut Electrical Discharge Machining (EDM) process.

The niobium disks are lapped from one side and fixed on the pre-machined flat aluminum fixture. The fixture along with workpiece is mounted on the machine by using vacuum clamping. In the case of precision machining, it is crucial to align the workpiece with the spindle rotation axis. The precise dial indicator is utilized for dialing the workpiece.

Fig. 1 Nanoform-200, Single Point Diamond Turning (SPDT) machine

The experiments are performed by utilizing Taguchi's L9 orthogonal array. Three input parameters with their three levels are selected for the experimentation, viz., feed rate, spindle speed, and depth of cut. The selected machining input variables and their levels are given in Table 1. Each parameter has 3 levels. Hence, on the basis of this orthogonal array, a given set of combination of input parameters is obtained which is given in Table 2.

To compute the optimal cutting parameters, after each experiment from the specified L9 orthogonal array, surface morphology is characterized. The roughness (nm) and waviness (μm) are selected as a response factor. An optical profiler is used for surface metrology. Signal to noise ratio (*S/N* ratio) is obtained from the measured surface quality parameters. In our case, since the aim is to minimize surface roughness and waviness, the smaller value of *S/N* ratio was targeted, hence minimum is the better approach that is adopted to obtain the *S/N* ratio. The basic formula behind calculating *S/N* value is as follow:

$$S/N = -10 * \log\left(\sum (Y^2)/n\right)$$

Table 1 Shortlisted machining parameter and their levels

Parameters	Units	Level 1	Level 2	Level 3
Spindle speed	rpm	1000	2000	3000
Feed rate	mm/min	1	5	10
Depth of cut	μm	2	4	6

Table 2 L9 orthogonal array

Run	Spindle speed (rpm)	Feed rate (mm/min)	Depth of cut (μm)
1	1000	1	2
2	1000	5	4
3	1000	10	6
4	2000	1	4
5	2000	5	6
6	2000	10	2
7	3000	1	6
8	3000	5	2
9	3000	10	4

where '*Y*' represents the response value and '*n*' is number experiments.

3 Result and Discussion

In the current work, surface roughness and surface waviness are taken as the response parameters for the analysis. For which the measurements are done on the optical profilometer and then the results are analyzed using Taguchi's analysis. The results obtained are being discussed in the following subsections.

3.1 Optimization of Parameters for Minimum Surface Roughness

Taguchi technique-based optimization is performed based on the measured surface roughness values and calculated *S/N* ratios for each experiment as given in Table 3. The influence of machining parameters and their significance ranking is done by utilizing surface roughness and *S/N* ratio values as shown in Tables 4 and 5, respectively. The values of Tables 4 and 5 are used to obtain the mean effect and *S/N* ratio plots as shown in Figs. 2 and 3, respectively. The plots suggest that optimum parameters to attain low value of surface roughness are level 2 of each parameter, i.e., feed rate of 5 mm/min, spindle speed of 2000 rpm, and depth of cut of 4 μm. Also, the slopes of plots and ranking tables show that spindle speed is the most significant parameter followed by depth of cut and feed rate. The possible reasons for dominance of spindle speed and depth of cut over feed rate are high hardness of niobium and variation of temperature while varying depth of cut and spindle speed. The detailed 3D surface topology for surface roughness measurements are shown in Fig. 4.

Table 3 *S/N* Ratio and surface roughness values

Combinations	Spindle speed (rpm)	Feed rate(mm/min)	Depth of cut (µm)	3D surface roughness, Sa (nm)	*S/N* ration (dB)
1	1000	1	2	929	−59.3603
2	1000	5	4	722	−57.1707
3	1000	10	6	816	−58.2338
4	2000	1	4	541	−54.6639
5	2000	5	6	764	−57.6619
6	2000	10	2	792	−57.9745
7	3000	1	6	830	−58.3816
8	3000	5	2	588	−55.3875
9	3000	10	4	797	−58.0292

Table 4 Response average S/Ratios: Surface roughness

Level	Spindle speed	Feed rate	Depth of cut
1	−58.25	−57.47	−57.57
2	−56.77	−56.74	−56.62
3	−57.27	−58.08	−58.09
Delta	1.49	1.34	1.47
Rank	1	3	2

Table 5 Response table for means: Surface roughness

Level	Spindle speed	Feed rate	Depth of cut
1	822.3	766.7	769.7
2	699.0	691.3	686.7
3	738.3	801.7	803.3
Delta	123.3	110.3	116.7
Rank	1	3	2

3.2 Optimization of Parameters for Minimum Surface Waviness

Waviness represents the low-frequency errors in surface topology and it is an important parameter that define the surface functionality. Same as surface roughness the optimization of input parameters is performed based on the measured surface waviness values and *S/N* ratios are calculated for each experiment as given in Table 6. The effect of machining parameters and their significance ranking is done by utilizing surface waviness and *S/N* ratio values as given in Tables 7 and 8 respectively. The values of Tables 7 and 8 are used to obtain the mean effect and *S/N* ratio plots as

Main Effects Plot for Means

Data Means

Fig. 2 Main effects plot for surface roughness means
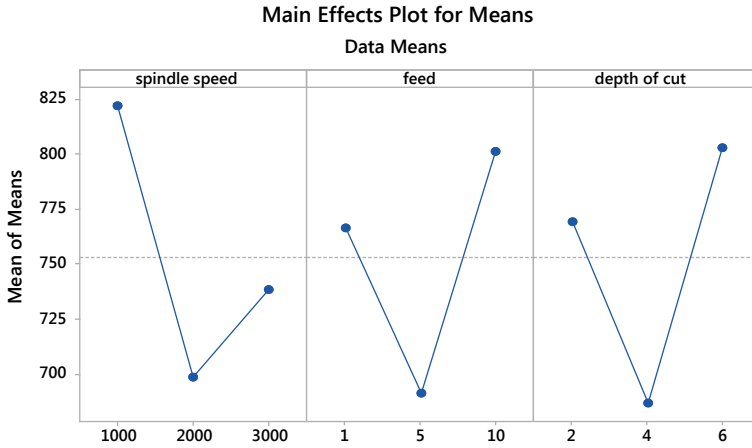
Main Effects Plot for SN ratios

Data Means
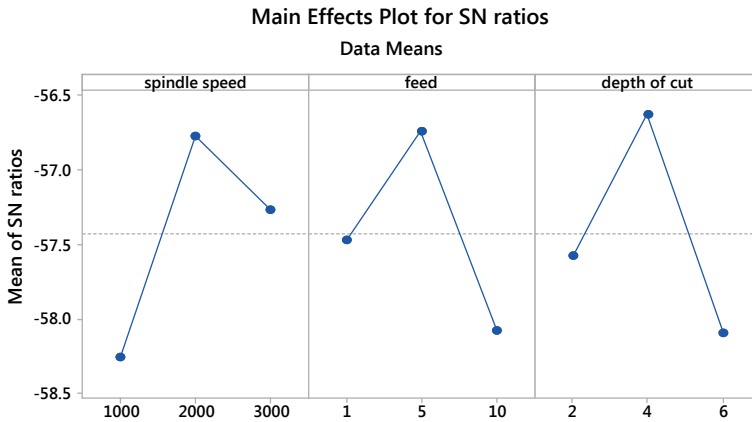
Signal-to-noise: Smaller is better

Fig. 3 Main effects plot for surface roughness *S/N* ratios

shown in Figs. 5 and 6, respectively. By analyzing the plots, it can be concluded that moderate level of spindle speed, lower level of feed rate, and a moderate level of depth of cut are optimum to achieve the minimum surface waviness. The plots suggest that optimum parameters to obtain minimum surface waviness are spindle speed of 2000 rpm, feed rate of 1 mm/min, and depth of cut of 4 μm. Also, the slopes of plots and ranking tables show that spindle speed is the most influencing parameter followed by feed rate and depth of cut. The detailed 3D surface topology for surface waviness measurements is shown in Fig. 7.

The experimental results reveal that optimum machining parameters for surface roughness and waviness are not the same. The decision for the optimum parameter is
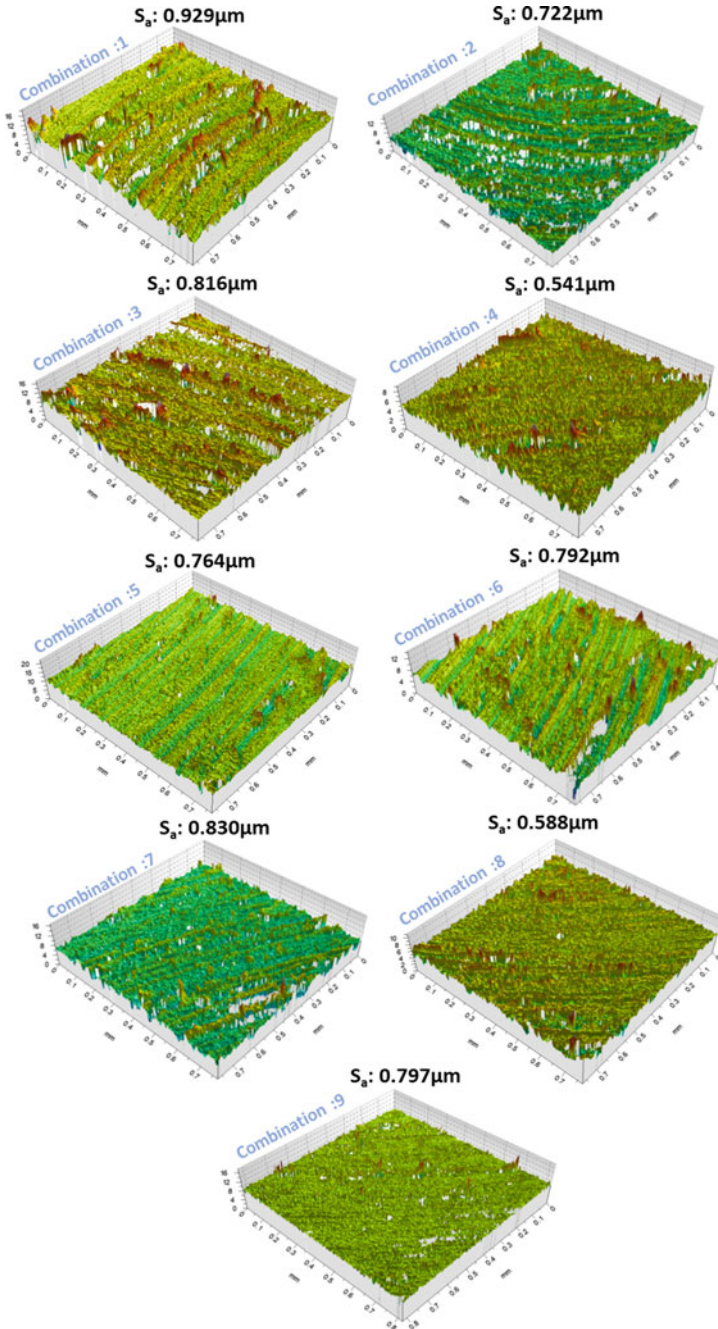
Fig. 4 3D surface topology for surface roughness

Table 6 *S/N* ratio and surface waviness values

Run	Spindle speed (rpm)	Feed rate (mm/min)	Depth of cut (μm)	Waviness, Wa (μm)	*S/N* ratio
1	1000	1	2	3.24	−10.2109
2	1000	5	4	2.3	−7.23456
3	1000	10	6	3.13	−9.91089
4	2000	1	4	0.565	4.959031
5	2000	5	6	1.57	−3.91799
6	2000	10	2	1.77	−4.95947
7	3000	1	6	1.09	−0.74853
8	3000	5	2	0.934	0.593062
9	3000	10	4	1.82	−5.20143

Table 7 Response average for *S/N* ratios: Surface waviness

Level	Spindle speed	Feed rate	Depth of cut
1	−9.119	−2.000	−4.859
2	−1.306	−3.520	−2.492
3	−1.786	−6.691	−4.859
Delta	7.813	4.690	2.367
Rank	1	2	3

Table 8 Response table for means: Surface waviness

Level	Spindle speed	Feed rate	Depth of cut
1	2.890	1.632	1.981
2	1.302	1.601	1.562
3	1.281	2.240	1.930
Delta	1.609	0.639	0.420
Rank	1	2	3

a tradeoff between the achieved value of roughness and waviness. Also, the decision can be taken on the basis of the importance of response parameters based on the application. We targeted the better surface roughness for the SRF cavity; hence, the optimum parameters are selected as, feed rate of 5 mm/min, spindle speed of 2000 rpm, and depth of cut of 4 μm. The machining cut is performed by setting optimum parameters. The surface roughness of 107 nm and waviness of 0.55 μm is achieved. Significant improvement can be seen on surface roughness while machining with optimum machining parameters. In future other techniques can be utilized to optimize the multi-objectives simultaneously.
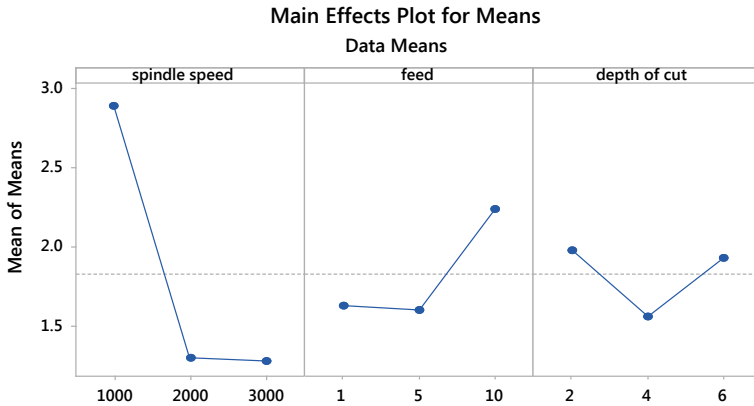
Fig. 5 Main effects plot for waviness means
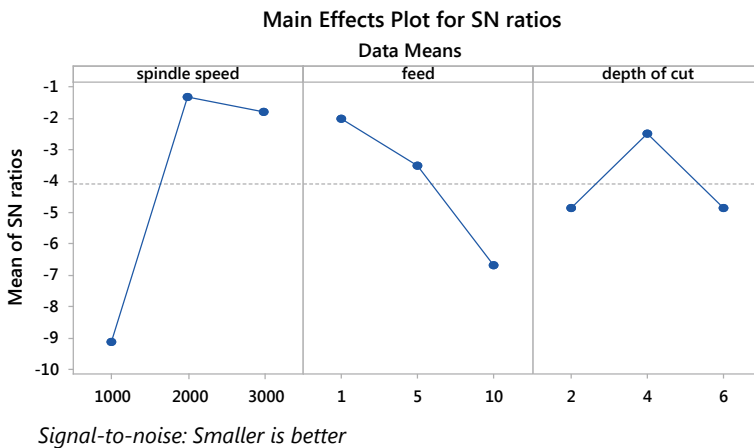
Fig. 6 Main effects plot for waviness S/N ratios

4 Conclusion

Machining experiments on niobium material are performed by varying the important machining parameters, i.e., feed rate, spindle speed, and depth of cut by utilizing CBN cutting tool. The detailed measurement of surface topology in terms of surface finish and waviness is performed to know the effects of machining parameters. It is found that moderate values of depth of cut 4 μm, spindle speed 2000 rpm, and feed rate 5 mm/min are optimum to achieve minimum surface roughness and waviness. The current study is helpful to understand the effect of machining parameters on surface quality. The current study is only a feasibility study and detailed analysis can be
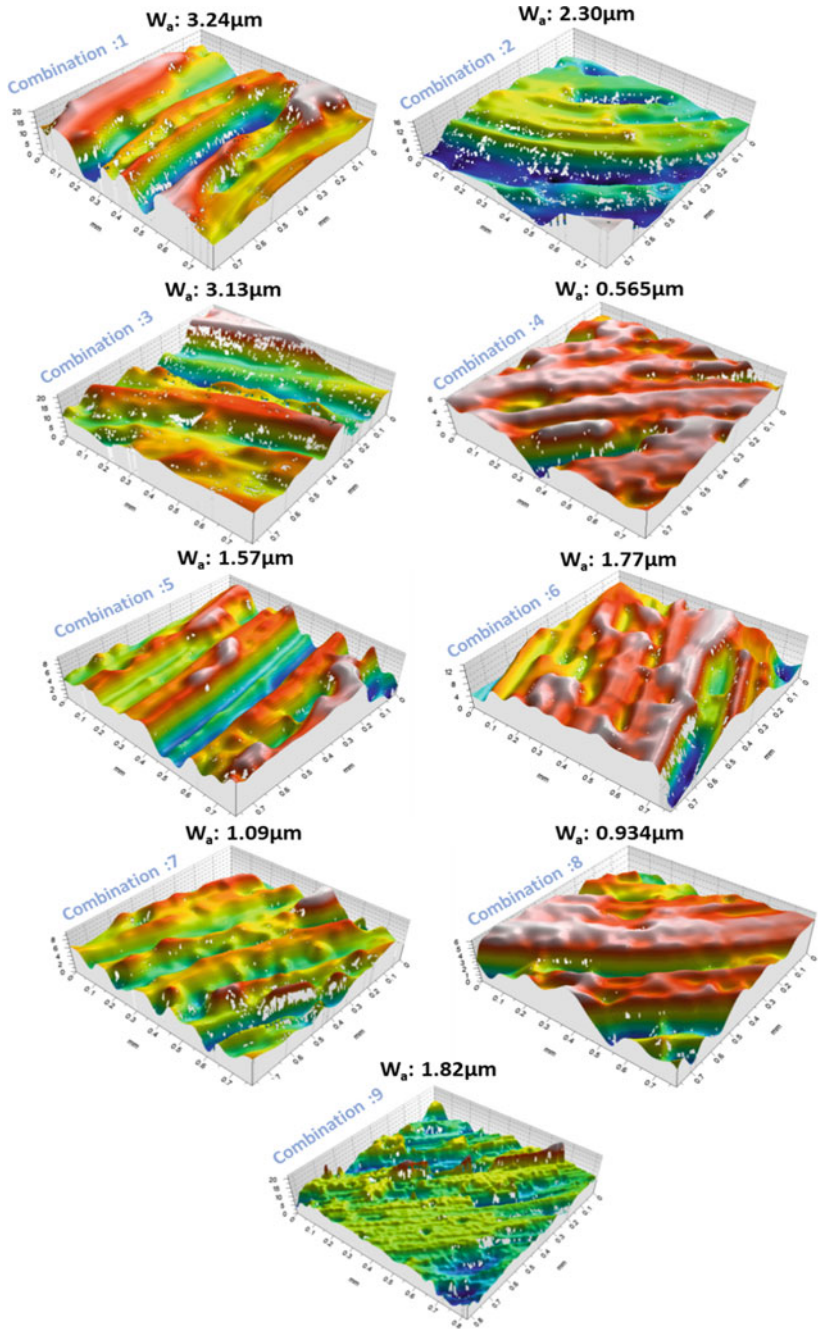
Fig. 7 3D surface topology for surface waviness

performed in future to understand the precision machining of niobium material in depth.

References

1. Pfister, H., et al.: Superconducting cavities. Cryogenics **16**(1), 17–24 (1976)
2. Boffo, C. et al.: Optimization of the BCP processing of elliptical Nb SRF cavities. FERMILAB-CONF-06-181-TD (2006)
3. Ciovati, G., Hui, T., S.G. Corcoran.: Buffered electrochemical polishing of niobium. J. Appl. Electrochem. **41**(6), 721–730 (2011)
4. Zhao, L. et al.: Laser polishing of niobium for superconducting radio-frequency accelerator applications. Phys. Rev. Special Topics Accel. Beams **17**(8), 083502 (2014)
5. Olsson, M. et al.: Surface roughness and sub-surface deformation measurements in machining of niobium. Procedia CIRP **71**, 413–417 (2019)
6. Aouici, H. et al.: Analysis of surface roughness and cutting force components in hard turning with CBN tool: Prediction model and cutting conditions optimization. Measurement **45**(3), 344–353 (2012)
7. Mamalis, A.G., Kundrak, J., Gyani, K., et al.: On the dry machining of steel surfaces using superhard tools. Int. J. Adv. Manuf. Technol. **19**(3), 157–162 (2002)
8. Sharma, R. et al.: A hybrid fabrication approach and profile error compensation for silicon aspheric optics. Proc. Inst. Mech. Eng. B J. Eng. Manuf. **233**(5), 1600–1607 (2019)
9. Mishra, V. et al.: Ultra-precision diamond turning process. Micro Nano Machin. Eng. Mater. 65–97 (2019) (Springer, Cham)
10. Mandal, S. et al. Fiber bragg grating sensor for temperature measurement in micro turning of optical surfaces with high surface integrity. Int. J. Optomechatron. **7**(4), 244–252 (2013)
11. Khatri, N. et al.: An experimental investigation on the influence of machining parameters on surface finish in diamond turning of silicon optics. International Conference on Society for Optics and Photonics 2015, vol. 9654. (2015)
12. Singh, K. et al.: Investigation of tool life and surface roughness during single point diamond turning of silicon. Int. J. Sci. Res. **2**(6), 265–267 (2013)
13. Mishra, V. et al.: Generation of freeform surface by using slow tool servo. Freeform Opt. Opt. Soc. Am. (2017)

Parametric Optimization Based on Mechanical Characterization of Fused Deposition Modelling Fabricated Part Using Utility Concept

Dilip Kumar Bagal, Abhishek Barua, Ajit Kumar Pattanaik, Siddharth Jeet, and Dulu Patnaik

1 Introduction

The decline of manufactured goods improvement cycle time is a paramount apprehension in commerce to persist economical in the open market and henceforth, emphasis has moved from old-fashioned product improvement practice to quick fabrication practices similar to rapid prototyping (RP). Fused deposition modelling or some time coined as FDM is a RP process which constructs object or parts by piling and bonding melted deposits in a single trend. This technique employs very thin preheated thermoplastic filaments as a feed to nozzle tip which deposits the thermoplastic layer by layer for building any part. In wide-ranging manufacturing applications, these manufactured parts sometimes become unsuitable because of their low mechanical strength. As a consequence, significant determinations have been committed by various investigators to advance the mechanical strength of the parts [1–9].

In this present exploration, emphasis on valuation of mechanical strength of part was made-up with the help of fused deposition modelling. The whole experimentations are planned in Taguchi method using L27 Orthogonal array. From the experimental data, the process constraints such as raster angle, layer thickness, air gap, orientation and raster width which considerably influence the mechanical strength

D. K. Bagal · A. K. Pattanaik (✉)
Department of Mechanical Engineering, Government College of Engineering, Kalahandi,
Bhawanipatna, Odisha, India
e-mail: ajitpgcek@gmail.com

A. Barua · S. Jeet
Department of Mechanical Engineering, Centre for Advanced Post Graduate Studies, BPUT,
Rourkela, Odisha, India

D. Patnaik
Department of Electrical Engineering, Government College of Engineering, Kalahandi,
Bhawanipatna, Odisha, India

Table 1 Properties of commercially available ABS M30 [1–9]

Parameter	Value
Density	1040 kg/m^3
Rockwell hardness	109.5 HRC
Ultimate strength (Tensile)	36 MPa
Yield strength (Tensile)	32 MPa
Young's modulus	2.413 GPa
Elongation at break	7%
Layer thickness	0.18–0.25 mm

of processed part are to be optimized. Consequent optimization of the stated process constraints to maximize the responses using Taguchi-based Utility concept for multi-objective optimization of part build characteristics is also done.

2 Experimental Analysis and Methodology

2.1 Material Used for Fabrication

Acrylonitrile Butadiene Styrene (ABS M30) is used for fabrication test specimen. It comprises acrylonitrile, styrene and butadiene resins (90–100%) with some percentage of tallow, mineral oil and wax (0–2%). ABS-M30 has about 25–70% more strength than regular ABS material. Layer bonding in ABS M30 is considerably tougher than regular ABS which makes it ideal for any type of modelling, purposeful prototyping, development of tools and production parts [1–9] (Table 1).

2.2 Specimen Fabrication

The 3D models of the test specimens were modelled with the help of CATIA V5 R21 solid modelling software. After the development of the models, their STL files were exported to FDM software (Insight). Here, factors are fed according to the experiment design for fabrication of the specimens. Bendable filament of ABS M30 is provided from a filament spool to head of nozzle of the FDM machine. All the testing specimens were made-up using FORTUS 400mc machine for their respective distinctive measurement.

2.3 Design of Experiments and Specimen Testing

Here, five parameters of FDM process are identified as significant factors, viz., raster angle, layer thickness, air gap, orientation and raster width. Henceforth they are designated for studying their impact on the responses. All the factors' level was designated in accord with the allowable lowest and highest settings acclaimed by the apparatus manufacturer, practice and real industrial uses. Fixed parameters and control parameters are provided in Tables 2 and 3, respectively.

The tensile test of the test specimens depicted in Fig. 1a was executed using automated material testing system (Model: BSUT 60JD, Make: Blue Star) with crosshead speeds of 1 mm/s. Similarly, compressive strength and three-point bending tests of the respective specimen shown in Fig. 1a, b at break of the test specimens were done using the same machine used for tensile test with crosshead speed of 2 mm/min [3, 5, 8]. For determination of impact strength of specimen depicted in Fig. 1c, Charpy test was performed in pendulum impact tester (Model: IT-30, Make: Fuel Instruments & Engineers Pvt. Ltd.). During testing of the specimen, quick and powerful knock by hammer pendulum was given which struck the specimen with 4 m/s of speed. The impact energy engaged through the respective specimen is calculated using the variation in the potential energy of the original and ending point of pendulum hammer. Impact strength is calculated using Eq. (1) for the specimen [5] (Fig. 2).

$$\text{Impact strength} = \frac{\text{impact energy in joules}}{4\,\text{mm} \times 3.2\,\text{mm}\ (\text{for the given specimen})} \tag{1}$$

Table 2 Fixed parameters [1–9]

Parameter	Value
Part fill style	Perimeter or raster
Counter width	0.4064 mm
Part internal style	Solid normal
Observable surface	Normal raster
X Y & Z contract feature	1.0038
Perimeter to raster air gap	0.0000 mm

Table 3 Control parameters and their levels [1–9]

Parameters	Symbol	Levels		
		1	2	3
Layer thickness	A	0.127 mm	0.178 mm	0.254 mm
Part orientation	B	0°	15°	30°
Raster angle	C	0°	30°	60°
Raster width	D	0.4064 mm	0.4654 mm	0.5064 mm
Air gap	E	0.000 mm	0.004 mm	0.008 mm
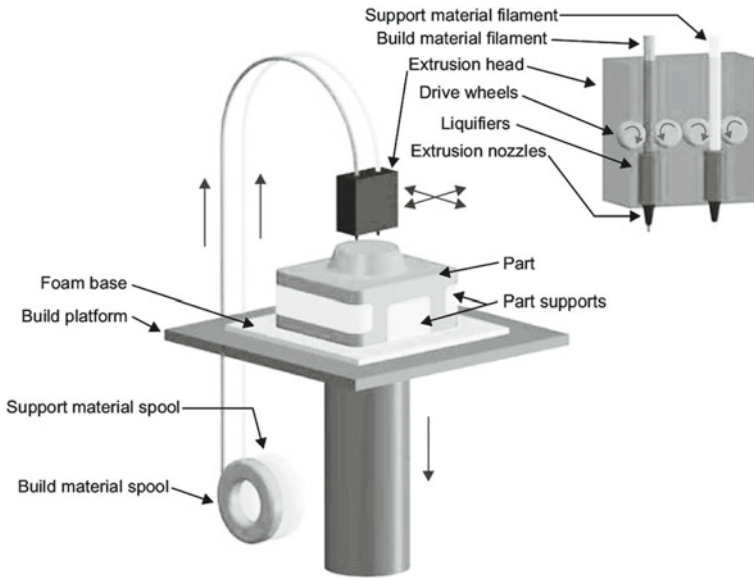
Fig. 1 FDM process
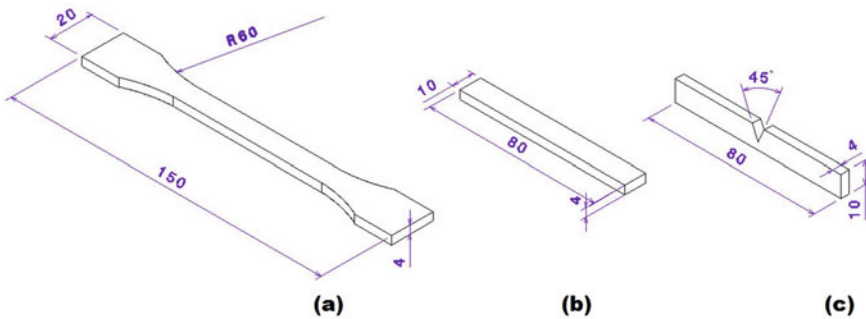
Fig. 2 a Tensile test and compressive test sample, **b** Flexural test sample, **c** Impact test sampling. (All dimensions are in mm) (ASTM D638)

2.4 Utility Concept

In Utility concept, the combined utility function is stated according to Eq. (2) [10–14]:

$$U(y_1, y_2, \ldots, y_n) = f(U_1(y_1), U_2(y_2), \ldots, U_n(y_n)) \tag{2}$$

where $U_j(y_j)$ is utility of jth attribute, n is no. of estimation conditions. The whole utility function is the total sum of discrete utilities shown as follows:

$$U(y_1, y_2, \ldots, y_n) = \sum_{j=1}^{n} U_j(y_j) \tag{3}$$

The general utility function can be expressed after allocating weights to the attributes as follows:

$$U(y_1, y_2, \ldots, y_n) = \sum_{j=1}^{n} w_j U_j(y_j) \tag{4}$$

For defining utility value of every attributes, a preference scale is constructed. The preference number (P_j) can be stated as follows:

$$P_j = A_j \times \log\left(\frac{y_j}{y_j'}\right) \tag{5}$$

Where y_j and are observed and standard values, respectively; A_j is continual for jth trait. The minimum value for is used for favourable norms and supreme value is used in case of non-favourable norms. A_j can be calculated as [10–14]:

$$A_j = \frac{9}{\log\left(\frac{y_j}{y_j}\right)} \tag{6}$$

The overall utility value (U) is calculated using the following equation:

$$U = \sum_{j=1}^{n} w_j P_j \text{ subject to the constraint that } \sum_{j=1}^{n} w_j = 1 \tag{7}$$

3 Results and Discussions

All the testing samples were fabricated by means of Taguchi's experimental design as presented in Table 4. In accordance with the design of experiment, 27 experimental runs are done in the FDM setup. After fabrication of part specimen, flexural strength, compressive strength, impact strength and tensile strength are recorded in Table 5 along with the L27 orthogonal array of input constraints.

For optimizing FDM process parameters by employing Utility concept, first Eqs. (5) and (6) were used to construct the preference scales for flexural strength, impact strength, tensile strength and compressive strength.

Table 4 Orthogonal array L27 of the experimental runs and responses

Expt. No.	A	B	C	D	E
1.	0.127	0	0	0.4064	0
2.	0.127	0	0	0.4064	0.004
3.	0.127	0	0	0.4064	0.008
4.	0.127	15	30	0.4654	0
5.	0.127	15	30	0.4654	0.004
6.	0.127	15	30	0.4654	0.008
7.	0.127	30	60	0.5064	0
8.	0.127	30	60	0.5064	0.004
9.	0.127	30	60	0.5064	0.008
10.	0.178	0	30	0.5064	0
11.	0.178	0	30	0.5064	0.004
12.	0.178	0	30	0.5064	0.008
13.	0.178	15	60	0.4064	0
14.	0.178	15	60	0.4064	0.004
15.	0.178	15	60	0.4064	0.008
16.	0.178	30	0	0.4654	0
17.	0.178	30	0	0.4654	0.004
18.	0.178	30	0	0.4654	0.008
19.	0.254	0	60	0.4654	0
20.	0.254	0	60	0.4654	0.004
21.	0.254	0	60	0.4654	0.008
22.	0.254	15	0	0.5064	0
23.	0.254	15	0	0.5064	0.004
24.	0.254	15	0	0.5064	0.008
25.	0.254	30	30	0.4064	0
26.	0.254	30	30	0.4064	0.004
27.	0.254	30	30	0.4064	0.008

(1) *For compressive strength,*

Optimum value $\left(X^{*}_{\text{compressive}} \right) = 16.071$ MPa

Minimum acceptable value $\left(X^{'}_{\text{compressive}} \right) = 11.05$ MPa

(assumed, as all the experiential values of compressive strength in Table 5 are in between 11.05 and 16.07).

Using these values and Eqs. (5) and (6), the compressive strength preference scale is

$$P_{\text{compressive}} = 55.2654 \log \left(X_{\text{compressive}} / 11.05 \right) \tag{8}$$

Table 5 Output responses for experimental runs

expt. no.	Compressive strength (MPa)	Tensile strength (MPa)	Flexural strength (MPa)	Impact strength (MJ/m^2)
1.	12.98	14.34	33.98	0.3786
2.	11.92	13.28	34.10	0.3886
3.	12.88	13.29	31.12	0.3951
4.	14.02	16.64	34.30	0.4125
5.	12.96	15.58	34.42	0.4225
6.	13.91	15.60	31.44	0.4290
7.	16.07	16.24	32.12	0.3804
8.	15.01	15.18	32.24	0.3904
9.	15.97	15.19	29.26	0.3969
10.	12.11	14.26	31.37	0.3926
11.	11.05	13.20	31.49	0.4025
12.	12.00	13.22	28.51	0.4091
13.	13.36	15.11	32.44	0.4371
14.	12.30	14.05	32.56	0.4471
15.	13.25	14.06	29.58	0.4536
16.	13.66	15.78	32.81	0.4068
17.	12.60	14.72	32.93	0.4168
18.	13.55	14.73	29.95	0.4233
19.	12.42	13.39	35.82	0.3871
20.	11.36	12.33	35.94	0.3971
21.	12.32	12.34	32.96	0.4036
22.	12.41	14.50	28.85	0.3941
23.	11.35	13.45	28.97	0.4040
24.	12.31	13.46	25.99	0.4106
25.	12.68	14.44	31.99	0.3914
26.	11.62	13.38	32.11	0.4014
27.	12.57	13.39	29.13	0.4079

(2) *For tensile strength*

Optimum value $\left(X^*_{\text{tensile}}\right)$ = 16.7109 MPa

Minimum acceptable value (X'_{tensile}) = 12.33 MPa
(assumed, as all the observed values of tensile strength in Table 5 are in between 12.33 and 16.64).

Using these values and Eqs. (5) and (6), the tensile strength preference scale is

$$P_{\text{tensile}} = 68.2097 \log(X_{\text{tensile}}/12.33) \tag{9}$$

(3) *For flexural strength,*

Optimum value $\left(X^*_{\text{flexural}}\right) = 37.1859\,\text{MPa}$

Minimum acceptable value $\left(X'_{\text{flexural}}\right) = 25.99\,\text{MPa}$

(assumed, as all the observed values of flexural strength in Table 5 are in between 25.99 and 35.94).

Using these values and Eqs. (5) and (6), the flexural strength preference scale is

$$P_{\text{flexural}} = 57.8326 \log(X_{\text{flexural}}/25.99) \qquad (10)$$

(4) *For impact strength*

Optimum value $\left(X^*_{\text{impact}}\right) = 0.4369\,\text{MJ/m}^2$

Minimum acceptable value $\left(X'_{\text{impact}}\right) = 0.3786\,\text{MPa}$

(assumed, as all the observed values of impact strength in Table 5 are in between 0.3786 and 0.4536).

Using these values and Eqs. (5) and (6), the preference scale for impact strength is

$$P_{\text{impact}} = 144.7803 \log(X_{\text{impact}}/0.3786) \qquad (11)$$

(5) *The weights to all four quality characteristics have been assigned as 0.25*

The value of the overall utility value was computed using Eq. (7). Table 6 shows the utility data calculated using the above equations.

Figure 3 shows the SN-ratio plot of utility value of FDM process constraints. Essentially, the larger the utility value, the superior is the multiple performance features. In Table 7 and Fig. 3, the arrangement of A1, B2, C3, D2 and E1 displays the largest value of the SN ratio for input factors A, B, C, D and E correspondingly. Thus, A1, B2, C3, D2 and E1 is the optimum parameter combination for improving compressive strength, strength, impact strength, flexural strength and tensile of the FDM build part (Fig. 4).

Table 8 gives the analysis of variance (ANOVA) for the calculated values of utility factor. According to Table 8, factor A, layer thickness with contribution of 37.37% is the most significant controlled parameters for fabrication of FDM processed part followed by factor B, part orientation with 31.00%; factor D, raster width with 15.95%; factor C, Raster angle with 10.08% and factor E, air gap with 4.92%, of contribution when maximization of compressive strength, impact strength, tensile strength and flexural strength are concurrently measured.

$S = 0.2963$, R–Sq $= 99.33\%$, R–Sq(adj) $= 98.90\%$

Table 6 Utility data based on multiple responses

Run. no.	Compressive strength preference number (P_j)	Tensile strength preference number (P_j)	Flexural strength preference number (P_j)	Impact strength preference number (P_j)	Utility value (U)
1.	3.8752	4.4629	6.7359	0.0037	3.7694
2.	1.8330	2.1928	6.8236	1.6311	3.1201
3.	3.6772	2.2193	4.5276	2.6740	3.2745
4.	5.7192	8.8767	6.9737	5.3763	6.7365
5.	3.8341	6.9314	7.0606	6.8717	6.1744
6.	5.5358	6.9539	4.7872	7.8316	6.2771
7.	8.9999	8.1547	5.3194	0.3018	5.6939
8.	7.3641	6.1597	5.4122	1.9216	5.2144
9.	8.8401	6.1829	2.9769	2.9597	5.2399
10.	2.1971	4.3051	4.7286	2.2736	3.3761
11.	0.0000	2.0224	4.8236	3.8439	2.6725
12.	1.9846	2.0490	2.3276	4.8509	2.8030
13.	4.5557	6.0112	5.5710	9.0126	6.2876
14.	2.5730	3.8610	5.6629	10.4247	5.6304
15.	4.3632	3.8860	3.2529	11.3321	5.7086
16.	5.0947	7.3007	5.8533	4.5070	5.6889
17.	3.1579	5.2453	5.9441	6.0230	5.0926
18.	4.9066	5.2692	3.5624	6.9959	5.1835
19.	2.8169	2.4375	8.0604	1.3971	3.6779
20.	0.6784	-0.0001	8.1436	2.9892	2.9528
21.	2.6099	0.0284	5.9704	4.0099	3.1546
22.	2.7975	4.8036	2.6224	2.5133	3.1842
23.	0.6572	2.5605	2.7257	4.0777	2.5053
24.	2.5904	2.5866	0.0000	5.0810	2.5645
25.	3.3014	4.6741	5.2228	2.0856	3.8210
26.	1.2076	2.4208	5.3159	3.6606	3.1512
27.	3.0986	2.4470	2.8708	4.6705	3.2717

3.1 Confirmation Experiment

The optimal conditions using Utility concept are A1, B2, C3, D2, E1, respectively. The predicted utility factor can be computed by using the optimal parameters as

$$\mu_{\text{predicted}} = a_{2m} + b_{1m} - 3\mu_{\text{mean}} \tag{12}$$

Main Effects Plot for SN ratios

Data Means

Signal-to-noise: Larger is better

Fig. 3 SN-ratio graph with factors and their levels

Table 7 Response table for utility value

Level	A	B	C	D	E
1	13.765	10.052	11.273	12.192	13.095
2	13.078	13.407	12.034	13.618	11.675
3	9.869	13.253	13.405	10.902	11.942
Delta	3.896	3.355	2.132	2.716	1.420
Rank	1	2	4	3	5

where a_{2m} and b_{1m} are discrete mean values of utility factor with optimum level values of respective parameters and μ_{mean} is the total mean of utility factor. Table 9 shows the confirmatory test results [15, 16].

4 Conclusions

In this study, the FDM process was employed to fabricate ABS M30 parts. The process parameters were augmented using Utility concept. Purposeful relationship between process parameters and the responses (tensile strength, compressive strength, impact strength and flexural strength), for FDM built parts has been established using the optimization techniques. Based on experimental investigations done for selecting prime combination of process constraints for FDM part, few of the imperative conclusions drawn are as follows:

Residual Plots for SN ratios
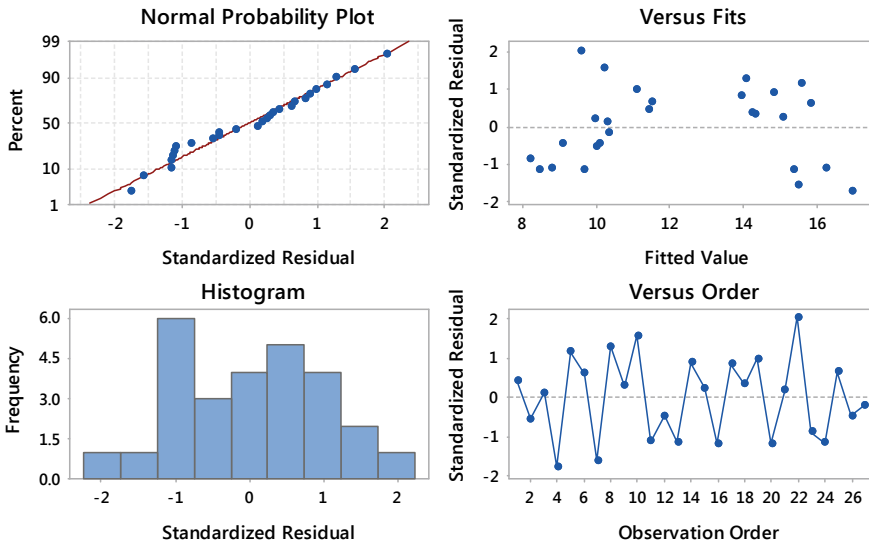
Fig. 4 Residual plot for SN-ratio graph

Table 8 Utility factor ANOVA result

Factor	D.O.F.	Seq SS	Adj SS	Adj MS	F-test	P-test	% Contribution
A	2	77.847	77.847	38.9237	443.26	0.000	37.37
B	2	64.592	64.592	32.2961	367.79	0.000	31.00
C	2	21.007	21.007	10.5036	119.61	0.000	10.08
D	2	33.233	33.233	16.6166	189.23	0.000	15.95
E	2	10.252	10.252	5.1259	58.37	0.000	4.92
Residual error	16	1.405	1.405	0.0878			0.67
Total	26	208.337					

Table 9 Confirmatory experiment outcome

Optimal setting	Predicted S/N ratio	Experimental S/N ratio
A1 B2 C3 D2 E1	7.37043	6.9366

(1) The best levels of process constraints for maximum flexural strength, tensile strength, compressive strength and impact strength for FDM processed part are part orientation of 15°, layer thickness of 0.127 mm, raster angle of 60°, air gap of 0.0004 mm and raster width of 0.4654 mm.

(2) To control the impact strength, compressive strength, flexural strength and tensile strength of FDM built part, the contribution of layer thickness is the supreme controlled parameters in comparison with other process parameters.

(3) The validation of equation for prediction of multi-response performance index was done by directing confirmation experiment.

This study has perceived that layer thickness is the chief controlling factor for attaining higher compressive strength and tensile strength. Thus, this study opens up further scope of optimization of the Fused Deposition Modelling characteristics with a more number of method constraints and impacts on convoluted geometrical parts, for attaining an improved part building superiority more rapidly.

References

1. Mahapatra, S.S., Sood, A.K.: Bayesian regularization-based Levenberg–Marquardt neural model combined with BFOA for improving surface finish of FDM processed part. Int. J. Adv. Manuf. Technol. **60**, 1223–1235 (2012)
2. Sahu, R.K., Mahapatra, S.S., Sood, A.K.: A study on dimensional accuracy of fused deposition modeling (FDM) processed parts using fuzzy logic. J. Manuf. Sci. Prod. **13**(3), 183–197 (2013)
3. Sood, A.K., Ohdar, R.K., Mahapatra, S.S.: Parametric appraisal of mechanical property of fused deposition modelling processed parts. Mater. Des. **31**, 287–295 (2010)
4. Panda, S.K., Padhee, S., Sood, A.K., Mahapatra, S.S.: Optimization of fused deposition modelling (FDM) process parameters using bacterial foraging technique. Intell. Inf. Manage. **1**, 89–97 (2009)
5. Sood, A.K., Ohdar, R.K., Mahapatra, S.S.: Experimental investigation and empirical modelling of FDM process for compressive strength improvement. J. Adv. Res. **3**, 81–90 (2012)
6. Padhi, S.K., Sahu, R.K., Mahapatra, S.S., Das, H.C., Sood, A.K., Patro, B., Mondal, A.K.: Optimization of fused deposition modeling process parameters using a fuzzy inference system coupled with Taguchi philosophy. Adv. Manuf. **5**(3), 231–242 (2017)
7. Sood, A.K., Ohdar, R.K., Mahapatra, S.S.: Parametric appraisal of fused deposition modelling process using the grey Taguchi method. Proc. Inst. Mech. Eng. B J. Eng. Manuf. **224**(1), 135–145 (2010)
8. Barua, A., Jeet, S., Bagal, D.K., Agrawal, P.K., Pattanaik, A.K.: Comparative analysis based on MCDM optimization of printing parameters affecting compressive and tensile strength of fused deposition modelling processed parts. Int. J. Techn. Innov. Modern Eng. Sci. **5**(2), 383–392 (2019)
9. Barua, A., Jeet, S., Cherkia, H., Bagal, D.K., Sahoo, B.B.: Parametric optimization of FDM processed part for improving surface finish using MOORA technique and desirability function analysis. Int. J. Appl. Eng. Res. **14**(13), 1–7 (2019)
10. Kumar, Y., Singh, H.: Multi-response optimization in dry turning process using taguchi's approach and utility concept. Procedia Mater. Sci. **5**, 2142–2151 (2014)
11. Gupta, M.K., Sood, P.K.: Optimizing multi characterstics in machining of AISI 4340 steel using taguchi's approach and utility concept. J. Inst. Eng. C **97**(1), 63–69 (2016)
12. Singaravel, B., Selvaraj, T.: Application of desirability function analysis and utility concept for selection of optimum cutting parameters in turning operation. J. Adv. Manuf. Syst. **15**(1), 1–11 (2016)

13. Varma, K.R., Kaladhar, M.: Multiple performance characteristics optimization of hard turning operations using utility based-taguchi approach. J. Mech. Eng. **45**(2), 73–80 (2015)
14. Bagal, D.K., Parida, B., Barua, A., Jeet, S., Sahoo, B.B.: Multi-parametric optimization in CNC dry turning of chromoly steel using taguchi coupled desirability function analysis and utility concept. Int. J. Appl. Eng. Res. **14**(13), 21–26 (2019)
15. Barua, A., Jeet, S., Bagal, D.K., Satapathy, P., Agrawal, P.K.: Evaluation of mechanical behavior of hybrid natural fiber reinforced nano SiC particles composite using hybrid taguchi COCOSO method. Int. J. Innov. Technol. Explor. Eng. **8**(10), 3341–3345 (2019)
16. Bagal, D.K., Barua, A., Jeet, S., Satapathy, P., Patnaik, D.: MCDM optimization of parameters for wire-EDM machined stainless steel using hybrid RSM-TOPSIS, genetic algorithm and simulated annealing. Int. J. Eng. Adv. Technol. **9**(1), 366–371 (2019)

Recharging Aquifers Through Percolation and Filtration: An Integrated Approach

Punj Lata Singh, Paritosh Rawat, and Amit Maurya

1 Introduction

Water scarcity while living on a blue planet is quite rhetorical as water being the most abundant resource available on Earth is being continuously depleted by the current practice of usage. According to the Economical definition, scarcity is defined as a gap between the available insufficient resources and theoretically limitless needs. Therefore, the issue of water scarcity is regarded as a resource management problem where clean water is the limited available resource and the increasing consumption is linked with growing population, rapid urbanisation and higher standard of living [1, 2]. Rapid construction and proliferation of concrete have led to a decrease in already existing water recharging areas because of which the groundwater recharging mechanism has been hampered; this has made water scarcity an issue of not only national interest but of a global level. Rainwater is the purest source of water in the world as it directly reaches us without coming in contact with the soil and rocks [3]. This, however, is not the real scenario as practically when the raindrops reach the earth's atmosphere they get contaminated because of the high concentration of carbon dioxide and nitrogen in the air which makes them acquire slight acidity, therefore, making them unsafe for human consumption [4]. Lack of appropriate equipment and facilities has made it difficult to capture and store rainwater because of which clean water is a big concern in India as one person dies from water-related disease every minute and four people die across the globe [5, 6] (Fig. 1).

P. L. Singh (✉) · P. Rawat · A. Maurya
Department of Civil Engineering, Amity School of Engineering and Technology, Amity University Uttar Pradesh (AUUP), Noida, Uttar Pradesh, India
e-mail: plsingh@amity.edu

P. Rawat
e-mail: paritoshbvn@gmail.com

A. Maurya
e-mail: amitmr490@gmail.com
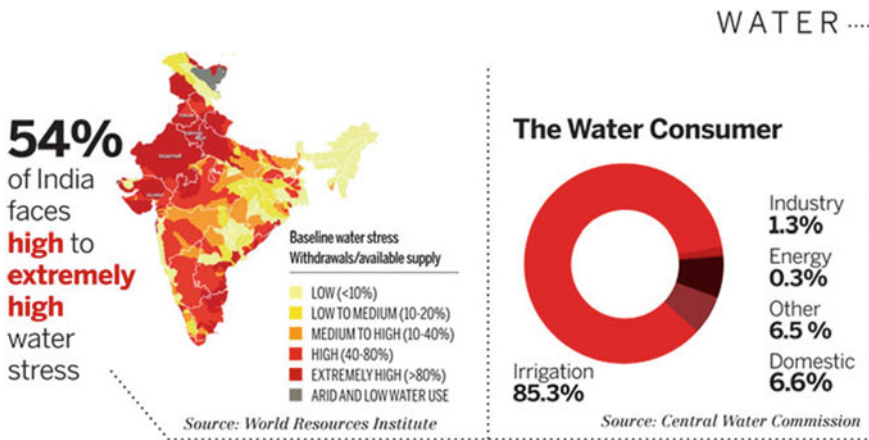
Fig. 1 Water crisis map according to the central water commission

Many regions in India have become over reliant on groundwater, which has resulted to an unsustainable practice of water being consumed faster than it is replenished naturally. This corrupt practise of depleting the groundwater has caused water tables to deteriorate incessantly [7]. The condition of groundwater in the National Capital Territory of Delhi, India is even worse. Commercialization in Delhi has made it impossible to recharge the groundwater table [8]. According to a report released by NITI Aayog on the Composite Water Management Index (CWMI) in June 2018, Delhi would run out of groundwater by 2020 and more than 600 million people would face high-to-extreme water stress which related to the growing national groundwater crisis [9]. Hence, replenishing the groundwater and recharging the aquifers in areas like Delhi has become a problem of utmost concern for the people [10]. The issue addressed here is about the improper recharging of groundwater and inefficient management of rainwater that flows through surfaces, pavements and doesn't reach the ground properly [11]. Aquifers are saturated zones with huge amount of water present below the water table; this water is present only in usable quantities and in certain places as underground water source. They are considered as an active ecosystem rather than static reservoirs of water. The amount of water which would be available in an aquifer depends upon the process of percolation. Percolation is defined as the process of water slowly passing through a filter. The percolation threshold factor decides the saturation point of an aquifer, and where the water would get accumulated in a groundwater table [12].The major issue with depletion of groundwater in India is related with the problem of overexploitation and inefficient recharging of these aquifers. The rate at which these aquifers are depleting is more than the recharging rate; hence the problem is increasing at an alarming rate [13, 14]. The natural process of recharging aquifers has become problematic because of the presence of contaminants which pollute the surface runoff water. Hence, there is a need to treat this water before it reaches the aquifer [15, 16].

After properly deliberating upon the problems related to recharging of aquifers, a model design is contrived and experiments are performed in order to make the process of rainwater harvesting through surface runoff efficient and feasible. A percolation cum filtration system which consists of a tank-like structure in the form of a basic sand filter which provides essential filtration for the water entering has been made. A sedimentation tank has also been adopted so as to remove all the major solid impurities. Post primary filtration, the water is further passed through a layer of graphene oxide coated composite sand, which is prepared in laboratory, by process of sonication and magnetic stirring along with oxidants [17]. To determine the efficiency of the filter, water quality tests were performed to check the quality of incoming rainwater on an average basis.

2 Methodology

The strategy employed to address the issue is to create and provide a specific Percolation Tank, taking into account a particular catchment, from where the surface runoff is collected. An additional modification done here is the inclusion of appropriate filtrate layers in the artificially created percolation tank, which also filters the water so captured (Fig. 2).

2.1 Theory of Filtration

The filter system involved working of following four processes:

- Mechanical Straining: There are so many suspended particles present in water and particularly those, which are comparatively bigger in size than the voids of in the actual sand layers of the filter, can't pass through these voids and get arrested in them. The resultant water, in the end, will be free from all of them.

  Most of the particles are removed in upper sand layers.

- Flocculation and Sedimentation: It is generally observed that filters are more or less able to remove even those particles which are smaller in size than the size of voids present in the filter. The assumption that supports this observation is that

Fig. 2 Block diagram with all included steps for surface runoff treatment to access as per usability

void spaces actually act like tiny coagulation–sedimentation tanks. Therefore, the colloidal matter gets arrested in these voids as a gelatinous mass and henceforth attracts other finer particles. These finer particles, then, finally settle down in the voids, being removed permanently.

- Biological Metabolism: In the voids of the filter, certain kind of microorganisms and bacteria are present. They may be existent in the form of initial coatings, over the sand grins or the other possibility is that they may be caught during the process of filtration itself. Whatever may be the case though there is a certain amount of organic impurities as a survival food for existence and therefore, these organisms utilise most of the organic impurities and then convert them into harmless compounds by the process of biological metabolism.
- Electrolytic changes: The purifying action of filter can also be explained by the theory of ionisation. As per an explanation by this theory, the process of filtration that is done in the filter happens because of the change in chemical characteristics of the water. A further explanation to this is that the sand grains of the filter media involved and also the impurities in water, they carry electric charges, that are primarily opposite in nature. Therefore when these oppositely charged particles come into contact, they ultimately end up neutralising each other and hence change the character of the water itself and eventually purify it.

The filter is constructed with acrylic glass sheets, with subsequent layers of gravel (65, 40, 20, 6 mm), followed by a sand layer of 90 cm, which is then followed by a thin charcoal/activated carbon layer above which an HDPE mesh is laid, over which a fine sand layer of 30 cm is provided. The water enters the filter cum tank through a layer of sieves so as to remove additional content such as bigger stones or leaves, etc. Post filtration the water is collected into a collection tank, designed as per the harvesting potential and maximum rainfall over the catchment.

The next step for immediate filtration and consumption of water is an additional screening of the outflowing water through a layer of graphene oxide composite sand that enhances the quality in terms of physical parameters significantly which traditional filtration and other means are unable to do. The sand composite is prepared in laboratory by undertaking various procedures. Initial and final tests were conducted on inflowing and outflowing water, to discern the physical parameters before and after filtration and to verify the efficiency of the filter (Fig. 3).

The catchment area utilised for accumulating and analysing water and its properties for its further filtration and percolation was taken of Amity School of Engineering & Technology, Amity University, Noida, Uttar Pradesh. Further, to bring about accuracy in the results, the rainfall data for last 35 years over the closest stations, i.e. NCR, as per the Indian Meteorological Department, was collated to find out the maximum possible rainfall in this span of time (Table 1).

The given table gives us information about the annual average rainfall (in mm) for the last 35 years as recorded by the Indian Meteorological Department. For the purpose of average annual rainfall calculation, the rainfall data as per 31 December of every year is taken into account which provides the cumulative rainfall over the

A = 7885.08 m²

Fig. 3 Google Earth V9.2.92.0, Amity University, Uttar Pradesh. 28°32′39″ N and 77°20′03″ E. May 05, 2018. September 02, 2019

Table 1 35 years daily weather report rainfall data as per indian meteorological department

Year	Average annual rainfall (mm)
1982–1987	706.66
1988–1993	731.66
1994–1999	731.66
2000–2005	720.00
2006–2011	731.66
2012–2016	531.8

Max rainfall taken into account: 790 mm

year. The same was done for every yearly observation, i.e. from 1982 to 2016. The maximum rainfall taken into account was 790 mm (2011).

2.2 Analysis of Inflow Water

The water collected as runoff from the catchment was subjected to initial filtration, to identify and analyse the physical and biological parameters of the taken sample of water.

The tests were conducted as per IS: 3025 (Part 22) (1986, Reaffirmed 2003): Method of Sampling and Test (Physical and Chemical) for Water and Wastewater (Table 2).

Table 2 Input water parameters

Physical/Chemical parameter	Obtained results	Standard results/limits (As per IS:3025)
Colour	5.0	5–25
Odour	Objectionable	Unobjectionable
Ph	7.53	6.5–8.5
Total hardness	105	300–600
Iron	0.043	0.3–1
Chloride	135	250–1000
Residual chlorine	<0.1	0.2 (MIN)
Flouride	<0.01	1–1.5
Total dissolved solids	630	500–2000
Sulphate	44.9	200–400
Coliform organism	10	2–5
Nitrate	1.8	45–100
Chromium	<0.0.2	0.05
Total alkalinity	690	2–5

The collected rainwater was analysed and the following observations were recorded. The observed value of coliform organism was higher than the standard range set by the IS:3025 tests. This makes the collected water unfit for utilisation. A filtration system was required to treat this water, hence a sedimentation model is fabricated to perform test of filtration.

2.3 Design and Calculations

The primary analysis in the design process is that of the catchment, i.e. rooftop of the E Block, Amity University.

The area, maximum rainfall and the harvesting potential are calculated, and are as follows (Tables 3 and 4).

We have designed a filter unit to finally filter the water collected through the sedimentation tank. Preliminary assumptions for the filter are as follows (Figs. 4 and 5).

Sand gravel type filter consists of subsequent layers of pebbles, followed by sand and gravel of increasing size. In case of a charcoal filter everything remains the same, just an additional layer of charcoal comes into the filter to provide better adsorption and hence enhancing the quality of output water post filtration.

Table 3 Design of catchment and sedimentation tank

Criteria	Value
Area of catchment	7985.08 m^2
Max rainfall (last 35 years' record)	790 mm2
Harvesting potential (Area*Rainfall*0.7)	4416000 L
Capacity of sedimentation tank (V)	4416 m^3
Depth of sedimentation tank (h)	3.5 m
Area of sedimentation tank (A)	1261 m^2
Discharge (Q) (C*A$^{0.75}$)	576 m^3
Detention time	7.67 h

Table 4 Filter design

Depth	(2.5–3.5)m
Filter medium	Gravel, sand, activated carbon, HDPE mesh
Depth of sand layer	90 cm
Consecutive layers (Gravel)	(6, 20, 40, 65) mm
Fine sand layer	30 cm
Freeboard	0.3 m
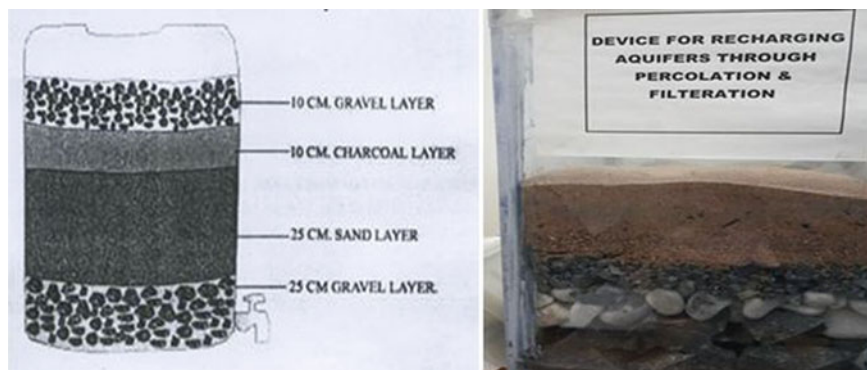
Fig. 4 Sand gravel filtration tank showing different layers and the designed device

The device which has been made for filtration of contaminated water works on the basic principle of filtration where the filtrate gets free from contaminants as it passes through the minute-sized filter particles. The tank comprises of the following components:

(a) Fine Sand
(b) Coarse Sand
(c) Pebbles
(d) Stones

Fig. 5 Sonication of graphene oxide solution

(e) Gravel.

Graphene oxide powder, hydrogen peroxide and fine sand are mixed by sonication method at 120 degrees celcius. The paste so obtained is again oven dried to get dry graphene oxide composite sand. This graphene oxide composite sand is used as the final filter medium for the outflowing water. Once it passes through the filter it is primarily filtered off major impurities and then upon passing through this composite the quality is highly enhanced in terms of physical parameters as well.

3 Results and Observations

The treated water was analysed and was compared with the input water. There was a significant decrease in the number of Coliform Organism. Changes were observed in the pH, iron content, chloride level, sulphate level, hardness level and the total dissolved solids. The filtered water was much clearer than the input water. Following are the output water observations made after testing it (Table 5).

Table 5 Output water observations

Physical/Chemical parameter	Obtained results	Standard results/limits (As per IS:3025)
Colour	<5.0	5–25
Odour	Objectionable	Unobjectionable
pH	7.05	6.5–8.5
Total hardness	95.0	300–600
Iron	0.033	0.3–1
Chloride	125	250–1000
Residual chlorine	<0.1	0.2 (MIN)
Flouride	<0.01	1–1.5
Total dissolved solids	480	500–2000
Sulphate	35	200–400
Coliform organism	4	2–5
Nitrate	1.6	45–100
Chromium	<0.0.2	0.05
Total alkalinity	510	–

4 Conclusion

The studies aimed at tackling the issue of water scarcity as well water quality through the method run off harvesting show a visible approach towards storing and utilising water for various purposes, in the best possible and safest permissible limits. The existing facilities and the catchment undertaken for study purposes show an ample harvesting potential, indicating the need for awareness and better usage of resources to do the same. Despite the uneven distribution of rainfall and erratic patterns, on an average there is a substantial amount of rainwater that can be harvested thus rendering the complex self-sufficient and sustainable. The sedimentation and filter tank designs done with respect to the available dimensions of the catchment prove to be effectively serving the purpose. The primary filtration suits the required and desired needs. As per CGWB reports, the sand available in Gautam Buddha Nagar is sandy/loamy, which serves the purpose of both storage as well as recharge. The preparation of graphene oxide sand composite and its utilisation for further screening of water significantly enhances its quality, providing parameters within the permissible limits of IS:3025, used for water quality analysis. The method and approach undertaken, thus, serve the twin purpose of recharging groundwater as well as purifying the stored water for primary and immediate consumption.

With the advent of graphene oxide in the arena of water filtration, there has been a significant upsurge in researches. It was majorly undertaken at University of Manchester, where it was proven to be highly useful in even desalination of seawater. In India, the usage of the same is still not prevalent. More so, using graphene oxide

as a sand composite in sand filters is a unique approach towards revolutionising the existing concept of traditional filtration methods. The future prospects involve various modifications of the composite to further make it easily and readily available and easier methods of preparation, accessible widely. The idea is also to enhance the economic feasibility of the filter system and make it easily usable and accessible thus serving the purpose for masses.

References

1. Anand, P.B.: Scarcity, entitlements and the economics of water in developing countries. Elgar, Northampton, MA (2007)
2. Postel, S.: The last oasis: Facing water scarcity. London (1992)
3. Ministry of Housing and Local Government (MHLG).: Guidelines for installing a rainwater collection and utilization system, 1999. Ministry of Housing and Local Government (2008)
4. Che Ani, A.I., Shaari, N., Sairi, A., Mohamad Zain, M.F., Mohamad Tahir, M.: Rainwater harvesting as an alternative water supply in the future. Eur. J. Sci. Res. 34(1), 132–140 (2009)
5. UNICEF.: Almost 2 billion more people need access to basic sanitation by 2015 to meet global target. (2005). http://www.unicef.org/media/media_27228.html
6. Sengupta, S., Kavarana, G.: Catch water where it falls: Toolkit on urban rainwater harvesting, pp. 3–9, 43–66. Centre for Science and Environment, New Delhi (2013)
7. Rodell, M., Velicogna, I., Famiglietti, J.S.: Satellite-based estimates of groundwater depletion in India. Nature 460, 999–1002 (2009). Macmillan Publishers Limited. https://doi.org/10.1038/nature08238,10.1038/nature08238
8. Dash, J.P., Sarangi, A., Singh, D.K.: Environ. Manage. 45, 640 (2010). https://doi.org/10.1007/s00267-010-9436-z
9. Composite Water Management Index (CWMI).: A national tool for water measurement, management & improvement. Niti Ayog (2018)
10. Dutta, P.S., Bhattacharya, S.K., Tyagi, S.K.: 18O studies on recharge of phreatic aquifers and groundwater flow-paths of mixing in the Delhi area. J. Hydrol. 25–36 (1996)
11. Chaterji, G., Jha, B.M.: Manual on artificial recharge of ground water. Ministry of water resources, Central Ground water board, Faridabad (2007)
12. Croke,B., Cornish,P., Islam, A.: Integrated assessment of scale impacts of watershed intervention. Elsevier 99–148. (2015). https://doi.org/10.1016/B978-0-12-800067-0.00005-0. ISBN 9780128000670
13. Hancock, P.J., Boulton, A.J., Humphreys, W.F.: Hydrol. J. 13, 98–111 (2005). https://doi.org/10.1007/s10040-004-0421-6
14. Kumar, R., Thaman, S., Agrawal, G., Sharma, P.: Rain water harvesting & ground water recharging in North Western Himalayan region for sustainable agricultural productivity. Univ. J. Environ. Res. Technol. 1–6 (2011)
15. Maliva, R., Guo, W., Missimer, T.: Aquifer storage and recovery: Recent hydrogeological advances and system performance. Water Environ. Res. 78, 2428–2435 (2007). https://doi.org/10.2175/106143006X123102
16. Dillon, P., Pavelic, P., Page, D., Beringen, H., Ward, J.: Managed aquifer recharge: An introduction. Waterlines Report No 13, Feb 2009 (2009). http://archive.nwc.gov.au/library/waterlines/13. Accessed 13 June 2016
17. Dikin, D.A., Stankovich, S., Zimney, E.J., Piner, R.D., Dommett, G.H.B., Evmenenko, G., Nguyen, S.T., Ruoff, R.S.: Preparation and characterization of graphene oxide paper. Nature 448, 457–460 (2007). https://doi.org/10.1038/nature06016